SEYED MEHDI QOREISHI

NUMERICAL MODELING OF THE BEHAVIOR OF ROCKFILL DAMS DURING CONSTRUCTION AND IMPOUNDMENT

Thèse présentée
à la Faculté des études supérieures et postdoctorales de l'Université Laval
dans le cadre du programme de doctorat en génie civil
pour l'obtention du grade de Philosophiae Doctor (Ph.D.)

DÉPARTEMENT DE GÉNIE CIVIL ET DE GÉNIE DES EAUX
FACULTÉ DES SCIENCES ET DE GÉNIE
UNIVERSITÉ LAVAL
QUÉBEC

2013

Résumé

Cette thèse vise à modéliser numériquement des barrages en enrochements pendant les phases de construction et de mise en eau. Ceci est fait en se basant sur des essais en laboratoire et l'analyse des données de l'instrumentation insitu. Des essais triaxiaux en compression monotone à déformation/contrainte contrôlée sont effectués sur des assemblages compactés de particules de granit. Les échantillons utilisés en laboratoire ont initialement été préparés à différentes densités sèches et à différentes granulométries. Une loi de comportement élastoplastique parfait, en considérant l'élasticité non linéaire est implémentée dans le logiciel FLAC. Ceci est fait pour modéliser le comportement des particules de roche pendant les essais. Le nouveau modèle est basé sur le comportement hyperbolique, en considérant le critère de rupture de Mohr-Coulomb avec une règle d'écoulement non associé pour considérer la dilatance à cause du cisaillement. La technique de relaxation des contraintes de Nobari-Duncan est également implémentée dans FLAC avec les procédures modifiées et les nouveaux algorithmes pour reproduire les déformations causées par le mouillage. À l'aide de neuf paramètres, le modèle réussi à reproduire le comportement observé pendant les essais triaxiaux et à caractériser l'assemblage des particules de roche. Les effets de temps et de saturation sont également discutés en détail. Finalement, le modèle est utilisé pour la modélisation des étapes de la construction et de la mise en eau du barrage en enrochement LG4 construit au Québec, Canada. Les résultats de la modélisation sont comparés avec les données de l'instrumentation. Aussi, les efforts antérieurs de modélisation de ce barrage et les avantages du nouveau modèle sont discutés.

Abstract

This thesis contributes to the field of numerical modeling of rockfill dams during construction and impoundment based on laboratory research and field instrumentation. Data is presented from monotonic triaxial compression tests, in both stress and strain-controlled conditions, on compacted assemblages of granite rock particles prepared in the laboratory using different initial dry densities and grain size distribution. A nonlinear elastic-perfectly plastic constitutive model is implemented into the commercial software, FLAC, to simulate the behavior of the rock particles during the tests. The new implemented model is the traditional hyperbolic model coupled with the Mohr-Coulomb plastic failure criteria, and with a non-associated flow rule to consider shear dilatancy. The Nobari-Duncan stress relaxation technique with modified procedures and algorithms is also implemented in FLAC to reproduce the collapse deformations due to wetting. Using nine parameters, the model is successful to capture the observed behavior in the triaxial tests and to characterize the assemblage of rock particles. The effects of time and saturation are also discussed in detail. Finally, the model is used to simulate the construction and impoundment stages of LG4 rockfill dam in Quebec, Canada. The results of the modeling of both stages are compared with the instrumentation data and previous efforts of the modeling of this dam and the advantages of the new model are discussed.

Foreword

This thesis is a part of the industrial chair at Laval University titled as «*optimisation du cycle de vie des barrages en remblai*» funded by CRSNG and Hydro Québec. The first phase of the research in this chair has started on autumn 2009 with the main objective to develop tools for analyzing and predicting the behavior of embankment dams in the Province of Québec. It is divided into three categories: (i) characterisation of the materials; (ii) instrumentation and monitoring the behavior of the dams; (iii) numerical modeling and prediction of the behavior of the dams.

The laboratory tests were conducted at the geotechnical lab of Laval University under supervision of Prof. Jean-Marie Konrad and Mr. François Gilbert. The material used in the experiments was gathered from the shell zone of Romaine-2 rockfill dam which was under construction during the course of this research. The simulations were carried out using the FLAC software. The computer codes and scripts and the results of the modeling are given in the appendices and are original. The data of the LG-4 rockfill dam was provided by Dr. Marc Smith from Hydro Québec who also shared his great experience in different dam projects in province of Québec.

I would like to thank my supervisor Professor Jean-Marie Konrad for giving me valuable advice and support whenever needed, and the supervisor of the laboratory Mr. François Gilbert for preparing the triaxial test setup and providing the results of the strain controlled tests presented in the third chapter. I would also like to extend my appreciation to the members of jury who studied my thesis and provided very useful comments to make it better: Prof. Eduardo Alonso from Universitat Politècnica de Catalunya, Prof. Serge Leroueil from Université Laval and Dr. Marc Smith from Hydro Quebec; and also to the other professors and staff of my university who shared their knowledge and experiences: Prof. Denis Leboeuf, Prof. Jean Côté, Dr. Marc Lebeau and Mr. Luc Boisvert. Last but not least, I gratefully thank my family and friends who supported me during the hard time and also for the great memories we had in the beautiful Quebec City.

I dedicate this work to my country Iran where
I have studied and acquired knowledge for
twenty years.

Table of contents

Résumé ii
Abstract iii
Foreword iv
Table of contents vi
List of tables viii
List of figures ix
Nomenclature xiii
1 Introduction 1
2 A review of constitutive models implemented in modeling the behavior of rockfill dams during construction and impoundment 9
2.1 Introduction 10
2.2 Physical and engineering properties of rockfill 10
2.3 Constitutive modeling 11
2.3.1 Linear elastic model 12
2.3.2 Non-linear elastic models 13
2.3.3 Anisotropic elastic model 18
2.3.4 Elasto-Plastic models 21
2.3.5 Barcelona model (critical state concept) 30
2.3.6 Hypoplastic models 35
2.4 Comparison of constitutive models 41
2.5 Conclusion 44
3 Modeling the behavior of a compacted assemblage of rock particles during monotonic triaxial compression tests 60
3.1 Introduction 61
3.2 Constitutive equations 62
3.2.1 Elastic formulation 64
3.2.2 Plastic formulation 65
3.3 Laboratory testing 67
3.3.1 Triaxial setup 68
3.3.2 Specimen preparation 68
3.3.3 Membrane penetration 69
3.3.4 Strain rate 69
3.4 Test results 70
3.5 Calibration of the implemented model 71
3.6 Discussion of the test results 74
3.6.1 Dilative behavior 75
3.7 Conclusion 76
4 Modeling the deterioration of contact points in a compacted assemblage of rock particles during monotonic triaxial compression 97
4.1 Introduction 98
4.2 Constitutive model 100
4.2.1 Dry-wet transition 101
4.2.2 Uniaxial compression condition 101
4.2.3 Triaxial compression condition 102

4.2.4 Application in numerical modeling 103
4.2.5 Creep deformations 106
4.3 Laboratory tests 106
4.3.1 Material tested 107
4.3.2 Specimen preparation 107
4.3.3 Triaxial setup 108
4.3.4 Strain rates in strain controlled tests 109
4.3.5 Stress rates in stress controlled tests 110
4.4 Test results 112
4.4.1 Strain controlled tests 112
4.4.2 Stress controlled tests 113
4.5 Implementation of the numerical model 115
4.5.1 Strain-controlled tests 115
4.5.2 Stress-controlled tests 116
4.6 Discussion of test results 118
4.7 Conclusion 118
5 Numerical modeling of the construction and impoundment stages of LG4 rockfill dam 148
5.1 Introduction 149
5.2 Constitutive model 149
5.3 LG4 dam 151
5.4 Parameters of the model 152
5.5 Analysis of the construction stage 154
5.6 Analysis of the impoundment of the reservoir 156
5.7 Conclusion 161
6 Conclusion 182
References 190
Appendix 1 – FISH scripts 197
1- HPD model (UDM) 198
2- Stress relaxation due to wetting 206
Appendix 2 – complete results of the modeling of LG4 214
1-construction stage 214
2-impoundement stage 214

List of tables

Table 1-1- high rockfill dams around the world 8
Table 2-1 – Application of different constitutive laws in modeling rockfill dams 59
Table 3-1. Triaxial test condition 93
Table 3-2. Hyperbolic parameters in the published test data of rockfill dams 94
Table 3-3. model parameters for the assemblage of granite particles in the conducted triaxial tests 96
Table 4-1- elasto plastic parameters of the implemented model 145
Table 4-2. Strain-controlled triaxial compression test conditions 145
Table 4-3- Stress-controlled triaxial compression test conditions 146
Table 4-4- calibrated elasto-plastic parameters of the tested material 147
Table 4-5- change of modulus numbers related to the duration of stress controlled tests. . 147
Table 5-1- Elastic and plastic parameters of HPD model 179
Table 5-2- Specifications for placement of materials of different zones of LG4 dam 179
Table 5-3- Elastic parameters used in previous simulations of the construction stage of LG4 dam. 180
Table 5-4- HPD model parameters for different zones of LG4 dam used in current study (dry material). 180
Table 5-5- Hydraulic conductivities of different zones of the dam. 181
Table 5-6 – Effects of saturation on the parameters of the HPD model; the values in parentheses are for saturated material 181

List of figures

Figure 1-1. Different stages of the lifespan of a rockfill dam: (a) preparation of the foundation, construction in layers; (b) increasing the level of the water of the reservoir in several steps; (c) operation: creep, changing the level of the reservoir, seismic motion 8
Figure 2-1 – Schematic of the Bi-linear model 46
Figure 2-2 – Schematic of the K-G model 46
Figure 2-3- Stress-strain curve for the nonlinear hyperbolic model; after Singh et al. (2009) 47
Figure 2-4- Introducing the inelasticity in hyperbolic model by the means of unloading-reloading modulus (Kur) 48
Figure 2-5- variation of bulk modulus with confining stress in logarithmic scale 49
Figure 2-6- Calculation of the collapse deformation due to wetting using triaxial test results and comparison of stress-strain and volume change curves for dry, wet, and dry-wet specimens; after Nobari and Duncan (1972) 50
Figure 2-7- Perfect plastic yield surfaces in principal stress space (a)Tresca (b)Von Mises (c) Mohr-Coulomb (d) Drucker-Prager 51
Figure 2-8- Drucker-Prager and Mohr-Coulomb yield surfaces in the deviatoric plane 52
Figure 2-9- Comparison of Lade and Matsuoka-Nakai failure surfaces with Mohr-Coulomb and circumscribed Drucker-Prager surfaces in the deviatoric plane. 53
Figure 2-10- Yield surfaces for Lade's double hardening model 54
Figure 2-11- Conical failure criteria of the Lade's double hardening model; and its expansion in deviatoric space 54
Figure 2-12- Predicted and measured behavior in triaxial tests of rockfill material from Roadford dam by (a) Mohr-Coulomb model with constant dilation angle; (b) Lade's model with stress dependent volumetric behavior; after Kovacevic et al. (2008). 55
Figure 2-13- Rockfill oedometer test setup with a relative humidity control system; after Oldecop and Alonso (2001) 56
Figure 2-14- Pressure dependence of the maximum void ratio e_{max}, the minimum void ratio e_{min}, and the critical void ratio e_c; after Bauer (2009). 57
Figure 2-15- Estimation of solid hardness from an isotropic compression test in a semi-logarithmic representation; after Bauer (2009). 57
Figure 2-16- Influence of the reduction of the solid hardness on the compression behavior 58
Figure 2-17- Influence of the reduction of the solid hardness on the limit void ratios. 58
Figure 3-1 typical stress-strain-volume change behavior of sand samples in triaxial tests; after Habib and Luong (1978) 78
Figure 3-2 Schematic of the implemented model 79
Figure 3-3 Granite rockfill particles 80
Figure 3-4- Gradation curve of the tested material 81
Figure 3-5 Triaxial specimen after the test 82
Figure 3-6 Observed stress-strain-volumetric behavior of the dry specimens in the monotonic triaxial tests 83

Figure 3-7 Observed stress-strain-volumetric behavior of the saturated specimens in the monotonic triaxial tests 84
Figure 3-8 Variations of hyperbolic parameters in published laboratory test data on rockfill 85
Figure 3-9 Calibration of the implemented model with the experimental data for dry specimens with density of 2000 kg/m3 (a) Calibration of φ0, ψ0, KE, KB, Rf at the confining pressure of 100 kPa (reference pressure) (b) Calibration of m, n, Δφ, and Δψ for a different confining pressure of 300 kPa. (c) Prediction of the behavior at 600kPa 86
Figure 3-10 Comparison of numerical model and experimental data for dry specimens with dry density of 1900 kg/m^3 87
Figure 3-11 Comparison of numerical model and experimental data for saturated specimens with dry density of 2000 kg/m^3 88
Figure 3-12 Comparison of numerical model and experimental data for saturated specimens with dry density of 1950 kg/m^3 89
Figure 3-13 Variations of steady state friction angle with confining stress, density, and saturation of the tested material. 90
Figure 3-14 Variations of dilation angle with confining stress, density, and saturation of the tested material. 91
Figure 3-15 Reference dilation angle 92
Figure 4-1.Schematic of the implemented constitutive model 120
Figure 4-2. Effect of adding water to air-dry specimen at constant axial pressure and at constant volume, in one-dimensional compression test; after Burland (1965) 121
Figure 4-3- Distribution of contact force in an assemblage of rock particles at constant stress condition. (a) Initial equilibrium (b) The disruption of contacts due to breakage of particles (c) redistribution after collapse or creep deformations; reaching a new equilibrium. 122
Figure 4-4- Comparison of stress-strain and volume change curves for dry, wet and dry-wet specimens in triaxial compression test; after Nobari and Duncan (1972) 123
Figure 4-5 – Modified grain size distribution of the triaxial specimens along with the prototype and parallel gradations. 124
Figure 4-6. Comparison of number of contact points and patterns of breakage of particles in ideal uniform and non-uniform samples. 125
Figure 4-7- Angular granite grains with different particle sizes used in preparation of the triaxial specimens 126
Figure 4-8- Influence of time on strength of concrete specimens; after Rűsch (1960) 127
Figure 4-9- Changing strain rate with time during each increment of stress-controlled test; in relation to different stages of creep; after Arenson and Springman (2005) 128
Figure 4-10– Vertical stress increments during the stress controlled triaxial compression tests 129
Figure 4-11. Stress-strain and volume change behavior of the specimens in the strain controlled triaxial compression tests 130
Figure 4-12- Applied vertical stress during the stress controlled triaxial compression test #2 131
Figure 4-13- Measured axial strain during the stress controlled triaxial compression test #2 132

Figure 4-14- Measured volumetric strains during the stress controlled triaxial compression test #2 133
Figure 4-15- Mean axial strain rates during the stress controlled triaxial compression test #2 134
Figure 4-16 – Stress-strain response of the specimen in stress controlled test #2 135
Figure 4-17- Volume change-axial strain response of the specimen in stress controlled test #2 136
Figure 4-18- Stress-strain behavior of the dry material in strain-controlled tests 137
Figure 4-19- Changes of volumetric strain of the dry material in strain-controlled tests 138
Figure 4-20- Stress-strain behavior of the saturated specimens in strain-controlled tests 139
Figure 4-21- Changes of volumetric strain of the saturated specimens in strain-controlled tests 140
Figure 4-22- Creep components of the dry specimen during the stress controlled test #2 followed by collapse deformations due to the saturation. 141
Figure 4-23- Gradual softening of the dry specimens with time during the stress controlled tests 142
Figure 4-24- Stress-strain relation of the specimens during the stress-controlled tests 143
Figure 4-25- Volume change of the specimens during the stress controlled tests 144
Figure 5-1- Cross section of LG4 dam at highest elevation of the crest 163
Figure 5-2- Grain size distribution of material used in construction of different zones of LG4 dam 163
Figure 5-3- Results of triaxial test on a rockfill material similar to that of the shell of LG4 dam (zone 3); after Marsal (1967) 165
Figure 5-4- Results of triaxial test on the sand and gravel of the filter zone (zone 2); after Massiéra et al. (1989) 166
Figure 5-5- Comparison of different constitutive behaviors of the rockfill material of the shell of LG4 dam in virtual triaxial compression tests, generated by FLAC at reference confining pressure $\sigma 3 = Pa = 100\ kPa$. 167
Figure 5-6- Finite difference mesh of LG4 dam 168
Figure 5-7- Settlement contours of LG4 dam at the end of construction 169
Figure 5-8- Measured settlements on the axis of the core of LG4 dam at the end of construction, with predictions of different constitutive models and parameters. 170
Figure 5-9- Elements reaching the failure envelope (in purple) during the simulation of construction stage. 171
Figure 5-10- Contours of Elastic modulus at the end of construction of LG4 dam 171
Figure 5-11- Calculated vertical stress contours of LG4 dam at the end of construction 172
Figure 5-12- Profiles of maximum principal stress (kPa) at different heights at the end of construction. 173
Figure 5-13- Profiles of minimum principal stress (kPa) at different heights at the end of construction. 173
Figure 5-14 - Hydraulic transit states during the flow calculations in the filter zone. 174
Figure 5-15- Collapse of the saturated elements result in shear stress on the face of saturation. 174
Figure 5-16- Calculated vertical displacement contours at the end of impoundment of LG4 dam 175
Figure 5-17- Calculated horizontal displacement contours at the end of impoundment of LG4 dam 175

Figure 5-18- Calculated vertical total stress contours at the end of impoundment of LG4 dam and comparison with measured values. 176
Figure 5-19- Calculated vertical effective stress contours at the end of impoundment of LG4 dam and comparison with measured values. 176
Figure 5-20- Contours of unloading stress due to wetting in the direction of the maximum principal stress 177
Figure 5-21- Contours of unloading stress due to wetting in the direction of the minimum principal stress 177
Figure 5-22 - Calculated horizontal effective stress contours at the end of impoundment of LG4 dam 178
Figure 5-23- Elements reaching the failure envelope (in purple) during the simulation of the impoundment 178

Nomenclature

Description	Symbol
parameter of the original hyperbolic model; parameter of anisotropic elastic model ; coefficient in the modified Nobari-Duncan procedures	a
parameter of the original hyperbolic model (Konder and Zelasko, 1963); parameter of anisotropic elastic model; coefficient in the modified Nobari-Duncan procedures	b
Bulk modulus	B
cohesion in Mohr-Coulomb failure criteria; parameter of anisotropic elastic model; coefficient in the modified Nobari-Duncan procedures	c
effective cohesion in Mohr-Coulomb failure criteria	c'
parameter of power-law model; parameter of Lade's double hardening model	C
uniformity coefficient; ratio of the sieve size that permits passage of 60% of the media by weight to the sieve size that permits passage of 10% of the media material by weight	C_u
parameter of anisotropic elastic model; coefficient in the modified Nobari-Duncan procedures	d
parameter of power-law model; strain rate tensor in hypoplasticity theory	D
the sieve size that permits passage of 60% of the media by weight	D_{60}
maximum grain size	D_{max}
parameter of anisotropic elastic model; void ratio	e
critical state void ratio	e_c
maximum void ratio	e_{max}
minimum void ratio	e_{min}
Young's modulus	E
initial or maximum Young's modulus at small axial strain (0.01 %) in hyperbolic formulation	E_i
maximum Young's modulus in dry condition	E_{id}
maximum Young's modulus in wet condition	E_{iw}
secant Young's modulus	E_s
secant Young's modulus in dry condition	E_{sd}

secant Young's modulus in wet condition	E_{sw}
tangential Young's modulus	E_t
parameter of anisotropic elastic model	f
failure function of HPD model	f^s
stiffness factor in hypoplastic model	f_s
density factor in hypoplastic model	f_d
failure function in elasto-plastic formulation	$F()$
potential function of HPD model	g^s
shear modulus	G
potential function in elasto-plastic formulation	$G()$
tangential shear modulus in K-G model	G_t
initial tangential shear modulus in K-G model	G_{t0}
solid hardness of the grain assembly under isotropic compression in hypoplastic model	h_s
maximum solid hardness before wetting in hypoplastic model	h_{s0}
current solid hardness in hypoplastic model	h_{st}
degraded solid hardness depending on the relative moisture content of the grains and time in hypoplastic model	h_{sw}
isotropic tensor-valued function in hypoplasticity theory	H
work hardening parameter for the conical failure surface of Lade's double hardening model	H_1
work hardening parameter for the cap failure surface of Lade's double hardening model	H_2
first stress tensor invariant	I_1
third stress tensor invariant	I_3
relative dilatancy index in Bolton theory of dilation	I_R
relative density index in Bolton theory of dilation	I_D
second deviatoric stress tensor invariant	J_2
second deviatoric stress tensor invariant at failure in anisotropic elastic model	J_{2f}
function of Lode's angle to define potential function of elasto-plastic models	$J_{2\eta}^f$
parameter of anisotropic elastic model	k
increase of cohesion with suction in Barcelona model	k_s

coefficient of lateral earth presser at rest	K_0
bulk modulus number in hyperbolic model	K_B
bulk modulus number of dry material in Nobari-Duncan stress relaxation technique	K_{Bd}
bulk modulus number of wet material in Nobari-Duncan stress relaxation technique	K_{Bw}
elastic modulus number in hyperbolic model	K_E
elastic modulus number of dry material in Nobari-Duncan stress relaxation technique	K_{Ed}
elastic modulus number of wet material in Nobari-Duncan stress relaxation technique	K_{Ew}
tangential bulk modulus in K-G model	K_t
initial tangential bulk modulus in K-G model	K_{t0}
unloading elastic modulus number in hyperbolic model	K_{ur}
parameter of Lade's double hardening model	l
bulk modulus exponent in hyperbolic model; material constant in Lade's double hardening model	m
bulk modulus exponent of dry material in Nobari-Duncan stress relaxation technique	m_d
bulk modulus exponent of wet material in Nobari-Duncan stress relaxation technique	m_w
slope of critical state strength in q-p space	M
material constant in Drucker-Prager failure function	M_{JP}
slope of critical state strength in dry condition	M_{dry}
slope of critical state strength in saturated condition	M_{sat}
function to consider the effect of suction on rockfill strength in Barcelona model; changes between two extreme values of M_{dry} and M_{sat}	$M(s)$
elastic modulus exponent in hyperbolic model	n
elastic modulus exponent of dry material in Nobari-Duncan stress relaxation technique	n_d
elastic modulus exponent of wet material in Nobari-Duncan stress relaxation technique	n_w
material constant in Lade double hardening model	N
function of friction angle to define the failure function in HPD model	N_φ
function of dilation angle to define the potential function of HPD model	N_ψ
mean stress; $(\sigma_1 + 2\sigma_3)/3$ in triaxial condition	p

hardening parameter in Barcelona model	p_0^*
function to define the yield stress for isotropic condition in Barcelona model	$p_0(s)$
function to consider the effect of suction on rockfill strength in Barcelona model	$p_s(s)$
threshold yield mean stress for the onset of clastic phenomena in Barcelona model	p_y
atmospheric pressure	P_a
deviatoric stress; $(\sigma_1 - \sigma_3)$ in triaxial condition	q
material constant in Lade double hardening model	R
empirical coefficient for adjusting the stress-strain curve in hyperbolic model	R_f
coefficient for adjusting the dry stress-strain curve in Nobari-Duncan stress relaxation technique	R_{fd}
coefficient for adjusting the wet stress-strain curve in Nobari-Duncan stress relaxation technique	R_{fw}
degree of saturation; suction in Barcelona model	s
initial suction in Barcelona model	s_0
material constant in Lade double hardening model	t
stress tensor	T
stress rate tensor	$\dot{T}$
normalized stress deviator	$\hat{T}^*$
accumulated plastic work associated with the conical failure surface in Lade's double hardening model	W_{p1p}
accumulated plastic work associated with the cap yield surface in Lade's double hardening model	W_{p2}
parameter of modified Nobari-Duncan stress relaxation technique to define maximum principal stress in wet condition from minimum principal stress in wet condition	x
parameter of modified Nobari-Duncan stress relaxation technique to define maximum principal stress in wet condition from minimum principal stress in wet condition	y
parameter of anisotropic elastic model; parameter of Lade's double hardening model; non-associativeness of potential function in Barcelona model; parameter of hypoplastic model	α
parameter of K-G model	α_G
parameter of K-G model	α_K
rate of change of clastic compressibility with total	α_s

suction in Barcelona model	
anisotropic factor in anisotropic elastic model; parameter of Lade's double hardening model; parameter of hypoplastic model	β
parameter of K-G model	β_G
plastic strains associated with the conical yield surface of Lade's double hardening model	$\Delta\varepsilon^{p1}$
horizontal strain increment (x axis) in plain strain formulation	$\Delta\varepsilon_x$
vertical strain increment (y axis) in plain strain formulation	$\Delta\varepsilon_y$
shear strain increment in x-y plane in plain strain formulation	$\Delta\gamma_{xy}$
change of friction angle with confining stress in HPD model	$\Delta\varphi$
horizontal stress increment (x axis) in plain strain formulation	$\Delta\sigma_x$
vertical stress increment (y axis) in plain strain formulation	$\Delta\sigma_y$
shear stress increment in x-y plane in plain strain formulation	$\Delta\tau_{xy}$
change of dilation angle with confining stress in HPD model	$\Delta\psi$
plastic expansive work in Lade's double hardening model	ΔW_{p1}
strain	ε
strain rate in strain controlled triaxial test	$\dot{\varepsilon}$
maximum principal strain	ε_1
intermediate principal strain	ε_2
minimum principal strain	ε_3
rate of change of maximum principal strain; rate of change of axial strain in triaxial setup	$\dot{\varepsilon}_1$
axial strain	ε_a
radial strain	ε_r
volumetric strain	ε_v
rate of change of volumetric strain	$\dot{\varepsilon}_v$
volumetric strain increment	$d\varepsilon_v$
elastic volumetric strain increment	$d\varepsilon_v^e$
plastic volumetric strain increment	$d\varepsilon_v^p$
friction angle in Mohr-Coulomb failure criteria	φ

steady state friction angle at the reference pressure in HPD model	φ_0
effective friction angle	φ'
critical state friction angle; constant volume friction angle	φ_c
critical state friction angle in triaxial strain condition	φ_c^{tr}
peak friction angle in triaxial strain condition	φ_p^{tr}
parameter of Lade's double hardening model	η_1
Poisson's ratio	ν
Lode's angle	θ
compressibility coefficient in Barcelona model	κ
compressibility coefficient in Barcelona model	κ_s
compressibility parameter related to the delayed nature of the particle breakage mechanisms in Barcelona model	λ^d
volumetric compressibility for saturated conditions in Barcelona model	λ_0^d
compressibility parameter in Barcelona model	λ^i
maximum principal stress; axial stress in triaxial setting	σ_1
maximum principal stress in dry condition just before wetting in Nobari-Duncan stress relaxation technique	σ_{1d}
maximum principal stress just after wetting in Nobari-Duncan stress relaxation technique	σ_{1w}
intermediate principal stress	σ_2
minimum principal stress; radial stress in triaxial setting	σ_3
minimum principal stress in dry condition before wetting in Nobari-Duncan stress relaxation technique	σ_{3d}
minimum principal stress just after wetting in Nobari-Duncan stress relaxation technique	σ_{3w}
confining pressure ; equal to radial stress in triaxial setting	σ_c
normal effective stress on the failure plane	σ_{nf}
plastic instantaneous compressibility in Barcelona model	$(\lambda^i - \kappa)$
deviatoric stress	$(\sigma_1 - \sigma_3)$
deviatoric stress in large deformations or in steady state	$(\sigma_1 - \sigma_3)_f$
ultimate deviatoric stress in hyperbolic formulation	$(\sigma_1 - \sigma_3)_{ult}$

effective shear stress on the failure plane	τ_f
material constant in Lade double hardening model; velocity of degradation of solid hardness in hypoplastic model	ω
dilation angle	ψ
dilation angle at reference pressure in HPD model	ψ_0

1 Introduction

Rockfill has been known since ancient times as a useful, reliable, and durable construction material and has been used in different types of structures with different construction methods (e.g. dumped, compacted in layers, hand or equipment placed). In the last century, rockfill dams have become recognized for their high resistant to seismic loads due to their large flexibility and capacity to absorb large seismic energy and for adaptability to widely varying site conditions, construction methods and economy. Moreover, they have been successfully constructed to great heights up to 340 m in Russia and up to 170 m in Canada (Table 1-1). Almost all of these dams have performed safely with no major evidence of instability. The economic advantages and good response of these dams to various site and loading conditions made them an excellent option in many regions of the world such as Quebec, China and Australia.

It seems obvious that the primary function of rockfill in embankment dams is to provide structural support for the impervious zone of the dam (e.g. till, clay or asphaltic core and concrete face). Many researchers made determination of properties of rockfill material using the procedures and concepts of soil mechanics in order to calculate the stress states and patterns of deformation inside the body of rockfill dams (e.g. conducting large scale triaxial or shear tests or application of Darcy's law and mechanics of continuum media in prediction of their behavior). Rockfill samples have extreme heterogeneity, great change in particle sizes (ranging from a few centimeters to few meters), variety of gradation, particle shape and mineral constituencies and predominant large average particle size (average particle size of at least 5 cm). Some researchers in the past such as Jansen (1988) assumed that it was impossible and impractical to adapt the soil mechanics-type tests and mathematical concepts to predict the behavior of such material. This resulted in the fact that many of these dams were constructed based on the designers' engineering judgements and experiences, and using the existing tables and closed form solutions of the time but without conducting adequate laboratory testing or any numerical modeling of the behavior. However each rockfill dam, as all other important geotechnical engineering structures, has its unique geometry and hydro-mechanical characteristics, and is required to be designed and constructed based on a detailed analysis of its behavior. All the details of construction, impoundment and operation should be justified by the means of numerical and theoretical analysis and laboratory testing.

Hunter and Fell (2003) reported the behavior of several rockfill dams around the world, considering the factors influencing the stress conditions, strength and compressibility of the embankment materials and the interaction between embankment zones. These previous field experiences have shown that although each rockfill dam behaves differently, there are some common important aspects at each stage of its life which must be considered when trying to model the behavior. Figure 1-1 shows the three main stages of the lifespan of a rockfill dam and the sub-stages as follows:

1. *Construction of the dam*: Preparation of the foundation and placement of the layers of material over foundation up to the desired level. Mechanical behavior of the whole structure is most important at this stage.

2. *Filling of the reservoir*: Rising the level of the water of the reservoir, flow of water through the body of the dam, collapse of saturated elements and subsequent stress adjustments. Analyzing the hydro-mechanical interactions must be considered at this stage.

3. *Dam Operation*: Time-dependent behavior, variation in reservoir level and possible seismic motions are the main features of this stage.

In order to have a reliable analysis of the rockfill embankments, it is important to provide physical explanations to the observations of the previous cases in the history and the laboratory experiments and to define constitutive equations to simulate the observed behavior using numerical models. This characterization of the behavior must be done for all stages of the lifespan of the dam as mentioned above by considering the most important physical aspects of the material in each stage. Some of the most important aspects of the behavior of material used in the construction of dams are nonlinearity and stress dependency of the parameters, plastic and dilative behavior, time-dependent and collapse settlements due to wetting. With the development of numerical procedures and advancement of laboratory testing methods in recent years, it has become more and more common to numerically model the behavior of such structures considering these important characteristics of the material. The design of rockfill dams is gradually improving by complements accomplished by theoretical analysis and laboratory testing research.

Different constitutive equations based on elasticity and/or plasticity theories have been proposed to predict the behavior of the granular material. Some of these models have been implemented into numerical codes by researchers around the world in order to predict the behavior of rockfill dams.

Linear elastic models were initially applied in modeling of the rockfill dams (e.g. Adikari and Parkins, 1982; Eisenstein and Law, 1977; Geddes et al., 1973; Naylor et al., 1986). The results were reasonable because the stress state was often far away from failure in those rockfill dams. Improving from linear elastic behavior, the non-linear models (Chu et al., 2010; Duncan et al., 1980a) and elasto-plastic analysis (Fu and Bauer, 2009; Lade, 1977; Oldecop and Alonso, 2001) have become widely accepted in recent years. More complex stress-strain relationships should be able to model the behavior of the rock particles more accurately. However the difficulty of the calibration of the parameters of these models using the limited test results for rockfill samples makes them less applicable in practice. Moreover the initial assumptions and experimental relations taken in the formulation of some of these constitutive models are not necessarily extendible to compacted samples of large rock particles as they exist in rockfill dams.

Selecting an appropriate stress-strain relationship is primarily involved with balancing simplicity and accuracy of the model. The hyperbolic model is probably the most applied and stable constitutive model which has been implemented in numerical modeling of rockfill dams of different kind worldwide. There is a large database available for calibration of the parameters based on general physical and engineering properties of rockfill samples. However it is inherently elastic and does not model plastic deformation in a fully logical way; it is also incapable of modeling the dilative behavior of compacted granular material. These shortcomings should be addressed in order to improve the results of the numerical model especially when a zoned dam with contrast in compressibility of different zones is considered. In addition, the relaxation technique in hyperbolic formulation which is used in the modeling of the collapse settlements due to wetting (Escuder et al., 2005; Nobari and Duncan, 1972) could be improved to increase the stability of the numerical model.

The main analytical method is either the finite element method (FEM) or the finite difference method (FDM) which allows for the stress and deformation behavior of the

rockfill dam in various conditions to be obtained and the possible deformation patterns or failure modes to be predicted (Cruz et al., 2009). In FDM method, the explicit solution is applied to solve the stress-strain equations and to calculate the response of the numerical mesh. This approach has the advantage that the solution is numerically stable even when the problem is not statically stable, allowing examination of large strains and displacements prior to failure. In addition, satisfying the dynamic equilibrium using a step-by-step explicit time domain procedure is more efficient in calculating the response of the geotechnical structures where the stress path affects the final response and the stages of construction should be modeled as close as possible to the reality. FLAC (Fast Lagrangian Analysis of Continua) (Cundall, 1987) is a commercial software which uses the finite difference method and also allows the user to input specific constitutive models. Large displacements and strains are calculated by updating the nodal coordinates of the finite difference grid. Also, the effect of pore pressure on the soil behavior is examined by analyzing the fluid-mechanical interactions. FLAC has been used widely for conducting academic research at universities and also as professional numerical modeling software in engineering firms. This fact has encouraged the direct application of the scientific findings in the industry.

In the current PhD research, the first two stages of the lifespan of rockfill dam mentioned above are considered for numerical modeling (i.e. construction and impoundment). Constitutive equations and procedures to calibrate the model and to characterize the behavior of rockfill in different stages of the simulation (e.g. hydro-mechanical interactions during impoundment) are presented. The predictions of the model are validated using the results of laboratory experiments and insitu instrumentation of LG4 dam constructed in Quebec from 1979 to 1981 and impounded from March 1983 to December 1983. The order of the presentation of these topics is as follows:

In chapter 2, different constitutive models mostly applied in the modeling of the behavior of granular material in dam engineering are reviewed (nonlinear elastic, anisotropic elastic, double hardening, critical state, hypoplastic). Considering the most important characteristics of rockfill material (nonlinearity, stress path dependency, plastic and dilative behavior, water and time effects), a comparison is made between these models. The hyperbolic model, if coupled with an appropriate failure envelope and a potential function

to take into account the plastic and dilative behavior is the most balanced model in terms of simplicity and accuracy. This is specially the case for the material used in the construction of dams in the Province of Quebec: rock particles with high compressive strength and small amount of collapse due to saturation.

In chapter 3, a new implementation of the *hyperbolic* model is presented which considers the non-linearity and stress-dependency of the parameters and overcomes the shortages of the classic model by considering both *plasticity* and *dilation* using the Mohr-Coulomb failure criteria and a non-associated flow rule. This new implementation is referred as HPD model in the coming chapters (H stands for the hyperbolic model, P for plasticity and D for dilation). The elastic and plastic formulations of this constitutive model are presented along with a discussion of the results of monotonic compression triaxial tests conducted on assemblages of compacted granite particles. Procedures to calibrate the nine parameters of the model are also presented using the test results and large database existing in the literature for both hyperbolic model and Mohr-Coulomb failure criteria. The HPD model is shown to be able to capture the key behaviors during the tests with fair accuracy.

The time-dependent and collapse settlements due to wetting are discussed in chapter 4. The modified stress relaxation technique with new algorithms to increase the stability of the numerical solution is used to calculate the amount of these deformations. The procedures are implemented into FLAC and validated using the data from several monotonic triaxial compression tests on dry, saturated and dry-saturated samples and in stress and strain controlled conditions. The samples in these triaxial tests have a more uniform particle distribution compared to the prototype rockfill. This was decided in order to increase the amount of (i) creep deformations and (ii) settlements due to wetting, during the experiments. These two phenomena are discussed based on the theories from fracture mechanics (Lade et al., 2010; Oldecop and Alonso, 2001). In this framework, particle breakage and deterioration of contact points generally control the behavior the rockfill masses over time and the deformations accelerate with the introduction of water in the form of liquid or vapor. The stress relaxation technique and the HPD model are shown to be capable of predicting this kind of behavior by changing the two compressibility parameters of the model over time in a logarithmic scale.

Finally in chapter 5, the HPD model is applied to the modeling of LG4 dam constructed in Quebec, Canada. The results of modeling are compared with the instrumentation data and the important observations of the field and numerical model are discussed.

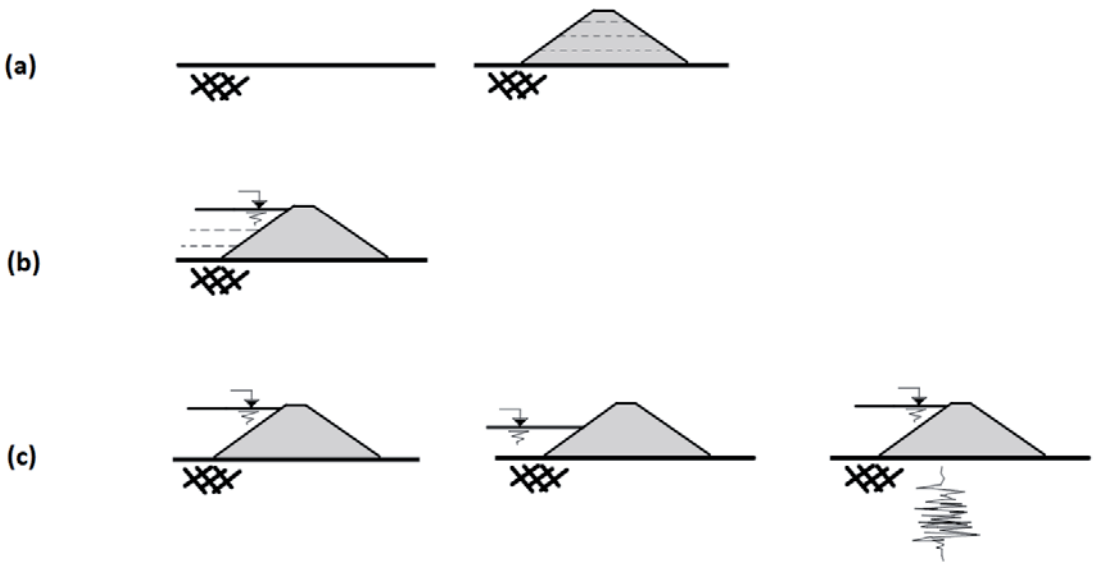

Figure 1-1. Different stages of the lifespan of a rockfill dam: (a) preparation of the foundation, construction in layers; (b) increasing the level of the water of the reservoir in several steps; (c) operation: creep, changing the level of the reservoir, seismic motion

Dam name	Country	Height (m)
Rogun	Russia	335
Nurek	Russia	300
Mica	Canada	242
Sainte Marguerite 3	Canada	170
La Grande 4	Canada	125
Oroville	USA	230
Areia	Brazil	160
El Infiernillo	Mexico	150

Table 1-1- high rockfill dams around the world

2 A review of constitutive models implemented in modeling the behavior of rockfill dams during construction and impoundment

2.1 Introduction

The purpose of this chapter is to explore the literature for the previous efforts made for the analysis of the behavior of the granular material in order to simulate two stages of the lifespan of a rockfill dam: construction and filling of the reservoir. This is a non-exhaustive study of constitutive models mostly applied in modeling of the behavior of granular material in dam engineering. Firstly, the physical and engineering properties of the so called rockfill material will be discussed followed by a brief description of constitutive modeling of the behavior of such material. The chapter will continue with presentation of various constitutive models utilized worldwide in the simulation of construction steps and reservoir impounding sequences of rockfill dams in an increasing order of complexity as:

- Isotropic linear elastic model
- Non-linear elastic models
  - Power law model
  - K-G model
  - Hyperbolic model
- Anisotropic elastic model
- Elasto-plastic models
  - Perfect plastic models
    - Mohr-Coulomb
    - Drucker-Prager
  - Double hardening model
- Barcelona model (based on critical state soil mechanics)
- Hypoplastic models (rate dependent models)

Finally, the most practical and applicable constitutive model which could represent the most important characteristics of the compacted rock particles in an embankment, while being relatively easy to calibrate and requiring less testing, will be identified and the possible modifications to improve the model will be presented.

2.2 Physical and engineering properties of rockfill

Rockfill is a kind of granular material which is composed of hard particles including sedimentary, igneous, and metamorphic rocks. The main physical properties of rockfill material are density, grain size distribution, void ratio, and particle shape which could be related to the engineering properties such as stress-strain relation, compressibility, and

strength of the material. The compressibility of the material is mainly controlled by arrangement of particles which is related to density and gradation. The same rock with different gradations will result in different compressibilities. The shear strength of rockfill includes the action of sliding friction and the interlock between particles which is affected by shear dilation and particle breakage.

When rockfill is wetted, additional deformation results. This phenomenon is similar to the collapse in soils. However, in soil mechanics, the assumption is that collapse happens due to the reduction of the negative pore water pressures, while in rockfill it is mostly caused by breakage of particle edges and rearrangement of grains. It occurs independently of the rockfill submersion. As long as the water reaches the contact points, even from a rain fall or high relative humidity, it might be sufficient to reduce the strength and provoke the collapse of the material. The amount of deformations decreases with increasing density or initial water content.

2.3 Constitutive modeling

In numerical modeling of rockfill dams, the constitutive model is the most important element of the analysis. The stress and deformation analysis needs comprehensive consideration of different factors including: stress-strain relationship, strength and deformation properties, non-linear work hardening, dilation, plastic yielding, anisotropy, collapse due to wetting, creep, stress path and stress history, composition of particles, etc. For such complicated material properties, there is no comprehensive model representing all factors. In practice, the development of the constitutive model is essentially limited to determine the mathematical model to best fit the observations of laboratory or field data using the main factors of the material's stress-strain relations. Most of the common constitutive models used for rockfill material are based on two main theories: (i) linear or non-linear elasticity, and (ii) elasto-plasticity. However, in the last decade, some other theories like critical state theory or hypo-plasticity have also been used to model rockfill materials. Although these theories seem to be superior to the previous ones at first, since they have been initially proposed for cohesive and soft soils, their applicability in modeling rockfill material is questionable. Furthermore, calibration of these models is much more

difficult and requires more laboratory testing with specific procedures which are not suitable for samples containing large rock particles.

The most important aspect in the analysis of granular material is the stress-dependency of properties which means all the deformation and strength parameters will change with the stress state. Moreover, the stress-strain relationship of granular material is highly non-linear. The changes of volume also impact the patterns of deformation and distribution of stress inside the body of the dam. Stress-dependency and nonlinearity could be well modeled using the nonlinear elasticity theory. However, for the proper consideration of the volume changes which include both volume reduction and dilation, and the plastic deformations, the elasto-plastic models with application of multiple yield surfaces and the non-associated flow rule are theoretically perfect. However these models still have many difficulties in determination of parameters, laboratory testing, and computational efforts. A nonlinear elastic model is more practical and applicable but has its own shortages. In the following sections, different constitutive equations will be presented along with pros and cons of each in the modeling of rockfill material.

2.3.1 Linear elastic model

Although soils are far from being linear elastic, because of simplicity, it is very common for geotechnical engineers to characterize the behavior of geomaterials using the idealized linear isotropic elastic model. The results are reasonable only if the stress state is far away from failure which usually prevails in rockfill dams. Hence it is not surprising that this kind of analysis has been successful in many case histories of rockfill dams worldwide (e.g. Adikari and Parkins, 1982; Eisenstein and Law, 1977; Geddes et al., 1973; Naylor et al., 1986). Only two elastic constants are needed to characterize the stress-strain behavior of isotropic linear materials which are often Young's modulus, E, and Poisson's ratio, ν. These constants can be estimated by *constant equivalent compressibility method* (Penman et al., 1971) which says that the internal distribution of vertical displacement during the construction of a thick layer can be predicted by the use of constant Young's modulus determined to give the correct final displacement of a point half-way up the complete layer.

NGI (1987) reported that the simple linear model gave better predictions of overall strains and displacements in different sections of Storvatn dam (a rockfill dam with asphaltic core constructed in Norway in 1987) than the more complicated models such as nonlinear elastic which were intended to be an improvement over the former. The measurements of internal displacements indicated that the strains prevailing inside the dam were small, and less than one percent and the materials were found to be linear in most laboratory and field tests in this low stress-strain range. The rockfill was sluiced and heavily compacted during the construction and impoundment of the dam followed closely the construction stage. The settlements were compensated during the construction stage and remained in the elastic zone. It was therefore possible to model the behavior in linear form in the numerical model and to accurately calculate the stresses and movements within the dam. On the other hand, more complicated models were more difficult to calibrate using the limited test data available for the materials of Storvatn dam which brought uncertainty into the calculations and resulted in the fact that the simple linear model was superior in this case.

Considering the behavior of the material during the first filling of the reservoir, Justo (1991) proposed procedures to model the behavior of the rockfill material after wetting using the linear elastic model and considering different separated processes of collapse, buoyancy, and water loading. The collapse of material after the filling of the reservoir was simulated by a decrease in Young's modulus of the material while keeping a constant Poisson's ratio. He showed the effectiveness of his method in the prediction of movements inside the body of two rockfill dams constructed in Spain: Yeguas dam and Martin Gonzalo dam (Justo, 1988). Justo and Saura (1983a) also developed a three-dimensional finite element method, linear-elastic in principle, considering the no-tension strength of rockfill and different moduli according to the direction of stress change. This method was applied to three-dimensional modeling of the Infiernillo dam and other rockfill dams with relatively good results (Justo et al., 1989).

2.3.2 Non-linear elastic models

These models were developed in an attempt to fit the data from different laboratory experiments such as triaxial or oedometric tests, and to consider important aspects of the behavior of granular material such as nonlinearity and stress-dependency, as well as the

relationship between the volumetric strain ε_v and axial strain ε_a or axial stress σ_a. There are several constitutive models which belong to this category such as power law model, K-G model, hyperbolic model and Chu et al. (2010) model which will be briefly explained in the following sections:

2.3.2.1 Power law model

Rowe (1971) developed the relationship between volumetric strain, ε_v, and axial stress, σ_a, in an oedometric compression test by a power law of the following form:

$$\varepsilon_v = C\left({\sigma_a}/{P_a}\right)^D \qquad \textit{[Eq. 2-1]}$$

Where P_a is the atmospheric pressure, C and D are dimensionless parameters. By differentiating this equation, the expression for the tangential Young's modulus, E_t, can be derived using the value of Poison's ratio, ν, estimated from theory of elasticity using the coefficient of lateral earth pressure at rest for normally consolidated soils K_0:

$$\nu = {K_0}/{(1 + K_0)} \qquad \textit{[Eq. 2-2]}$$

Where K_0 is related to the friction angle, φ, according to $K_0 = 1 - sin\varphi$, or determined from the odometer test as : $K_0 = \sigma_r/\sigma_a$, by measuring the radial stress, σ_r. At least three parameters are required in this model to represent loading conditions. With the results of oedometric tests, Skinner (1975) used the above relationship to derive the closed form solution for the settlement profile on the center line of an embankment constructed of rockfill. Naylor (1991) also applied this model in numerical analysis of embankment dams considering additional parameters to model unloading. Modeling other aspects such as the dilative-contractive volume change, wetting effects, or time-dependent deformations cannot be performed using this model.

2.3.2.2 K-G model

It was recognized a long time ago that modeling of soils in terms of the bulk modulus, K, and the shear modulus, G, had some advantages over the use of Young's modulus, E, and Poisson's ratio, ν (Naylor and Pande, 1981; Potts and Zdravkovic, 2001). This model is an

extension of the bi-linear model (Figure 2-1) which assumes that the bulk and shear stiffness are constant until the stress state reaches the failure condition; then the tangential shear modulus, G, is set to a very small value. In the modified Naylor's K-G model, the tangential (incremental) bulk, K_t, and shear, G_t, moduli are explicitly defined in terms of stress invariants:

$$K_t = K_{t0} + \alpha_K I_1 \qquad \textit{[Eq. 2-3]}$$

$$G_t = G_{t0} + \alpha_G I_1 + \beta_G J_2 \qquad \textit{[Eq. 2-4]}$$

Where I_1 is the first stress invariant and J_2 is the second deviatoric stress tensor which are representative measures of confining stress and shear stress, respectively. Parameters of the model are K_{t0}, α_K, G_{t0}, α_G, β_G. As with a bilinear model, the parameters can be selected such that the incremental shear stiffness becomes very small when failure is approached (i.e. setting a negative β_G).Values of the parameters of the failure surface (e.g. cohesion and friction angle if a Mohr-Coulomb failure surface is used) are therefore used when determining the values of the five mentioned input parameters. The resulting stress-strain curves for this model are shown in Figure 2-2. Although this model has relatively simple expressions, the parameters can only be determined by special isotropic compression tests and shear tests under the condition of constant confinement (i.e. $I_1 = cte$)

2.3.2.3 Hyperbolic model

The original hyperbolic model is attributed to Konder and Zelasko (1963). In its initial form it was originally formulated to fit undrained triaxial test results and was based on two parameters and the implicit assumption that Poisson's ratio was 0.5. This original model was based on the following hyperbolic equation:

$$(\sigma_1 - \sigma_3) = \frac{\varepsilon}{a + b\varepsilon} \qquad \textit{[Eq. 2-5]}$$

Where σ_1 and σ_3 are the major and minor principal stresses, ε the axial strain and a and b are material constants. However it has been extensively developed by Duncan and Chang (1970) by introducing some factors to modify Poisson's ratio with stress state. The number

of parameters needed to define the model also increased to nine and the model was applied in numerical modeling of dams (Seed et al., 1975). Later the elastic modulus and bulk modulus were formulated to change with stress state which were more representative of the behavior of geomaterials (Duncan et al., 1980a). The latter model is based on the generalized Hooke's law of elastic deformations and could be formulated for plain strain condition as follows:

$$\begin{Bmatrix} \Delta\sigma_x \\ \Delta\sigma_y \\ \Delta\tau_{xy} \end{Bmatrix} = \frac{3B}{9B-E} \begin{bmatrix} (3B+E) & (3B-E) & 0 \\ (3B-E) & (3B+E) & 0 \\ 0 & 0 & E \end{bmatrix} \begin{Bmatrix} \Delta\varepsilon_x \\ \Delta\varepsilon_y \\ \Delta\gamma_{xy} \end{Bmatrix} \qquad \textit{[Eq. 2-6]}$$

Where $\Delta\sigma_x$, $\Delta\sigma_y$ are normal stress increments, $\Delta\tau_{xy}$ is the shear stress increment, $\Delta\varepsilon_x$, $\Delta\varepsilon_y$ are normal strain increments, $\Delta\gamma_{xy}$ is the shear strain increment , E is Young's modulus , and B refers to the bulk modulus. By varying the values of Young's modulus and/or bulk modulus with the state of stresses, it is possible to model the soil behavior and the important characteristics which are nonlinearity, inelasticity, and stress-dependency.

Duncan and Chang (1970) considered changing Young's modulus, but with a constant bulk modulus. For this purpose, three coefficients were introduced: K_E, n, R_f which related the tangential modulus to the confining stress level (σ_3) and failure envelope as follows:

$$(\sigma_1 - \sigma_3) = \frac{\varepsilon}{\frac{1}{E_i} + \frac{\varepsilon}{(\sigma_1 - \sigma_3)_{ult}}} \qquad \textit{[Eq. 2-7]}$$

Where:

$$E_i = K_E P_a \left(\frac{\sigma_3}{P_a}\right)^n \qquad \textit{[Eq. 2-8]}$$

$$(\sigma_1 - \sigma_3)_f = R_f (\sigma_1 - \sigma_3)_{ult} \qquad \textit{[Eq. 2-9]}$$

As could be seen in Figure 2-3, the nonlinearity was modeled in the context of the above mentioned formulation and in a form of hyperbolic curve. In addition, as shown in Figure 2-4, by introducing a different modulus during unloading (K_{ur}) the inelasticity was

represented. The value of K_{ur} for unloading and reloading is between 1.2 to 3.0 times the value of K_E for loading, in rigid and soft soils, respectively.

Wong and Duncan (1974) employed the tangent value of Poisson's ratio which varied with confining pressure and percentage of strength mobilized to model the volume change behavior. For this purpose three different coefficients were introduced, which were d, G, and F. This was not a versatile approach for modeling soil behavior. Duncan et al. (1980a) introduced a more applicable formulation in which the bulk modulus of the soil varies with confining pressure, and is independent of the percentage of strength mobilized. At high stress levels, this assumption provides a more reasonable means of representing the mechanical properties of geomaterials. For this purpose, as shown in Figure 2-5, they introduced two new coefficients, K_B and m, in the following form:

$$B = K_B P_a (\frac{\sigma_3}{P_a})^m \qquad \textit{[Eq. 2-10]}$$

During the past years many analyses of rockfill dams have been based on this constitutive model and some computer codes have been developed for this purpose: ISBILD (Ozawa and Duncan, 1973), FEADAM (Duncan et al., 1984; Duncan et al., 1980b; Saboya and Byrne, 1993). In the application of this model, the following limitations should be understood and the model should only be used in appropriate conditions:

1. The model is based on the generalized Hooke's law and the equations are most suitable prior to failure.

2. The equations do not include volume changes due to changes in shear stress or shear dilatancy.

3. The parameters are empirical coefficients which depend on the limited range of testing conditions such as water content, soil density, and drainage condition. When the physical condition changes, the parameters also change.

The parameters of the hyperbolic model can also be determined by the means of a series of drained triaxial or oedometric tests. The procedures for estimating the parameters are

described by Duncan et al. (1980a). Other researchers have provided other methods (Massiéra et al., 1999) and the computer code KOEDO (Merheb-Harb, 1993) to determine these parameters more accurately, especially for the case of analysis of stress and deformation in embankment dams.

The hyperbolic model has shown to well represent the behavior of rockfill material during the past years (Cruz et al., 2009). Using the procedures introduced by Nobari and Duncan (1972), and later modified by Escuder et al. (2005), this model can be implemented to model the behavior of the dams during the filling of the reservoir. As shown in Figure 2-6, this is done by calculating the wet stresses and imposing an internal unloading (stress relaxation technique) at the moment of saturation, which is an important advantage over other constitutive models. However, the proposed procedures for modeling the collapse deformations involve an iterative procedure in which the values of principal stresses that minimize two complicated error functions must be obtained. This might introduce instability in the numerical process and needs to be improved. In addition, as mentioned above, there are some limitations in the hyperbolic model (i.e. plasticity and dilatancy) which also require to be solved if desired to be applied in modeling dams which may experience plastic deformations in some zones (e.g. high shear zones on the interfaces of zoned dams).

2.3.3 Anisotropic elastic model

Recently Chu et al. (2010) proposed a constitutive model for gravely soils based on the theory of elasticity which is characterized by the following features: (i) significant shear-induced volumetric deformations prior to failure; (ii) modulus stiffening under hydrostatic loading, and degradation under shearing similar to the relationships proposed by Lo Presti et al. (1999) and Tatsuoka et al. (1997); (iii) stress-induced anisotropy based on the concept presented by Weng et al. (2008) and Graham and Houlsby (1983). In this model, the Drucker–Prager criterion was adopted which had a linear failure envelope when expressed in terms of stress invariants of the three-dimensional stress components as:

$$\sqrt{J_{2f}} = \alpha I_1 + k \qquad \textit{[Eq. 2-11]}$$

Where J_{2f} is a representative measure of shear stress at failure, and parameters α and k are the slope and cohesive intercept of the Drucker–Prager failure envelope, respectively. Deformation moduli B and G vary according to the invariants of the stress tensor: I_1 (first stress invariant) and J_2 (second deviatoric stress tensor) which are representative measures of hydrostatic stress and shear stress, respectively. The initial shear modulus and bulk modulus are assumed to be linearly related to the hydrostatic stress as:

$$G_0 = a\left(\frac{1}{3}I_1\right) + b \qquad \textit{[Eq. 2-12]}$$

$$B_0 = c\left(\frac{1}{3}I_1\right) + d \qquad \textit{[Eq. 2-13]}$$

Where parameters a and c determine how rapidly the initial shear and bulk moduli increase as the confining pressure increases, and b and d are the initial shear and bulk moduli values with no confining pressure. The greater the four values, the higher shear and bulk modulus. The degradation behavior is considered nonlinear during all shearing phases as:

$$G = G_0\left[1 - \left(\frac{\sqrt{J_2}}{\sqrt{J_{2f}}}\right)^4\right] \qquad \textit{[Eq. 2-14]}$$

$$B = B_0\left[1 - \left(\frac{\sqrt{J_2}}{\sqrt{J_{2f}}}\right)^4\right] \qquad \textit{[Eq. 2-15]}$$

The increasing and decreasing of these modulus result in diverse deformational behavior. To incorporate the contraction–dilation characteristics of the deformation behavior, the compliance matrix in the principal stress coordinate was defined as:

$$\begin{bmatrix}\varepsilon_1\\ \varepsilon_2\\ \varepsilon_3\end{bmatrix}=\begin{bmatrix}\frac{1}{9B}+\frac{1}{3G} & \frac{1}{9B}-\frac{1}{6\beta G} & \frac{1}{9B}-\frac{1}{6\beta G}\\ \frac{1}{9B}-\frac{1}{6\beta G} & \frac{1}{9B}+\frac{1}{3G} & \frac{1}{9B}-\frac{1}{6\beta^2 G}\\ \frac{1}{9B}-\frac{1}{6\beta G} & \frac{1}{9B}-\frac{1}{6\beta^2 G} & \frac{1}{9B}+\frac{1}{3G}\end{bmatrix}\begin{bmatrix}\sigma_1\\ \sigma_2\\ \sigma_3\end{bmatrix} \qquad \textit{[Eq. 2-16]}$$

Where β is the anisotropic factor which can be calculated using the shear stress at failure and two model parameters (e and f) as:

$$\beta = e - f\sqrt{\frac{J_2}{J_{2f}}} \qquad \textit{[Eq. 2-17]}$$

When $\beta = 1$, the above compliance matrix is identical to the constitutive relationship of isotropic linear elastic materials. However, for compacted assemblages of rock particles under shearing, β can differ from 1. In such cases, shear-induced volumetric deformation occurs.

There are eight parameters required for this model which can be calibrated using the results of several triaxial tests. Material parameters have physical meanings and are relatively versatile in simulating gravelly soils under different loading conditions. However, the choice of Drucker-Prager failure envelope is not very suitable for the modeling of rock particle assemblages and the plastic deformations could not be predicted correctly. Moreover, introducing the anisotropic compliance matrix will make the future developments of the model very complex (i.e. for the prediction of other phenomena such as collapse deformations due to wetting or creep). The more reliable way of predicting the plastic deformations and shear-induced volume changes is the introduction of the failure envelope as established in the classical theory of elasto-plasticity and the use of more suitable failure envelopes for non-cohesive geomaterials.

2.3.4 Elasto-Plastic models

Comparing to the previously described models, elastoplastic stress-strain relationships are capable of modeling the behavior of geomaterials quite readily. In spite of the presence of different elastoplastic constitutive models in literature, these have not been widely used in modeling rockfill dams due to the following reasons: (i) Complexity of such analyses considering different materials and stages of construction and operation of a rockfill dam. (ii) Difficulties associated with testing rockfill materials and calibration of the constitutive models. (iii) Small zones of plastic yielding discovered in the previous attempts to model such structures using elastoplastic models. (iv) Limited existence of dilative behavior in rockfill dams (Potts and Zdravkovic, 2001). However, the modeling of plastic and dilative behavior has a more subtle advantage which concerns the pattern of deformation during yielding. This is clearly shown by Naylor et al. (1975) who analyzed the behavior during construction of embankment dams using different constitutive models. They showed that the patterns of deformation were sensitive to the type of model being used. Non-compatible results of the modeling with respect to the instrumentation data were also reported by other researchers who used elastic models to simulate the construction stage of rockfill dams. This was considerable especially for the excessive predictions of horizontal displacements (Boncompain and Massiéra, 1991; Kovacevic et al., 1994; NGI, 1987; Verma et al., 1985).

A large variety of elasto-plastic models are presented in the literature which have been proposed to characterize the stress-strain behavior of geomaterials. Many of them have been originated from the concept of critical state soil mechanics (i.e. Cam clay model and its modifications). As reported by Duncan (1994) most of the applications of these models in the analysis of embankment dams were associated with dams on soft ground where the overall behavior was governed by the soft materials of the foundation. Very few examples of application of such elasto-plastic models to predict the behavior of rockfill dams on solid rock foundations have been reported. This is due to the fact that rockfill can be considered as an extreme granular material and the suitability of critical state models to predict the behavior of such material is questionable (Potts and Zdravković, 1999). These models were originally developed for sedimentary clays. Compacted fills have behavior pattern similar to sands, and the elastoplastic models originally proposed for sands can better capture such behavior.

2.3.4.1 Perfect plastic models

The constitutive models in elastoplastic framework with perfect plastic behavior could have different failure envelopes such as Tresca, von Mises, Mohr-Coulomb, and Drucker-Prager. The yield surfaces of these models in the principal stress space are shown in Figure 2-7 (Potts and Zdravković, 1999). The first two models are generally expressed in terms of total stress and applied to undrained soil behavior, while the next two models consider the effective stress state which is a necessity in order to describe the general behavior of geomaterials. The two models, Mohr-Coulomb and Drucker-Prager, have been generally adopted in the numerical modeling of granular materials.

If the results of laboratory tests are plotted in terms of effective stresses, it is usual to assume that the tangent to the failure circles from several tests, performed with different initial effective stresses, is straight and can be expressed as:

$$\tau_f = c' + \sigma'_{nf} tan\varphi' \qquad \textit{[Eq. 2-18]}$$

Where τ_f and σ'_{nf} are the shear and normal effective stresses on the failure plane, and the cohesion, c', and friction angle, φ', are strength parameters of the model. This equation can be rewritten in the principal stress space as:

$$\sigma'_1 - \sigma'_3 = 2c'cos\varphi' + (\sigma'_1 + \sigma'_3)sin\varphi' \qquad \textit{[Eq. 2-19]}$$

This is called the Mohr-Coulomb failure criterion and is adopted as the yield function:

$$F(\{\sigma'\},\{k\}) = \sigma'_1 - \sigma'_3 - 2c'cos\varphi' - (\sigma'_1 + \sigma'_3)sin\varphi' \qquad \textit{[Eq. 2-20]}$$

In finite element modeling, it is more convenient to write this equation in terms of the stress invariants, I_1, J_2, θ which are representatives of mean effective stress, deviatoric stress, and inclination of major principal stress (Lode's angle):

$$I_1 = {}^1\!/_3\,(\sigma'_1 + \sigma'_2 + \sigma'_3) \qquad \textit{[Eq. 2-21]}$$

$$J_2 = \frac{1}{\sqrt{6}}\sqrt{(\sigma'_1 - \sigma'_2)^2 + (\sigma'_2 - \sigma'_3)^2 + (\sigma'_1 - \sigma'_3)^2} \qquad \textit{[Eq. 2-22]}$$

$$\theta = tan^{-1}\left[\frac{1}{\sqrt{3}}\left(2\frac{(\sigma'_2 - \sigma'_3)}{(\sigma'_1 - \sigma'_3)} - 1\right)\right] \qquad \textit{[Eq. 2-23]}$$

The principal stresses can be expressed in terms of these alternative invariants using the following expression:

$$\begin{Bmatrix}\sigma'_1\\ \sigma'_2\\ \sigma'_3\end{Bmatrix} = I_1\begin{Bmatrix}1\\1\\1\end{Bmatrix} + \frac{2}{\sqrt{3}}J_2\begin{Bmatrix}sin(\theta + \frac{2\pi}{3})\\ sin(\theta)\\ sin(\theta - \frac{2\pi}{3})\end{Bmatrix} \qquad \textit{[Eq. 2-24]}$$

Therefore, substituting these equations into the Mohr-Coulomb failure criterion and rearranging gives:

$$F(\{\sigma'\},\{k\}) = J_2 - \left(\frac{c'}{tan\varphi'} + I_1\right)g(\theta) \qquad \textit{[Eq. 2-25]}$$

Where:

$$g(\theta) = \frac{sin\varphi'}{cos\theta + \frac{sin\theta cos\varphi'}{\sqrt{3}}} \qquad \textit{[Eq. 2-26]}$$

It is evident from Figure 2-7 that when plotted in three dimensional principal stress space, Mohr-Coulomb yield surface has corners which imply singularities in the yield function (i.e. the partial derivatives with respect to the stress components are not unique at corners) and need to be dealt within the numerical analysis by the use of some elaborate computer codes. However, some earlier pioneers of the subject sought simplifications to overcome the corner problem without the use of more computer resources. The most common way to remove the edges was to modify the Mohr-Coulomb yield function so that it plots as a cylindrical cone. This can be achieved by replacing $g(\theta)$ in Mohr-Coulomb failure

criterion by a constant, M_{JP}, which means the yield function is independent of the direction of principal stresses. The yield function then becomes:

$$F(\{\sigma'\},\{k\}) = J_2 - \left(\frac{c'}{tan\varphi'} + I_1\right) M_{JP} \qquad \textit{[Eq. 2-27]}$$

Where M_{JP} is a material constant. This form of yield function is often called the Drucker-Prager or extended von Mises yield function. In Figure 2-8, the irregular hexagon of the Mohr-Coulomb surface is compared with the circular shape of the Drucker-Prager surface in the deviatoric plane. Two alternative Drucker-Prager circles are shown, one circumscribes, while the other inscribes the hexagon. The choice of the correct M_{JP} that provides the best fit of the circle to the hexagon is then required. Moreover, although the smooth shape of the Drucker-Prager surface excludes the singularities and consequently facilities the implementation of this model into the computer codes, but the simplification in the failure function deviates the model from the conventional soil mechanics concepts. This means that both yield and strength of the Drucker-Prager model are dependent on the intermediate principal stress and independent of the directions of the principal stresses. These differences can have serious effects in the analysis problems (Potts and Zdravkovic, 2001). Using the Mohr-Coulomb model has the advantage that the numerical model is compatible with the conventional soil mechanics.

As shown in Figure 2-9, Lade and Duncan (1975) and Matsuoka and Nakai (1974) have also suggested other failure surfaces which are continuous in deviatoric plane stresses by replacing the $g(\theta)$ function in Mohr-Coulomb failure criterion with the following expression:

$$g(\theta) = \sqrt{J_{2\eta}^{f}} \qquad \textit{[Eq. 2-28]}$$

Where $J_{2\eta}^{f}$ is a function of Lode's angle, θ, and can be obtained from different equations which were proposed for Lade's surface or Matsuoka and Nakai's surface, respectively. New model parameters are required in order to define these surfaces. Lade's surface is

more appropriate for modeling the granular material and will be discussed later in this chapter.

To complete the plastic formulation of perfectly plastic Mohr-Coulomb model, a plastic potential function is required. An associated flow rule was classically adopted as:

$$G(\{\sigma'\},\{m\}) = F(\{\sigma'\},\{k\}) \qquad \textit{[Eq. 2-29]}$$

Where $\{m\}$ and $\{k\}$ are potential and failure state factors, respectively. However there are three drawbacks to this approach: (i) the magnitude of the plastic volumetric strain (dilation) is much larger than observations in real geomaterials; (ii) once the soil yields, it will dilate forever, which is not correct for geomaterials reaching a constant volume condition at large strains. (iii) Using this formulation, the plastic volumetric strain is independent of the stress state and material properties (e.g. density and degree of saturation). The first drawback can be partly rectified by adopting a non-associated flow rule, where the plastic potential function is assumed to take a form similar to that of the yield surface but with friction angle(φ') replaced by a smaller dilation angle (ψ) which gives:

$$G(\{\sigma'\},\{m\}) = J_2 - \left(a_{pp} + I_1\right)g_{pp}(\theta) \qquad \textit{[Eq. 2-30]}$$

Where:

$$a_{pp} = \left(\frac{c'}{tan\varphi'} + I_{1c}\right)\frac{g(\theta_c)}{g_{pp}(\theta_c)} - I_{1c} \qquad \textit{[Eq. 2-31]}$$

$$g_{pp}(\theta) = \frac{sin\psi}{cos\theta\,\frac{sin\theta sin\psi}{\sqrt{3}}} \qquad \textit{[Eq. 2-32]}$$

The abbreviation pp in the above equations refers to *plastic potential* and c refers to the *current* stress state which is assumed to be on the yield surface. Although the use of a non-associated flow rule solves the first drawback mentioned above, and enables the magnitude of the incremental plastic volumetric strain to be restricted (due to smaller value of the

dilation angle compared to the friction angle), but this basic model still predicts increasing volumetric strains, no matter how far the soil is sheared or how much the confinement is (the next two drawback mentioned above). This is unrealistic and can give unreasonable predictions in some conditions, and should be corrected by modifying the angle of dilation with plastic strain and/or state of the stresses.

To summarize, the perfectly plastic Mohr-Coulomb model requires 5 parameters which are: $c', \varphi', \psi, E, \nu$. It is assumed to be perfectly plastic which means there is no hardening/softening law adopted in the formulations, and the parameters of the yield and potential functions are constant, independent of plastic strain and plastic work:

$$\{k\} = \{c', \varphi'\}^T \qquad \textit{[Eq. 2-33]}$$

$$\{m\} = \{\psi\}^T \qquad \textit{[Eq. 2-34]}$$

Although this restricts the ability to reproduce real soil behavior, it forms the basis of the classical soil mechanics. Further improvements to these equations can be made by introducing hardening or softening plasticity, or modification of potential function to better predict the volumetric strains. Development of critical state constitutive models is also a further advance in the use of plasticity theory in geomechanics; however the applicability of these concepts in modeling rockfill behavior is questionable from the points of view of determination of the correct parameters (i.e. laboratory and insitu testing), and applicability of these concepts to a medium containing very large rock particles.

The basic Mohr-Coulomb model has been used to model embankment dams worldwide (Hunter and Fell, 2003). It has the initial linear elastic formulations and the procedures introduced by Justo (1991) can be implemented to predict the collapse deformations due to wetting. The main shortages of this model in predicting the behavior of rockfill dams during construction and impoundment are the initial linear elastic part and independency of the elastic parameters to the stress state which can be replaced by nonlinear behavior with elastic constants to vary with stress and/or strain level. Moreover, the plastic potential function could be modified to take into account the dependency of the dilative behavior of the granular material to the stress state, density, and saturation ratio.

2.3.4.2 Double hardening model

The Lade double hardening model was proposed by Lade (1977) and involved two work hardening/softening yield surfaces, called *conical* and *cap* yield surfaces as shown in Figure 2-10. If a soil element is plastic and is on the both yield surface (e.g. Point (a) in Figure 2-10), its behavior depends on the direction of the stress path. If directed above these surfaces (into zones 2, 3, and 4 in Figure 2-10) it will expand one or both yield surfaces, depending on the stress path. However if the stress path is directed below the yield surfaces (into zone 1 in Figure 2-10) the behavior is considered nonlinear elastic. The purely elastic response is described by isotropic elasticity. Lade and Nelson (1984) derived an alternative expression for Young's modulus based on the principle of conservation of energy with the following expression:

$$E = NP_a\left[\left(\frac{3I_1}{P_a}\right) + \frac{6(1+\nu)}{(1-2\nu)}\left(\frac{J_2}{P_a}\right)^2\right]^{\omega} \qquad \textit{[Eq. 2-35]}$$

Where I_1 and J_2 are stress tensor invariants; P_a is the reference pressure (atmospheric pressure); ν is Poisson's ratio; ω and N are material constants. The Conical failure criterion has a curved shape in $I_1 - J_2$ space and a rounded triangular shape in the deviatoric plane as shown in Figure 2-11. The yield function has the following equation:

$$F_1(\{\sigma'\},\{k\}) = 27\left(\frac{{I_1}^3}{I_3} - 1\right)\left(\frac{3I_1}{P_a}\right)^m - H_1 = 0 \qquad \textit{[Eq. 2-36]}$$

Where m is material parameter; I_3 is stress tensor invariant and is related to the other invariants (I_1, J_2, and θ) using the following equation:

$$I_3 = {I_1}^3 - {I_1}^2 J_2 - \frac{4}{3\sqrt{3}}{J_2}^3\left(\frac{1}{2} + cos\theta\right)sin\theta \qquad \textit{[Eq. 2-37]}$$

The work hardening parameter (H_1) for the conical failure surface is given by the following equation:

$$H_1 = \eta_1 \left[\xi e^{(1-\xi)}\right]^{\frac{1}{q}} \qquad \textit{[Eq. 2-38]}$$

Where η_1 is material parameter; ξ and q are functions which relate the incremental plastic strains associated with the conical yield surface ($\Delta\varepsilon^{p1}$) with the plastic expansive work (ΔW_{p1}) and accumulated plastic work (W_{p1p}) using 4 material parameters ($\alpha, \beta,\ C, l$) as:

$$q = \alpha + \beta\left(\frac{\sigma'_3}{P_a}\right) \qquad \textit{[Eq. 2-39]}$$

$$\xi = \frac{\Delta W_{p1}}{W_{p1p}} = \frac{\{\sigma\}^T\{\Delta\varepsilon^{p1}\}}{CP_a\left(\frac{\sigma'_3}{P_a}\right)^l} \qquad \textit{[Eq. 2-40]}$$

The plastic non-associated potential function relating to this yield surface takes the following form:

$$G_1(\{\sigma'\},\{m\}) = 27I_1 + \left[27 + \left(\rho H_1 + R\left(\frac{\sigma'_3}{P_a}\right)^{\frac{1}{2}} + t\right)\left(\frac{P_a}{3I_1}\right)^m\right] I_3 \qquad \textit{[Eq. 2-41]}$$

Where R and t are material parameters; I_1, I_3 are the stress tensor invariants; and H_1 is the hardening parameter as defined before. The second yield surface forms a cap on the open end of the conical yield surface as shown in Figure 2-10. This cap surface is shaped as a sphere with its center at the origin of principal stress space. It is defined by the following equation:

$$F_2(\{\sigma'\},\{k\}) = 9{I_1}^2 + 2I_2 - H_2 \qquad \textit{[Eq. 2-42]}$$

Where I_2 is the stress tensor invariant defined as:

$$I_2 = {J_2}^2 - 3{I_1}^2 \qquad \textit{[Eq. 2-43]}$$

The work hardening parameter (H_2) for the cap failure surface is given by:

$$H_2 = {P_a}^2 \left[\frac{W_{p2}}{C P_a}\right]^{\frac{1}{p}} \qquad \textit{[Eq. 2-44]}$$

Where C and p are material parameters; W_{p2} is the accumulated plastic work associated with the cap yield surface. The plastic potential function is obtained by assuming associated flow rule conditions, therefore:

$$G_2(\{\sigma'\},\{m\}) = F_2(\{\sigma'\},\{k\}) \qquad \textit{[Eq. 2-45]}$$

To summarize, this model is an example of constitutive model that involves two yield surfaces and is based on concepts of nonlinear elasticity and isotropic work hardening/softening plasticity theory. This model is appropriate for simulating the behavior of granular materials and has been used at Imperial College for modeling the behavior of fill materials in the construction of embankments. However the fourteen input parameters in this model are difficult to derive from results of standard laboratory tests for rockfill material; moreover the model's implementation into numerical modeling analysis is not straight forward (Kovacevic et al., 1994) and need some specific techniques which makes the development of model for further analysis of the rockfill dam more complicated (e.g. collapse settlements due to wetting; time-dependent settlements). Kovacevic et al. (2008) have provided examples of its use in assessing movements of six embankment dams constructed in United Kingdom. This model predicted the horizontal movements reasonably well comparing to other models. The likely causes for good predictions are: (i) stress dependent potential plastic function in Lade's model which capture the different dilative behaviors at different stress states as shown in Figure 2-12; (ii) the ability of the Lade's model to account for the pre-peak plastic strains, which are qualitatively quite different from the elastic strains predicted by the models explained before. Yet Lade's model cannot correctly predict the deformations after the first reservoir impounding which is an important aspect in modeling an embankment dam. The following two constitutive models have been proposed recently in order to capture the behavior after wetting and in the long term. These models have been formulated in two different frameworks: critical state concept and hypoplasticity.

2.3.5 Barcelona model (critical state concept)

Alonso et al. (1990) presented a constitutive model for describing the stress-strain behavior of partially saturated soils (slightly or moderately expansive). This model was formulated within the framework of hardening plasticity using two independent sets of stress variables: the excess of total stress over air pressure and the suction. On reaching saturation, the mode1 becomes a conventional critical state model. This model was initially kept as simple as possible in order to provide a basic framework from which extensions would be possible, and was formulated for isotropic and biaxial stress states. The calibration was based on laboratory tests on compacted kaolin and a sandy clay samples.

Later, Oldecop and Alonso (2001) modified this basic model for rockfill materials to4 include the effect of water on compressibility and collapse phenomena. Breakage of rock particles and fracture propagation were basic underlying mechanisms controlled by the relative humidity of the air filling the rockfill voids. The results of oedometer tests on a quartzite slate rockfill, in which saline solutions were used in order to impose a controlled relative humidity to the air flow, were used to calibrate the proposed constitutive model (Figure 2-13). During the test, the air flows through the rockfill voids, impelled by the pump. In a wetting path, the relative humidity imposed by the solution in the air flow was larger than the current relative humidity within the rock pores. Water vapor was transported from the vessel to the rockfill voids by advection. Further transport of water vapor occurs from rockfill voids to rock pores by molecular diffusion owing to the relative humidity gradient created between rockfill voids and rock pores. From a thermo-dynamical point of view, water vapor condensed within the rock pores wherever the width of the pore was smaller than approximately twice the radius of curvature at equilibrium of the gas-liquid interface. The absorption of water by the rockfill specimen during the test was measured by recording the loss of weight of the solution vessel. The aim of this system was to produce a gradual variation in the specimen water content by adding controlled quantities of water in a uniform manner across the specimen. A significant finding of Oldecop and Alonso (2001) was that bringing the relative humidity within the specimen to its maximum (i.e.100% relative humidity) led to a collapse strain equal to that observed in flooded specimens.

The elasto-plastic constitutive model proposed by Oldecop and Alonso (2001) was consistent with the basic deformation framework and most of its parameters had a physical meaning. Alonso et al. (2005), Alonso et al. (2011), and Costa and Alonso (2009) applied this constitutive model in simulation of the construction stage and impoundment of Beliche dam and Lechago dam. Later, Oldecop and Alonso (2007) extended the model in a framework rooted on the phenomenon of crack propagation in rock particles induced by stress corrosion mechanisms to explain macroscopic observations from long-term strain records obtained in large-diameter oedometer tests on compacted gravels which demonstrated that strains could be linearly related with the logarithm of time. They proposed that delayed compressibility coefficients were proportional to the conventional stress-induced compressibility coefficients. A new model of crack propagation in loaded disc-shaped particles was developed in order to explain the nature of particle breakage and its relationship with time, macroscopic stress and total suction.

In the formulation of the Barcelona model, volumetric compressibility of rockfill is assumed to have two components, whose origins are a particle rearrangement and a particle breakage phenomenon. The second is highly dependent on the prevailing relative humidity (or, alternatively, the total suction, s) at the rockfill particles. The second mechanism is active beyond a threshold mean stress, p_y. Isotropic compressibility is described by the following equations:

$$d\varepsilon_v = \lambda^i dp \qquad if\ p \le p_y$$

$$d\varepsilon_v = \lambda^i dp + \lambda^d(s) dp \qquad if\ p > p_y \qquad \textit{[Eq. 2-46]}$$

where $d\varepsilon_v$ is the incremented volumetric strain, p is the mean total stress, and λ^i and $\lambda^d(s)$ are compressibility parameters. $\lambda^d(s)$, which is made dependent on total suction, describes a deformation mechanism based on particle breakage, and accounts for some macroscopic phenomena observed in rockfill testing: the compressibility of rockfill increases as the material is wetted, and the rockfill collapses, under constant confining stress, when the ambient relative humidity is increased. The superscript 'd' in $\lambda^d(s)$ alludes to the delayed

nature of the particle breakage mechanisms. An appropriate function for the clastic compressibility parameter $\lambda^d(s)$ was found to be:

$$\lambda^d(s) = \lambda_0^d - \alpha_s ln\left(\frac{s + P_a}{P_a}\right) \qquad \textit{[Eq. 2-47]}$$

Where λ_0^d is the volumetric compressibility for saturated conditions and α_s is a material parameter. The atmospheric pressure, P_a, is introduced to avoid indeterminacies for saturated conditions ($s = 0$). $\lambda^d(s)$ is restricted by $\lambda^d(s) \geq 0$.

Rockfill elastic behavior is characterized by two compressibility coefficients κ and κ_s, and a Poisson ratio, ν. The compressibility coefficients κ and κ_s are defined as follows:

$$d\varepsilon_v^e = \kappa dp = \frac{dp}{E} 3(1 - 2\nu)$$

$$d\varepsilon_v^{es} = \kappa_s \frac{ds}{s + P_a} \qquad \textit{[Eq. 2-48]}$$

Where the volumetric elastic strains $d\varepsilon_v^e$ and $d\varepsilon_v^{es}$ are induced by total stress and suction changes. It should be noted that the elastic bulk modulus defined in the above equations does not depend on the mean stress which is a shortcoming of the constitutive model for rockfill material with stress dependent compressibility. The swelling stiffness coefficient κ_s is, in general, very small, except for expansive claystones and shales, and a default value of zero is usually suitable.

For isotropic conditions, the yield stress, p_0, is defined by the following expression:

$$\begin{aligned} p_0(s) &= p_0^* && \text{if } p_0^* \leq p_y \\ p_0(s) &= p_y + \frac{(\lambda^i - \kappa)(p_0^* - p_y)}{\lambda^i + \lambda^d(s) - \kappa} && \text{if } p_0^* > p_y \end{aligned} \qquad \textit{[Eq. 2-49]}$$

Where p_0^* defines the position of the yield curve, and it was identified as the yield stress for a very dry rockfill. A simple volumetric hardening was proposed to follow the evolution of p_0^*:

$$dp_0^* = \frac{d\varepsilon_v^p}{\lambda^i - \kappa} \qquad \textit{[Eq. 2-50]}$$

Where the plastic volumetric strains, $d\varepsilon_v^p = d\varepsilon_v - d\varepsilon_v^e$, may be obtained through consistency conditions.

The model was extended to triaxial stress conditions (stress variables $p = (\sigma_1 + 2\sigma_3)/3$; $q = \sigma_1 - \sigma_3$) by means of a family of elliptical yield curves similar to the constitutive equations which are based on critical state concept. The yield surface, F, in a space (p, q, s) was defined by

$$F(p, q, s) = q^2 - M^2(s)[p + p_s(s)][p_0(s) - p] = 0 \qquad \textit{[Eq. 2-51]}$$

The constitutive model based on the elliptical yield function was a simple choice but provided satisfactory results as shown by Alonso et al. (2005). The effect of suction on rockfill strength was introduced through parameters $p_s(s)$ and $M(s)$. Parameter $p_s(s)$ provides an apparent cohesive intercept that serves to approximate the real non-linear strength envelopes found in testing. The dependence of the critical-state slope M on s also helps to introduce suction effects on rockfill limiting shear conditions. $p_s(s)$ is simply defined as a linear function of suction:

$$p_s(s) = k_s s \qquad \textit{[Eq. 2-52]}$$

Where k_s is a material parameter. As the available experimental data on rockfill often consist of tests performed on dry or flooded specimens, $M(s)$ was defined in terms of two extreme values: M_{dry} and M_{sat}. M_{dry} corresponds to the relative humidity existing at the laboratory and M_{sat} corresponds to saturated conditions. The transition from M_{sat} to M_{dry} takes place for an increase in suction from a zero value, when the specimen is saturated, to a very high value, typically a few tens or even hundreds of MPa for the relative humidity prevailing in laboratories. The following experimental expression was proposed by Alonso et al. (2005) to model this variation:

$$M(s) = M_{dry} - (M_{dry} - M_{sat})\left(\frac{M_{sat}}{M_{dry}}\right)^{s/10^{Pa}} \qquad \textit{[Eq. 2-53]}$$

In order to maintain the model's simplicity, the same non-associated manner proposed for the cohesive soils by Alonso et al. (1990) was considered for the rockfill, and a potential function G was defined using an additional material parameter, α, as follows:

$$G(p, q, s) = q^2 - \alpha M^2(s)[p + p_s(s)][p_0(s) - p] = 0 \qquad \textit{[Eq. 2-54]}$$

Altogether there are 12 parameters in this model: elastic modulus, E, Poisson's ratio ν, Plastic instantaneous compressibility $(\lambda^i - \kappa)$, clastic compressibility for saturated condition λ_0^d, the rate of change of clastic compressibility with total suction α_s, slope of critical state strength for dry condition M_{dry}, slope of critical state strength for saturated condition M_{sat}, increase in cohesion with suction k_s, threshold yield mean stress for the onset of clastic phenomena p_y, non-associativeness of plastic potential function α, initial suction s_0, initial mean yield stress p_0^*. Several laboratory tests are required to calibrate the parameters of the model for a particular rockfill material including large-scale oedometer and triaxial tests with the requirement of controlling the relative humidity of the samples during the tests.

The compressibility relations for the rockfill were described by linear functions relating strain and stress. The threshold stress p_y and the hardening parameter p_0^*, have no equivalent in the case of unsaturated soils. An important aspect, from a fundamental perspective, is that the suction term, s, has a different meaning in this constitutive model. In soil mechanics, it is generally accepted that, for low-plasticity unsaturated soils and silts, s is identified with the capillary or matric component of suction. However, the role of suction in the case of rockfill as utilized in this model is different. Following the ideas of Oldecop and Alonso (2001) suction controls the velocity of crack propagation in rockfill particles. Therefore no direct mechanical action should be assigned to the suction term in this case. It is a state variable externally controlled by boundary conditions and flow phenomena. The crack propagation velocity depends on the total energy of the water on propagating cracks, and therefore it is measured by the relative humidity or, alternatively, by the total suction.

An alternative formulation was also proposed by Oldecop and Alonso (2001) in which the isotropic compressibility, yield surface and hardening law were expressed in terms of rock water content (instead of suction). However the general trends were similar to what explained here, and this alternative approach had not any advantage over the explained one. The distinction may prove significant in situations in which the chemical composition of the water, which controls the osmotic component of total suction, is a relevant variable. But this is probably not very important in applications in dam engineering.

To sum up, the initial critical state model based on unsaturated soil mechanics concepts which was proposed by Alonso et al. (1990) have been very successful in capturing the behavior of cohesive soils. However the extension of this model to characterize the behavior of rockfill material which is an extreme granular material might be questionable. The particular definition of suction within rock pores, the elliptical shape of the failure envelope and formulation of the potential function which lacks the stress dependency of the volumetric behavior as required for granular material are the main shortages. The difficulty of the calibration of the parameters and test procedures will limit the application of this constitutive model in practice of dam engineering. However this model is of the most advanced constitutive models which have been successfully applied in modeling of the behavior of compacted rock particles in dam engineering.

2.3.6 Hypoplastic models

The previous constitutive model for wetting deformations was developed in order to relate the wetting deformation to the degree of saturation and the so-called suction of the rockfill material and fall into the scope of unsaturated soil mechanics. These kinds of models can capture particular properties of wet and fine grained materials, but rarely reflect the time dependent reduction of the stiffness of weathered materials. Hypo-plasticity introduced the so-called solid hardness in the sense of a continuum description to take into account the state of weathering of the material over time. With a degradation function for the solid hardness, the time dependent evolution of creep and stress relaxation could be modeled. Similar procedures can be implemented to predict the behavior of the material during wetting.

The concept of hypo-plasticity was generally developed to model clay or soft soils without recourse to the concepts in elasto-plasticity theory such as yield surface, plastic potential function and decomposition of deformations into elastic and plastic parts (Gudehus, 2004; Huang et al., 2006; Masin, 2005, 2007). In hypo-plasticity, the constitutive equation is of the rate type, where the objective stress rate tensor, $\dot{T}$, is expressed by an isotropic tensor-valued function, H, that depends on the simplest case on the current effective stress tensor, T , and the strain rate tensor, D:

$$\dot{T} = H(T, D) \qquad \textit{[Eq. 2-55]}$$

Using the above equation, the inelastic material properties are modeled with an incrementally nonlinear form, where the tensor function, H, in the above equation is decomposed into the sum of the tensor function $L{:}D$, which is linear in the rate of deformation D, and the tensor function $N\|D\|$, which is nonlinear in D:

$$\dot{T} = H(T, D) = L{:}D + N\|D\| \qquad \textit{[Eq. 2-56]}$$

Using this concept, Bauer and Zhu (2004) were the first to model the wetting deformation of stressed and moisture-sensitive weathered rockfill materials in a simplified manner by a reduction of the solid hardness which was implemented in the tensor function, H, in the above equation. In this context, the so-called solid hardness is related to the isotropic compression of the grain assembly in the way of a continuum description and does not mean the hardness of an individual grain (Gudehus, 2004).

Recently some hypo-plastic constitutive models were proposed for modeling the long term behavior and wetting deformation of weathered and moisture-sensitive rockfill materials. These models take into account the influence of the current density, the effective stress state, the moisture sensitive solid hardness and the rate of deformation. The most advanced one which could be implemented in modeling of the rockfill behavior was proposed by Fu and Bauer (2009) with embedding of an evolution equation for the reduction of the solid hardness over time which permits the prediction of creep and stress relaxation. This hypo-plastic constitutive equation for the evolution of the stress is based on nonlinear tensor-valued functions depending on the current void ratio, stress, deformation rate, moisture

dependent solid hardness, and rate of reduction of the solid hardness. In this kind of hypo-plastic constitutive model, an additional term appears which is proportional to the rate of the solid hardness and to the current stress state. The void ratio e is taken into account as an additional state variable in the constitutive equation and is related to the strain rate tensor as:

$$\dot{e} = (1 + e)trD \qquad \textit{[Eq. 2-57]}$$

With maximum and minimum limits and the critical value (referring to the critical state of the material) which are all pressure dependent and decrease with an increase of the mean pressure $p = tr(T)/3$, as illustrated in Figure 2-14.

The upper bound e_{max} is related to an isotropic compression starting from the loosest possible skeleton with grain contacts, and it can be approximated for a wide range of pressures using the following compression relation proposed by Bauer (1996):

$$e_{max} = e_{max0} exp\left[\left(\frac{3p}{h_s}\right)^n\right] \qquad \textit{[Eq. 2-58]}$$

Where e_{max0}, denotes the value of e_{max} for p = 0. h_s is the solid hardness of the grain assembly under isotropic compression and has the dimension of stress. As shown in Figure 2-15, the quantity of h_s is defined for the isotropic stress ($3p$) at which the compression curve in a semi-logarithmic representation shows the point of inflection (Bauer, 2009). The exponent n is a dimensionless constant and is related to the inclination of the compression curve. For high pressures, the void ratio in the above equation tends to zero, which can be explained by grain plasticization and grain crushing. The same pressure dependence for e_{max} on p is postulated by Gudehus (1996) for the other void ratios e_c, and e_{min} as:

$$\frac{e_{max}}{e_{max0}} = \frac{e_{min}}{e_{min0}} = \frac{e_c}{e_{c0}} = exp\left[\left(\frac{3p}{h_s}\right)^n\right] \qquad \textit{[Eq. 2-59]}$$

where e_{c0} and e_{min0}, are the appropriate void ratios for p = 0 and are obtained with conventional index tests. Using these values and concepts, the proposed tensor function of the hypoplastic constitutive equation has the following representation:

$$\dot{T} = f_s[L{:}D + f_d N\|D\|] \qquad \textit{[Eq. 2-60]}$$

with:

$$L{:}D = \hat{a}^2 D + tr(\hat{T}D)\hat{T} \qquad \textit{[Eq. 2-61]}$$

$$N = \hat{a}\left(\hat{T} + \hat{T}^*\right) \qquad \textit{[Eq. 2-62]}$$

Where:

$$\hat{T} = \frac{T}{tr(T)} \qquad \textit{[Eq. 2-63]}$$

$$\hat{T}^* = \hat{T} - \frac{I}{3} \qquad \textit{[Eq. 2-64]}$$

$\hat{a}$ is adopted to the stress limit condition given by Matsuoka and Nakai (1974), as illustrated in Figure 2-9, and is related to the critical friction angle φ_c, the current normalized stress deviator $\hat{T}^*$, and its Lode angle θ as:

$$\hat{a} = \frac{sin\varphi_c}{3 - sin\varphi_c}\left[\sqrt{\frac{8/3 - 3\left\|\hat{T}^*\right\|^2 + \sqrt{3/2}\left\|\hat{T}^*\right\|^3 cos(3\theta)}{1 + \sqrt{3/2}\left\|\hat{T}^*\right\| cos(3\theta)}} - \left\|\hat{T}^*\right\|\right] \qquad \textit{[Eq. 2-65]}$$

The influence of the mean pressure p and the current void ratio e on the response of the constitutive equation is taken into account with the stiffness factor f_s and the density factor f_d. The dilatancy behavior, the peak stress ratio, and strain softening are related to the density factor f_d, which represents a relation among the current void ratio e, the pressure dependent critical void ratio e_c, and minimum void ratio e_{min}:

$$f_d = \left(\frac{e - e_{min}}{e_c - e_{min}}\right)^{\alpha} \qquad \textit{[Eq. 2-66]}$$

Where $\alpha < 0.5$ is a model parameter. The stiffness factor f_s mainly depends on the solid hardness h_s, the mean pressure p, and the ratio of the maximum void ratio e_{max} to the current void ratio e. The full representation of the density factor reads as:

$$f_s = \left(\frac{e_{max}}{e}\right)^{\beta} \left[\frac{8sin^2\varphi_c}{(3 - sin\,\varphi_c)^2} + 1 - \frac{2\sqrt{2}\,sin\,\varphi_c}{3 - sin\,\varphi_c}\left(\frac{e_{max0} - e_{min0}}{e_{c0} - e_{min0}}\right)^{\alpha}\right]^{-1} \cdot \frac{h_s(1 + e_{max})}{n e_{max}\left\|\hat{T}^*\right\|^2}\left(\frac{3p}{h_s}\right)^{1-n} \qquad \textit{[Eq. 2-67]}$$

Where β is a model parameter. This relation is obtained from a consistency condition that links the compression relation with the general form of the constitutive equation, as outlined by Gudehus (1996). In order to model the influence of reduction of the stiffness of a stressed rockfill due to the reaction with water or over time (creep deformations), the constant solid hardness h_s is replaced by the moisture- and history-dependent state quantity h_{st} which reduces over time or with increasing moisture. The influence of the reduction of the solid hardness on the compression behavior is shown in Figure 2-16. The current state of the solid hardness, h_{st}, ranges within $h_{sw} < h_{st} < h_{s0}$. Herein, the upper limit h_{s0} is the solid hardness before wetting and the lower limit h_{sw} is the final degraded quantity depending on the relative moisture content of the grains (and also the time span in the creep analysis). The reduction of the solid hardness also leads to a reduction of the pressure dependent limit void ratios and critical void ratio, which is more pronounced for higher stress levels, as illustrated in Figure 2-17.

If a reaction with water takes place, the process of reduction of the soil hardness is modeled using the following evolution equation as proposed by Bauer (2009):

$$\dot{h}_{st} = -\frac{h_{st} - h_{sw}}{\omega} \qquad \textit{[Eq. 2-68]}$$

Where the parameter ω is related to the rate of reduction of the solid hardness with time, h_{st} denotes the current state, and h_{sw} denotes the final value of the solid hardness (i.e. h_{sw} depends on the state where the reaction of the solid material with water is completed). Wetting can lead to a continuation of the process of disintegration of the grain material, and

the value of h_{sw} is not a material constant. The above relation reflects the experimental observation that the amount of the rate of reduction of the solid hardness is higher for a larger difference between h_{st} and h_{sw}. For $h_{st} = h_{sw}$, the reduction rate is zero. The integration of this equation over time yields the solid hardness h_{st} as a function of the reduction time t, which is represented by the following exponential function (Fu and Bauer, 2009):

$$h_{st} = h_{sw} + (h_{s0} - h_{sw})exp(-\frac{t}{\omega}) \qquad \textit{[Eq. 2-69]}$$

This equation describes the time dependent transition which is the reduction of the solid hardness from the dry state h_{s0} to the final state reached under the water saturated state h_{sw}.

Altogether there are 10 parameters in this hypoplastic model (α, β, n, e_{max0}, e_{min0}, e_{c0}, φ_c , h_{s0}, h_{sw} and ω). Assuming that all these parameters are independent of the moisture content of the sample (which is not necessarily true), the only parameters related to the degradation of the material are the solid hardness for the water saturated state h_{sw} and the degradation velocity ω. The value of h_{sw} can be calibrated based on a drained isotropic compression test for the water saturated material, and the value of ω can be related to a creep or stress relaxation tests. The other constitutive parameters can be calibrated for the dry (and saturated) state of the material based on the experiments on the rockfill material and reproducing the results with numerical models. Several types of tests are required to estimate the correct values of these parameters: triaxial tests, compression tests, index tests. Some of these constitutive constants which don't have a clear physical meaning are more difficult to calibrate (i.e. α,β,n).

There are some experimental relations in the proposed model which are not necessarily applicable to all kind of rockfill materials (e.g. the relation for pressure dependency of the upper bound void ratio e_{max} to the isotropic pressure p and postulation of its parameters for the other void ratio limits e_c, and e_{min}). Both relations for stiffness and density factors (f_s and f_d) which are key factors in definition of the constitutive model are based on these experimental relations. Moreover, the critical friction angle φ_c is assumed to be constant

for the material regardless of the state of stress or water content, which is not true as shown by other researchers such as Barton and Kjarnesli (1981), Leps (1970), and Marachi et al. (1969). These shortages bring uncertainty in the implementation of this model in dam engineering, although the rate dependency of these kinds of constitutive models makes them suitable for modeling the creep phenomena in rockfill material. The simple idea of reduction of the solid hardness from the dry state to the final state using a single parameter (rather than changing the whole set of the parameters due to wetting) is interesting and can be used in other more stable methods (e.g. hyperbolic model) to predict the wetting or creep deformations.

2.4 Comparison of constitutive models

In reviewing constitutive laws spanning from linear elastic to models based on critical state concept, Naylor (1991) concluded that a stress-strain law should ideally incorporate the following characteristics of the rockfill material in order to successfully capture the behavior of this material during construction and impoundment of a rockfill dam:

1. The increase in bulk stiffness which occurs with increasing stress level (i.e. the concave form of an isotropic compression or oedometer stress-strain curve)

2. The reduction in shear stiffness which occurs with increasing deviator stress (i.e. the convex form of the triaxial test deviator stress-strain curve)

3. A Mohr-Coulomb or similar type of failure criterion. This implies that an incremental shear modulus tends to zero as the failure state is approached.

4. A higher stiffness on unloading

5. The effects of dilatancy, i.e. the tendency of a stiff soil such as a well compacted granular fill to increase its volume on shearing.

6. Collapse settlement, i.e. the reduction in volume of initially dry material when saturated (or even wetted).

The models described in this chapter were divided into elastic and elasto-plastic models (except for the hypoplastic models which are based on completely different concepts). The elastic models incorporate characteristics (1), (2) and (6) and to some extent (3) but not (5). Characteristic (4) can also be incorporated in elasticity only by user decision on what constitutes unloading and the alternation of stiffness parameters for the region in which this occurs. Basic elasto-plastic models incorporate characteristics (3), (4) and to some extent (5) but not (1), (2) nor (6). The more advanced elasto-plastic and hypoplastic models can in principal incorporate all of the above six characteristics, but implementation is different.

In Table 2-1, a brief comparison is made between the discussed constitutive models. The simplest models (i.e. linear elastic, anisotropic elastic and elastic-perfectly plastic models) have many limitations in capturing the key behaviors and their implementations are recommended to the initial stages of the modeling and where there are no zones of strongly differing stiffness. On the other hand, the advanced constitutive models (i.e. double hardening, hypoplastic and critical state models) have many limitations in calibrating and require much more laboratory testing and computer resources which make the implementations very difficult and only a few cases have been practically modeled using these models. The nonlinear elastic models are the most common constitutive laws applied in dam engineering in which the simplicity and accuracy are well balanced.

Among the different nonlinear elastic models, the hyperbolic model has been the most applied constitutive model in simulating rockfill dams around the world. It has the advantages that it can capture the nonlinear and stress-dependent behavior and that the parameters involved has physical significance and can be evaluated using the results of the conventional triaxial tests. However it is inherently elastic and does not model plastic deformation in a fully logical way; it is also incapable of modeling the dilative behavior of compacted granular material. In spite of these shortcomings, Duncan (1992) reported more than twenty successful cases from the literature which have implemented the hyperbolic stress-strain relationship in the finite element analysis of the embankment dam. These cases involved analysis that was done mostly after, and also a few before the fact (type C1 and type A predictions according to Lambe's classification). Cruz et al. (2009) also mentioned more examples of such implementation in modeling the behavior of CRFDs (i.e. Concrete

Face Rockfill Dam) in China, Brazil and Australia. This brings up the fact that the hyperbolic model is probably the most stable constitutive model which has been implemented in numerical modeling of rockfill dams of different kinds worldwide and that there is a big database available for calibration of the parameters based on general physical and engineering properties (such as particle gradation and density).

As explained by Potts and Zdravkovic (2001), there has been some efforts to couple the hyperbolic relation with some perfectly plastic failure criteria (such as Mohr-Coulomb) in an attempt to improve the prediction of the plastic deformations and dilative behavior. This is especially important when modeling zoned dams with contrast in compressibility of different zones. However the basic elasto-plastic laws which have been used for this purpose were themselves limited in predicting the correct behavior of the compacted rock particles. As a matter of fact, both the yield and potential functions of Mohr-Coulomb failure criteria need to be modified before coupling. Provided that these functions of the Mohr-Coulomb model be modified to capture the key behavior of compacted assemblages of rock particles as exist in rockfill dams (e.g. stress dependency of both friction and dilation angle), it can very well cover the shortcomings of the hyperbolic model as shown in Table 2-1.

Most of the efforts in modifying the yield function of the Mohr-Coulomb model were to overcome the corner problem which implied singularities in the basic model during numerical modeling (as shown in Figure 2-9). However the additional parameters which exist in the modified continuous failure surfaces (i.e. failure surfaces without corners in the deviatoric plane) require more laboratory testing to be calibrated for a given material which again introduces uncertainties and difficulties in the modeling process (e.g. Lade double hardening model). Alternatively, these corners can be dealt with in the computer program; this involves some elaborate computer codes which inevitably results in the use of more computer resources. Considering the existing powerful computers these days, this is not an important issue anymore. Stress-dependency of the failure envelope and dilation angle is much more important to consider as a modification of the constitutive law to better capture the behavior of compacted assemblages of rock particles.

The associated (or even non-associated) flow rule with constant dilation angle in the Mohr-Coulomb model has also restrictions in prediction of volumetric strains on failure envelope (Figure 2-12). The previous efforts in addressing this problem were to allow the angle of dilation to vary with plastic strain using some hardening or softening rules and introducing new parameters for the model. Although this was logical but the dependency of the dilation angle to the confining stress and the physical properties of the material (e.g. density, degree of saturation) have not been fully addressed in these strain hardening laws. These are important issues of the behavior of the granular material (Bolton, 1986) that should also be considered in modeling of rockfill dams during construction and impoundment.

2.5 Conclusion

A summary of constitutive models which have been used in the past to model the behavior of rockfill dams during construction and impoundment was presented in order of increasing complexity. Selecting an appropriate stress-strain relationship is primarily involved with balancing simplicity and accuracy. While it seems reasonable that more complex stress-strain relationships should be able to model the behavior of the rock particles more accurately, there is no benefit in using a very complex relationship to analyze the problem where the simpler representation of the stress-strain behavior would result in an acceptable accuracy. Moreover the applicability of the more complex constitutive models in simulating the rockfill material is often questionable because of: (i) the difficulty of the calibration of the model using the limited test results of such material in practice, and (ii) the initial assumptions and experimental relations taken in the formulation of these constitutive models are not necessarily extendible to compacted samples of large rock particles as exist in rockfill dams.

In the province of Quebec where this study is done, the rock particles used in the construction of rockfill dams have high compressive strength and good resistance to saturation. However, the dams are generally designed to have several zones with different compressibilities which introduces zones with high shear, and the need to consider plasticity and dilation. The hyperbolic model, if coupled with an appropriate failure criterion, seems to be the most balanced constitutive law for the purpose of modeling rockfill dams in Quebec during construction and impoundment. The modified failure and

the potential functions should consider the dependency of both friction angle and dilation angle to key physical properties of the rock particles (e.g. stress state, density and degree of saturation). Another potential enhancement to this model is the algorithms proposed by Nobari and Duncan (1972) and modified by Escuder et al. (2005) in a finite difference context which are not robust and should be improved in order to increase the stability of the simulation of the wetting process.

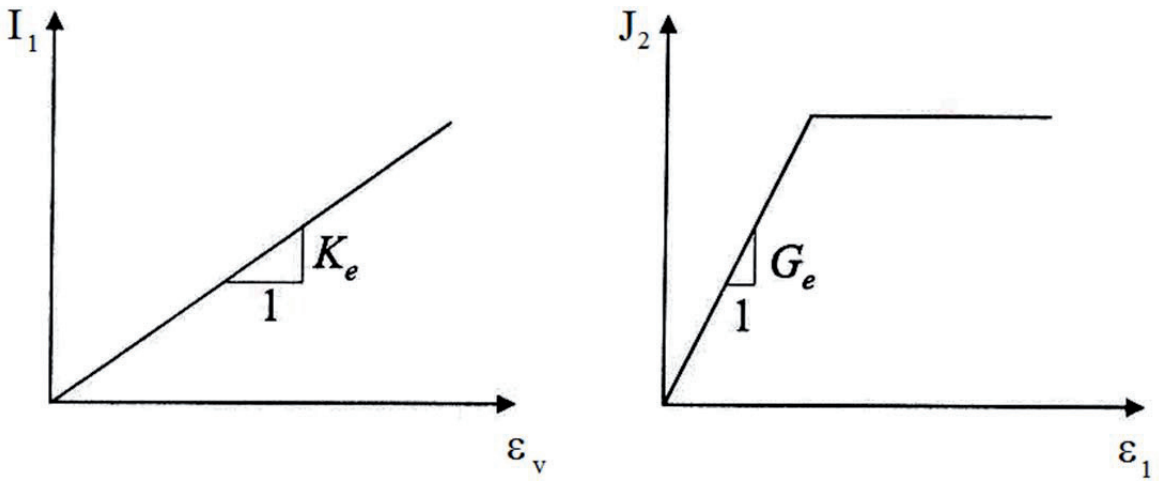

Figure 2-1 – Schematic of the Bi-linear model

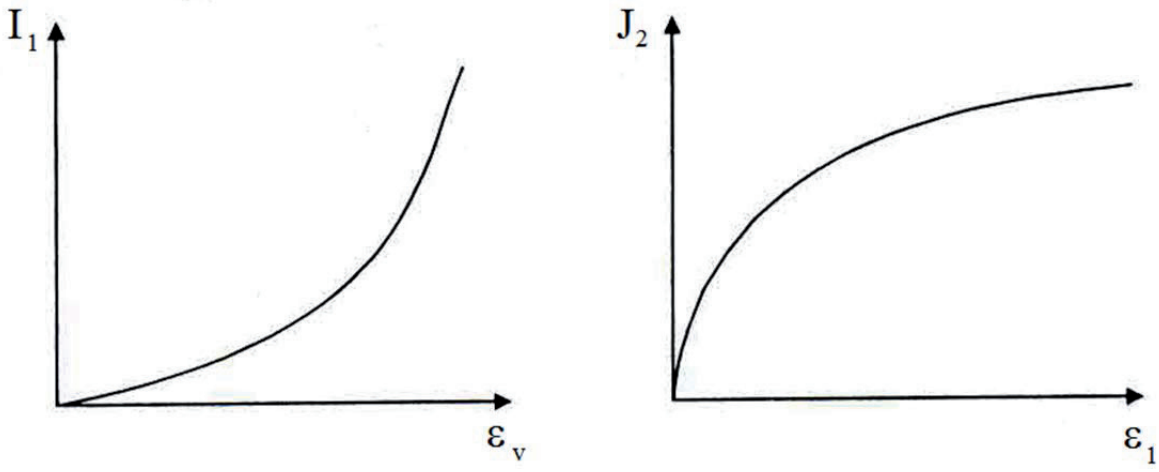

Figure 2-2 – Schematic of the K-G model

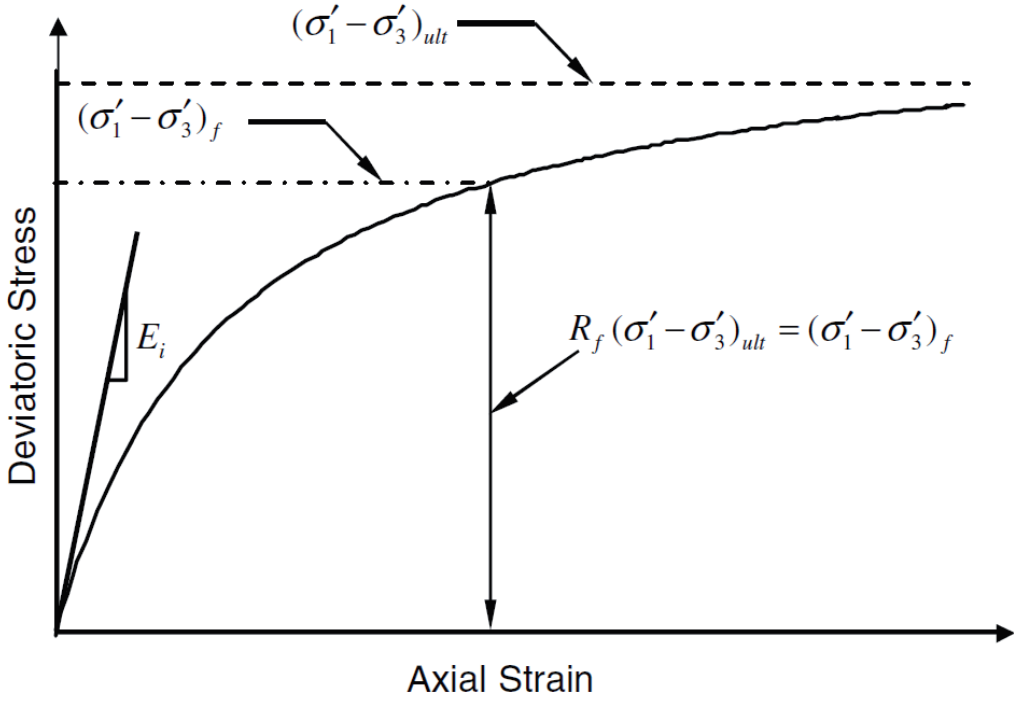

Figure 2-3- Stress-strain curve for the nonlinear hyperbolic model; after Singh et al. (2009)

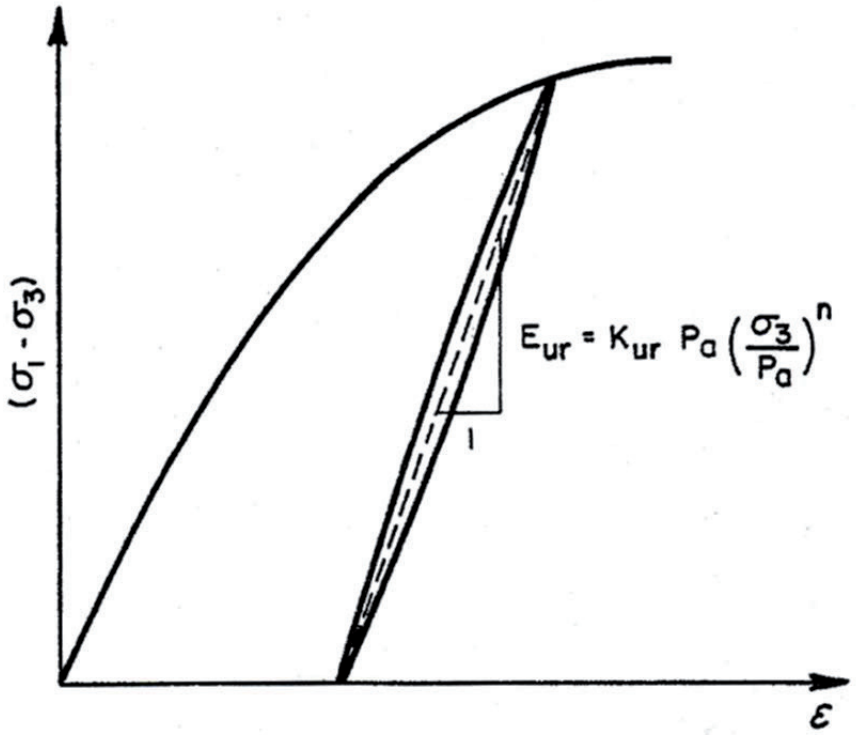

Figure 2-4- Introducing the inelasticity in hyperbolic model by the means of unloading-reloading modulus (Kur)

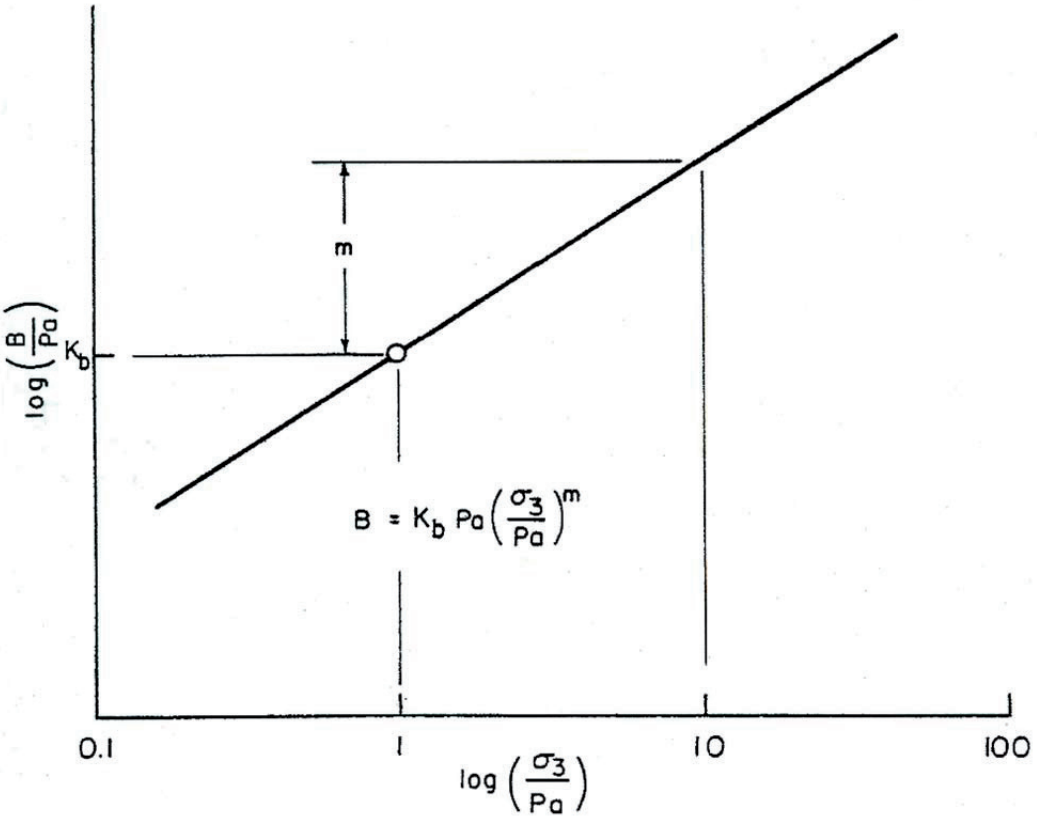

Figure 2-5- variation of bulk modulus with confining stress in logarithmic scale

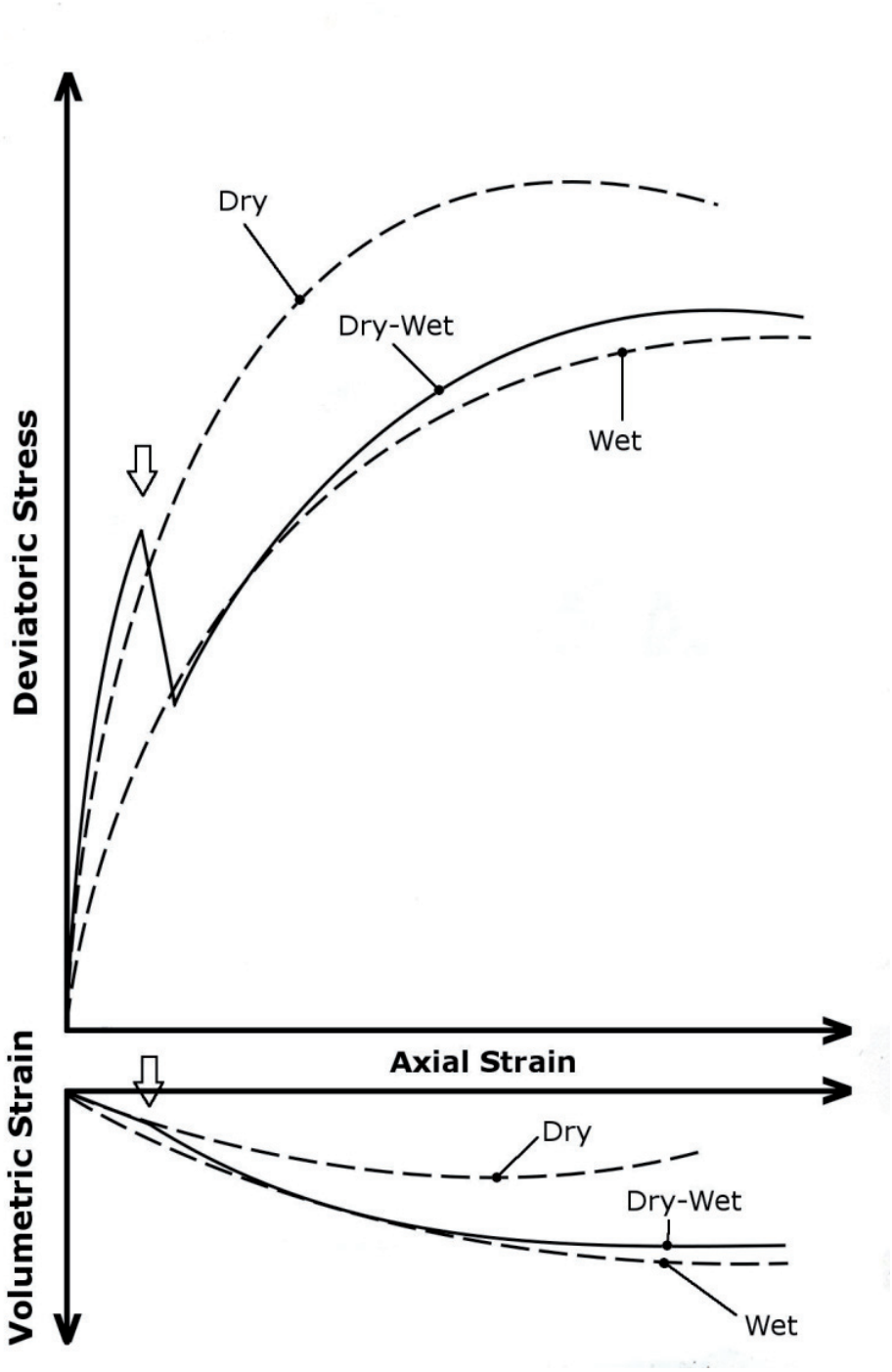

Figure 2-6- Calculation of the collapse deformation due to wetting using triaxial test results and comparison of stress-strain and volume change curves for dry, wet, and dry-wet specimens; after Nobari and Duncan (1972)

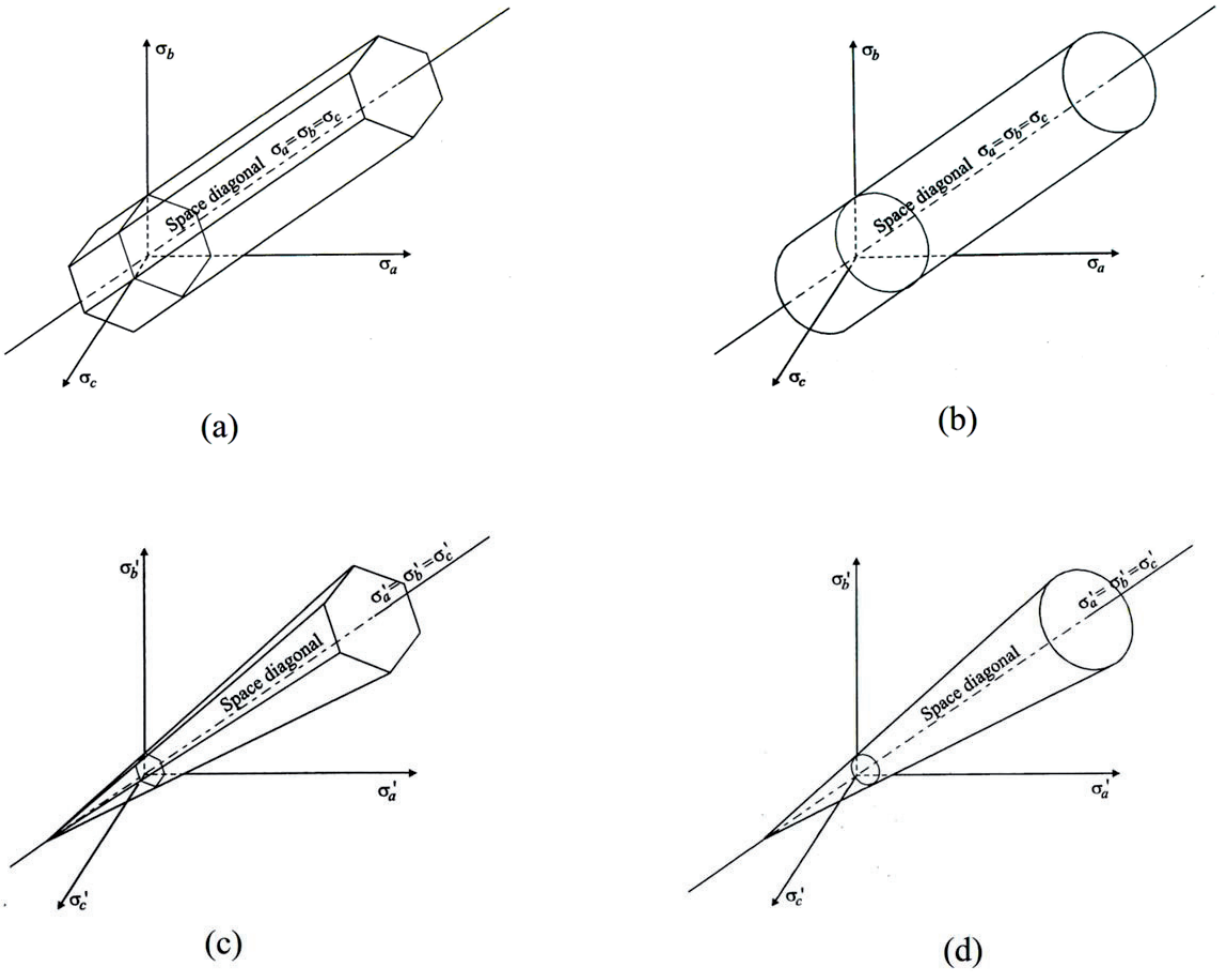

Figure 2-7- Perfect plastic yield surfaces in principal stress space (a)Tresca (b)Von Mises (c) Mohr-Coulomb (d) Drucker-Prager

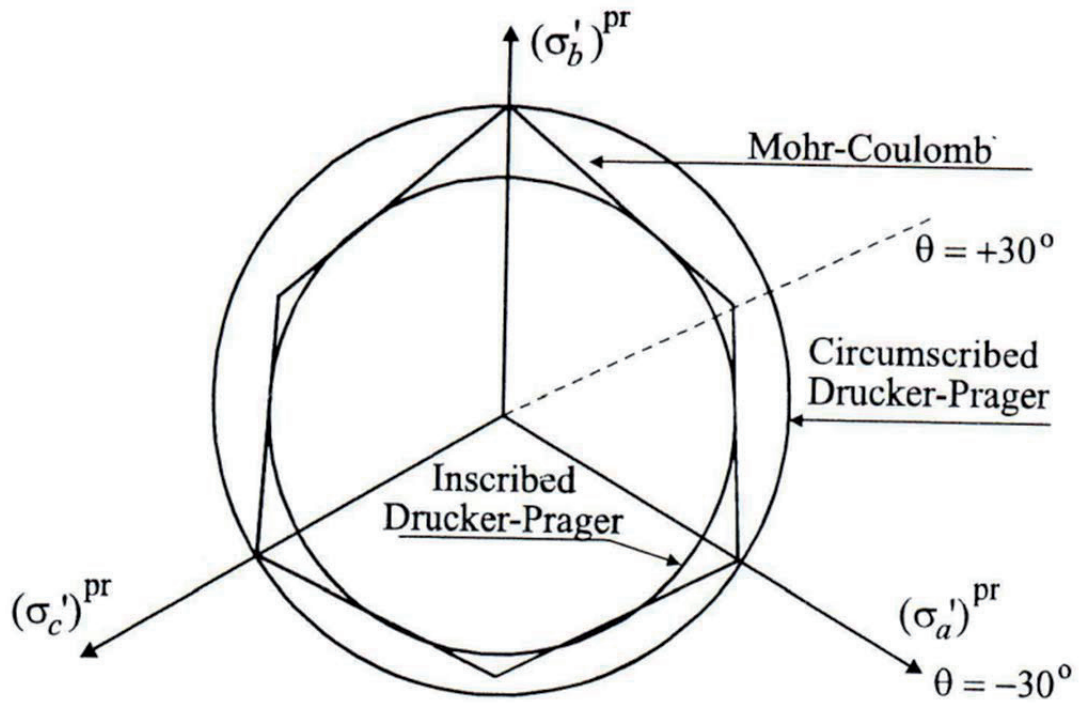

Figure 2-8- Drucker-Prager and Mohr-Coulomb yield surfaces in the deviatoric plane

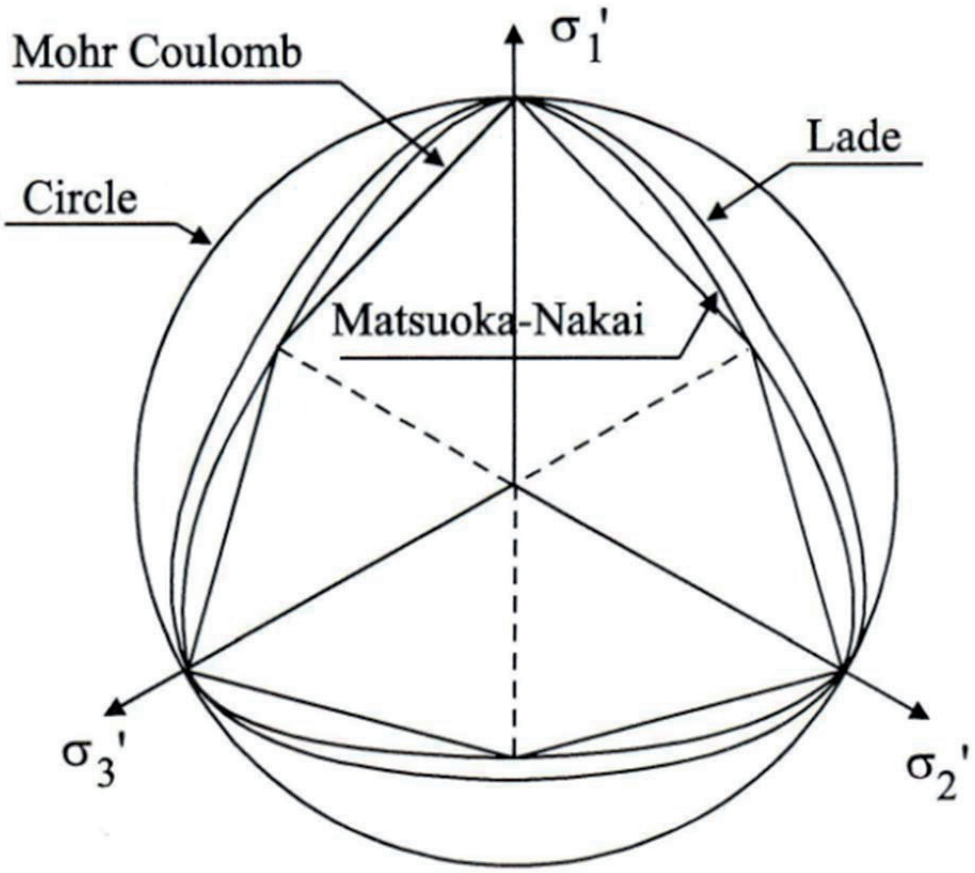

Figure 2-9- Comparison of Lade and Matsuoka-Nakai failure surfaces with Mohr-Coulomb and circumscribed Drucker-Prager surfaces in the deviatoric plane.

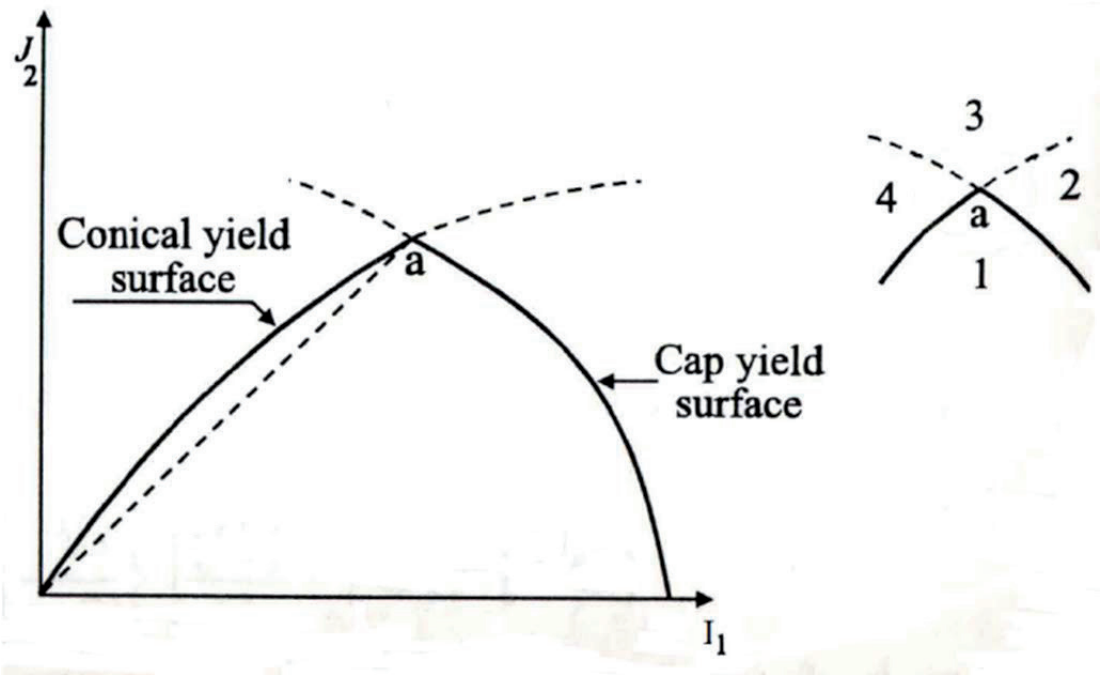

Figure 2-10- Yield surfaces for Lade's double hardening model

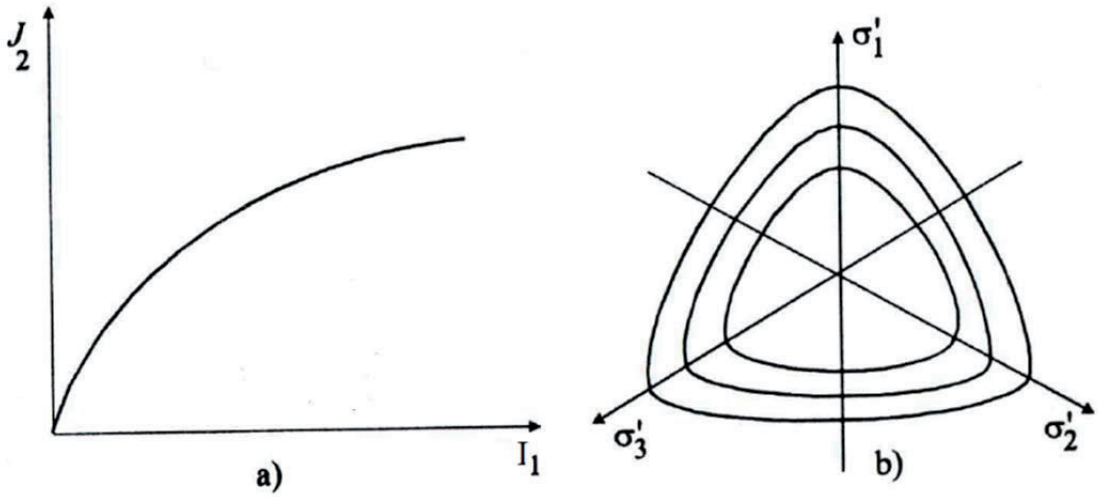

Figure 2-11- Conical failure criteria of the Lade's double hardening model; and its expansion in deviatoric space

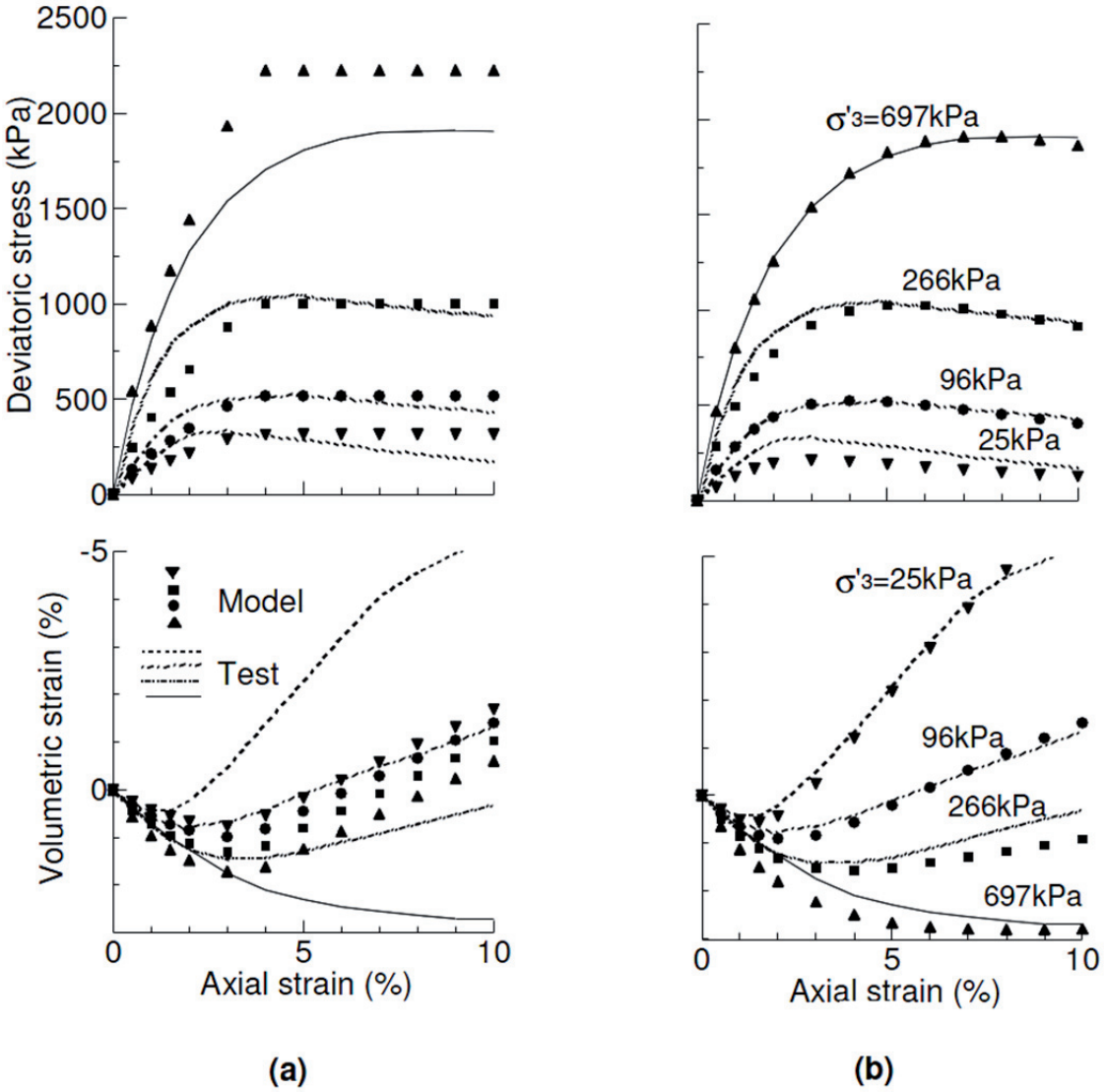

Figure 2-12- Predicted and measured behavior in triaxial tests of rockfill material from Roadford dam by (a) Mohr-Coulomb model with constant dilation angle; (b) Lade's model with stress dependent volumetric behavior; after Kovacevic et al. (2008).

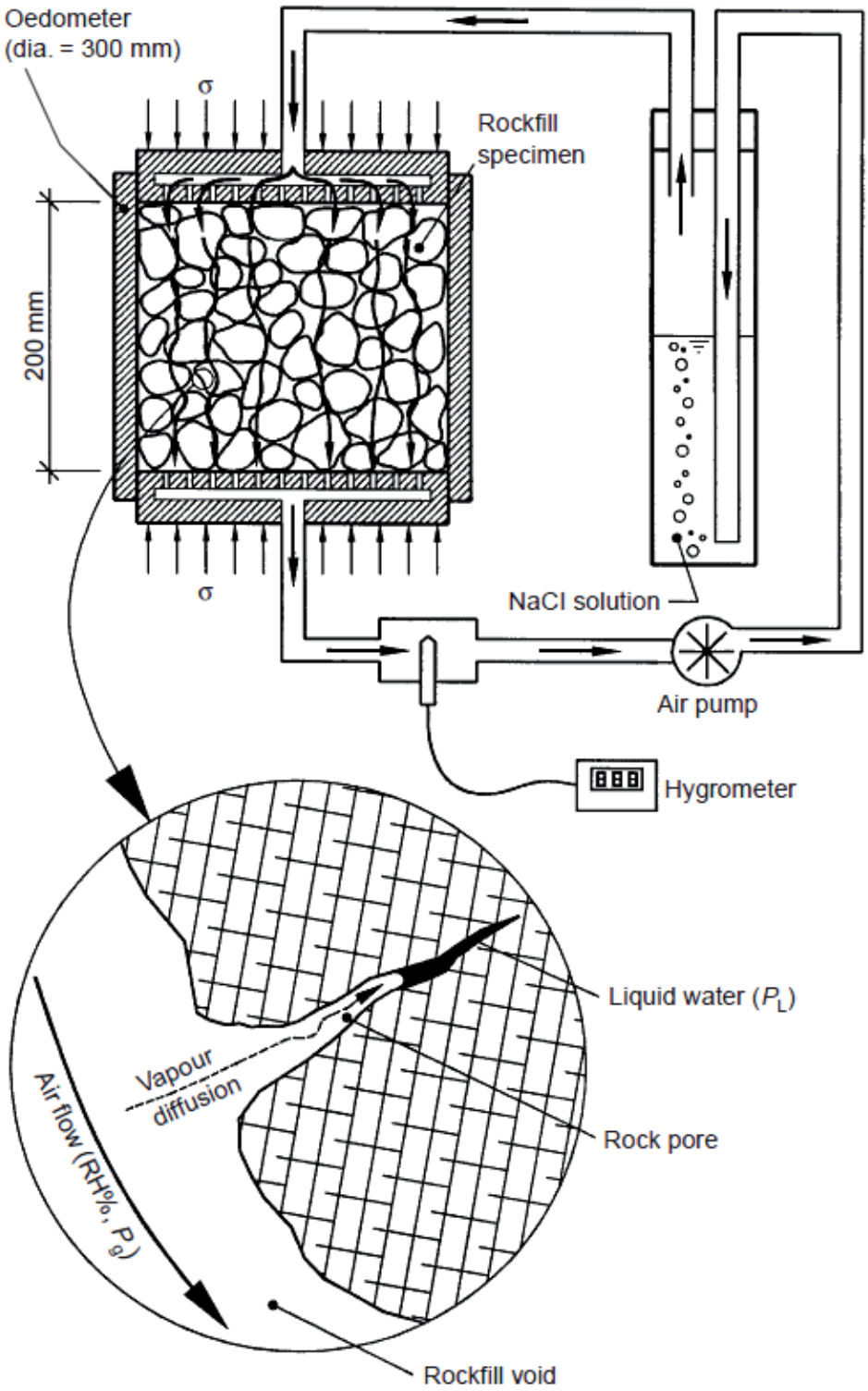

Figure 2-13- Rockfill oedometer test setup with a relative humidity control system; after Oldecop and Alonso (2001)

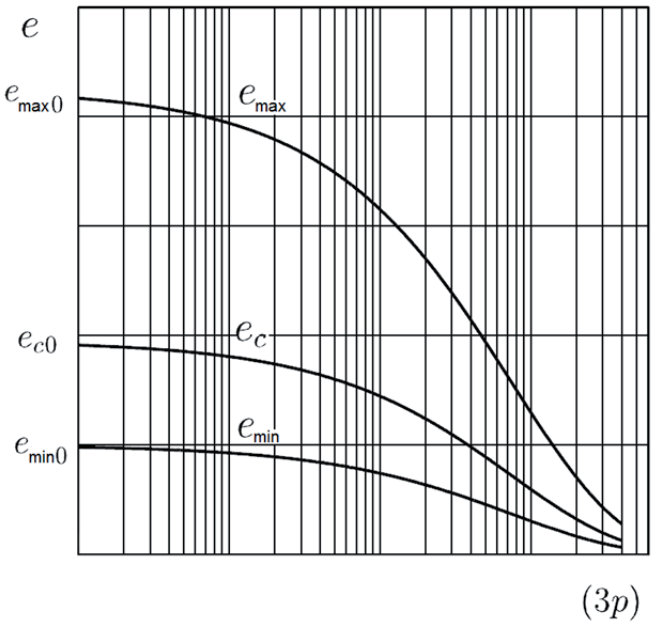

Figure 2-14- Pressure dependence of the maximum void ratio e_{max}, the minimum void ratio e_{min}, and the critical void ratio e_c; after Bauer (2009).

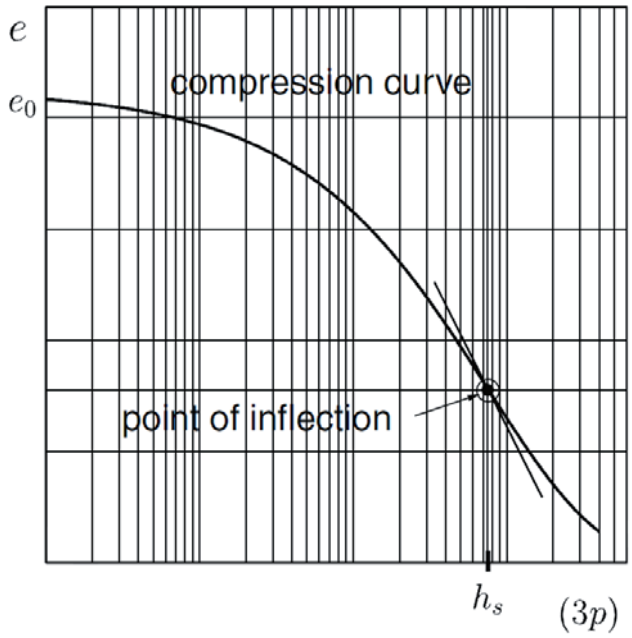

Figure 2-15- Estimation of solid hardness from an isotropic compression test in a semi-logarithmic representation; after Bauer (2009).

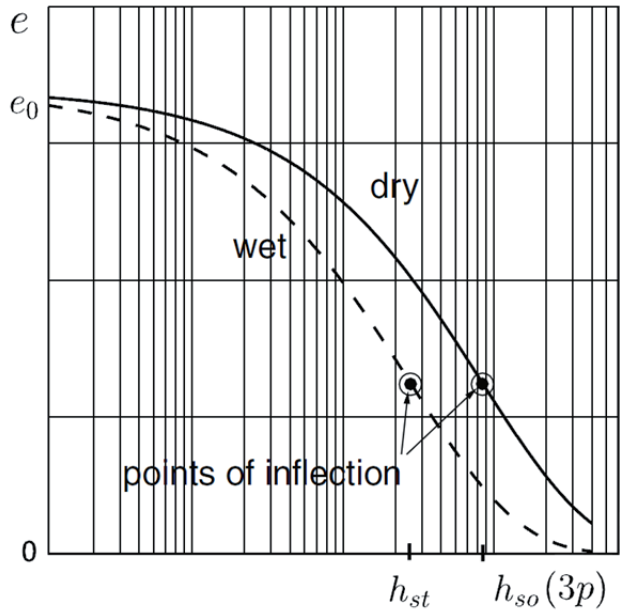

Figure 2-16- Influence of the reduction of the solid hardness on the compression behavior

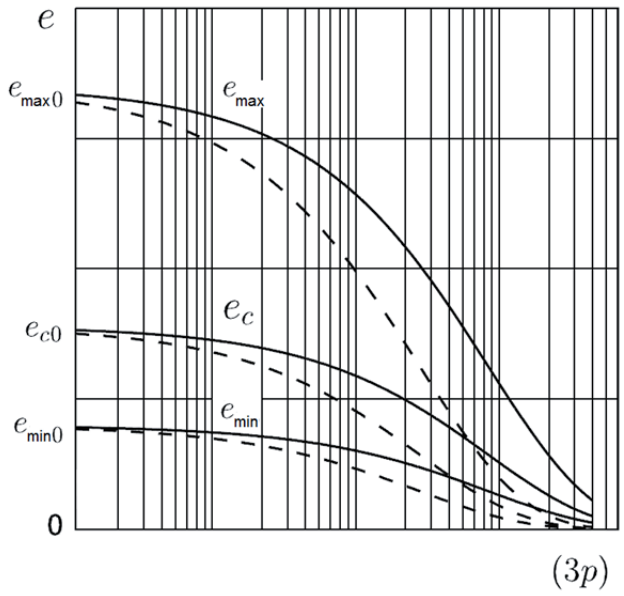

Figure 2-17- Influence of the reduction of the solid hardness on the limit void ratios.

	nonlinearity	stress-dependency	plastic deformation and unloading	dilative behavior	collapse due to wetting	creep deformations	Calibration of parameters	Application in dam engineering
linear elastic	No	No	No	No	Yes	to some extent	very easy	Extensively used in the past but not lately.
Non-linear elastic	Yes	Yes	to some extent	No	Yes	to some extent	easy	Several applications
Anisotropic elastic	Yes	Yes	No	Yes	No	No	not easy	Not applied
perfectly plastic	No	No	to some extent	to some extent	to some extent	No	easy	Considering an initial linear elastic behavior
Double hardening	Yes	Yes	Yes	Yes	to some extent	No	difficult	Some applications in Imperial College
Barcelona	Yes	to some extent	Yes	to some extent	Yes	to some extent	difficult	Few applications
Hypoplastic	Yes	Yes	Yes	Yes	Yes	Yes	difficult	Not applied

Table 2-1 – Application of different constitutive laws in modeling rockfill dams

3 Modeling the behavior of a compacted assemblage of rock particles during monotonic triaxial compression tests

3.1 Introduction

Testing and numerical modeling of the behavior of rockfill materials based on soil mechanics concepts have been a challenge for both engineers and scientists. The difficulty arises from the comparatively unique nature and extremely wide-ranging variations of the material. Many researchers have tried to make determination of the properties of rockfill conform to usual procedures and concepts of geotechnical engineering (Barton and Kjarnesli, 1981; Jansen, 1988; Leps, 1970; Marachi et al., 1972). In addition, different constitutive equations based on elasticity and/or plasticity theories have been proposed to predict the behavior of coarse grained non-cohesive soils (Chu et al., 2010; Duncan and Chang, 1970; Fu and Bauer, 2009; Oldecop and Alonso, 2001). Some of these equations have been used worldwide to predict the behavior of rockfill masses. The data needed to calibrate the parameters of these models are often obtained from performed laboratory tests.

In order to have satisfactory predictions of rockfill behavior, the parameters of the model such as elastic modulus, bulk modulus, plasticity parameters, etc. need to be determined as precisely as possible using typical geotechnical testing procedures. However, due to the problems which exist in testing a rockfill sample with irregular boulders up to 2 m in size, there is the inevitable need for simplifying procedures (e.g. using parallel grain-size distribution with smaller maximum particle size (Lowe, 1964) which would lead to the introducing the grain size factor). This brings up the idea to keep the constitutive equations less complex, considering only the important characteristics of the particular problem involved. Hence, the parameters of the model could be more confidently determined with less testing required.

With the ultimate goal of modeling rockfill in dams, the traditional hyperbolic model have shown to be stable and to capture the behavior relatively well (Massiéra et al., 1989; Mellah et al., 2000; Saboya and Byrne, 1993). The main advantage of this model is its simplicity while being capable of representing the nonlinearity and stress dependency of the material. However as mentioned by Duncan et al. (1980a) there are two shortages of this model which could mistakenly affect the results of the modeling of a rockfill dam: (i) due to its elastic formulations the behavior at and after failure cannot be modeled correctly; and (ii) the relationships do not include shear dilatancy.

It has thus been decided to introduce a failure envelope in the formulation of the constitutive model to predict the behavior of the material at failure in order to apply this model confidently in the simulations. Moreover, by introducing the plastic formulation with a non-associated flow rule, both of the above mentioned problems can be overcome. This is especially important when the dam contains different zones. The interface regions could undergo high shear stresses and could reach the failure envelope and possibly have a dilative behavior. Houlsby (1991) summarized different classical methods for representing the dilatancy of granular soils in the context of plasticity. He showed that all the equations express the concept that dilation rate is primarily controlled by density, but also reduces with increasing stress level. This kind of behavior has to be considered in the definition of the flow rule in the current study.

In this paper the nonlinear elastic relationships proposed by Duncan et al. (1980a) are modified and coupled with the Mohr-Coulomb failure criteria and a non-associated flow rule to consider shear dilatancy based on the theory presented by Rowe (1962). These constitutive equations are implemented into the commercially code, FLAC, to reproduce the observed behavior of an assemblage of rock particles in drained monotonic compression triaxial tests conducted in strain controlled conditions. Finally, by comparing results of the modeling and data from the laboratory, limitations and effectiveness of the implemented model are discussed.

3.2 Constitutive equations

The constitutive relations implemented in this paper are the elastic hyperbolic model coupled with the Mohr Coulomb failure criteria. Both of these models deal with the minimum and maximum principal stresses which make the coupling very effective. The schematic is shown in Figure 3-2: A model which is capable of capturing the nonlinear behavior prior to failure as well as the plastic deformations on the yield surface. It sould be noticed that the initial hyperbolic shape does not predict the plastic deformations which occur from the onset of shearing. The empirical unloading-reloading modulus which had been introduced by Duncan et al. (1980a) for this purpose is omitted as there is no need for such criterion in a monotonic test setup. Moreover, the stress criterion in the definition of this modulus is not reliable to capture the unloading and reloading in complex stress paths

and could have led to unrealistic energy production during the simulation. Neglecting this empirical coefficient could often increase the stability of the numerical model. The more reliable way of predicting the plastic deformations is the introduction of the failure envelope as established in the classical theory of elasto-plasticity.

Mohr-Coulomb model which is the simplest realistic model for geomaterials has been well established in geotechnical engineering practice. Geomaterials are modeled as elastic below and plastic on the failure envelope. When the stress state reaches the Mohr-Coulomb failure envelope, the plastic deformations can be properly determined using elasto-plasticity formulations. Both shear and volumetric plastic strain increments can be related using a non-associated flow rule and a dilation angle. In the original Mohr-Coulomb model, elastic and plastic parameters remain constant throughout the analysis which is a simplification of the real behavior. However, in this research, hyperbolic equations are used to update the parameters during the simulation and before the failure envelope is reached. The calculation of the dilation parameters are also considered as follows.

Dilative behavior in compacted packages of grains should be generally considered in terms of energy and related to the secant friction angle as demonstrated by Rowe (1962). Using this concept, Bolton (1986) has shown that the friction angle, in any given confining stress, could be calculated as:

$$\varphi' = \varphi'_c + \psi \qquad \textit{[Eq. 3-1]}$$

Where φ' is the secant friction angle; φ'_c is the constant volume friction angle at large strains (or the steady state friction angle as referred in this paper); ψ is the dilation angle. In the above equation, the shear strength is related to the rate of dilation. In reality, the rate of dilation is changing during the shearing of a compacted soil, and as a result, a peak is normally observed in the stress-strain curve. This is obvious in the typical results of triaxial tests performed on compacted sand samples as shown by Habib and Luong (1978) in Figure 1-1. there are three important states in this figure: characteristic state, peak friction angle and critical state. The dilative behavior starts at characteristic state and the rate of dilation increases until it reaches its maximum value corresponding to the pick friction angle. The dilation reduces afterwards and finally reaches the zero volumetric change at

critical state. However due the fact that large rock particles break under high stresses near failure envelope before they override, this peak is normally not observed in the results of triaxial tests on rockfill samples. In other words, due to the particle breakage the dilative behavior of compacted assemblages of rock particles are not accompanied with a large pick in stress-strain curve. In the implemented model, it is assumed that the rate of dilation is constant under any given confining stress (i.e. Perfect plasticity formulation is utilized with no strain hardening involved) and the secant friction angle is not changing and no peak is considered. This is an approximation and should be understood when using this model in simulations. Monitoring the plastic strains and limiting the rate of dilation of the elements is also essential in this approach. That is why dotted line was shown in Figure 3-2.

3.2.1 Elastic formulation

Hyperbolic formulations, like those introduced by Konder and Zelasko (1963) and Duncan and Chang (1970) have been adopted for plain strain condition and based on the generalized Hooke's law of elastic deformations in the following form :

$$\begin{Bmatrix} \Delta\sigma_x \\ \Delta\sigma_y \\ \Delta\tau_{xy} \end{Bmatrix} = \frac{3B}{9B-E} \begin{bmatrix} (3B+E) & (3B-E) & 0 \\ (3B-E) & (3B+E) & 0 \\ 0 & 0 & E \end{bmatrix} \begin{Bmatrix} \Delta\varepsilon_x \\ \Delta\varepsilon_y \\ \Delta\gamma_{xy} \end{Bmatrix} \qquad \textit{[Eq. 3-2]}$$

Where $\Delta\sigma_x$, $\Delta\sigma_y$ are normal stress increments; $\Delta\tau_{xy}$ is shear stress increment; $\Delta\varepsilon_x$, $\Delta\varepsilon_y$ are normal strain increments; $\Delta\gamma_{xy}$ is shear strain increment; E is Young's modulus; B is bulk modulus. By linking the elastic parameters to the stress state, it is possible to model the soil behavior and the important characteristics of it, which are, nonlinearity and stress-dependency. In each increment of the analysis the elastic parameters are updated as follows:

$$B = K_B \left(\frac{\sigma_c}{P_a}\right)^m \qquad \textit{[Eq. 3-3]}$$

$$E = K_E \left(\frac{\sigma_c}{P_a}\right)^n \qquad \textit{[Eq. 3-4]}$$

Where K_E and K_B are modulus numbers; n and m are modulus exponents; P_a is the reference pressure (atmospheric pressure); σ_c is the confining stress. These equations imply higher modulus with increasing confinement. The rate of this increase is defined by the modulus exponents m and n.

The nonlinear stress-strain curve can be represented by the equation of the following form:

$$(\sigma_1 - \sigma_3) = \frac{\varepsilon}{\frac{1}{E} + \frac{\varepsilon}{(\sigma_1 - \sigma_3)_{ult}}} \qquad \textit{[Eq. 3-5]}$$

$(\sigma_1 - \sigma_3)_{ult}$ is related to the compressive strength at failure by:

$$(\sigma_1 - \sigma_3)_{ult} = \frac{(\sigma_1 - \sigma_3)_f}{R_f} \qquad \textit{[Eq. 3-6]}$$

R_f is an empirical coefficient used to adjust the stress-strain curve. A database of 20 different rockfill samples from published dam sites worldwide is shown in Table 3-2. $R_f = 0.7$ is often a suitable default setting. $(\sigma_1 - \sigma_3)_f$ can be derived from Mohr-Coulomb failure criterion and expressed as:

$$(\sigma_1 - \sigma_3)_f = \frac{2\sigma_c sin\varphi}{1 - sin\varphi} \qquad \textit{[Eq. 3-7]}$$

This formulation implies decreasing of the tangent elastic modulus with increasing shear stress while the bulk modulus is independent of the percentage of the strength mobilized (Duncan et al., 1980a).

3.2.2 Plastic formulation

The Mohr-Coulomb failure criterion was considered for the material. Because there is no cohesion in rockfill, the failure envelope involves only the friction angle (φ). Despite this simple choice of soil behavior, it will be illustrated that the model is capable of capturing the rockfill behavior. Yield and potential functions have similar forms but with different parameters. The yield function is defined by:

$$f^s = \sigma_1 - \sigma_3 N_\varphi \qquad \textit{[Eq. 3-8]}$$

Where:

$$N_\varphi = \frac{1 + sin\varphi}{1 - sin\varphi} \qquad \textit{[Eq. 3-9]}$$

The potential function has the following form:

$$g^s = \sigma_1 - \sigma_3 N_\psi \qquad \textit{[Eq. 3-10]}$$

Where:

$$N_\psi = \frac{1 + sin\psi}{1 - sin\psi} \qquad \textit{[Eq. 3-11]}$$

Four parameters reflecting the plastic behavior are required in order to determine the friction and dilation angles corresponding to the yield and potential functions described above. These can be written as:

$$\varphi = \varphi_0 - \Delta\varphi log\left(\frac{\sigma_3}{P_a}\right) \qquad \textit{[Eq. 3-12]}$$

$$\psi = \psi_0 - \Delta\psi log\left(\frac{\sigma_3}{P_a}\right) \qquad \textit{[Eq. 3-13]}$$

Where φ_0 is the fiction angle at reference pressure P_a; $\Delta\varphi$ is the change of friction angle with confining stress; $\psi_0$is the dilation angle at reference pressure P_a; $\Delta\psi$ is the change of friction angle with confining stress; The reference friction angle (φ_0) is the steady state friction angle (also known as constant volume friction angle, φ_c) at the reference pressure (P_a). It is dependent on the mineralogy, particle shape, and grain size distribution of the material, but not on the density or degree of saturation. However, there is much influence of all these physical properties on the reference dilation angle (ψ_0).

Bolton (1986) assumes a unique steady state angle based on a large database of tests on granular materials which leads to the correlation for triaxial strain as:

$$\varphi_p^{tr} - \varphi_c^{tr} \cong 3I_R \qquad \textit{[Eq. 3-14]}$$

This is a modified version of [Eq.3-1] for triaxial formulation, where φ_p^{tr} is the peak friction angle in triaxial strain condition; φ_c^{tr} is the constant volume friction angle (i.e. steady state friction angle) in triaxial strain condition; I_R is a relative dilatancy index which relates the relative density (I_D) and applied confining stress level (σ_c) as:

$$I_R = I_D(10 - ln\sigma_c) - 1 \qquad \textit{[Eq. 3-15]}$$

Bolton (1986) also found that the rate of dilation was independent of the strain and could be defined as:

$$-\dot{\varepsilon}_v/\dot{\varepsilon}_1 = 0.3\, I_R \qquad \textit{[Eq. 3-16]}$$

This supports the idea of a unique angle of dilatancy as this angle is related to the ratio of volumetric strain to axial strain as shown by Schanz and Vermeer (1996). Moreover, [Eq. 3-15] and [Eq. 3-16] suggest that the rate of dilation increases linearly with density and decreases linearly with logarithm of applied stress. This kind of behavior was implemented in the constitutive equations as shown in [Eq. 3-13].

3.3 Laboratory testing

A laboratory testing program was undertaken to evaluate the behavior of the compacted assemblages of rock particles under monotonic loading. This program was also designed to study the effects of saturation, confining stress, and density on the stress-strain-volumetric characteristics of theses specimens. The data from these tests is used to calibrate the parameters of the implemented model. Five sets of angular granite grains with different uniform particle sizes were used to prepare the specimens to be tested (Figure 3-3). These sets were obtained from crushing and sieving the granite boulders from the shell zone of the Romaine2 dam, which was under construction in Quebec, at the time of the experimental

program. For each specimen being tested, the appropriate quantities of oven-dried grains were mixed according to the parallel gradation curve to the prototype rockfill as shown in Figure 3-4. It should be noted that the maximum particle size of the specimens was 25 mm which is a rather a gravel sample.

3.3.1 Triaxial setup

Polished stainless steel end platens were used in all tests. The platens had several holes to provide drainage of water during the saturated tests. Fine wire meshes wrapped in paper filters were used on both platens to prevent the fine soil particles to block these drainage holes. Nominal sample dimensions were a height of 300 mm and a diameter of 150 mm. The samples were initially subjected to the desired confining pressure (i.e. 100, 300, or 600 kPa) and then axially strained at 5% per hour for dry tests; and 1% per hour in drained condition for saturated tests. The samples were saturated by allowing water to pass through the base of the triaxial cell and using the top drainage system for removing air voids. This allows reaching saturation degrees up to a maximum of 92%. In order to reach higher degrees of saturation some additional techniques are required which was not considered in the current study. The data were collected every 30 seconds by an acquisition system and recorded using a dedicated personal computer. The test conditions are summarized in Table 3-1.

3.3.2 Specimen preparation

The samples were prepared in a split mold attached to the base pedestal of the triaxial test equipment. In order to minimize density variation within a specimen, five equal pre-weighted and oven-dried portions of the granite rock particles were mixed and compacted to a predetermined height. Initial dry densities of 1800 and 1900 kg/m^3 were targeted using the vibratory compaction. The application of the confining stress to the specimen resulted in an uncontrolled increase of the initial density obtained in the mold, which was more evident in the saturated samples (Table 3-1). The increased density was considered in the analysis and calculated by measuring the volumetric changes of the specimen during the consolidation stage.

3.3.3 Membrane penetration

There is a phenomenon referred to membrane penetration in any triaxial test of grainy materials (Kiekbusch and Schuppener, 1977; Lade and Hernandez, 1977; Molenkamp and Luger, 1981). This is due to the fact that the sample is subjected to a confining stress, and could be problematic in measurements of volumetric change when CIU testing is conducted and pore pressure builds up. However, the difficulty in the conducted CID tests with specimens containing angular grains up to 20 mm in size was the rupture of the rubber membrane during the axial straining of the samples. This was especially important for the dry samples. Even a tiny hole in the membrane would have introduced the water to the samples and distorted the desired test conditions as well as volumetric measurements. Thin plastic sheets were loosely attached around the rubber membrane to form a stiff cylindrical support against the penetration of the angular rock particles. A second rubber membrane was installed over the plastic sheets to seal the whole specimen during the triaxial testing. Figure 3-5 shows the specimen after the experiment. The colored plastic sheets are visible underneath the translucent membrane. The grains have slightly deformed the plastic sheets and the rubber membranes. However, the sealing membranes were not damaged and functioned very well during the tests.

3.3.4 Strain rate

The effects of rate of straining on the stress-strain behavior of the specimens in triaxial tests have been firstly reported by Whitman (1957b). In a strain-controlled test, if the rate of straining is smaller, the more time is allowed for the sample to relax. Consequently, smaller shear stresses are calculated at a given deformation increment. The final result is a stress-strain curve which plots lower. Matesic and Vucetic (2003) have reviewed the previous experimental studies and confirmed that axial strength, and secant modulus increase approximately linearly with the logarithm of the strain rate. The rates included in their research ranged between 0.00003 and 3000 %/s.

The appropriate choice of the rate of straining depends on the characteristics of the material being tested as well as the geotechnical problem involved. While the common strain rate chosen for monotonic testing of sands is about 1 %/min (approximately 0.01 %/s), larger rates are useful in studying the cyclic behavior. Whitman (1957a) and Mitchell (1976)

reported that clays are much more susceptible to this rate effect. In this research, the large scale tests were performed with the ultimate goal of modeling the behavior of rock particles in a rockfill dam. The strain rates chosen for the assemblages of relatively large rock particles were 5 and 1 %/hour (approximately 0.001 and 0.0003 %/s) for dry and saturated tests, respectively. The strain rates were reduced for the saturated samples in order to provide the full drainage condition during the experiments.

3.4 Test results

The stress-strain curves and the volumetric changes during the axial straining of the dry samples at various densities, and confining stresses are shown in Figure 3-6. All of the six tests in these figures display the same general trends: nonlinear behavior at the beginning of the tests followed by a constant strength at higher strains; the samples tested did not display much strain-softening characteristics. The following behaviors were also observed:

1. The rigidity of the specimens increased with both confining stress and density.

2. The steady state strength of the specimen was increased with confining stress; there was not much influence of density or degree of saturation observed in this final strength.

3. There was not much dilation observed for the specimens with densities of 1900 kg/m^3. However, as the densities were increased to 2000 kg/m^3, the dilative behavior was recorded.

4. The rate of dilation decreased with confining stress. At confining stress of 300 kPa and above, no dilation were observed for the specimens with the density of 1900 kg/m3. The stress threshold for dilative behavior was more than 600 kPa when the density rose to 2000 kg/m^3.

Six saturated samples were axially strained in drained condition in order to study the effects of water. The stress-strain-volumetric curves are shown in Figure 3-7. The same general behaviors mentioned above were also observed in these figures. However, the saturation decreased the rigidity and the rate of dilation; steady state strength at confining pressures of 100, 300 and 600 kPa are 400, 950, 1450 kPa for both dry and saturated specimens.

3.5 Calibration of the implemented model

The previously described constitutive equations were implemented into the commercial software FLAC 6.0 (ITASCA Consulting Group, 2008). Single-element tests were done with FLAC, exercising the implemented model over stress paths similar to those of the physical tests, and plotting the similar graphs to compare the results and calibrate the parameters of the model. The initial parameters chosen for the model were selected from published laboratory test data on rockfill as shown in Table 3-2 (Adikari and Parkins, 1982; Broughton, 1970; Casagrande, 1965; Duncan et al., 1980a; Feizi-Khankandi et al., 2008; Hall and Gordon, 1963; Marachi et al., 1969; NGI, 1987; Saboya and Byrne, 1993). The data in this table were used to plot the variations of the six hyperbolic parameters respectively in Figure 3-8.

The relatively rounded shapes of the graphs for R_f and φ show the less variability of these two parameters in different rockfill samples. The hyperbolic fitting parameter R_f changes from a minimum of 0.51 for a sub-rounded quartzite with D_{60}=10 mm used in the transition zone of Furnas dam to a maximum of 0.80 for a massive basalt with maximum particle size of 500 mm and C_u=14 used in the shell of Foz do Areia dam. A value of $R_f = 0.70$ would be a good initial guess for most rockfill material. This value could slightly increase with angularity and maximum size of the particles. The friction angle φ varies from a maximum of 58 degree for a rounded sandy gravel with D_{60}=10 mm and C_u=17 used in Rowallan dam to a minimum of 38 degree for a mixture of massive basalt and fault breccia used inside the body of Foz do Areia dam.

The two modulus numbers K_E, and K_B which represent the shear and volumetric rigidity of the material vary significantly in different rockfill samples as reported in the literature. This is also obvious from the irregular shape of the graphs for these two parameters in Figure 3-8. The elastic modulus number K_E changes from a minimum of 210 for a sub-angular granite gneiss with D_{60}=79 mm, C_u=20, and unit weight of 1980 kg/m^3 used in the shell of Mica dam to a maximum of 3000 for a well compacted crushed rock with maximum particle size of 40 mm, and unit weight of 2150 kg/m^3 used in the transition zone of Storvatn dam. The volumetric modulus number K_B changes from a minimum of 52 for a badly compacted angular diorite with D_{60}=93 mm, C_u=5 , and unit weight of 1700 kg/m^3

used in the shell of Infiernillo dam to a maximum of 1650 for the well compacted crushed rock used in the transition zone of Storvatn dam mentioned above. Both of these coefficients increase with density and uniformity coefficient, and decrease with angularity and maximum size of the particles.

The two modulus exponents n, and m which represent the dependency of the shear and volumetric modulus to the changing of the confining stress as stated in [Eq. 3-3] and [Eq. 3-4] vary in different rockfill samples as shown in Figure 3-8. The higher exponents mean more dependency of the rigidities to the changing confining stress. The shear modulus exponent n varies from a minimum of 0.1 in Foz do Areia dam to a maximum of 0.65 in Garmrood dam. The volumetric modulus exponent m changes from a minimum of 0.0 in Round Butte dam to a maximum of 0.57 in Furnas dam. Both of these exponents increase with angularity and maximum size of the particles.

It should be noted that the hyperbolic parameters are not fundamental soil properties, but only values of empirical coefficients which represent the behavior of the material under certain conditions. Therefore they are not unique and different sets of parameters could represent a single material. Considering the physical properties of the specimens being tested which are D_{max}=20 mm, D_{60}=9 mm, C_u=11, and angular rock particles with dry densities between 1900 and 2000 kg/m^3, the hyperbolic parameters were initially selected as shown in Table 3-3. These parameters were subsequently modified to best fit the observed behavior at the reference confining pressure (i.e. 100 kPa) for both dry and saturated specimens with different densities, as shown in Table 3-3. The order in which the parameters were modified was:

1. Friction angle φ_0 using the final strength of the material as stated in [Eq. 3-7]

$$(\sigma_1 - \sigma_3)_f = \frac{2\sigma_c sin\varphi}{1 - sin\varphi} \qquad \textit{[Eq. 3-7]}$$

2. Shear modulus number K_E and the fitting parameter R_f to best fit the initial nonlinear stress-strain behavior

3. Bulk modulus number K_B and dilation angle ψ_0 to best fit the volumetric behavior.

4. The test results in a different confining stress (i.e. 300 kPa) were required to calibrate modulus exponents n, and m as well as two other plastic parameters $\Delta\varphi$, and $\Delta\psi$. As these four parameters represent the change of the behavior with confining stress.

The above procedure is shown in Figure 3-9 for dry specimens with density of 2000 kg/m^3. The versatility of the model was tested using the same set of fitted parameters to predict material responses under a different stress path (i.e. confining pressure of 600 kPa). The calculated stress-strain-volumetric behaviors are shown in Figure 3-10 to

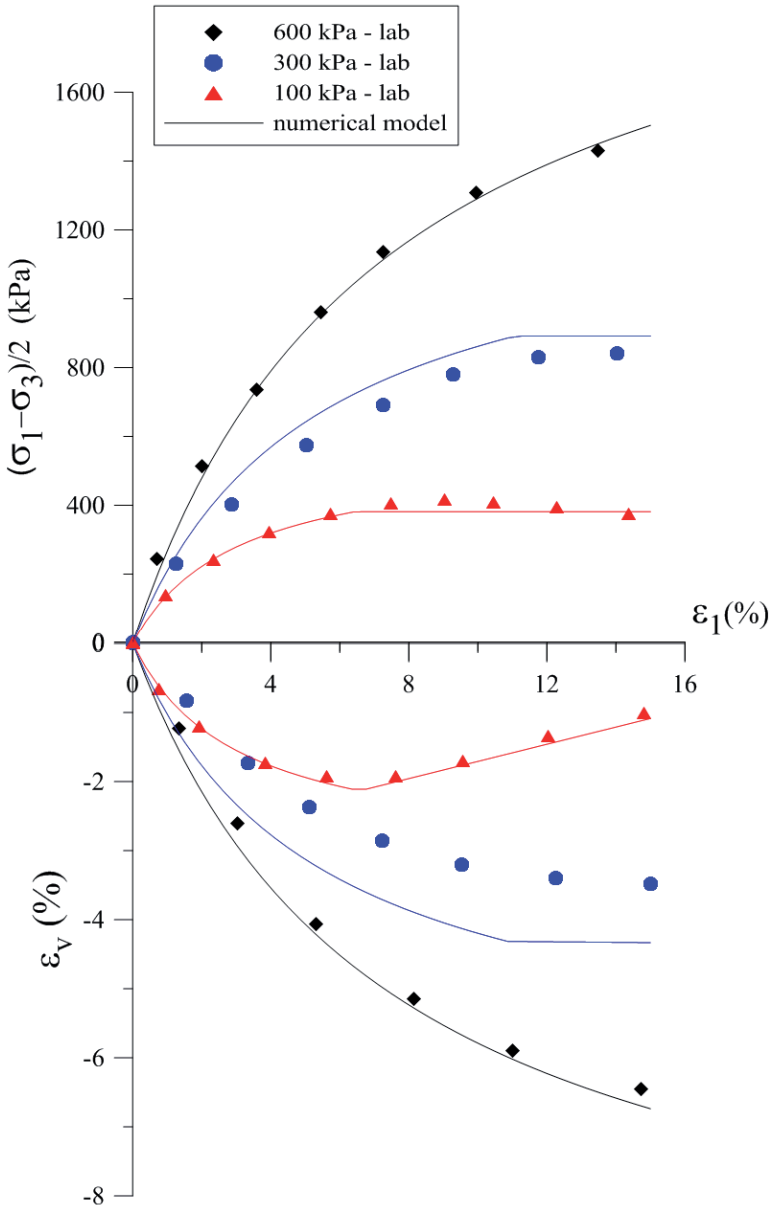

Figure 3-12 for other tests along with the experimental data. In each figure, the performance of the implemented model is demonstrated by comparing laboratory results with model simulation results.

3.6 Discussion of the test results

Except for the slight strain-hardening characteristics of the samples with density of 2000 kg/m^3, the model was able to capture the behaviors of the tested material with a good precision. Model parameters used in reproduction of the tests are given in Table 3-3.

Comparing the calibrated parameters of the model in different tests resulted in the following conclusions which conform to the previously discussed behaviors of the specimens in the tests:

1. Variations of steady state friction angle in different tests can be observed in Figure 3-13. The intersection of the curves with the vertical axis represents the reference friction angle (φ_0). The slope of the curves represents the change of friction angle with logarithm of the confining stress ($\Delta\varphi$). Neither changing the density, nor saturation of the specimen had much influence on the friction angle (φ_0 and $\Delta\varphi$) and the steady strength of the material. As expected, these two parameters were related to the intrinsic properties of the material being tested such as mineralogy, particle shape and the size of the grains.

2. All other plastic and elastic parameters reduced after saturation. However, the major changes were observed in the modulus numbers (K_E and K_B) which indicated a softer response of the saturated samples to the shearing stress. The decrease of the dilation angle with saturation (ψ_0) also means less dilative behavior of the wetted samples.

3. The modulus numbers (K_E and K_B) and the reference dilation angle (ψ_0) increased with density.

4. Modulus exponents (n and m) decreased with density, which means as the specimens become denser the behavior would be less dependent to changes of confining stress.

3.6.1 Dilative behavior

Figure 3-14 presents the linear relation between the calculated dilation angles and logarithm of confining stress in the tests which demonstrated dilative behavior. The intersection of the curves with the vertical axe represents the reference dilation angle ψ_0. The slope of the curve represents the change of friction angle with logarithm of the confining stress $\Delta\psi$. The parallel curves of denser samples (dry density of 2000 kg/m3) suggest the independence of $\Delta\psi$ to the density and the degree of saturation. A value of $\Delta\psi$=10.8 was calculated for these

specimens. The same slope was assumed for the less compacted material as shown by dotted lines in Figure 3-14 which could be related to the unchanging mineralogy, shape and size of the grains. Also, the intersection of the curves with the horizontal axe in this figure indicates the minimum confining pressure at which the dilation of a specimen with a given density would be suppressed.

Figure 3-15 indicates the linear increase of the reference dilation angle ψ_0 with density for both dry and wet specimens. The calculated values of this parameter suggest a decrease of 1.5 degrees as a result of wetting of the tested material. The linear relation in this figure corresponds to the assemblage of particles in the current study and may not be used directly to estimate the reference dilation angle of other samples of rockfill. This linear relation is however similar to the [Eq. 3-15] presented by Bolton (1986), and suggests that no dilation would be expected for dry densities less than 1880 kg/m^3 and 1910 kg/m^3 for dry and saturated specimens, respectively. Also, the intersection of the curves with the horizontal axe in Figure 3-14 indicates the minimum confining pressure in which the dilation would be suppressed in any given density.

3.7 Conclusion

The chapter described a relatively simple constitutive model and examined its performance by comparing it to the results of the conducted triaxial tests on assemblages of granite rock particles from a dam site in Quebec, Canada. Drained monotonic compression tests were conducted in strain controlled condition on both dry and saturated specimens with different densities and confining pressures. The data from these tests were used to calibrate the parameters of the presented model. The constitutive model was the nonlinear hyperbolic model coupled with mohr-coloumb failure criteria. This model was capable of capturing the following characteristics observed in the labratory: (1) modulus stiffening due to increasing confinment and modulus degradation due to increasing shear stress (2) steady state strength and plastic deformations on the failure envolope (3) shear induced volumetric changes or dilative behavior of dense samples.

The main shortcoming of the model was that it could not capture the plastic deformations occuring from the very beginning of the shear loading of rockfill material; indicating that

the model is not appropriate in problems involving unloading-reloading loops and hysteresis behavior. Also, it could not capture the strain hardening behavior and the peak friction angle in very dense samples. However, with the use of nine parameters, the model was shown to provide satisfactory predictions of the observed behavior during monotonic compresion triaxial tests on samples with dry densities of 1900 to 2000 kg/m^3, respectively. The parameters of the model are relalated to the physical properties of the assemblages of rock particles such as density, shape and size of the grains, and degree of saturation. They can be determined from the results of triaxial tests or existing database in the literature for both hyperbolic and Mohr-Coulomb models which makes it an efficient constitutive model to be used in engineering practice.

The ultimate goal of this research was to predict the behavior of the rockfill material of Romaine2 dam with the use of the simplest constitutive equations while keeping only the most important aspects of the problem. Nobari and Duncan (1972) and Escuder et al. (2005) have introduced procedures to reproduce the plastic deformations caused by wetting using the hyperbolic model. This opens new possibilities for future research which could be the implementation of these procedures into the current model in order to simulate the behavior of the rockfill during construction and first impoundment of the dam.

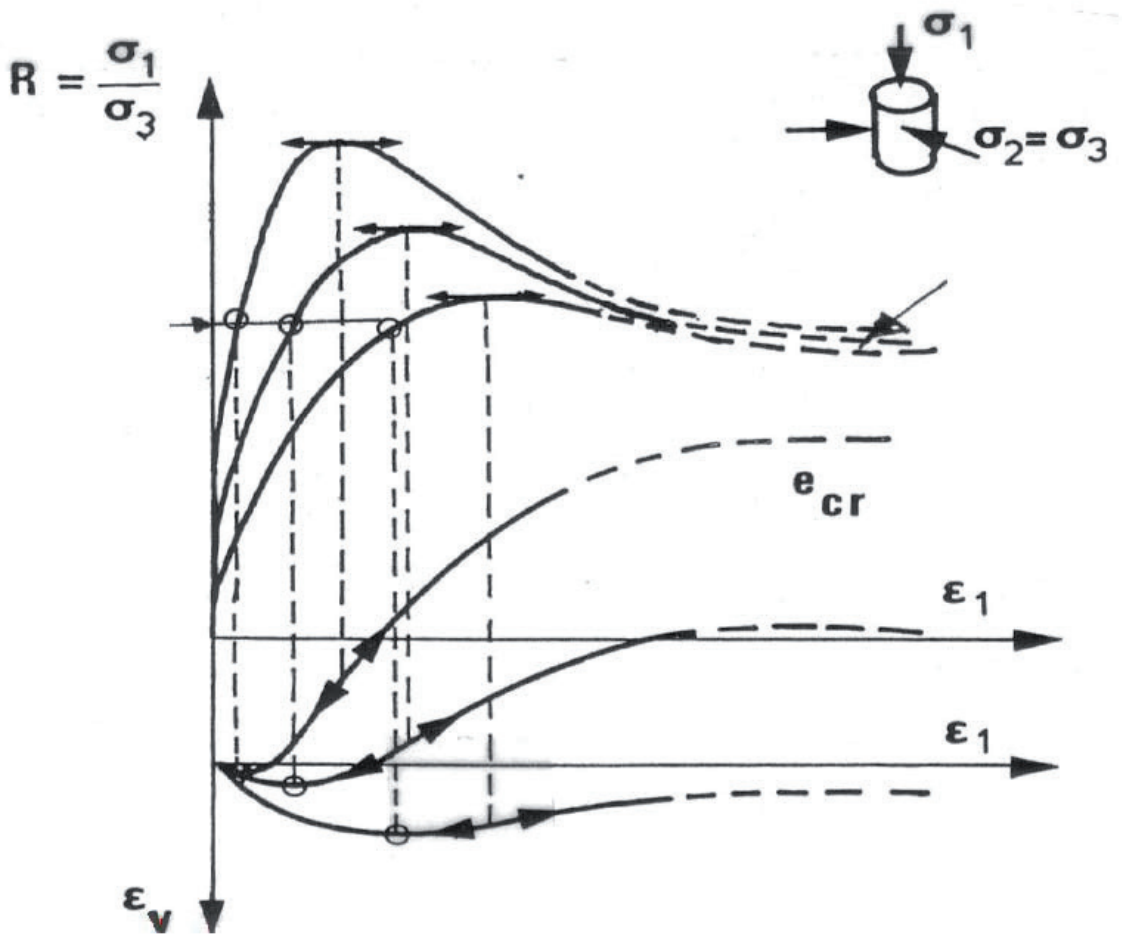

Figure 3-1 typical stress-strain-volume change behavior of sand samples in triaxial tests; after Habib and Luong (1978)

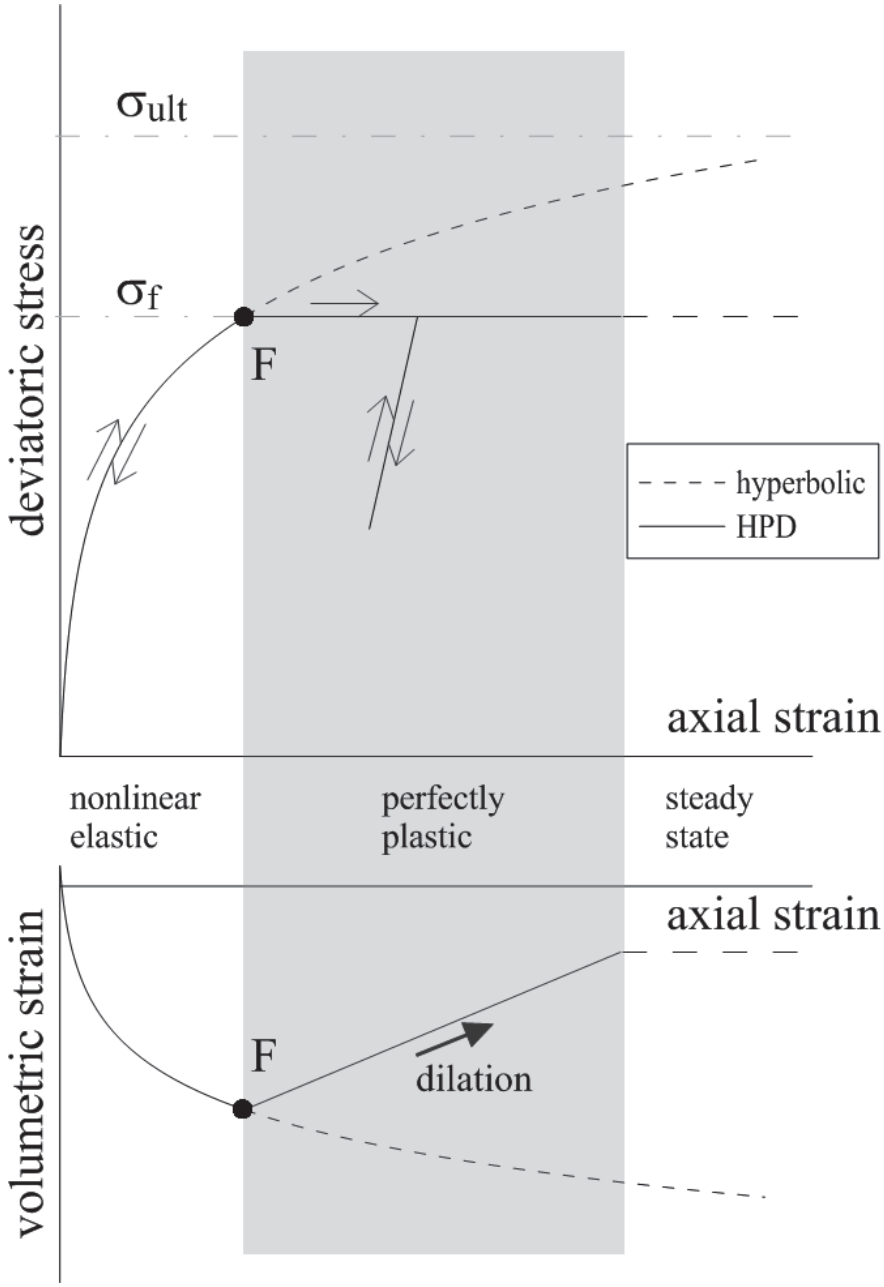

Figure 3-2 Schematic of the implemented model

Figure 3-3 Granite rockfill particles

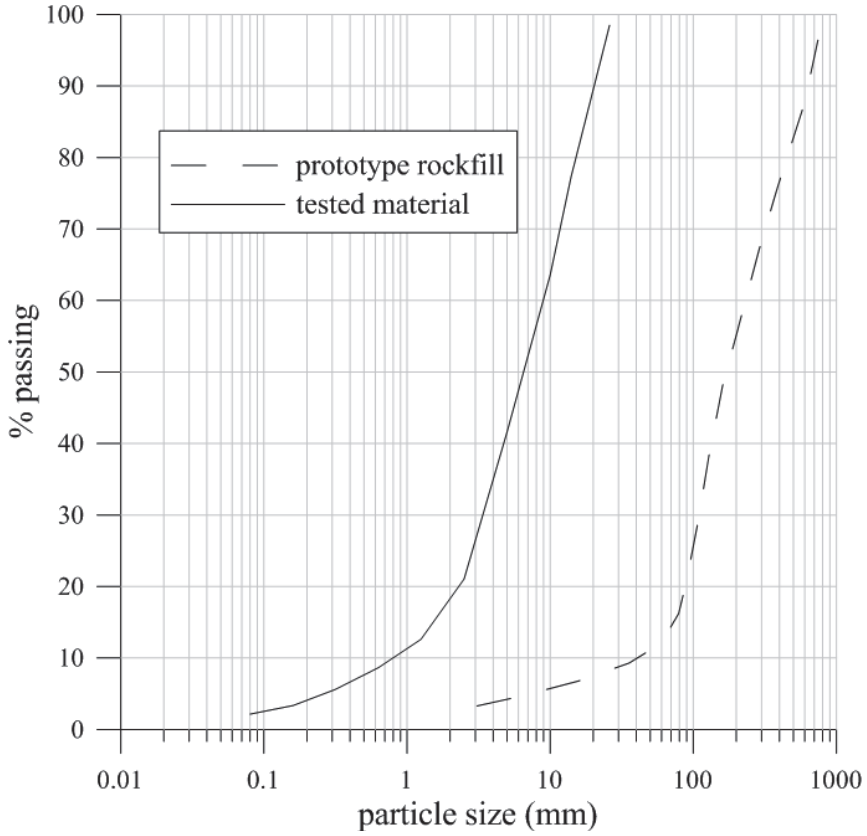

Figure 3-4- Gradation curve of the tested material

Figure 3-5 Triaxial specimen after the test

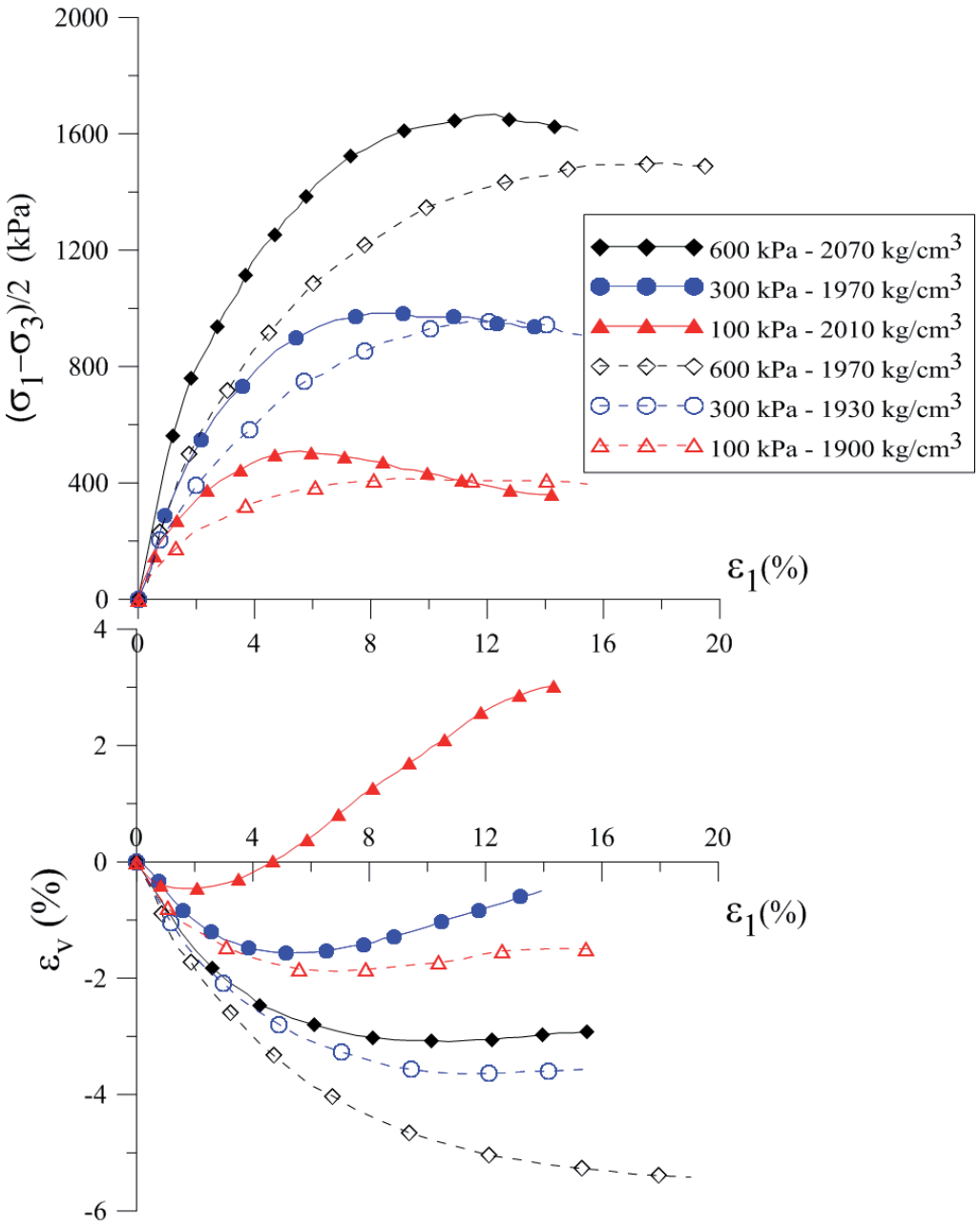

Figure 3-6 Observed stress-strain-volumetric behavior of the dry specimens in the monotonic triaxial tests

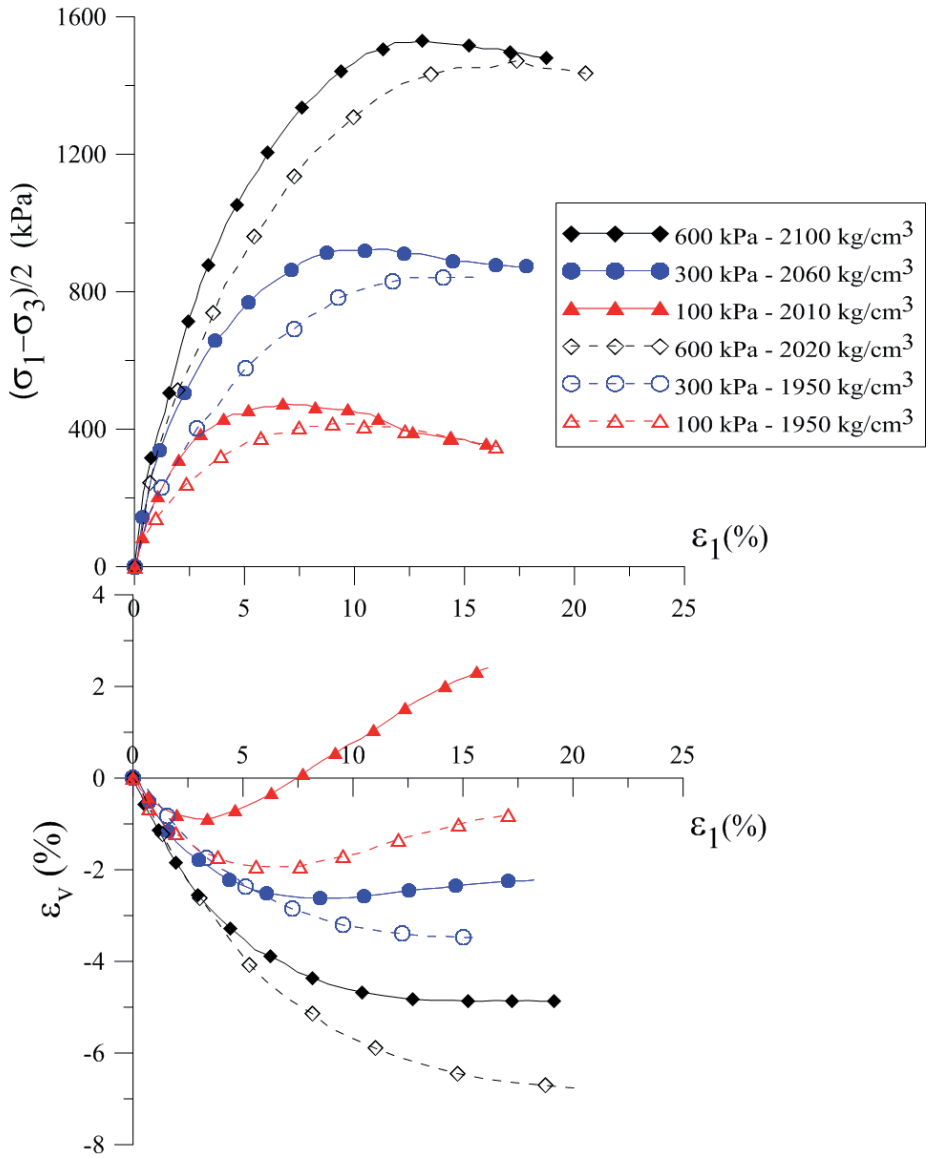

Figure 3-7 Observed stress-strain-volumetric behavior of the saturated specimens in the monotonic triaxial tests

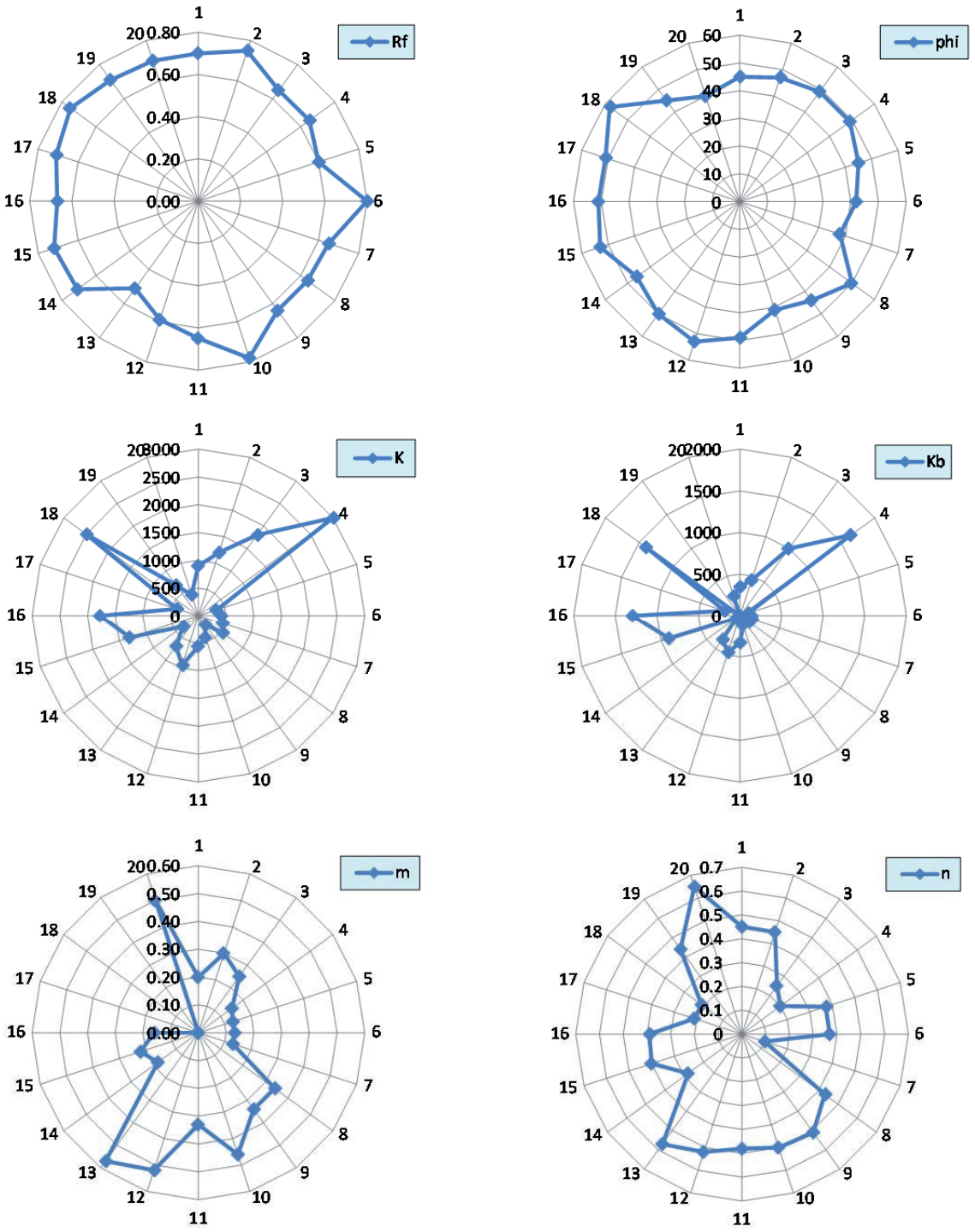

Figure 3-8 Variations of hyperbolic parameters in published laboratory test data on rockfill

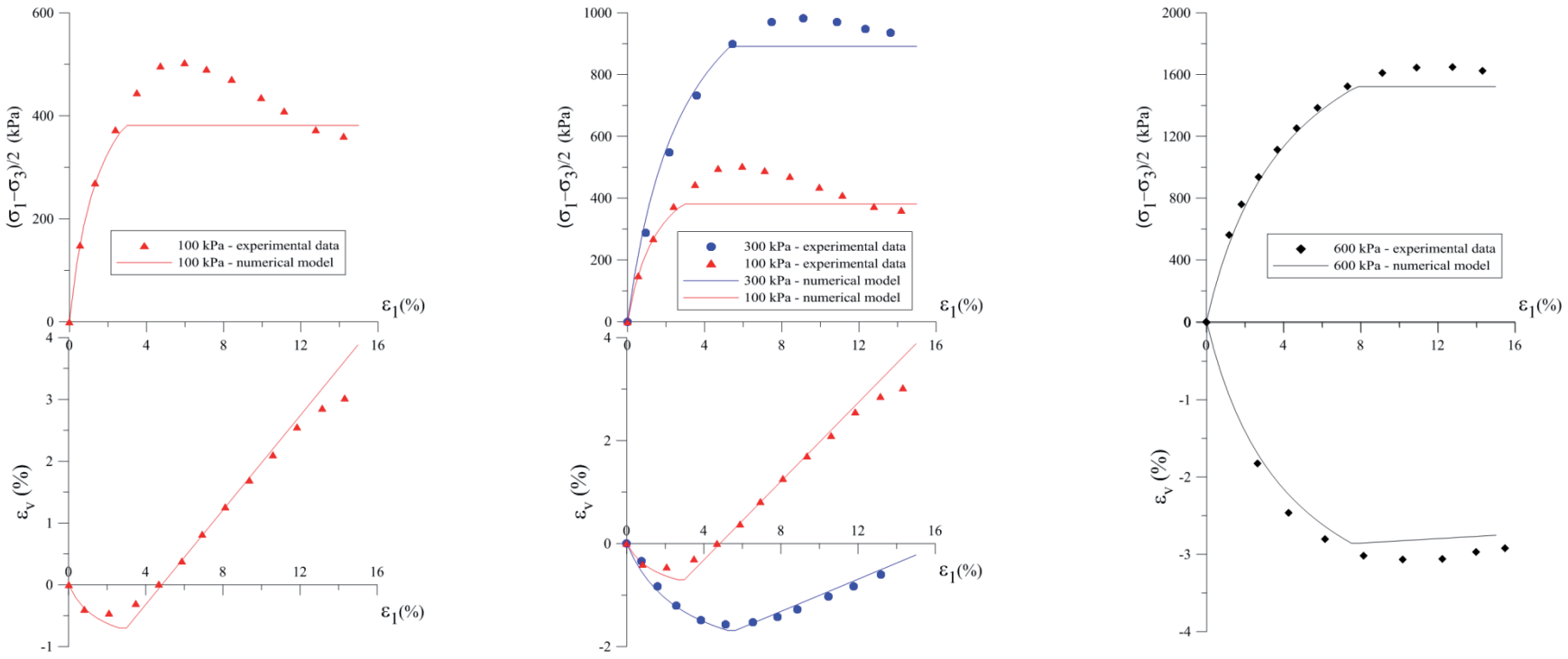

(a) (b) (c)

Figure 3-9 Calibration of the implemented model with the experimental data for dry specimens with density of 2000 kg/m3 (a) Calibration of φ_0, ψ_0, K_E, K_B, R_f at the confining pressure of 100 kPa (reference pressure) (b) Calibration of m, n, $\Delta\varphi$, and $\Delta\psi$ for a different confining pressure of 300 kPa. (c) Prediction of the behavior at 600kPa

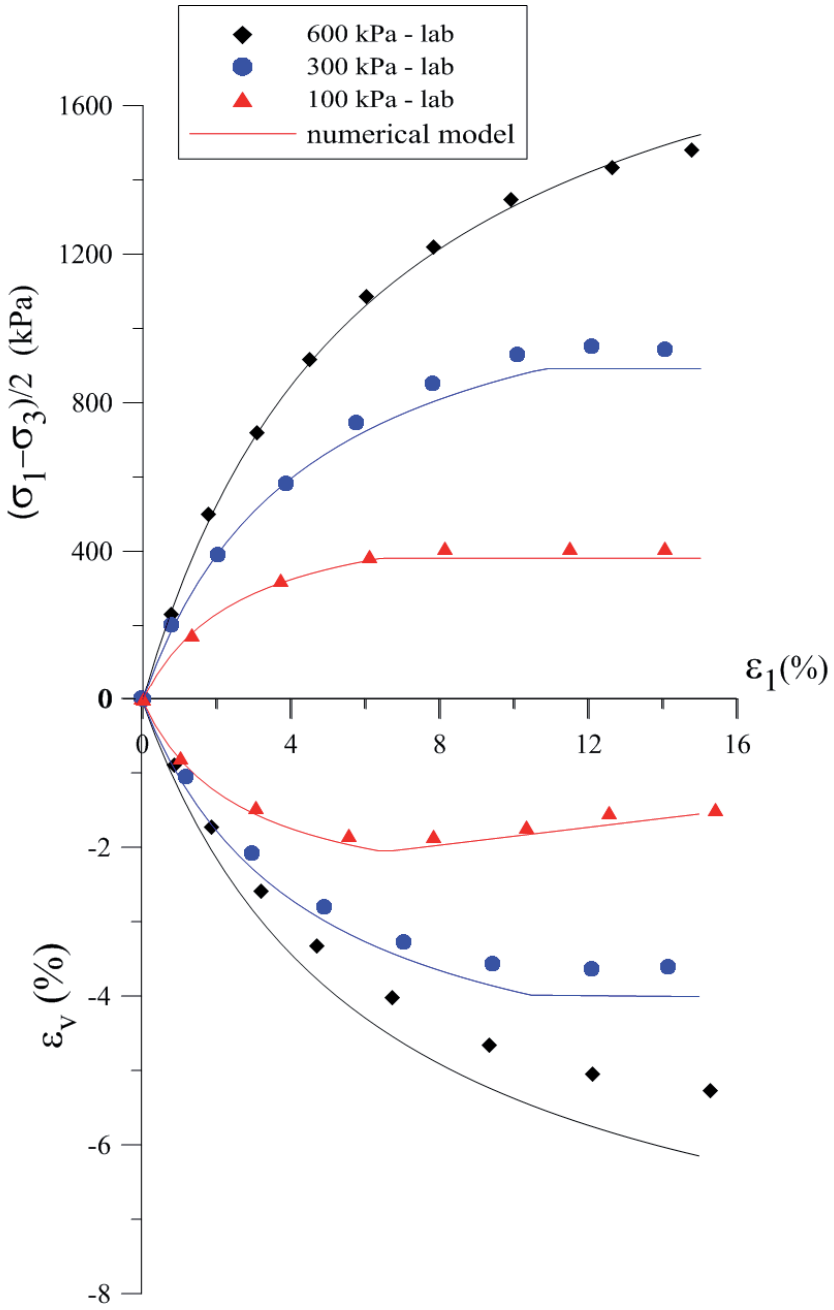

Figure 3-10 Comparison of numerical model and experimental data for dry specimens with dry density of 1900 kg/m^3

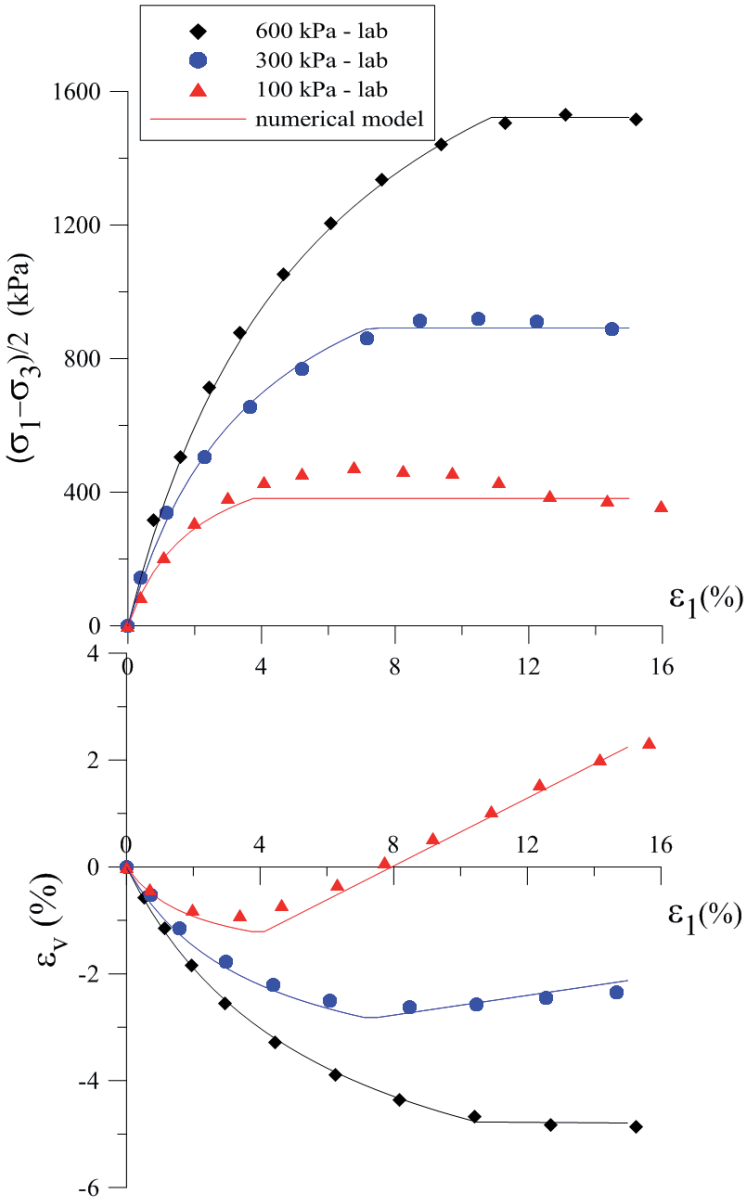

Figure 3-11 Comparison of numerical model and experimental data for saturated specimens with dry density of 2000 kg/m^3

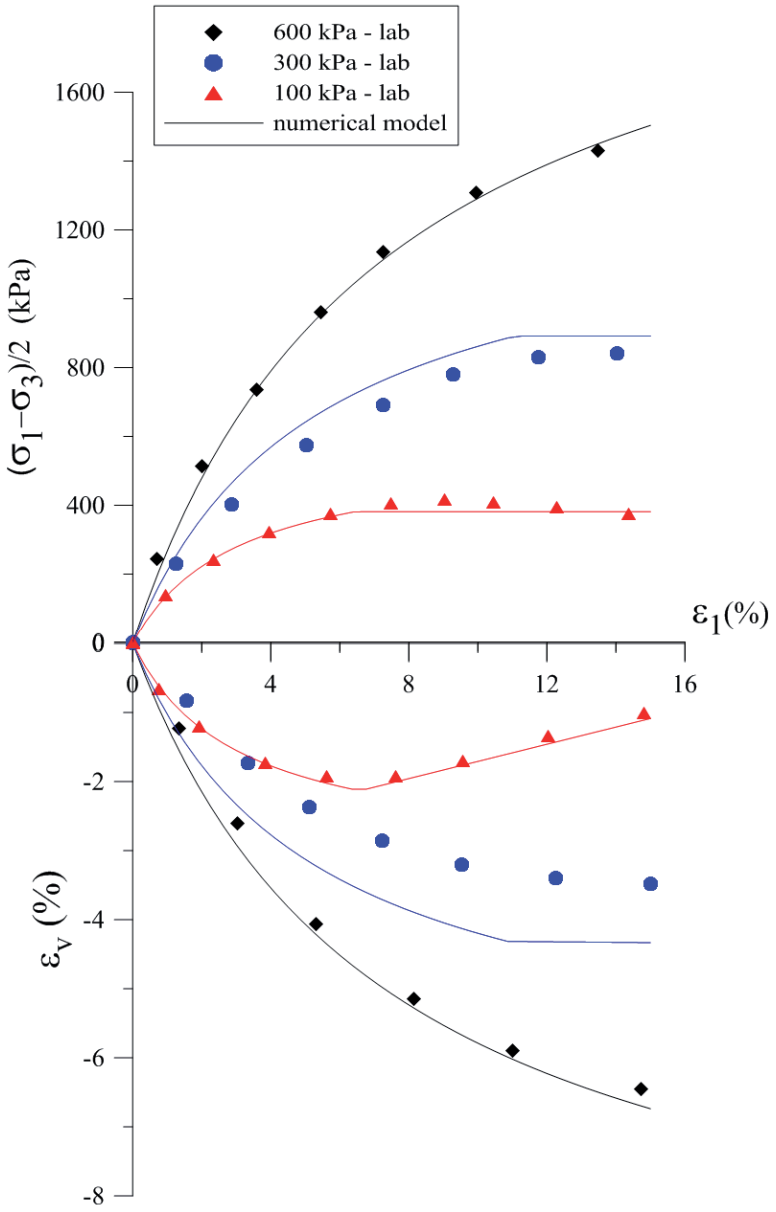

Figure 3-12 Comparison of numerical model and experimental data for saturated specimens with dry density of 1950 kg/m^3

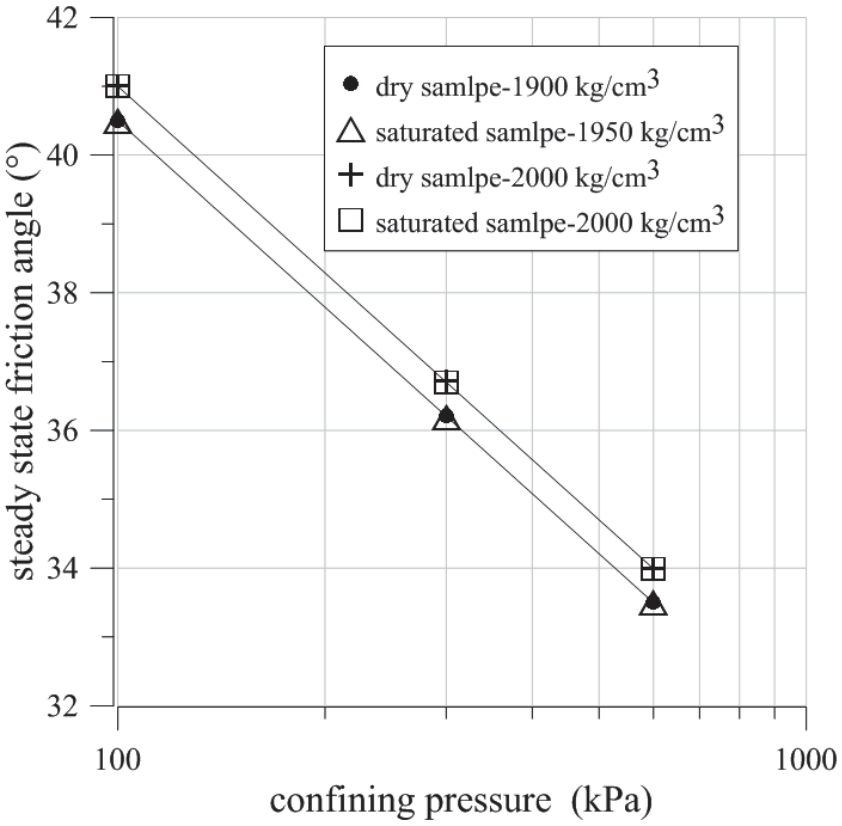

Figure 3-13 Variations of steady state friction angle with confining stress, density, and saturation of the tested material.

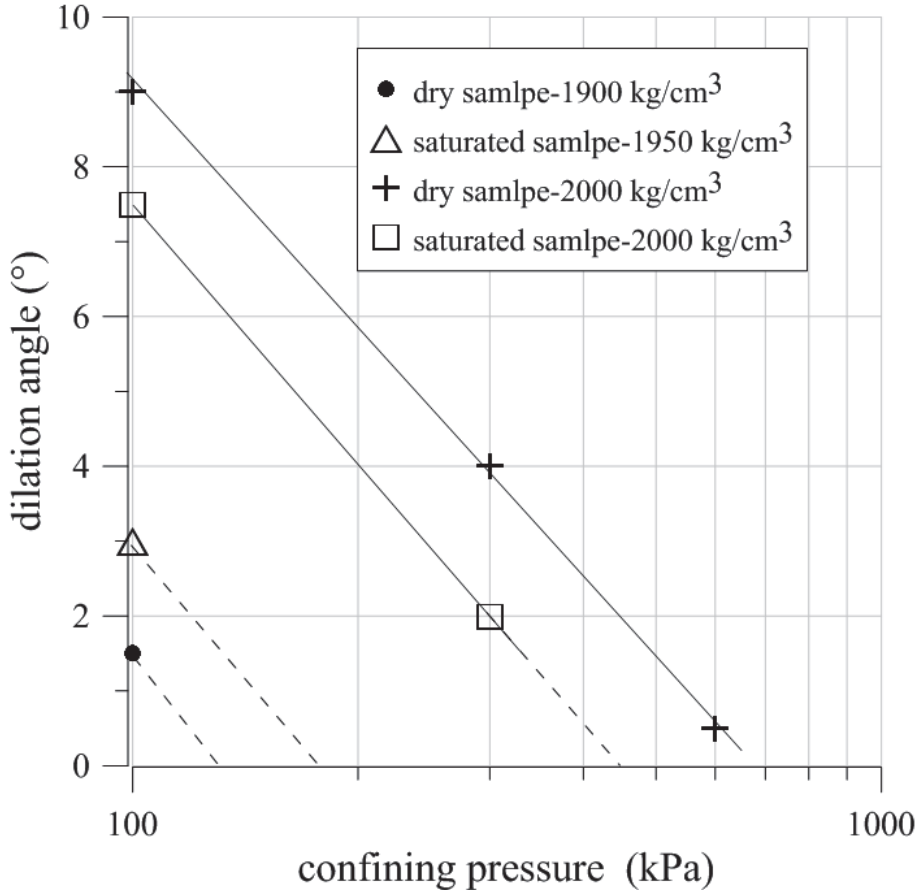

Figure 3-14 Variations of dilation angle with confining stress, density, and saturation of the tested material.

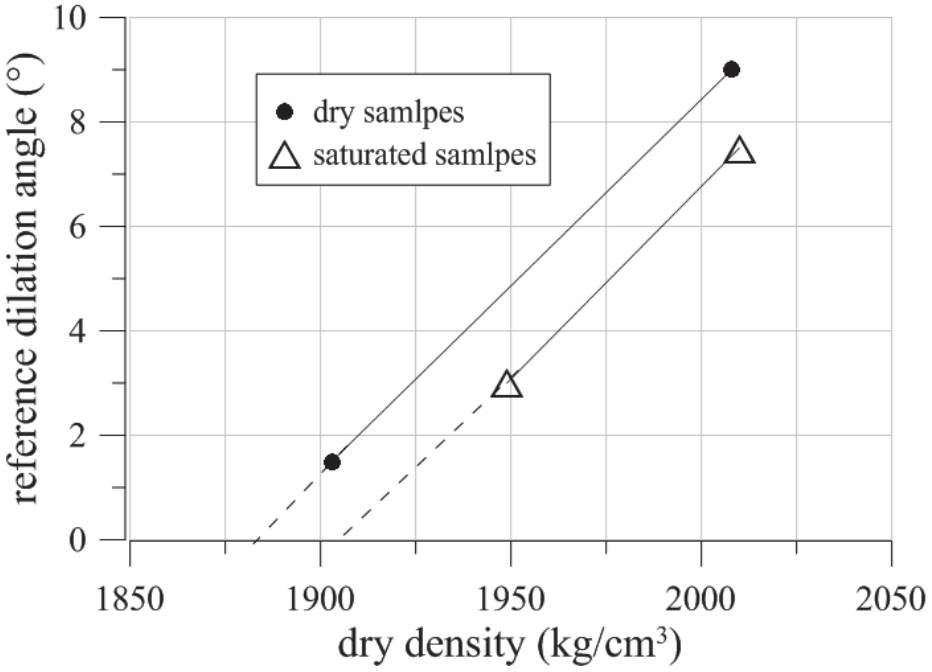

Figure 3-15 Reference dilation angle

confining stress (kPa)	test condition	initial dry density (kg/m^3)	Dry density after (kg/m^3)	deformation rate (%/hr)
100	dry	1810	1900	5
		1920	2010	5
	saturated	1810	1950	1
		1900	2010	1
300	dry	1810	1930	5
		1900	1970	5
	saturated	1810	1950	5
		1900	2060	1
600	dry	1810	1970	5
		1900	2070	5
	saturated	1810	2020	1
		1900	2100	1

Table 3-1. Triaxial test condition

	Rockfill description			physical properties			hyperbolic parameters					
	Dam	rockfill position	material	Particle size	compaction	unit	φ	K_E	K_B	n	m	R_f
1	Storvass	outer shell	well graded rock material- suitable mineral composition - limited brittleness and flakiness	D_{max} =800 mm	8 passes of 13 ton vibrating roller, 1.6 m layers	2000	45	900	350	0.45	0.20	0.70
2		inner shell		D_{max} =400 mm	8 passes of 13 ton vibrating roller, 0.8m layers	2050	47	1200	450	0.45	0.30	0.75
3		outer transition		D_{max} =200 mm	4 passes of 6 ton vibrating roller, 0.4 m layers	2150	49	1800	1000	0.25	0.25	0.65
4		inner transition	crushed rock	D_{max} =40 mm	6 passes of 2 ton vibrating roller, 0.2 m layers	2150	49	3000	1650	0.2	0.15	0.65
5	Foz do Areia	beneath concrete face	Massive basalt	D_{max} =1000 mm ,C_u=6	4 passes of vibrating roller, 0.8m layers	2120	45	350	100	0.37	0.13	0.60
6		outer shell		D_{max} =500 mm ,C_u=14	4 passes of vibrating roller, 1.6 m layers	1980	42	400	150	0.37	0.13	0.80
7		inside body	mixture of massive basalt and fault breccias	-	4 passes of vibrating roller, 0.8m layers	-	38	460	150	0.1	0.13	0.65
8	Netzahu	rockfill	sub-angular conglomerate	D_{60}=47 mm, C_u=52	D_r=70%	1910	50	540	135	0.43	0.34	0.64
9	Mica	outer shell	sub-angular granite gneiss	D_{60}=79 mm, C_u=20	D_r=95%	1980	44	210	100	0.51	0.34	0.64
10		inner shell	sub-angular sandy gravel	D_{60}=22 mm, C_u=95	D_r=50%	-	41	420	125	0.5	0.46	0.78

Table 3-2. Hyperbolic parameters in the published test data of rockfill dams

	Rockfill description			physical properties			hyperbolic parameters					
	Dam	rockfill position	material	Particle size	compaction	unit weight	φ	K_E	K_B	n	m	R_f
11	Furnas	shell	sub-rounded quartzite	D_{60}=10 mm	-	-	49	560	330	0.48	0.33	0.65
12		outer transition		D_{60}=25 mm	-	-	53	950	470	0.52	0.52	0.59
13		inner transition		D_{60}=10 mm	-	-	50	690	360	0.57	0.57	0.51
14	Infiernillo	shell	angular diorite,	D_{60}=93 mm, C_u=5	D_r=50%	1700	46	340	52	0.28	0.18	0.71
15	Oroville	outer shell	rounded silty sandy gravel(GP)	D_{60}=18 mm, C_u=4	D_r=100%	2370	53	1300	900	0.4	0.22	0.72
16		inner shell	rounded amphibolites gravel(GP)	D_{60}=13.2 mm, C_u=37	D_r=100%	2430	51	1780	1300	0.39	0.16	0.67
17	Round Butte	shell	angular crushed basaltic rock	D_{60}=15 mm, C_u=2.5	D_r=100%	1590	51	410	195	0.21	0	0.71
18	Rowallan	-	rounded sandy gravel	D_{60}=10 mm, C_u=17	D_r=100%	2160	58	2500	1400	0.21	0	0.75
19	Talbingo	rockfill	-	-	-	2040	45	680	-	0.44	-	0.71
20	Garmrood	shell	-	-	-	2000	40	400	250	0.65	0.50	0.70

Table 3-2 (continued). Hyperbolic parameters in the published test data of rockfill dams

	Corresponding figure	γ(kg/	K	n	K	m	R_f	ϕ	Δ	ψ	Δ
Initial		1900-	2	0.	1	0.	0.	4	-	-	-
dry	Figure 3-10	1900	2	0.	6	0.	0.	4	9	1	1
	Figure 3-9	2000	3	0.	1	0	0.	4	9	9	1
saturat		1950	1	0.	6	0.	0.	4	9	3	1
		2000	2	0.	1	0	0.	4	9	7	1

*The dry densities are considered at the end of consolidation.

Table 3-3. model parameters for the assemblage of granite particles in the conducted triaxial tests

4 Modeling the deterioration of contact points in a compacted assemblage of rock particles during monotonic triaxial compression

4.1 Introduction

Propagation of fissures and deterioration of the contact points between the individual particles are key factors in the analysis of the behavior of granular material and could be caused by increasing stress level or even at an unchanged stress state over time. The latter has been addressed as static fatigue or delayed fracture by Lemaître and Chaboche (1990) and Lade et al. (2010) and as time-dependent or creep behavior of rockfills by others (e.g. Oldecop and Alonso, 2007; Silvani et al., 2009). The fact that presence of water in the form of liquid or vapor will accelerate this process is well established in many articles. Researchers including Nobari and Duncan (1972), Maranha das Neves and Veiga Pinto (1989), Justo (1991), Bonelli and Anthiniac (2000), Touileb et al. (2000), and Lade and Karimpour (2010) have shown the profound influence of water on chemical reactions that lead to weakening and failure of the crack tips on the surface of the grains. This propagation of micro fissures in the particles produce new slides inside the granular mass; the interlocks between grains break and they collapse seeking more stable positions. A very common example of such phenomena is the settlement in the upstream slope shell of rockfill dams during the first impoundment.

Different constitutive equations spanning between linear elastic methods (Justo and Saura, 1983b) and hypo plastic models (Fu and Bauer, 2009) have been proposed to predict the behavior of the rockfill material during and after the saturation. Oldecop and Alonso (2001) proposed a constitutive model based on the unsaturated soil mechanics to calculate the collapse deformation of the rockfill sample caused by wetting or increased relative humidity (i.e. introduction of water in the form of liquid or gas). This model is useful to predict the deformations of the downstream as well as upstream shell of the rockfill dam, and requires several oedometric and triaxial tests in different relative humidity to be calibrated. This model was implemented into finite element software Code Bright and used to model different dams in Europe (Alonso et al., 2005; Alonso et al., 2011; Costa and Alonso, 2009).

The more complex models are expected to capture the so called collapse phenomenon with greater precision. However those models also need more parameters to be determined; hence more laboratory testing is required. This might not always be practical

in engineering practice nor financially justified when dealing with heterogeneous rockfill samples with boulders up to 2 meters in diameter. Simplifying procedures are required in both laboratory testing (e.g. using parallel grain-size distribution with smaller maximum particle size(Lowe, 1964)) and determination of the parameters and this will introduce approximation and uncertainty into the modeling process; which brings us to the point to keep the constitutive equations less complex, considering only the important characteristics of the particular problem involved.

With the ultimate goal of predicting the deformations of the upstream shell of the rockfill dams, Nobari and Duncan (1972) presented procedures to predict plastic deformations caused by wetting using the hyperbolic model (Duncan and Chang, 1970) and based on internal unloading of the rockfill material during saturation. These procedures were implemented in finite element software FEADAM to predict deformations of the upstream shell of rockfill dams during the first reservoir filling (Duncan et al., 1980b). The equations were later modified by Duncan et al. (1984) in a finite element concept and by Escuder et al. (2005) in a finite difference concept in order to consider the modified formulation of the hyperbolic model presented by Duncan et al. (1980a). The parameters of this model can be calculated using the results of the triaxial tests on dry and saturated samples. Moreover, provided that the rate of softening of the material is known in time, the same procedures could be employed to predict the time-dependent deformations in a creep analysis (Escuder, 2001). Triaxial tests at changing strain or stress rate are required for this purpose.

In this chapter two series of monotonic triaxial compression tests were conducted on assemblages of compacted rock particles prepared in the laboratory. Firstly, strain-controlled tests were performed at different confining stress on both dry and saturated specimens to characterize the behaviors respectively. Secondly, stress-controlled tests were conducted on dry samples, applying a changing rate of deviatoric stress over time to investigate the time effects on deformations. The water was then added at different stress levels which were maintained constant during the saturation process in order to calculate the deformations caused by wetting. These experimental data were used to calibrate the constitutive model which was the hyperbolic model coupled with Mohr-Coulomb failure

criteria and a non-associate flow rule to consider shear dilatancy. The time and wetting effects were modeled using the modified procedures presented by Nobari and Duncan (1972), and Escuder et al. (2005) in a finite difference context, and new algorithms were presented to solve these equations.

4.2 Constitutive model

The constitutive model addressed in this paper is the non-linear hyperbolic model coupled with Mohr-Coulomb failure criteria and a non-associated flow rule to consider dilatancy of the compacted granular material. The coupling was done in order to overcome the two shortages of the traditional hyperbolic model as mentioned by Duncan et al. (1980a): (i) due to its elastic formulations the behavior at and after failure cannot be modeled correctly; and (ii) the original relationships do not include shear dilatancy. In the previous chapter, it was shown that by coupling the hyperbolic model with the Mohr-Coulomb failure criteria, the model has a satisfactory precision in the prediction of the behavior of compacted assemblages of rock particles, in both dry and saturated conditions. Moreover the parameters of the model was estimated relatively simple from the results of the convectional triaxial tests or from the large database which exist in the literature for both hyperbolic and Mohr-Coulomb models.

There are total of 9 parameters in this model as shown in Table 4-1. Five parameters are needed to define the nonlinear elastic behavior before the failure envelope is reached. The post-failure behavior is simulated using perfectly plastic formulation and a non-associated flow rule, requiring four more parameters in order to estimate the friction and dilation angles corresponding to the yield and potential functions in this model, respectively. The schematic of this model is shown in Figure 4-1. It was shown in the previous chapter that the same behaviors would be observed for both dry and saturated specimens, except for a slight decrease in some of the characteristics (i.e. rigidity and dilation); as a result, the stress-strain-volumetric curves for the saturated samples will be plotted below those of the dry samples. These different dry and saturated constitutive curves will be used in the calculation of the collapse deformations in the dry-wet transition state.

4.2.1 Dry-wet transition

Considering the concepts of classical soil mechanics (Taylor, 1948; Terzaghi, 1943), when fluid flows through a porous medium, there are three forces acting on the solid matrix: the solid weight, the buoyancy and the seepage force (Bear, 1972). Based on this principle, when the water is raised inside a dry rockfill mass, the effective stress is decreased and the swelling of the material is expected. However what happens in reality is often different: during the saturation of the geomaterials in the field (e.g. impoundment of rockfill dam) the sudden collapse under constant stress conditions has been observed worldwide. However, in rockfill material the settlements are due to the catalytic effect of water in propagation of micro fissures in individual rock particles as mentioned before, and could be regarded as accelerated creep deformations. Additional procedures are required to characterize this kind of behavior when modeling the dry-wet transition of the granular material in the context of classical soil mechanics (i.e. effective stress principal) which is explained as follows.

4.2.2 Uniaxial compression condition

Burland (1965) conducted a series of one-dimensional tests to study the collapse deformation as the water was introduced into dry samples of granular material. He measured the deformations due to wetting in both stress and strain controlled uniaxial tests and in both cases the final conditions of void ratio and pressure were found to be very close to the compression curve for a specimen which was wetted prior to loading. He concluded that whether the specimen is loaded first and then wetted, or wetted first and then loaded does not appear to make any difference in the magnitudes of strains induced by both wetting and compression. In other words, when the dry specimen is loaded and then wetted, the behavior will shift from dry to the initially saturated specimen and will follow that kind of behavior afterwards. This finding was an important step in calculating the collapse deformations using the difference between the dry and saturated constitutive curves at the moment of wetting. As shown in Figure 4-2, there are two different main paths between the dry and saturated stress-strain curves: (i) path A-C which shows the amount of the collapse deformations during the wetting in a constant stress condition, and (ii) path A-B which shows the amount of the relaxation of stress

during this process in a constant strain condition. The latter was employed in the numerical methods as shown by King (1965), and Nobari and Duncan (1972) in which the changes in stress due to creep or wetting collapse during a time interval were computed by calculating the amount of stress relaxation which would occur if there were no strains during the time interval. These stress changes were subtracted from the values at the beginning of the increment, and then equilibrium was restored by applying statically equivalent nodal point forces. A similar computational procedure has been adopted in the analysis of movements and stress changes due to wetting in the current research but in a triaxial setting.

4.2.3 Triaxial compression condition

In Figure 4-3, the dry-wet transition is shown in a triaxial setup, and in a constant stress condition. In Figure 4-3 (a) an assemblage of dry rock particles is schematically shown with distribution of the contact forces; initially the internal stresses are in balance with the applied stresses and the system is in equilibrium. In Figure 4-3 (b) the transition state is shown which corresponds to the wetting process in the collapse calculations or alternatively as a time interval in creep analysis. As a result of the propagation of the microfissures, some particles break and leave the interlock between the grains. The disruption of these contact points and slippage of the grains leads to an internal unloading in an undrained condition. This stage corresponds to the path A-B in Figure 4-2. The final state is shown in Figure 4-3(c), in which the deformations have taken place in all directions and the element is again in equilibrium with the unchanged applied stress (corresponding to the path B-C in Figure 4-2). Figure 4-4 shows a comparison of the constitutive curves for dry, wet, and dry-wet specimens in triaxial compression test. The dry-wet transition was performed in a constant strain condition, and the behavior of the dry-wet specimen approximately followed the initially wet specimen, after wetting. It should be noted that the insitu condition is often the constant stress during the creep deformations or wetting collapse. However, using the stress relaxation technique, as explained above, it is possible to model the collapse phenomena in a constant strain condition.

4.2.4 Application in numerical modeling

Two assumptions are required for reproducing the explained physical phenomenon in a numerical model in the triaxial condition in order to calculate the collapse movements in the specimen:

1. After saturation, the deformations will be equal to the difference between the dry and wet constitutive curves. This assumption was firstly proposed by Burland (1965), and confirmed by many researchers since then. Without taking this assumption it was almost impossible to predict the collapse deformations from individual laboratory tests on dry and saturated specimens.

2. The principal stress directions remain constant during the saturation process. Provided that the amount of relaxation stresses are not very large compared to the initial stress state, the directions of the principal stress do not change during the process (Nobari and Duncan, 1972). On the other hand, when the material is very sensitive to wetting, rotation of principal axis might occur, which introduces error in the calculations.

These assumptions let the calculation of the amount of the internal unloading occurring in Figure 4-3 (b) to be statically applied as equivalent nodal point forces in a numerical analysis. The objective is to calculate these unloading stresses which are equal to the differences between wet (or saturated) stresses (σ_{1w}, σ_{3w}) and dry stresses (σ_{1d}, σ_{3d}) at the moment of wetting. This is possible if both dry and wet stress-strain-volume curves are known for the given material.

Escuder et al. (2005) applied this methodology in a finite difference context. In their method, the calculation of the equivalent wet stress state involved formulating an iterative procedure in which the values of principal stresses were obtained by minimizing two error functions (two equations and two unknowns systems). However, in this research in order to reduce the complexity of the iterative procedure and to minimize the computational effort during the numerical simulation, the equations were separated into two independent systems to calculate the two unknowns (σ_{1w}, σ_{3w}) separately, and each one with desired precision. This enhancement also increased the stability of the numerical

procedure. The minimum principal stress (σ_{3w}) is firstly calculated. Knowing the first unknown, the maximum principal stress (σ_{1w}) can be readily calculated. The main difficulty is then to calculate the minimum principal stress in the wet condition. The known parameters and condition in this system of equations are: (1) the dry stress state (σ_{1d}, σ_{3d}); (2) dry and wet behaviors (i.e. stress-strain-volume change curves); (3) constant strain condition.

Writing the hyperbolic functions for the dry and wet conditions and using algebraic manipulation yield the final equation as:**Erreur ! Source du renvoi introuvable.**This nonlinear equation could be solved using any numerical method such as bracketing, Newton, or Bisection (Press et al., 2007) provided that the answer is between two given limits (0 and σ_{3d}). In the above equation the unknown is ($x \equiv \sigma_{3w}$) and the coefficients are all known and could be computed before the iterative procedure starts as follows:

$$a = \frac{2.c.cos\varphi}{1 - sin\varphi} \qquad \textit{[Eq. 4-1]}$$

$$b = \frac{2sin\varphi}{1 - sin\varphi} \qquad \textit{[Eq. 4-2]}$$

$$c = R_{fw}.K_{Ew}.P_a{}^{(1-n_w)}.\varepsilon_a \qquad \textit{[Eq. 4-3]}$$

$$d = \frac{3.K_{bw}.\varepsilon_v}{K_{Ew}.P_a{}^{(m_w-n_w)}.\varepsilon_a} \qquad \textit{[Eq. 4-4]}$$

Where P_a is atmospheric pressure; c, φ are cohesion and friction angle of the material (this is the general solution for the hyperbolic formulation; in the current study of the granular rock particles, the cohesion is assumed to be zero); K_{Bw}, K_{Ew} are modulus numbers of the saturated material; m_w, n_w are modulus exponents of the saturated material; R_{fw} is the fitting coefficient of the saturated material; $\varepsilon_a, \varepsilon_v$ are axial and

volumetric strains at the moment of saturation. These strains can be computed using the known dry stress state and dry parameters using the following algorithm:

1. Calculation of maximum deviatoric stress in dry condition as:

$$(\sigma_1 - \sigma_3)_{fd} = \frac{2cCos\varphi + 2\sigma_{3d}sin\varphi}{1 - sin\varphi} \qquad \textit{[Eq. 4-5]}$$

2. Calculation of the initial Young's modulus in dry condition as:

$$E_{id} = K_{Ed}P_a\left(\frac{\sigma_{3d}}{P_a}\right)^{n_d} \qquad \textit{[Eq. 4-6]}$$

3. Calculation of secant Young's modulus in dry condition as:

$$E_{sd} = \left(1 - \frac{R_f(\sigma_1 - \sigma_3)_d}{(\sigma_1 - \sigma_3)_{fd}}\right) \times E_{id} \qquad \textit{[Eq. 4-7]}$$

4. Calculation of dry bulk module as:

$$B_d = K_{Bd}P_a\left(\frac{\sigma_{3d}}{P_a}\right)^{m_d} \qquad \textit{[Eq. 4-8]}$$

5. Calculation of axial strain in dry condition as:

$$\epsilon_a = \frac{(\sigma_1 - \sigma_3)_d}{E_{sd}} \qquad \textit{[Eq. 4-9]}$$

6. Calculation of volumetric strain in dry condition as:

$$\epsilon_v = \left(\frac{E_{id}}{3B_d}\right)\left(\frac{(\sigma_1 - \sigma_3)_{fd}\epsilon_a}{(\sigma_1 - \sigma_3)_{fd} + R_{fd}E_{id}\epsilon_a}\right) \qquad \textit{[Eq. 4-10]}$$

Where K_{Ed}, K_{Bd} are modulus numbers of the dry material; m_d, n_d are modulus exponents of the dry material; R_{fd} is fitting coefficient of the dry material. Once the minimum principal stress (σ_{3w}) is determined from [Eq. 4-1], the maximum principal stress (σ_{1w}) is readily calculated using the following equation:

$$\sigma_{1w} = \sigma_{3w} + \frac{x}{1 + y} \qquad \textit{[Eq. 4-11]}$$

Where:

$$x = \varepsilon_a . E_{iw} = \varepsilon_a . K_{Ew} P_a \left(\frac{\sigma_{3w}}{P_a}\right)^{n_w} \qquad \textit{[Eq. 4-12]}$$

$$y = \frac{\varepsilon_a . R_{fw} . E_{iw}}{(\sigma_1 - \sigma_3)_{fw}} = \frac{\varepsilon_a (1 - sin\varphi) . R_{fw} . K_{Ew} . P_a \left(\frac{\sigma_{3w}}{P_a}\right)^{n_w}}{2c . cos\varphi + 2\sigma_{3w} . sin\varphi} \qquad \textit{[Eq. 4-13]}$$

Afterwards, the procedure is the same as explained by Nobari and Duncan (1972); it consists of relaxation of the wetted element based on the new wet stress state and bringing the element into equilibrium with the new boundary conditions which includes the buoyancy forces as well as pore water pressure distribution.

4.2.5 Creep deformations

The micro structural concepts discussed in Figure 4-3 are also applicable for the creep problem provided that the time interval is long enough to let the micro fissures to propagate which leads to the breakage of rock particles and deterioration of contact points. The mathematical solution for the calculation of creep deformations is the same as that of the previously explained dry-wet transition. The objective is to calculate the stress state at the end of a given time interval which corresponds to the wet stresses (σ_{1w}, σ_{3w}) in the previous formulations. The known stress state at the beginning of this time interval corresponds to dry stress state (σ_{1d}, σ_{3d}) in the previous equations. This procedure is possible if the rate of softening of the granular material is known over the desired period of time, and the constitutive curves are known for the given material at both intervals. In order to acquire such data, laboratory tests with changing rate of loading is required to investigate the time effects in the behavior of the rock particles.

4.3 Laboratory tests

A laboratory testing program was designed to study the behavior of rock particles under monotonic loading and to characterize the time effects and saturation of the specimens in a triaxial setting. Both strain-controlled and stress-controlled tests were considered in the experimental program. The strain-controlled tests were conducted using a constant rate of straining on individual dry and saturated specimens at different confining stress to estimate the corresponding behaviors and to obtain the stress-strain-volume change

curves in both dry and saturated conditions. Stress-controlled tests were conducted using a changing rate of deviatoric stress over time on dry samples to investigate the time effects. The water was consequently added and the collapse deformations were calculated in a constant stress condition. The data from these tests was used to calibrate the parameters of the implemented model, and to verify the discussed procedures and algorithms.

4.3.1 Material tested

The rock particles used in this study were obtained from crushing and sieving the granite boulders of the shell zone of the Romaine 2 dam, which was under construction in Quebec, at the time of the experimental program. The grain size distribution of the material was determined using the prototype rockfill material as shown in Figure 4-5. There are three different curves in this figure which correspond to (i) prototype rockfill gradation conforming to the standard distribution used for the rockfill dams in Quebec, (ii) a parallel gradation using the technique explained by Lowe (1964), and (iii) the gradation used in the current experiments in which the percentage of fines was reduced from that of the parallel gradation in order to have a more uniform distribution with higher void ratios, and less contact points between the rock particles.

The grain size distribution was modified in order to increase the magnitude of the deformations caused by deterioration of the contact points over time or by wetting. Figure 4-6 compares these contact points and breakage patterns in ideal uniform and non-uniform samples. Uniform samples have fewer contact points compared to non-uniform distribution. Under stress-controlled test conditions grain crushing occurs at lower stress levels in uniform specimens samples since there will be higher stresses accumulated at the fewer contact points between grains (Omidvar et al., 2012). Moreover, uniform samples exhibit a yield-type response in a wider range of strains as the broken grains rearrange into the voids as shown in the lower schemes of Figure 4-6 (Hendron, 1963).

4.3.2 Specimen preparation

Five sets of angular granite grains with different uniform particle sizes were used to prepare the specimens for the test as shown in Figure 4-7. For each specimen being

tested, the appropriate quantities of oven-dried grains were mixed according to the modified gradation curve shown in Figure 4-5. The samples were prepared in a split mold attached to the base pedestal of the triaxial test equipment. In order to minimize density variation within a specimen, five equal pre-weighted portions of the granite rock particles were mixed and compacted using the vibratory compaction to a predetermined height corresponding to the dry density of 1700 kg/m^3. After removing the mold, thin plastic sheets were loosely attached around the rubber membrane to form a stiff cylindrical support against the penetration of the angular rock particles. A second rubber membrane was then installed over the plastic sheets to seal the whole specimen during the triaxial testing.

4.3.3 Triaxial setup

Polished stainless steel end platens were used in both test series in order to minimize end-restraint effects caused by the penetration of rock particles. The platens had several holes to provide drainage of water during the saturated tests. Fine wire meshes wrapped in paper filters were installed on both platens to prevent the fine soil particles to block the drainage holes. In all the tests, the nominal height of the sample was 300 mm and the nominal diameter was 150 mm. Two different apparatus were designed in order to conduct the stress and strain-controlled tests separately. The data in both test series were collected and recorded every one minute using a dedicated acquisition system.

In the strain controlled device, the base platen was fixed while the upper platen displaced downwards to strain the sample at an adjustable rate. The dry and saturated samples were initially subjected to the desired confining pressure (i.e. 100, 300, or 600 kPa) and then axially strained at 5% per hour for dry tests; and 1% per hour in drained condition for saturated tests. The samples were saturated before the application of confining stress and by allowing water to pass through the base of the triaxial cell and using the top drainage system for removing air voids. The strain controlled test conditions are summarized in Table 4-2.

In stress-controlled tests, the dry specimens were firstly subjected to the confining stress of 200 kPa. The deviatoric stress was then applied using a hydraulic valve, controlled by

a computer. The base platen was fixed while the axial deformation was measured using the installed LVDT on the top platen. The vertical stress was increased in steps of about 50 kPa and kept constant while the axial and volumetric deformations were measured with time. This procedure was repeated until the desired deviatoric stress was reached when the water was added to the specimen through the base of the triaxial cell to reach a saturation degree of more than 90%. The stress state maintained constant during and after the saturation in order to simulate the constant stress condition. The collapse deformations were measured over several hours until the axial strain rate became constant or very small. The stress controlled test conditions are summarized in Table 4-3.

4.3.4 Strain rates in strain controlled tests

The effects of rate of straining on the behavior of the specimens in a triaxial test have been firstly reported by Whitman (1957b). This is an important issue to consider due to the viscous nature of geomaterials which is a well-established fact in geotechnical engineering practice (e.g. Leroueil and Hight, 2002; Mitchell, 1976). If the rate of straining is smaller, the more time is allowed for the sample to relax, allowing the development of smaller shear stresses at a given deformation increment. The final result is a stress-strain curve which plots lower. Matesic and Vucetic (2003) have reviewed the previous experimental studies on clay and sand samples and confirmed that axial strength, and secant modulus increase approximately linearly with the logarithm of the strain rate. The rates included in their research ranged between 10^{-5} and 10^{3} %/s. Blanton (1981) have reviewed the previous experiments on rock samples and concluded that a small constant rate of increase in strength with increasing rate of deformation in logarithmic scale was often expected. However, he observed a sudden increase in strength above the strain rate of about 10^{2} %/s. The rates included in his study ranged between 10^{-6} and 10^{3} %/s.

Considering the relation between the size of the particles being tested and the explained rate effect, Whitman (1957a) and Mitchell (1976) reported that clays were much more susceptible to this effect than the granular material and that strain-rate effect in soils generally increases with plasticity index and water content. Moreover, Blanton (1981) suggested that although higher strain rates resulted in a more brittle response of the rock

specimens, the increase in the failure stress was negligible for the strain rates below 10^{-2} %/s. Similar results were reported by Lade et al. (2009) for drained triaxial compression triaxial tests on crushed coral sand performed with a constant effective confining pressure of 200 kPa, showing no time-effect for strain rates below 1.7 %/hour (approximately 10^{-3} %/s).

To sum up, the appropriate choice of the rate of straining depends on the characteristics of the material being tested as well as the geotechnical problem involved. While the common strain rate chosen for monotonic testing of sands is about 1 %/min (approximately 10^{-2} %/s), the larger rates which result in higher axial strength, and secant modulus of the specimens are useful in studying the cyclic behavior. In this research, the large scale monotonic triaxial compression tests in a strain-controlled condition were performed with the ultimate goal of modeling the behavior of rock particles in a rockfill dam. Hence, the strain rates chosen for testing these assemblages of relatively large rock particles were chosen 5 and 1 %/hour (approximately 10^{-3} and 3×10^{-4} %/s) for dry and saturated tests, respectively. The strain rates were reduced for the saturated samples in order to provide the full drainage condition during the experiments. These intermediate rates keep the time effect minimized for the material being tested, and provide a reference basis for the comparison with the results of the stress-controlled tests.

4.3.5 Stress rates in stress controlled tests

Mehta and Monteiro (1993) and Rűsch (1960) studied the rate-effect on the behavior of the structural concrete in stress controlled uniaxial compression tests following by creep experiments. The general behavior of the concrete samples is shown in Figure 4-8 in terms of applied load versus strain with time after loading at an age of 56 days as a parameter. There are three limiting lines in this figure, enclosing all possible relationships between stress and strain: (i) the elastic straight line relationship denoted as E_c on the left of the diagram for extremely short duration of loading; (ii) the creep limit as a curved line on the lower right of the diagram corresponding to a supposedly infinite duration of loading; (iii) a failure limit at the top of the diagram which shows decreasing strength for increasing load duration, and is negligible for test durations over 7 days. During the creep

experiments, when the stress state of the sample kept constant, the creep deformation of the sample is shown by horizontal arrows towards adjacent constitutive curves corresponding to longer test durations. The amount of the creep deformations depend on the duration of the creep test, as well as the sustained stress state of the sample.

Geomaterials behave similarly in the sense that their crushing strength is time dependent. Lade and Karimpour (2010) showed that overall stress-strain-time behavior of granular specimens or particles of brittle solids exhibit the delayed fracture indicated in Figure 4-8: As the stress on the specimen is held constant below the short-term fracture stress, the time to fracture increases with decreasing stress. In particular, during a stress-controlled triaxial compression test of granular material, if the rate of axial loading is larger, the less time is allowed for the sample to creep during the test; allowing the development of smaller deformations at a given load increment which results in recording a more rigid behavior of the material being tested. However, more deformations will be observed consequently during the creep test or after introducing the water as a catalyzer of the creep phenomenon.

Standard stress-controlled test methods often require that in triaxial tests of materials the vertical stress be applied at a certain constant rate. This requirement cannot be satisfied at high deviatoric stress for samples exhibiting an elasto plastic behavior since the rate of deformation would become extremely high in the yield range which leads to misleading results. Arenson and Springman (2005) conducted stress controlled triaxial tests in which the vertical stress was increased in each loading increment when the axial strain rate became constant or very small. The general trend of the behavior of the specimens in each stress increment is shown schematically in Figure 4-9. The three stages of the creep phenomena could be identified in this figure: primary, secondary or steady state and tertiary creep. The latter was characterized by an increase in the strain rate up to the creep rupture and was recorded only at high deviatoric stress near failure; while at lower deviatoric stress, the strain rate didn't change after reaching the values corresponding to the steady-state creep. In order to study the softening behavior of the materials over time, reaching this minimum strain rate at each stress increment is a more rational requirement than that all the tests to be carried out under constant rate of loading.

For this reason, the logarithmic scale of time was considered in the current study for applying the deviatoric stress to the specimens of the assemblages of rock particles over time as shown in Figure 4-10. The solid line shows the theoretical stress increments over time based on a logarithmic relation, while the points are the actual measurements during the tests which differ slightly due to errors in the experiments. This pattern of loading was consistent with the constant strain rates used in the strain-controlled tests (i.e. strain rates between 10^{-3} and 10^{-4} %/s); and was applied in all stress controlled tests on dry specimens in order to have a consistent rate of loading. It should be noted that if constant rate of loading had been chosen for the stress controlled tests, these strain rates could not have been reached consistently in all stress increments.

At the last stage of each stress-controlled triaxial test, after the specimen was saturated, it was allowed to deform at its final stress state for an extended time interval in order to approach the final creep limit as mentioned in Figure 4-8. The value of 10^{-4} %/s was considered for the target strain rate at this final stage. This also helped to calculate the collapse deformations due to wetting.

4.4 Test results

4.4.1 Strain controlled tests

The stress-strain and volume change curves during the axial straining of the both dry and saturated samples at different confining stresses are shown in Figure 4-11. The test results display the same general trends: nonlinear behavior at the beginning of the tests followed by a constant strength at higher strains. Due to relatively low densities of the samples being tested, they did not display strain-hardening characteristics. Except for the dry sample tested at confining stress of 100 kPa which showed a slight dilative behavior, other specimens contract entirely during the triaxial compression tests with no peak friction angle.

As expected, the stress-strain results of the tests with higher confining stress plot higher which means both rigidity and steady state strength of the specimens were increased with confining stress. Comparing the behavior of the dry and saturated specimens shows that:

1. Saturation decreased slightly the axial stiffness of the specimens. This is obvious by comparing the stress-strain curves of saturated specimens which plotted lower than those of the dry specimens at the same confining pressures.

2. The steady strength at large strains did not change much with saturation. At confining pressures of 100, 300 and 600 kPa, the final strength of both dry and saturated samples were measured about 350, 800 and 1300 kPa, respectively.

3. Saturation decreased the volumetric stiffness of the samples at lower confining stresses. This is evident by examining the volume change curves at both confining pressures of 100 and 300 kPa which show more volume change for saturated specimens at any given axial strain during the tests. However, the contractive behavior of the specimens at high confining stress of 600 kPa was almost the same.

4. The slight dilative behavior of the dry specimen at confining pressure of 100 kPa was not recorded for the saturated sample which shows that saturation decreased the rate of dilation.

The above general trends conform to the previously conducted strain controlled triaxial compression tests on denser specimens with different grain size distributions, as reported in the previous chapter. The time effects and collapse deformations due to wetting of the rock particles will be studied using the results of the stress controlled tests.

4.4.2 Stress controlled tests

Typical test data for the stress controlled test on the compacted assemblages of rock particles are shown on Figure 4-12 to Figure 4-15. In test #2, the dry sample was first subjected to an isotropic stress condition equal to 200 kPa, and subsequently to an increase in vertical stress applied in incremental steps up to 470 kPa, using the previously discussed logarithmic pattern as shown in Figure 4-10 and Figure 4-12. After reaching the desired deviatoric stress, the water was introduced into the sample, and the deformations were continuously recorded at constant stress state and in drained condition for several hours until the minimum strain rate of $\dot{\varepsilon} = 10^{-4}$ %/s was reached.

Volume change and axial strain were measured during the isotropic consolidation in order to modify the dry densities as shown in Table 4-3, and during the application of the deviatoric stress as shown in Figure 4-13 and Figure 4-14. Following each increase of the vertical stress, abrupt shifting of both axial and volumetric deformations was observed. The rates of deformations then decreased over time in each stress increment. As expected, after the specimen was saturated at the last stage of the test, sudden collapse of the specimen was observed without any change in the stress state; which could be related to the important role of water in accelerating the rate of deformations due to the deterioration of the contact points.

Figure 4-15 shows the rates of axial strain during the triaxial test. The high recording frequency, the low strains and the resolution of the installed LVDT at 0.001 mm caused the strain rates to oscillate around the mean value. The peak values in this figure range between $\dot{\varepsilon} = 5 \times 10^{-2}$ and $\dot{\varepsilon} = 8 \times 10^{-2}$ %/s, and correspond to the increases of the vertical stress; except for the last peak of $\dot{\varepsilon} = 4 \times 10^{-3}$ which corresponds to the saturation of the specimen, and is more than 10 times smaller than the previous values. At each stress increment, the peak value was followed by a steep decline in the strain rate, converging to the minimum value which bracket between $\dot{\varepsilon} = 10^{-3}$ at the beginning of the experiment, and $\dot{\varepsilon} = 10^{-4}$ $\%/s$ at the end. However, the strain rates did not reach any absolute minimum in any of the stress increments of the entire experiments, which means no tertiary creep was observed for the material being tested.

Typical stress-strain-volume change curves are shown in Figure 4-16, and Figure 4-17 for the stress controlled test #2 with the end of each stress increment marked. Because of the nonlinearity in stress-strain behavior of geomaterials in triaxial testing, the deformations in each increment increased with the deviatoric stress, same as the observed behavior in strain-controlled tests. However, the creep deformations were also added to these measured deformations due to the fact that time intervals were prolonged as the test proceeded. This time effect was more important at final stages that the sample was kept at constant stress state for several hours.

4.5 Implementation of the numerical model

The hyperbolic model coupled with Mohr-Coulomb failure criteria was implemented into the commercial software FLAC 6.0 (ITASCA Consulting Group, 2008). All the laboratory experiments were modeled using the software, exercising the implemented model over stress paths similar to those of the physical tests, and plotting the similar graphs to compare the results and to calibrate the parameters of the model. The modified stress relaxation algorithms were also implemented into FLAC in order to model the following behaviors observed during the stress-controlled tests: (i) the softening of material over time and calculation of creep deformations; (ii) the dry-wet transition stage and calculation the collapse deformations due to wetting.

4.5.1 Strain-controlled tests

The data from strain-controlled tests was used to characterise the behavior of the compacted assemblages of rock particles being tested in both dry and saturated conditions and to calibrate both elastic and plastic parameters of the implemented model. The calibration was done using the explained procedure in the previous chapter and in the following order:

1. An initial set of parameters were estimated based on the physical properties of the specimens such as density, grain size distribution, and angularity of the rock particles. The calibrated parameters of the previous chapter were considered due to the fact that the same rock particles were used to assemble the specimens, with a slight change in the particle size distribution and density.

2. The first parameters to be fine-tuned were φ_0, $\Delta\varphi$, and R_f. At confining pressures of 100, 300 and 600 kPa, the final strength of both dry and saturated samples were measured about 350, 800 and 1200 kPa, respectively which corresponded to the reference friction angle of $\varphi_0 = 41°$ and a decrease in friction angle with confining stress of $\Delta\varphi = 8°$. The value of $R_f = 0.73$ adjusts the stress-strain curve with the hyperbolic formulation for both dry and saturated specimens.

3. Different elastic modulus numbers were calculated for the dry and saturated samples, respectively: $K_{Ed} = 200$, $K_{Ew} = 180$; which was due to the fact that saturation decreased the rigidity of the samples. However, these values were not very different which meant that the hard granite rock particles were not very sensitive to the saturation (i.e. the elastic modulus number was 10% smaller in the saturated condition).

4. The bulk modulus numbers of the dry, and saturated specimens were calculated as: $K_{Bd} = 50$, $K_{Bw} = 40$, respectively; which showed 20% decrease in volumetric rigidity of the samples as a result of the introduction of the water.

5. The modulus exponents were calculated as $n = 0.05$, and $m = 0$ for both dry and saturated specimens. The small values of these coefficients showed that the behaviors were not greatly dependent to the changes of the confining pressure.

6. The only observed dilative behavior was during the straining of the dry specimen at the reference confining pressure of 100 kPa, which corresponded to the reference dilation angle of $\psi_0 = 5°$. The decrease of $\Delta\psi = 10°$ in dilation angle with confining stress were considered in order to nullify the dilation angle at higher confining pressures. The reference dilation angle was equal to zero for the saturated specimens.

Table 4-4 summarizes the calculated parameters for both dry and saturated specimens. Except for the slight decrease of the both modulus numbers, and the reference dilation angle, the rest of the parameters were not changed with saturation. The calculated stress-strain and volume change curves using these parameters in the FLAC software are shown in Figure 4-18 and Figure 4-19 along with the experimental data for dry material. In each figure, the performance of the implemented model is demonstrated by comparing laboratory data with the results of the simulation.

4.5.2 Stress-controlled tests

Since similar specimens were used in both strain and stress-controlled tests, the previously calibrated model could be ideally implemented to reproduce the results of the

stress controlled tests. However, the specific testing procedure with changing time intervals in the stress controlled tests introduced the strain rate effects, and creep components into the measured deformations. As stated by Tatsuoka et al. (2008), and Augustesen et al. (2004), granular materials are not necessarily governed by the same basic mechanism observed for clays known as *isotach* behavior (i.e., there is a unique stress-strain-strain rate relation for a given soil).The less dependency of the behavior to the changes in strain rate , and the crushing of the grains during the triaxial compression tests are the main reasons for the *non-isotach* behavior of the tested material, and different stress-strain relations obtained from the stress and strain-controlled test methods.

Unless the observed behavior during the strain-controlled tests, the typical stress-strain behavior for the conducted stress controlled tests did not fit over a single hyperbolic curve with constant rigidity (or modulus number) as shown in Figure 4-22. The observed behavior was enclosed between the upper and lower limits corresponding to the first and last stress increments, with time intervals of 0.5 and 17 hours, respectively. As the testing proceeded and the time intervals increased, more creep deformations were recorded which suggested a softer response of the material over time, with stress-strain curve plotted lower. This kind of behavior was similar to the time-dependant behavior of the concrete samples as explained in Figure 4-8. In order to characterise this time-dependent behavior, the modified stress relaxation technique was implemented in FLAC to reproduce the creep deformations, which are distinguished by horizontal lines in each stress increment of Figure 4-22. Using an iterative procedure, the modulus number of the model was adjusted in each increment, while other parameters were kept constant, in order to reach the same deformations as observed in the laboratory. The gradual decrease of the elastic modulus number as calculated in the numerical model for all the three stress-controlled tests are shown in Figure 4-23. The logarithmic relation shown in this figure was the same for all the three tests and complied with the creep phenomenon discussed before, i.e., the rate of softening of the material decreases over time to reach a steady state creep. At the final stage, after the water was introduced into the specimen, collapse of the rock particles due to wetting was measured. The same stress relaxation technique implemented in FLAC was used to model this behavior. A 10% decrease of the

latest modulus number was calculated in order to reproduce these collapse deformations in the numerical model.

4.6 Discussion of test results

The calculated stress-strain-volume change behavior of the specimens during the stress-controlled tests is summarized in Figure 4-24, and Figure 4-25, along with the experimental data. The elasto-plastic parameters used in these simulations are exactly the same as those calculated from strain-controlled tests as shown in Table 4-4, except for the modulus numbers which changed with both test methods, and durations. The change of modulus numbers related to the duration of stress-controlled test are summarized in Table 4-5. After the water was added into the specimens at different stress states, additional deformations were generated in the samples. Using the proposed algorithms and procedures (i.e. modified stress relaxation), the numerical model calculated these deformations with good precision.

The fact that the same set of parameters, except for the modulus numbers, was implemented in the FLAC to reproduce the entire results of the laboratory, and yet the model was able to capture the behaviors of the tested material with a good precision, shows the versatility of the numerical model in capturing the observed behaviors. Smaller values of modulus numbers were calculated with increasing duration of the stress-controlled tests of the dry material which indicates softer behavior of the specimens over time. These time effects must be considered when choosing the parameters of the model from results of laboratory tests and in the short and long term analysis of real engineering problems.

4.7 Conclusion

The behavior of a compacted assamblage of granite rock particles during the triaxial compression testing was discussed in this chapter with an emphesize on time effects and saturation. Two series of experiments were conducted in strain-controlled and stress-controlled conditions on both dry and saturated samples. A relatively simple constitutive model was also implemented in commercial software FLAC to reproduce the results of the experiments and to capture the stress-strain-volume change behavior observed in the

laboratory. The model was the traditional hyperbolic model coupled with the Mohr-Coulomb failure criteria. The stress relaxation procedures proposed by Escuder et al. (2005) were also modified and implemented in FLAC in order to simulate the deterioration of contact points and deformations which were caused by keeping a constant anisotropic stress over time and augmented by saturation.

The results of the modeling has shown to have good agreements with the labratoray tests. Generally, the strain controlled parameters for dry and wet samples can be used to reproduce the stress-controlled tests or to model the deformations in constant stress condition. Only two of the total nine parameters of the model has shown sensitivity to the test method as well as rate of loading: the elastic modulus number(K_E) and bulk modulus number(K_B) which represent the shear and volumetric rigidity of the material, respectively. These parameters are considered as the key parameters in calculating the time-dependent as well as the collapse deformations due to wetting of the material, using the stress relaxation procedure which requires both dry and saturated parameters.

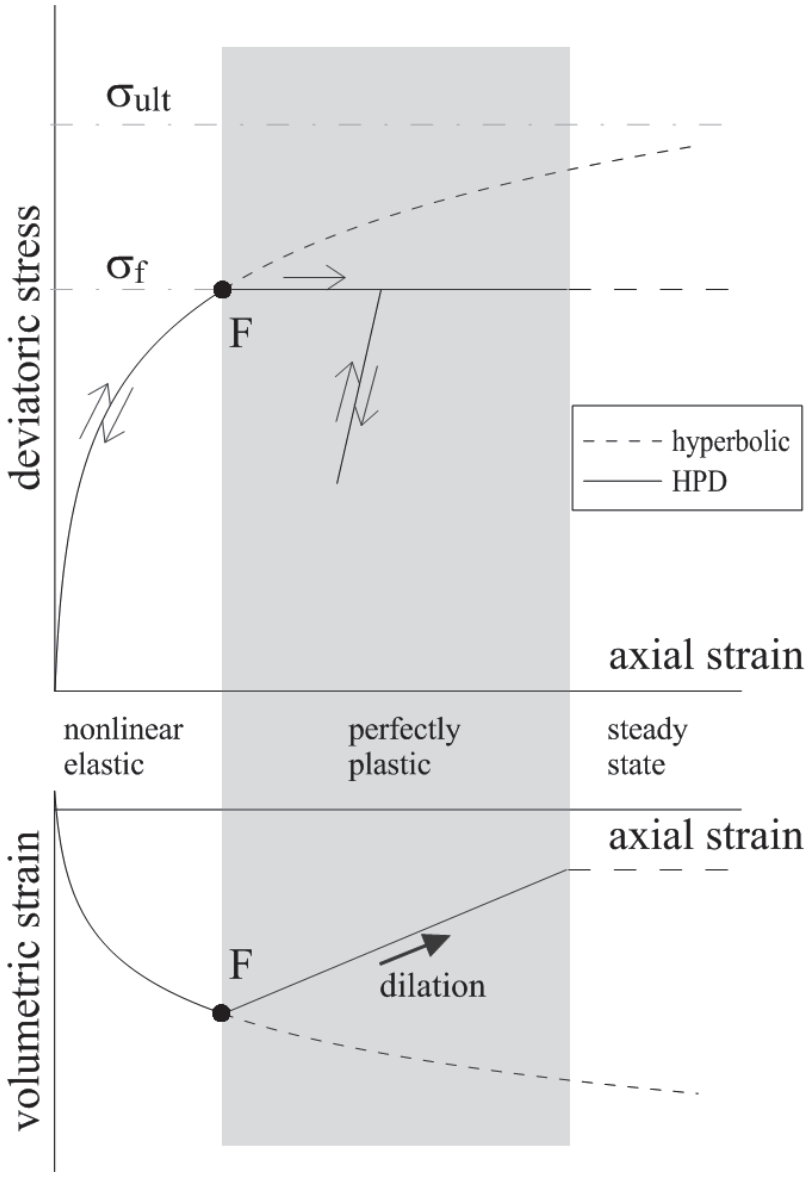

Figure 4-1.Schematic of the implemented constitutive model

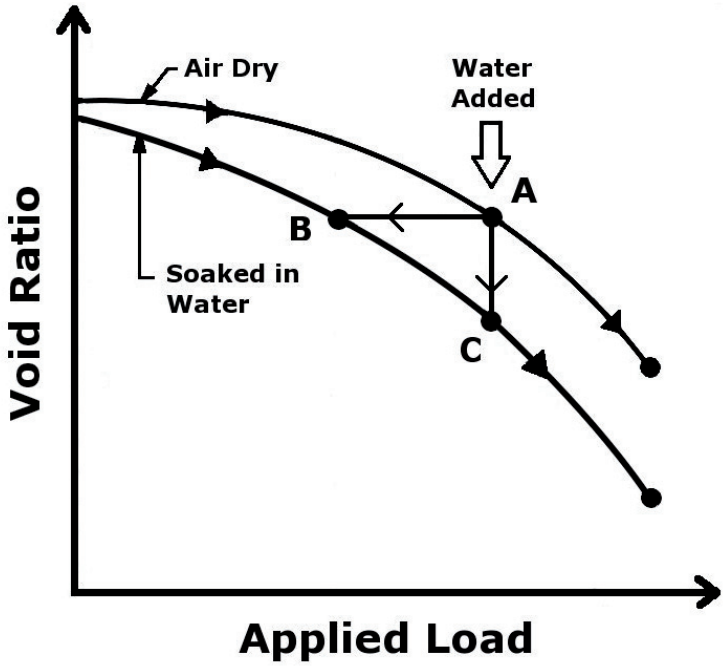

Figure 4-2. Effect of adding water to air-dry specimen at constant axial pressure and at constant volume, in one-dimensional compression test; after Burland (1965)

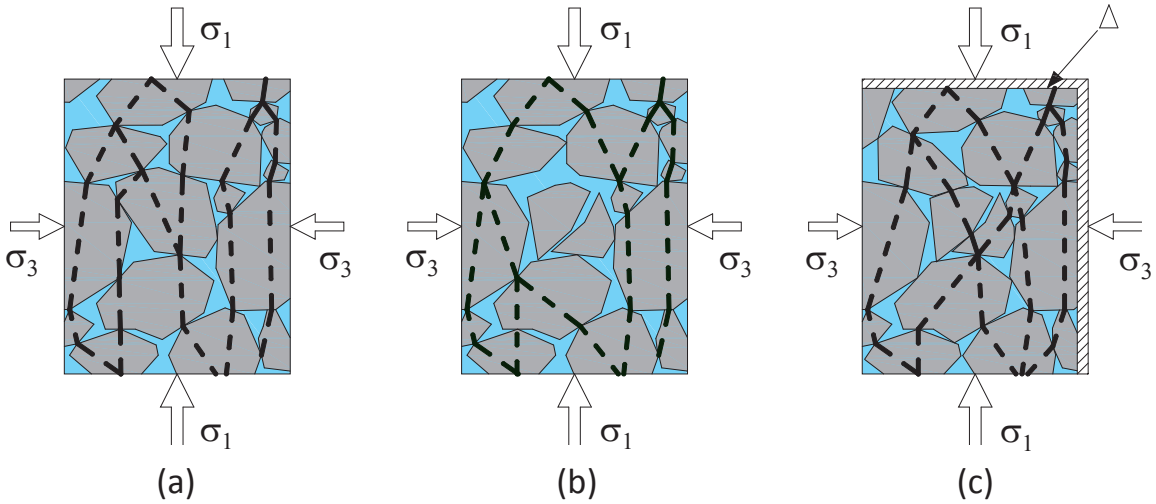

Figure 4-3- Distribution of contact force in an assemblage of rock particles at constant stress condition. (a) Initial equilibrium (b) The disruption of contacts due to breakage of particles (c) redistribution after collapse or creep deformations; reaching a new equilibrium.

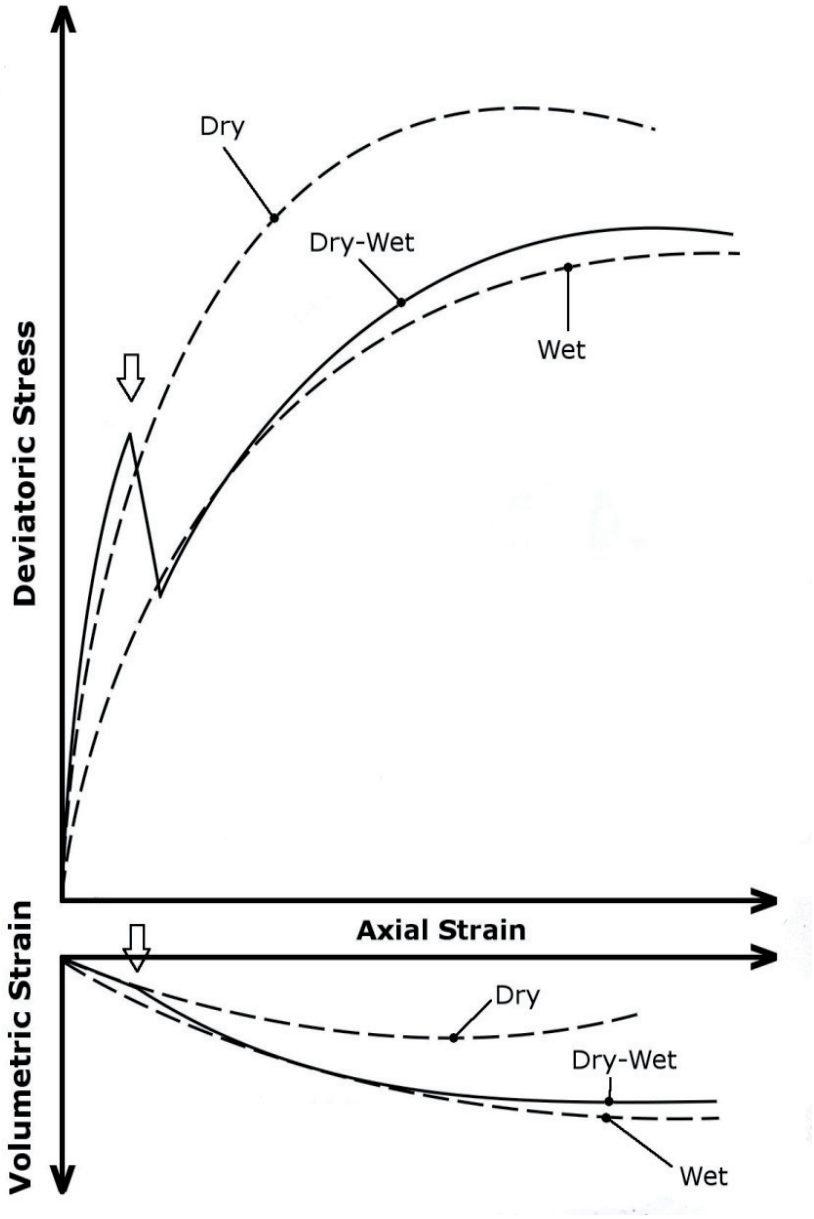

Figure 4-4- Comparison of stress-strain and volume change curves for dry, wet and dry-wet specimens in triaxial compression test; after Nobari and Duncan (1972)

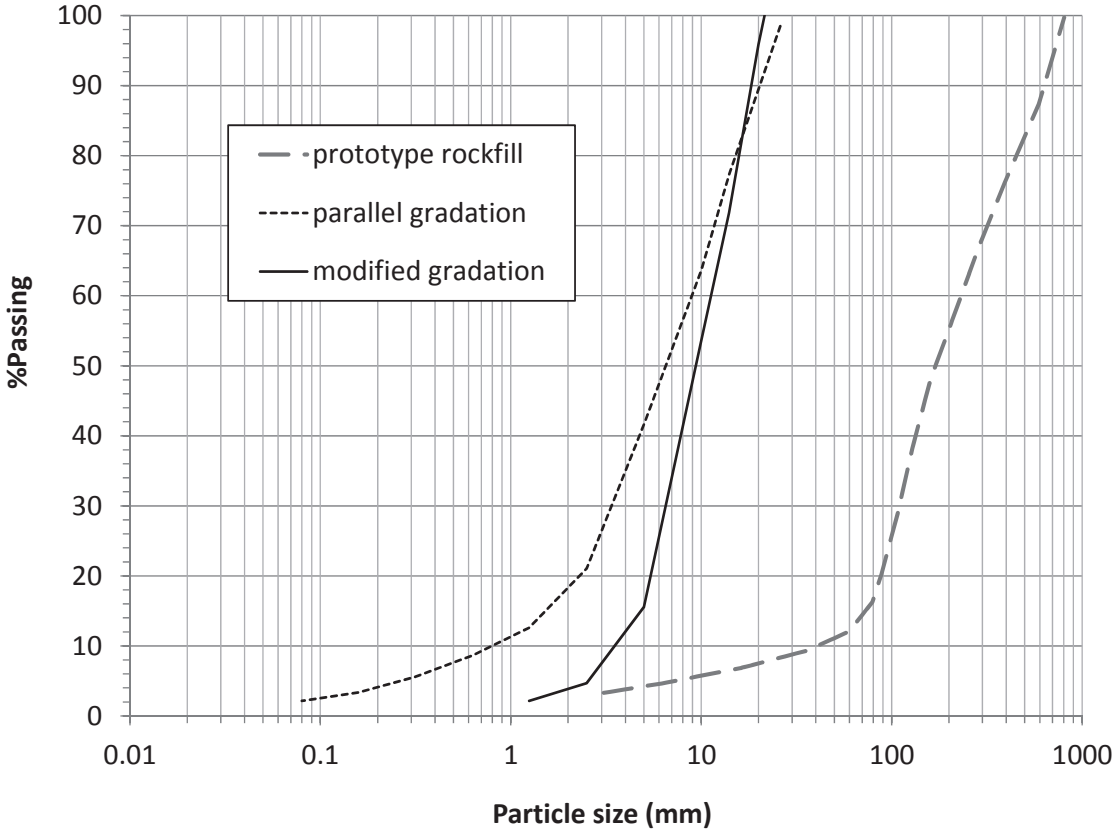

Figure 4-5 – Modified grain size distribution of the triaxial specimens along with the prototype and parallel gradations.

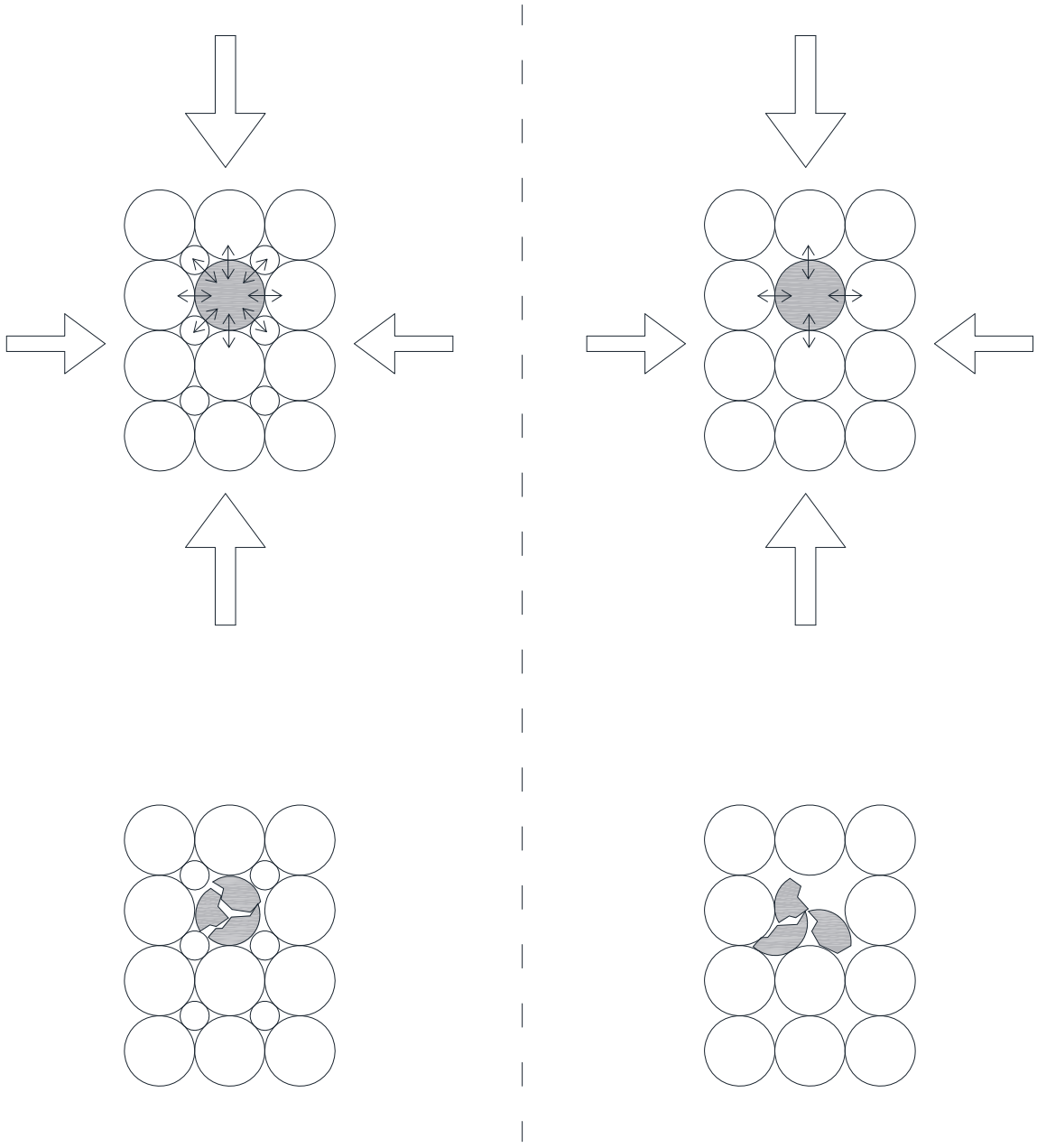

Figure 4-6. Comparison of number of contact points and patterns of breakage of particles in ideal uniform and non-uniform samples.

Figure 4-7- Angular granite grains with different particle sizes used in preparation of the triaxial specimens

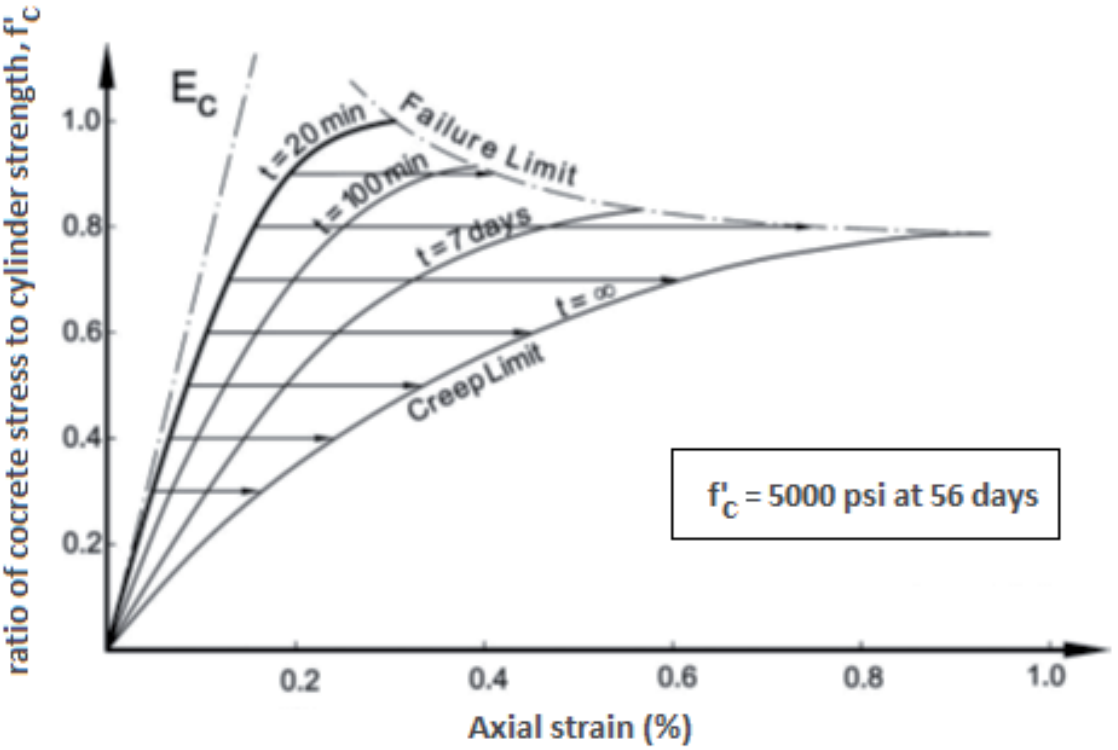

Figure 4-8- Influence of time on strength of concrete specimens; after Rűsch (1960)

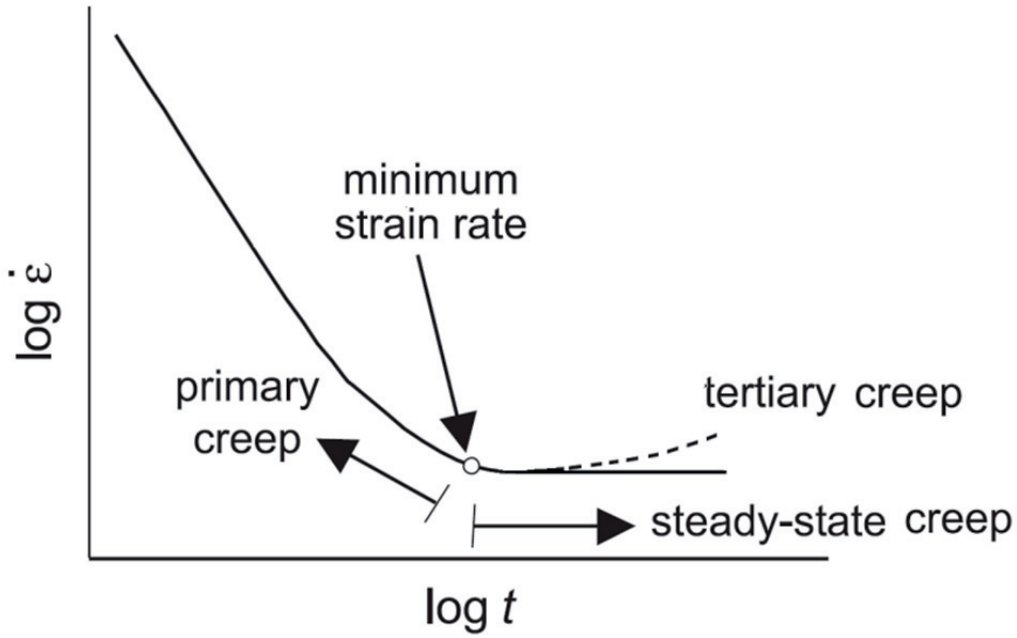

Figure 4-9- Changing strain rate with time during each increment of stress-controlled test; in relation to different stages of creep; after Arenson and Springman (2005)

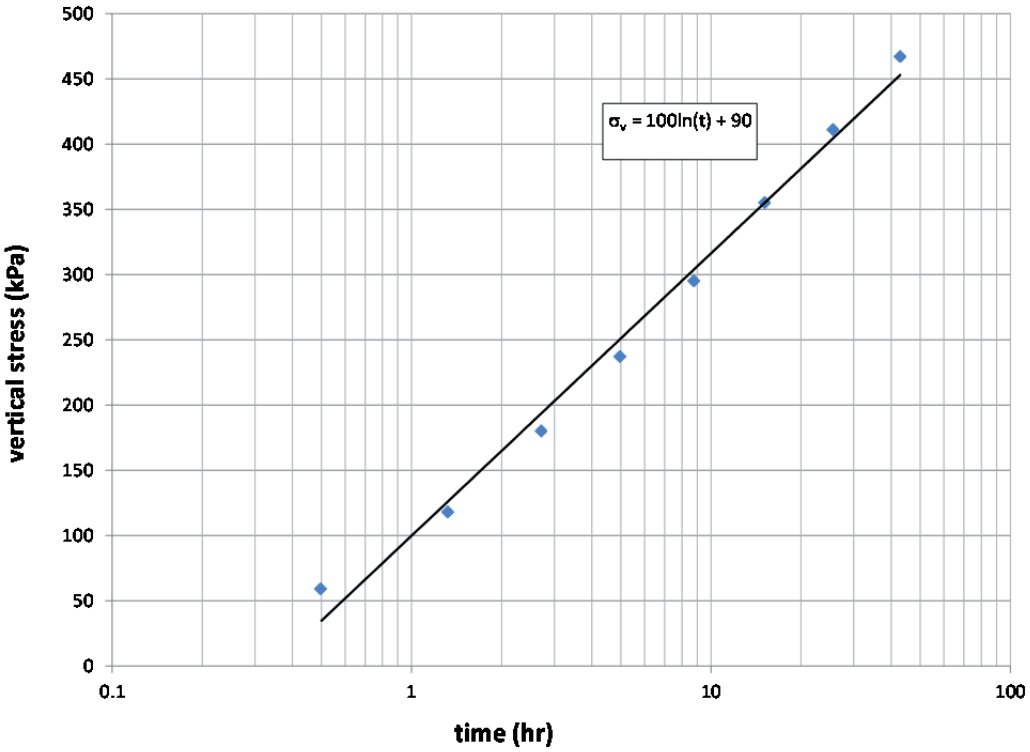

Figure 4-10– Vertical stress increments during the stress controlled triaxial compression tests

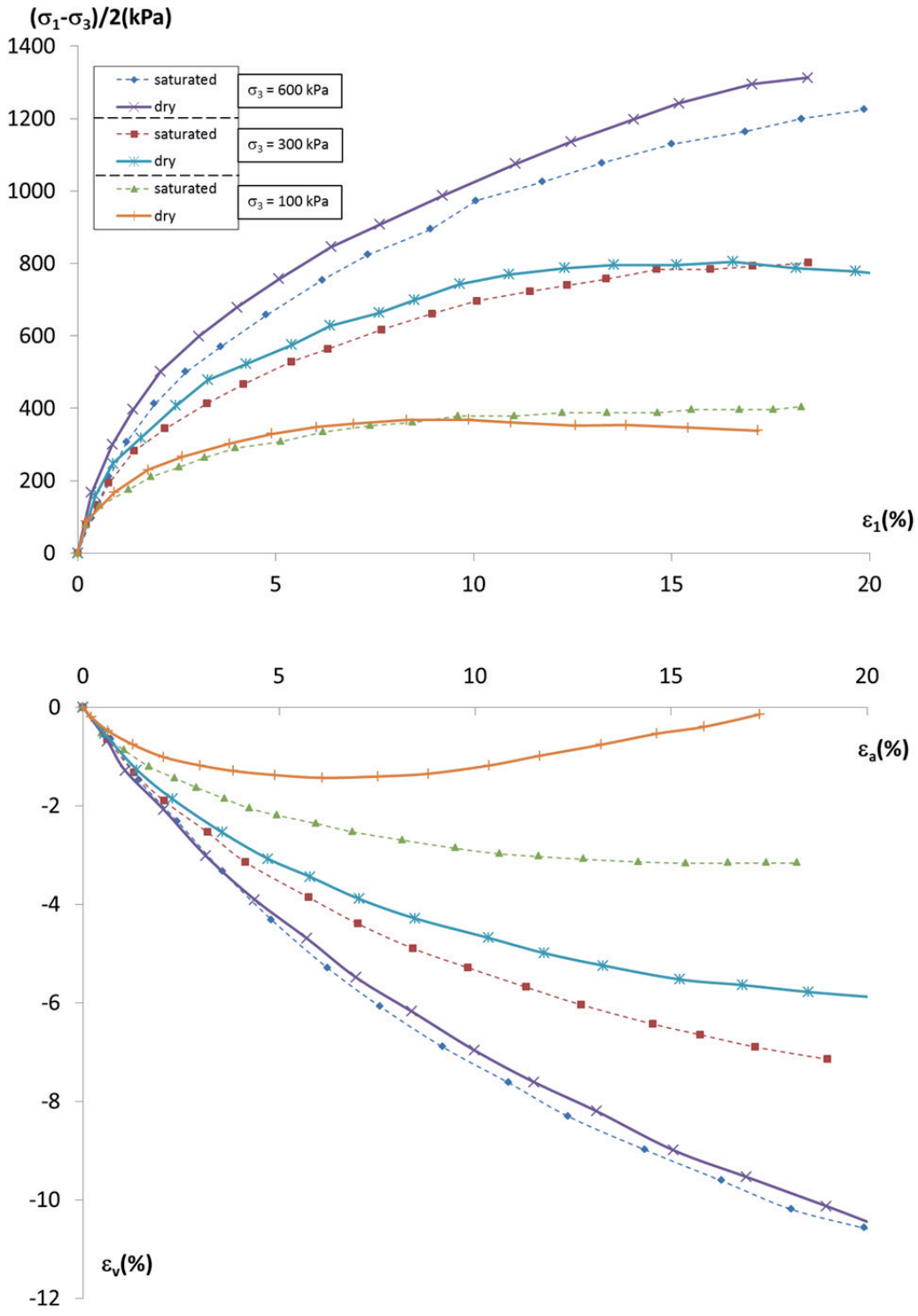

Figure 4-11. Stress-strain and volume change behavior of the specimens in the strain controlled triaxial compression tests

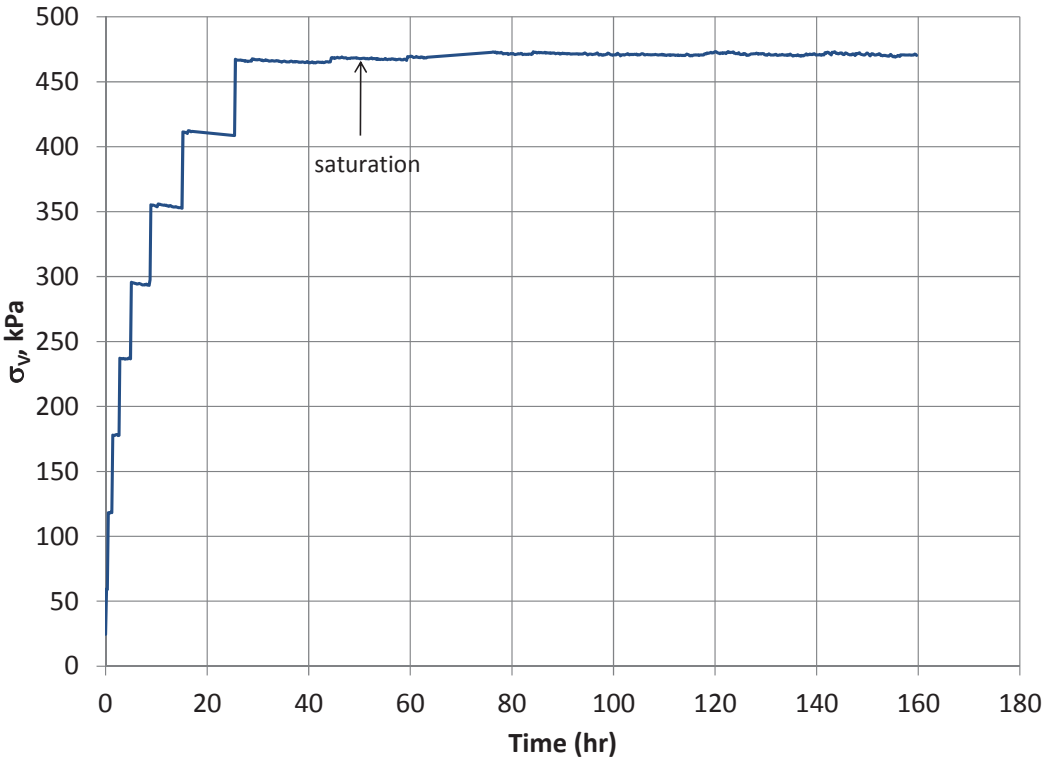

Figure 4-12- Applied vertical stress during the stress controlled triaxial compression test #2

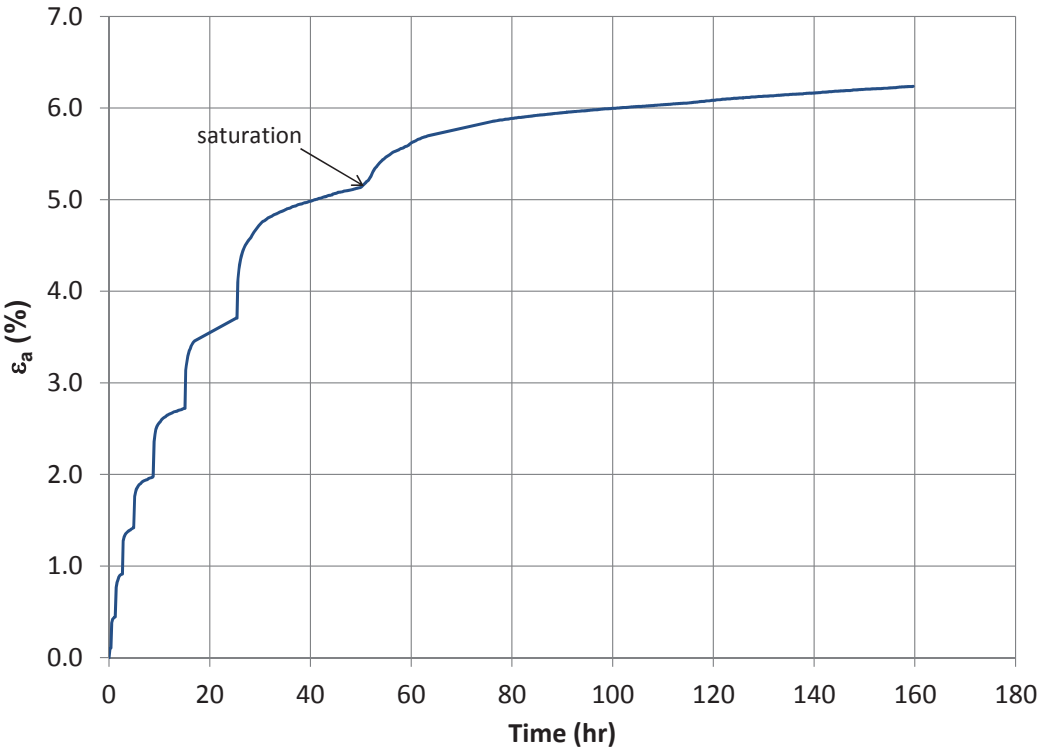

Figure 4-13- Measured axial strain during the stress controlled triaxial compression test #2

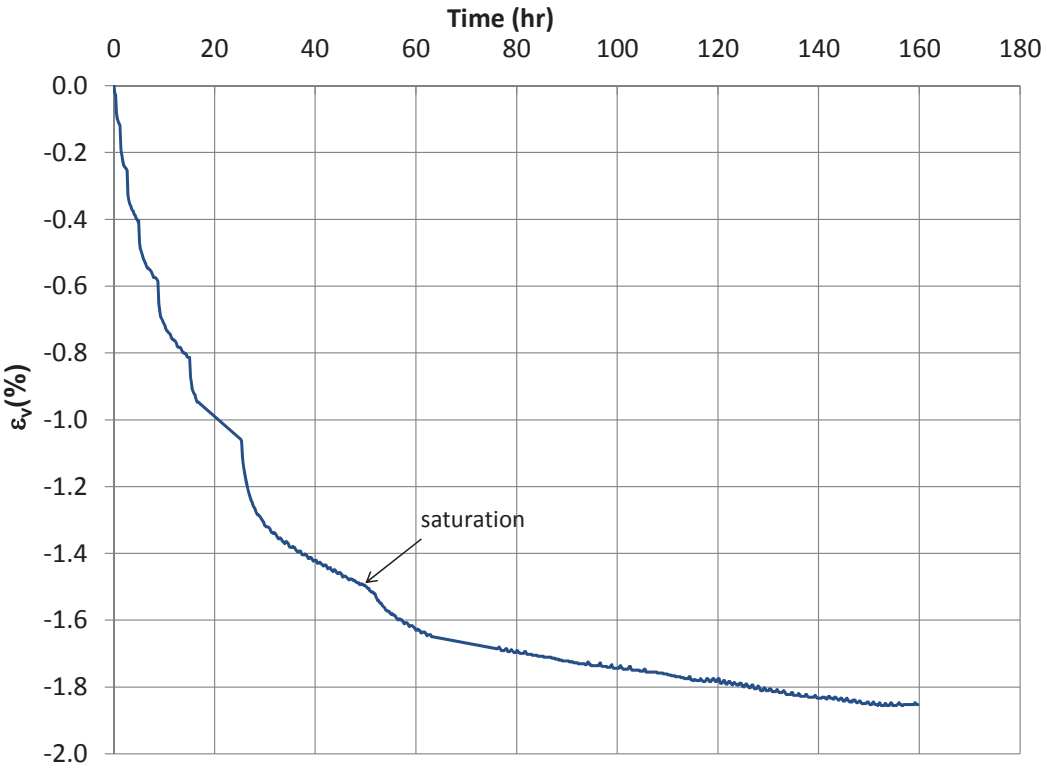

Figure 4-14- Measured volumetric strains during the stress controlled triaxial compression test #2

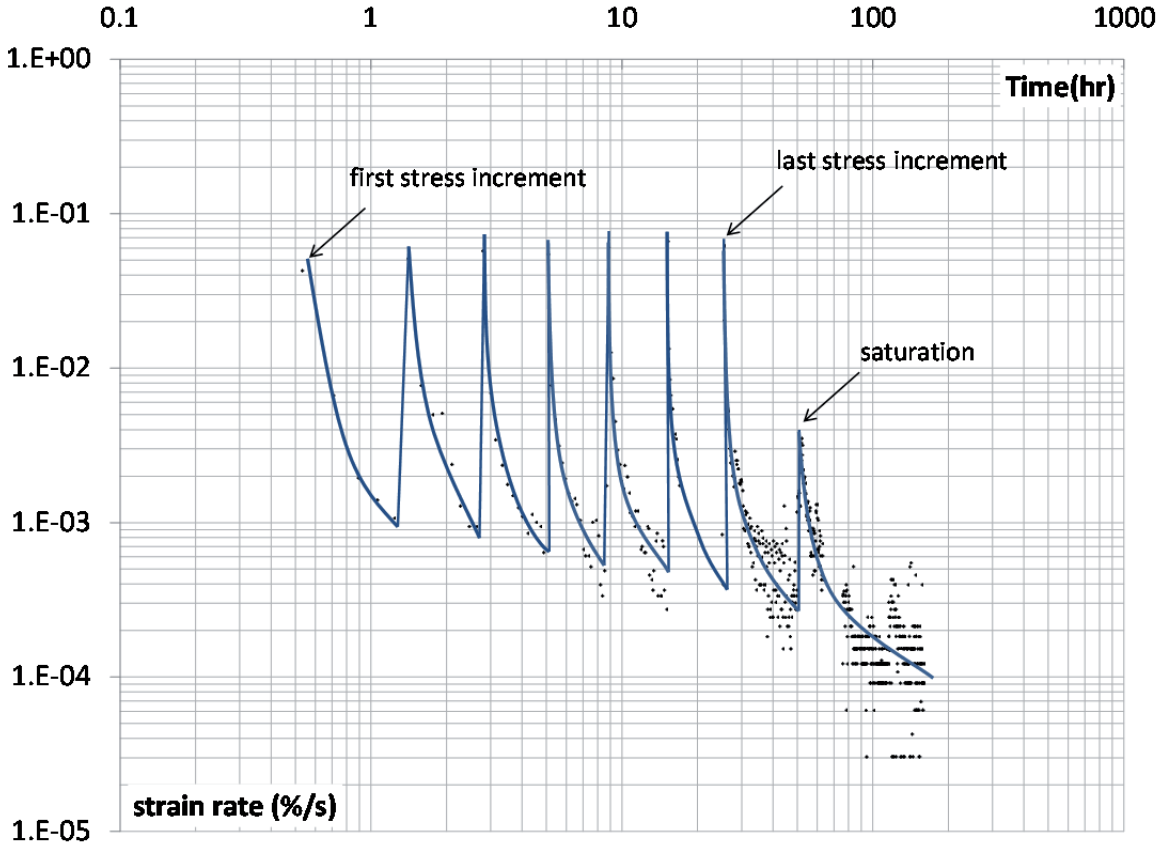

Figure 4-15- Mean axial strain rates during the stress controlled triaxial compression test #2

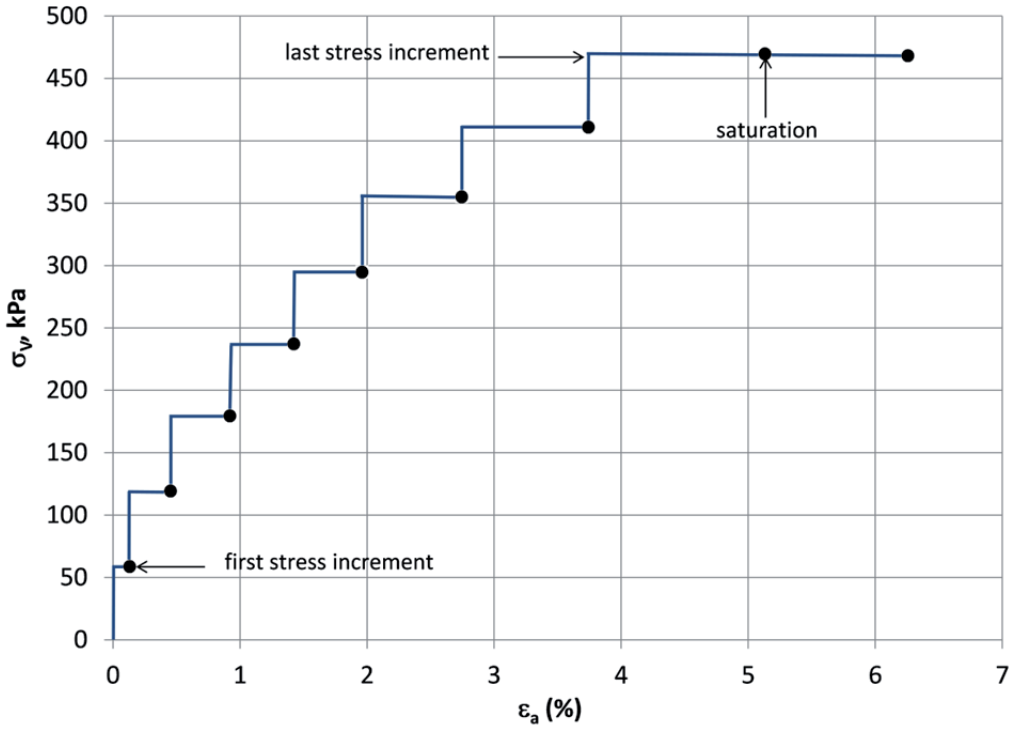

Figure 4-16 – Stress-strain response of the specimen in stress controlled test #2

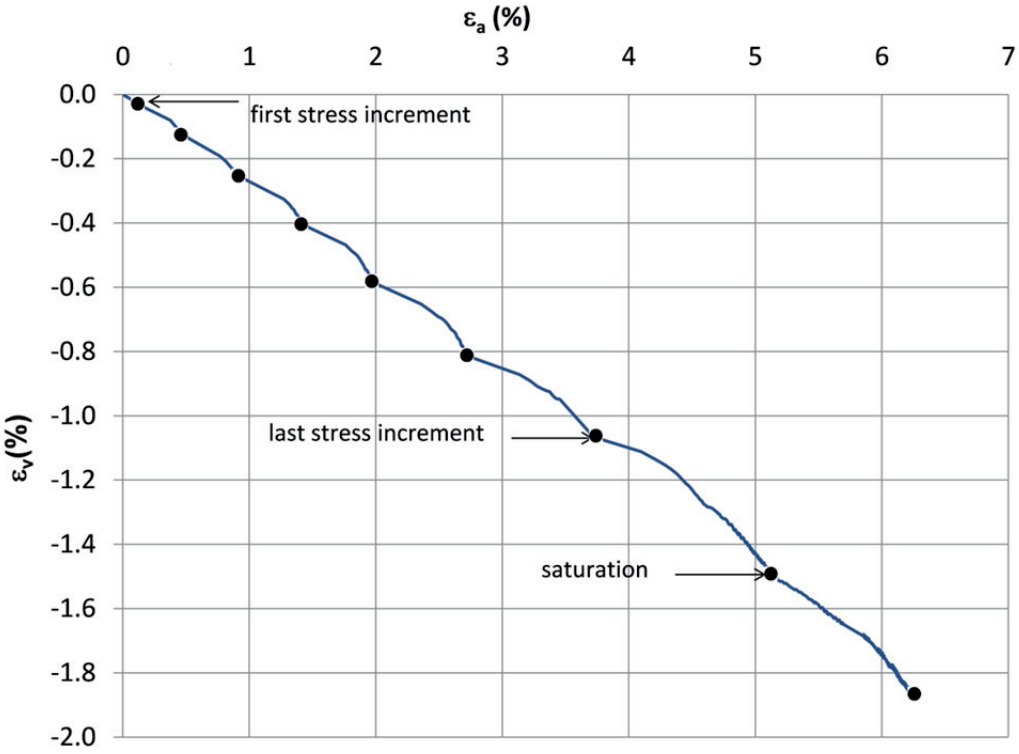

Figure 4-17- Volume change-axial strain response of the specimen in stress controlled test #2

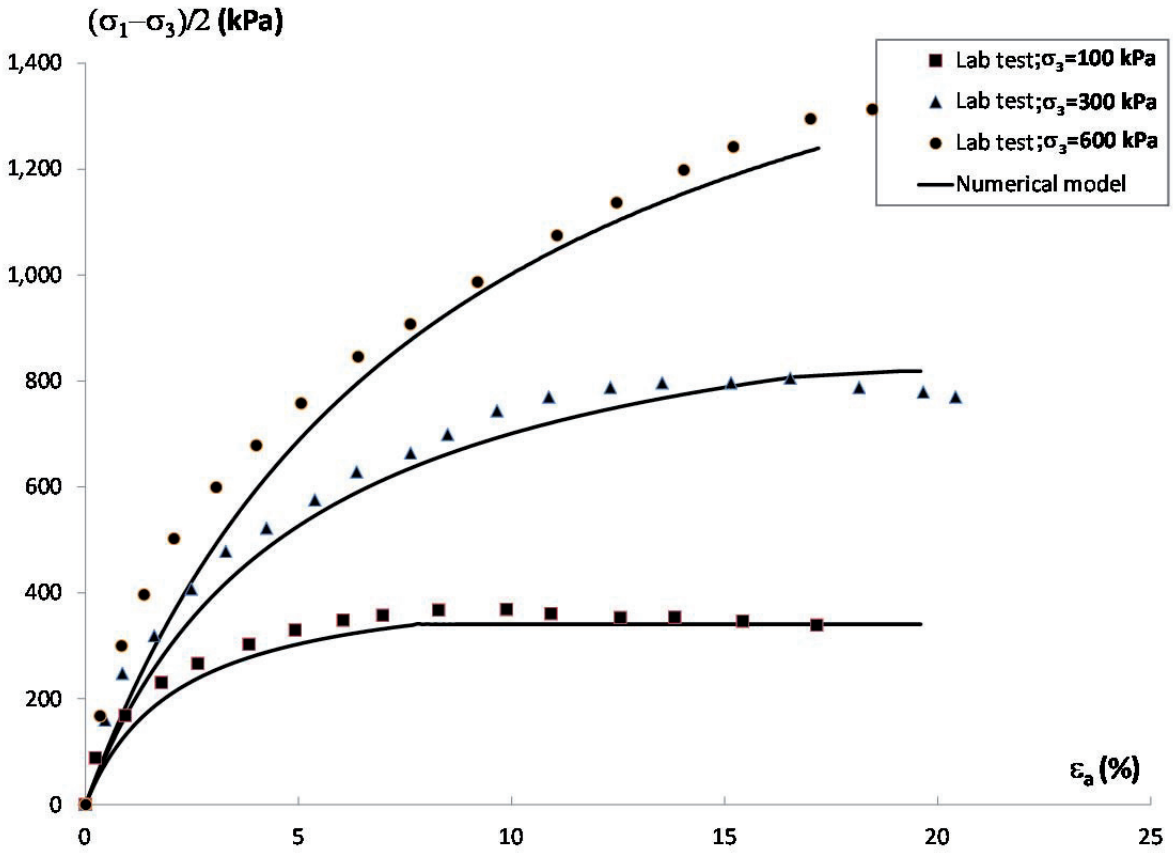

Figure 4-18- Stress-strain behavior of the dry material in strain-controlled tests

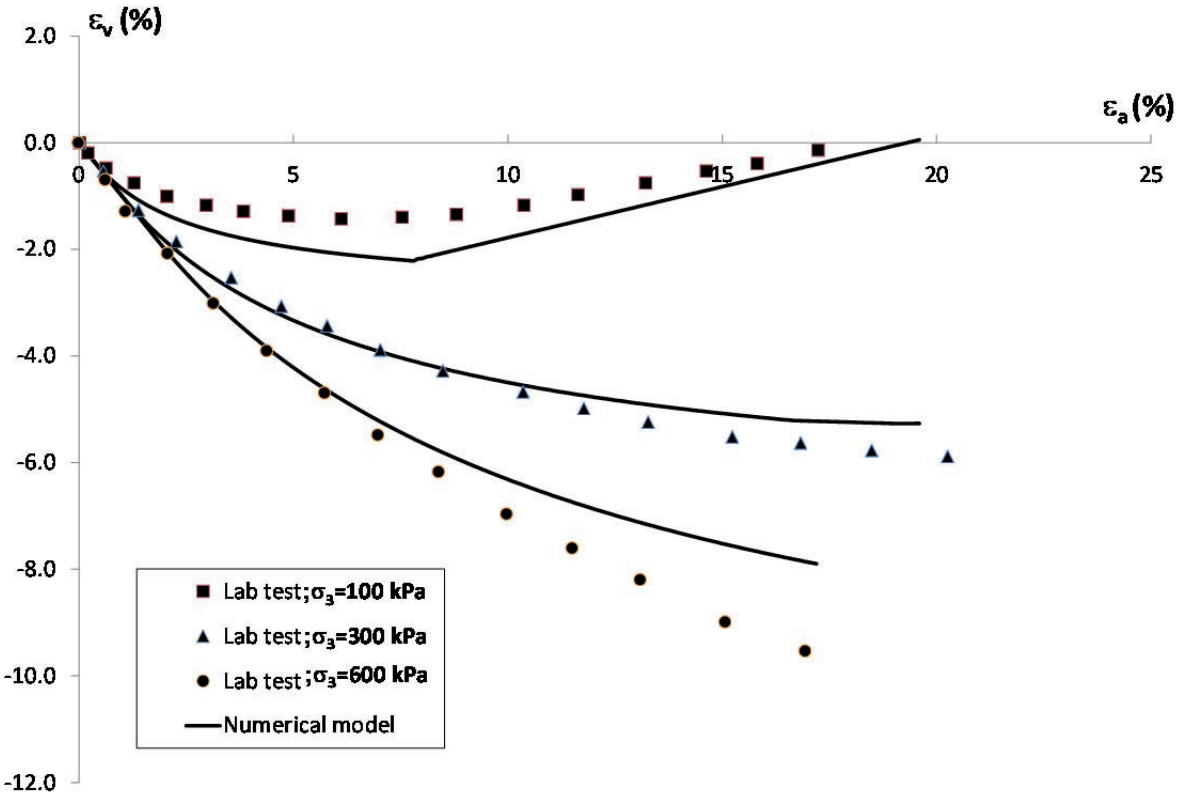

Figure 4-19- Changes of volumetric strain of the dry material in strain-controlled tests

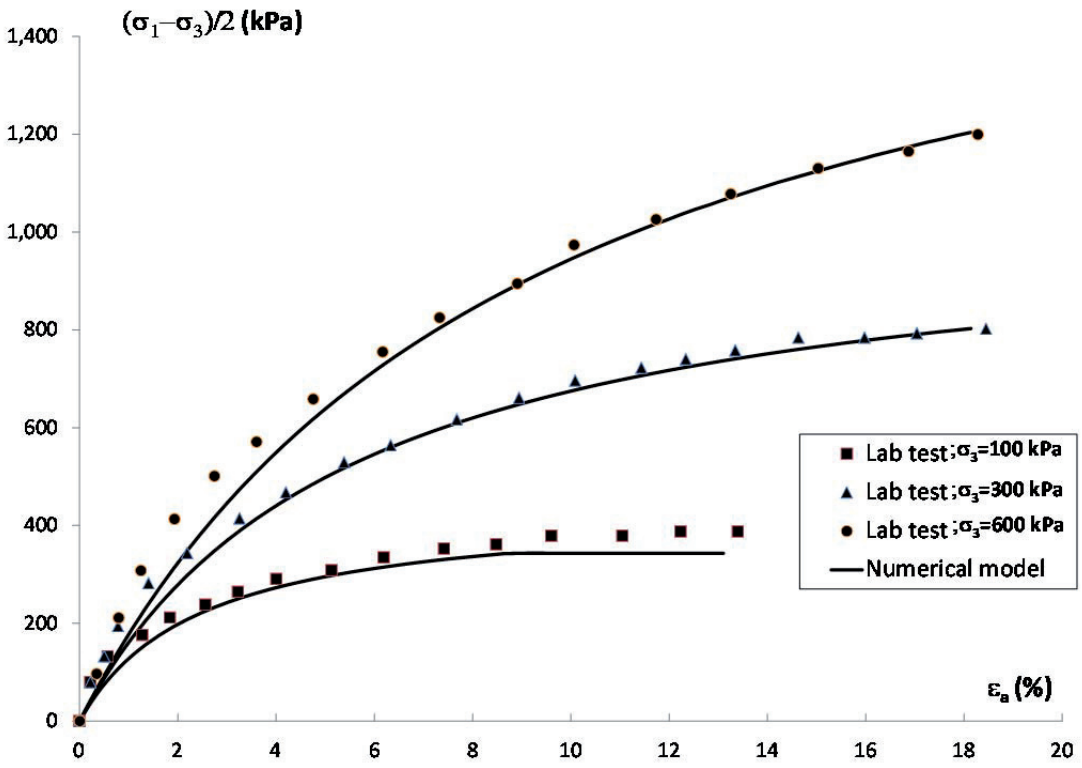

Figure 4-20- Stress-strain behavior of the saturated specimens in strain-controlled tests

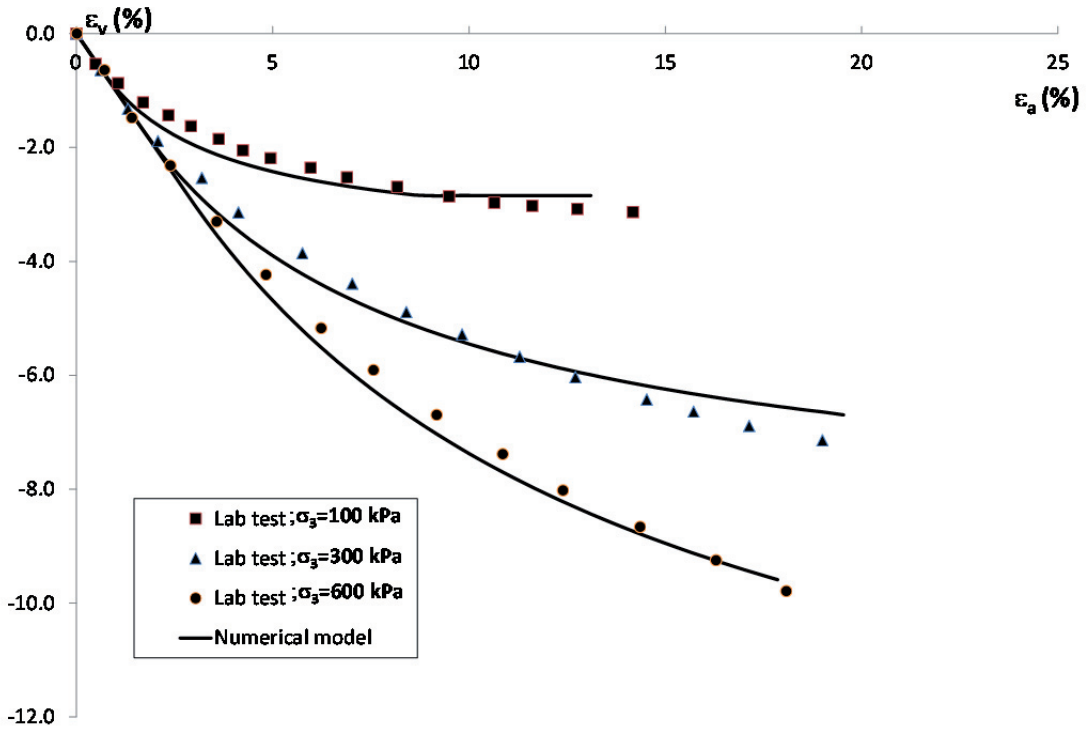

Figure 4-21- Changes of volumetric strain of the saturated specimens in strain-controlled tests

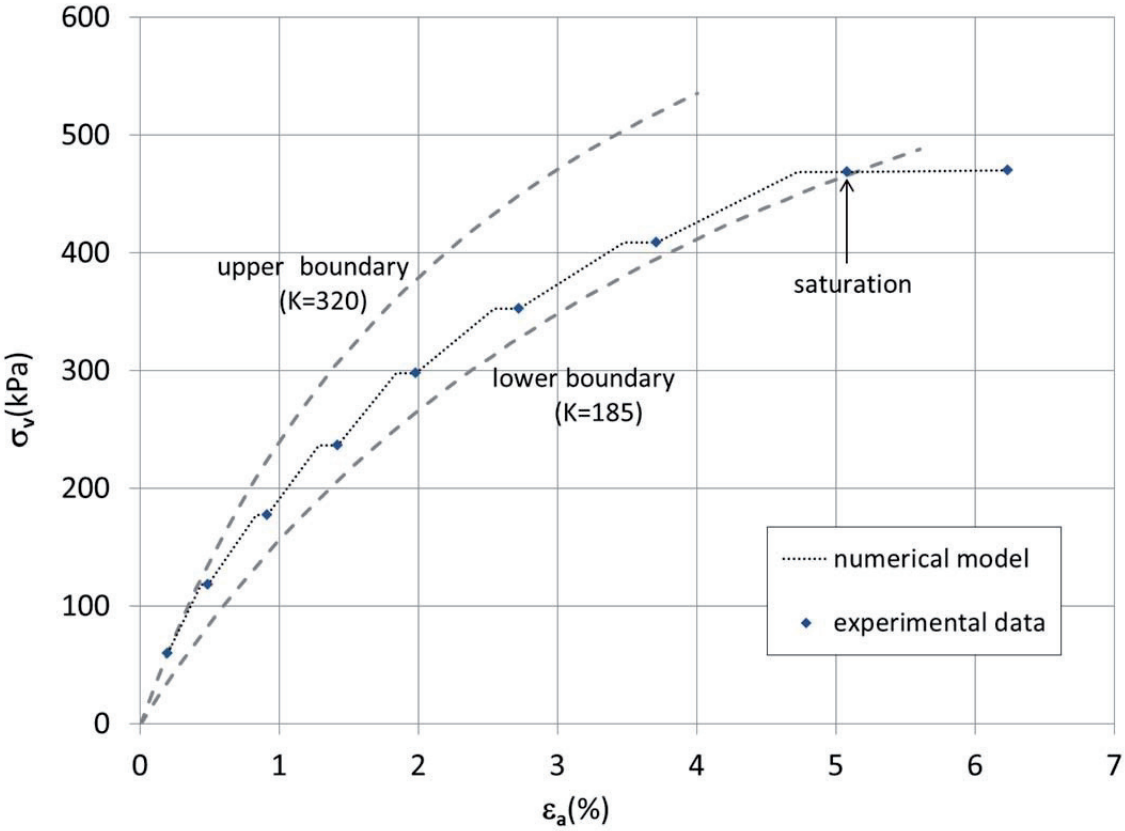

Figure 4-22- Creep components of the dry specimen during the stress controlled test #2 followed by collapse deformations due to the saturation.

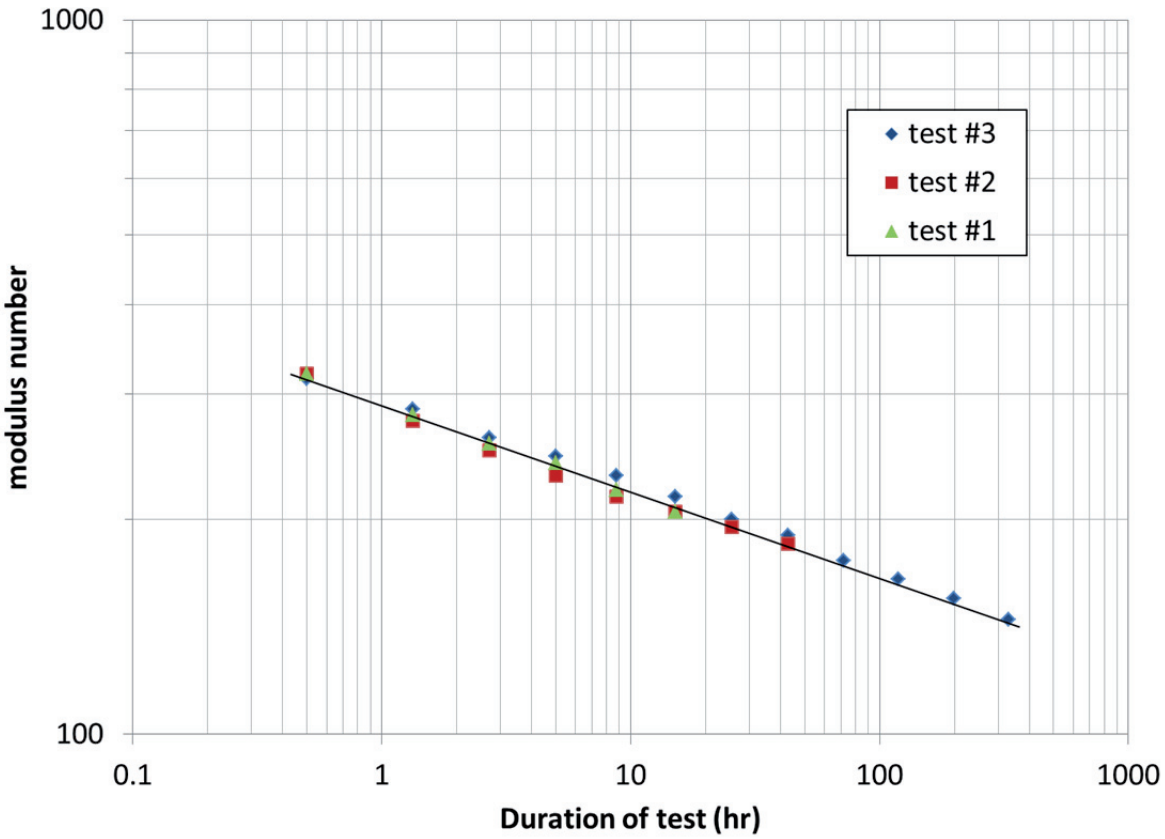

Figure 4-23- Gradual softening of the dry specimens with time during the stress controlled tests

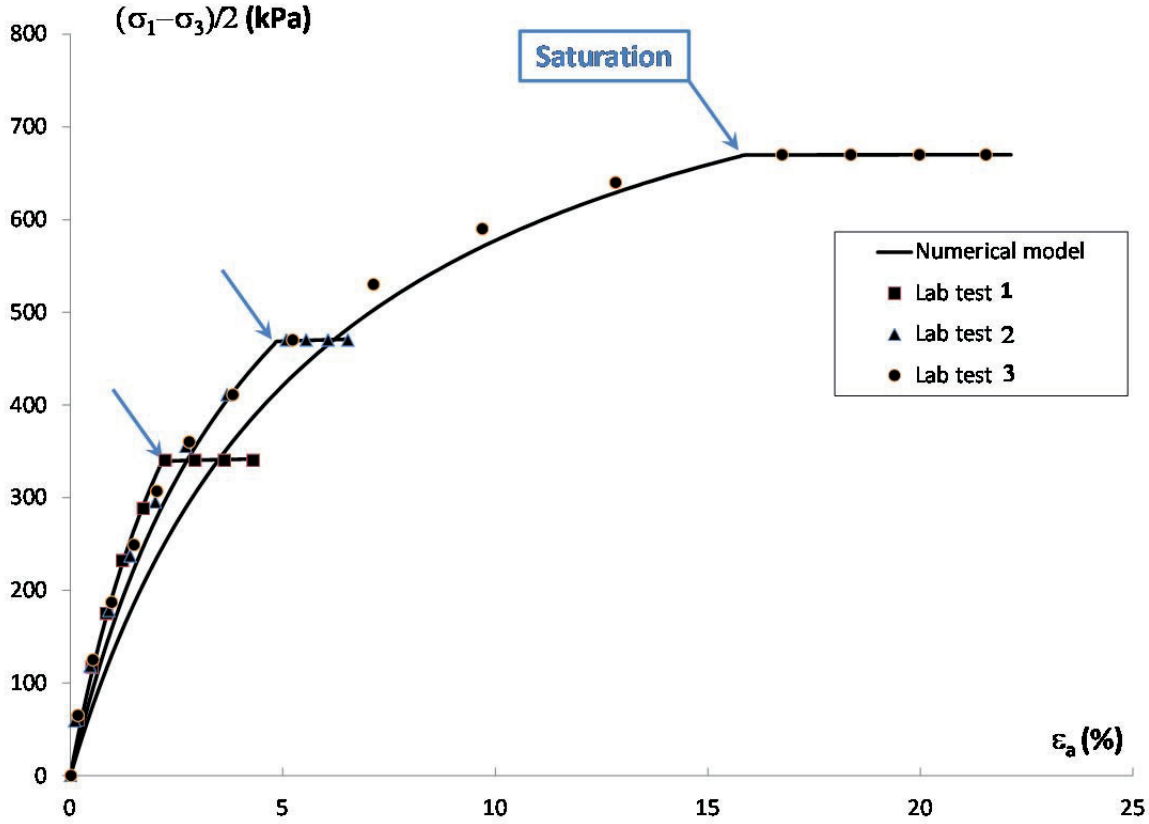

Figure 4-24- Stress-strain relation of the specimens during the stress-controlled tests

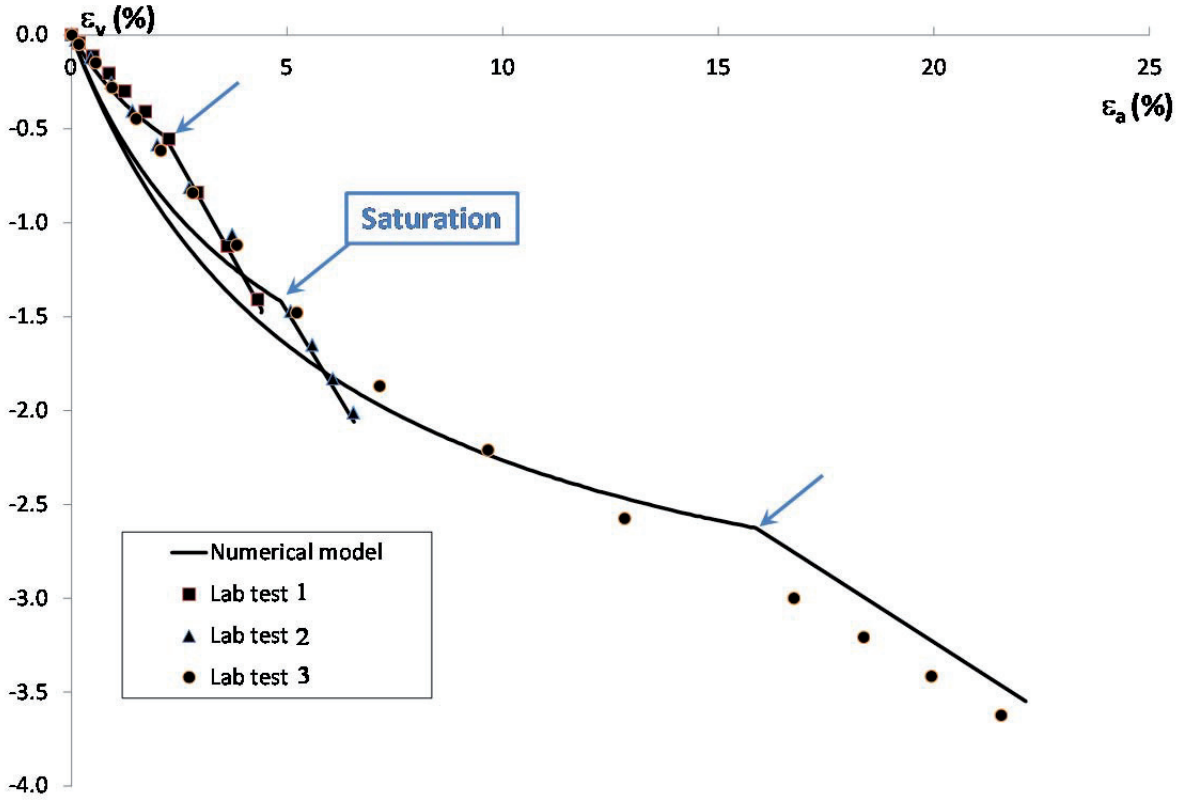

Figure 4-25- Volume change of the specimens during the stress controlled tests

Elastic parameters		Plastic parameters	
K_E	Elastic modulus number	ϕ_0	fiction angle at reference pressure P_a
n	Elastic modulus exponent	$\Delta\phi$	change of friction angle with confining stress
K_B	Bulk modulus number	ψ_0	dilation angle at reference pressure P_a
m	Bulk modulus exponent	$\Delta\psi$	change of friction angle with confining stress
R_f	coefficient to adjust the stress-strain curve (default value=0.7)		

Table 4-1- elasto plastic parameters of the implemented model

confining stress (kPa)	test condition	initial dry density (kg/m^3)	Dry density after (kg/m^3)	strain rate (%/hr)
100	dry	1660	1740	5
	saturated	1660	1770	1
300	dry	1660	1790	5
	saturated	1660	1770	1
600	dry	1660	1810	5
	saturated	1660	1820	1

Table 4-2. Strain-controlled triaxial compression test conditions

test number	dry density after isotropic consolidation* (kg/m^3)	Saturation			
		constant deviatoric stress (kPa)	time span** (hr)	degree of saturation	strain rate at the end of saturation (%/s)
1	1750	340	15-150	93%	5×10^{-5}
2	1730	470	45-160	94%	10^{-4}
3	1740	670	340-600	92%	10^{-4}

*Confining stress of 200 kPa was adopted for all stress controlled tests
**The origin of time was considered at the beginning of the application of the vertical stress

Table 4-3- Stress-controlled triaxial compression test conditions

	Dry material	Wet material
K_E	200	180
n	0.05	0.05
K_B	50	40
m	0	0
R_f	0.73	0.73
$\phi_0(^o)$	41	41
$\Delta\phi(^o)$	8	8
$\psi_0(^o)$	5	0
$\Delta\psi(^o)$	10	10

Table 4-4- calibrated elasto-plastic parameters of the tested material

Test	Duration (hr)	K_E	K_B
1	15	240	210
2	45	190	110
3	340	150	85

Table 4-5- change of modulus numbers related to the duration of stress controlled tests.

5 Numerical modeling of the construction and impoundment stages of LG4 rockfill dam

5.1 Introduction

In the previous chapters, the HPD model (i.e. *hyperbolic* model implemented in FLAC along with components of *plasticity* and *dilation* from Mohr-Coulomb failure criteria) was presented and shown to be capable of capturing the key characteristics of compacted rock particles as observed in the large scale triaxial tests. The nine parameters of the model, as shown in Table 5-1, are relatively easy to calibrate for the dry material using triaxial test results or alternatively using the existing database in the literature for both hyperbolic model and Mohr-Coulomb failure criteria. It was also shown that wetting of the material resulted in reductions of both stiffness coefficients (K_E and K_B) and reference dilation angle (ψ_0); all other parameters were almost unchanged for a given material regardless of the degree of saturation. The stress relaxation technique can be used to numerically reproduce the collapse phenomenon resulting from wetting of a granular material (Escuder et al., 2005; Nobari and Duncan, 1972). New algorithms were also proposed to solve the system of equations used in the stress relaxation technique in order to improve the stability of the numerical model. The HPD model and the procedures to simulate the wetting collapse were successfully validated using triaxial tests as described in the previous chapters.

In this chapter, the constitutive model and the procedures are applied to simulate the construction stage and impoundment of LG4, a dam constructed in Quebec, Canada. The instrumentation data is compared with the results of the modeling and the behavior of the dam is discussed using the numerical model and the insitu recordings.

5.2 Constitutive model

The HPD constitutive model which is the hyperbolic model coupled with Mohr-Coulomb failure criteria and a non-associated flow rule to consider dilatancy was explained extensively in the previous chapters along with procedures for simulating the collapse of rockfill material due to wetting. The constitutive model and the proposed algorithms were validated using the results of laboratory tests on compacted assemblages of rock particles. In this section, a brief description is given of the different parameters of the model and the post failure behavior which is based on the Mohr-Coulomb failure criteria.

There are total of nine parameters in this model: four parameters reflecting the plastic response (i.e. irreversible deformations and shear induced volumetric changes); and five parameters reflecting the nonlinear stress-dependent elastic behavior. The plastic parameters are used to define the stress-dependent yield and potential functions. The elastic parameters are used to calculate the two tangent elastic modulus of the hyperbolic model (i.e. Young's modulus E and bulk modulus K) in the generalized Hooke's law of the following form:

$$\begin{Bmatrix} \Delta\sigma_x \\ \Delta\sigma_y \\ \Delta\tau_{xy} \end{Bmatrix} = \frac{3K}{9K-E} \begin{bmatrix} (3K+E) & (3K-E) & 0 \\ (3K-E) & (3K+E) & 0 \\ 0 & 0 & E \end{bmatrix} \begin{Bmatrix} \Delta\varepsilon_x \\ \Delta\varepsilon_y \\ \Delta\gamma_{xy} \end{Bmatrix} \qquad \textit{[Eq. 5-1]}$$

In the theory of elasticity there are total of four parameters. The two other parameters which are Poisson's ratio ν and shear stiffness G are not independent variables but related to the above hyperbolic elastic parameters (E and K). As failure envelope is reached, the formulation of the constitutive model switches to the Mohr-Coulomb model with post-failure values for elastic modulus which are calculated using the following equations:

$$E_f = K_E \times \left(\frac{\sigma_3}{P_a}\right)^n \qquad \textit{[Eq. 5-2]}$$

$$K_f = K_B \times \left(\frac{\sigma_3}{P_a}\right)^m \qquad \textit{[Eq. 5-3]}$$

Where K_E and K_B are modulus numbers; n and m are modulus exponents; σ_3 is the minimum principal stress; and P_a is the reference pressure. Unless the initial elastic parameters of the hyperbolic model, both of these post failure elastic parameters are independent of the shear stress. These elastic parameters are dependent to the minimum stress (σ_3) and characterise the behavior of the material in unloading and reloading loops after the failure envelope is reached, as shown in the second part of the schematic of model in Figure 3-2. The post failure parameters also consist of the stress-dependent friction angle (φ) and dilation angle (ψ) as:

$$\varphi = \varphi_0 - \Delta\varphi log\left(\frac{\sigma_3}{P_a}\right) \quad \textit{[Eq. 5-4]}$$

$$\psi = \psi_0 - \Delta\psi log\left(\frac{\sigma_3}{P_a}\right) \quad \textit{[Eq. 5-5]}$$

These parameters are required in order to define the yield and potential functions of the Mohr-Coulomb type in the following forms:

$$f^s = \sigma_1 - \sigma_3\left(\frac{1 + sin\varphi}{1 - sin\varphi}\right) \quad \textit{[Eq. 5-6]}$$

$$g^s = \sigma_1 - \sigma_3\left(\frac{1 + sin\psi}{1 - sin\psi}\right) \quad \textit{[Eq. 5-7]}$$

These two functions have similar forms but different parameters. The smaller values of the dilation angle enable the magnitude of the incremental plastic volumetric strain to be restricted. Moreover, the dependency of dilation angle to the confining stress and degree of saturation are important characteristics of compacted assemblages of rock particles, as demonstrated in previous chapters.

5.3 LG4 dam

La Grande 4 (LG4) main dam, situated 460 km from the mouth of the La Grande River in the James Bay Territory, is the second largest structure of the La Grande Complex of James Bay hydroelectric development located in northern Quebec, Canada. The La Grande Complex covers 176,000 km^2. LG4 main dam has maximum height of 125 m, crest length is about 4 km and has fill volume of about 19,000,000 m^3 (Paré et al., 1984). LG4 main dam is a zoned earth-rock fill with central till core protected by large and well compacted sand and gravel filter and transition zones. The dam was constructed almost entirely on bedrock composed of granite and gneiss of Precambrian age. The typical cross-section of LG4 main dam is shown in Figure 5-1. The geomaterials used for various embankment dams of the La Grande Complex were relatively homogeneous. The grain size distributions of the material used in different zones and the specifications used for placement of these materials are shown in Figure 5-2 and Table 5-2, respectively.

During the construction of the La Grande Complex, a comprehensive instrumentation was installed in dikes and embankment dams to measure deformations, stresses, and pore pressures. The instrumentations consist of inclinometers, settlement cells, linear extensometers, surface monuments, electrical and stand-pipe piezometers, total pressure cells, and weirs to measure seepage flow. These allowed monitoring the behavior of the embankment during the construction and the filling up the reservoir, as closely as possible. In the current study, the instrumentation data which was published in several previous papers was used to study the behavior and to compare with numerical results. The reliability of these instrumentations and methods of interpretation of field data are not discussed here.

5.4 Parameters of the model

Previous researchers have implemented the hyperbolic model into finite element codes to simulate the construction and filling of the reservoir of this dam. It was shown that although the trends indicated by numerical modeling analysis were generally confirmed by instrumentation data, final results were very sensitive to the input values used in the hyperbolic model. Therefore, one of the most important aspects in the past researches was to determine the exact values of the parameters to represent the material used in the construction of the dam. Marsal (1967) performed large scale triaxial tests of a rockfill material similar to that of the LG4 dam (Figure 5-3). The results of triaxial tests conducted on samples from the filter and transition zones are also shown in Figure 5-4 (Massiéra et al., 1989). These test data were used to estimate the parameters of the models in the past.

A first analysis of the dam behavior at the end of construction was presented by Garneau et al. (1982). A more comprehensive review of the instrumentation data, including those of the filling up the reservoir was made by Verma et al. (1985). Post-construction analyses clearly showed that studies made at the design stage had underestimated the elastic modulus of the till core, the granular filters, and the granular shell (Massiéra et al., 1989); resulting in excessive settlement predictions. With a review of the data of deformations obtained in situ, Boncompain and Massiéra (1991) concluded that the main reason for this underestimation of modulus was the fact that model parameters were

extracted from saturated triaxial tests, while in the real site the situation was much different during construction. A new evaluation of parameters was done by Massiéra et al. (1999). They performed the oedometric compression tests for the till core and for the sand and gravel of filters and transitions on partially saturated samples. They also recommended the values from a report from Norwegian Geotechnical Institute for the shell of the LG4 dam (NGI, 1987).

In Table 5-3, the evolution of the parameters of the hyperbolic model for LG4 dam as proposed by the above mentioned researchers in the past years is shown. The set of parameter in the first column does not have the coefficients to define the Bulk modulus (i.e K_B and m) because in the classic hyperbolic model, proposed by Duncan and Chang (1970), the Poisson's ratio (instead of bulk modulus) was related to the stress level which did not represent the behavior of the material in high pressures and was later modified by Duncan et al. (1980a). The second column refers to the set of parameters proposed by Massiéra et al. (1989) which overestimated the compressibility of the material, resulting in excessive settlement predictions. These parameters were originally estimated before the dam was constructed and correspond to a type A prediction (i.e. a prediction which was made before the fact, according to Lambe's classification). The third column refers to the set of parameters utilized by Szostak-Chrzanowski and Massiéra (2004) which were modified in order to produce the same deformations as recorded in the field, in a type C prediction (i.e. a prediction which was made after the construction of the dam). Table 5-4 summarizes the parameters of the elasto-plastic model (i.e. HPD model) used in the current study of the LG4 dam. These parameters are almost identical with those proposed by Szostak-Chrzanowski and Massiéra (2004) but plasticity and dilative behavior were also introduced.

Figure 5-5 compares the stress-strain relation of different constitutive behaviors of the rockfill material of the shell of LG4 dam in virtual triaxial compression tests, generated numerically at reference confining pressure of $\sigma_3 = 100\, kPa$. In this figure, the soft elastic behavior refers to the set of parameters with overestimated compressibility of the material, while the rigid elastic behavior refers to the modified set of parameters to reproduce the same patterns of deformation as recorded in the field. Szostak-

Chrzanowski and Massiéra (2004) derived the latter set of parameters from the shell of Storvatn dam, a rockfill dam with asphaltic core constructed in Norway, which used a higher compaction energy than in LG4 dam. In other words, the post-construction model increased the rigidity of the material in order to produce the same deformation patterns as recorded in the field. Regarding the conducted triaxial tests as shown in Figure 5-3 and Figure 5-4, the material used in the construction of the LG4 dam demonstrated dilative behavior and should be considered in the constitutive model in order to correctly represent the characteristics of the construction material as shown in Table 5-4 and Figure 5-5.

5.5 Analysis of the construction stage

A two-dimensional plain strain finite difference model was developed from the section of the dam with maximum height, as shown in Figure 5-6. This section was chosen because it has the maximum deformation and stresses and has the most critical condition both during construction and impoundment. The construction stage was simulated using the multi-stage modeling technique meaning that the placement of the material was done by placing twenty horizontal layers. By increasing the number of layers, the height of the elements will be reduced and the behavior of the model will be closer to the real dam. Ideally the height of the elements should be equal to the real height of layers in construction stage. Each layer consisted of the five zones of the dam: The till core at the center protected by two transition zones (filters) and two zones of rockfill shell. The model parameters assigned to the elements of each zone are those shown in Table 4. Considering the relatively high rigidity of the bedrock foundation, the displacements of the bottom nodes of the dam were fixed.

The settlement contours of the elements of the dam are shown in Figure 5-7. The general trends of the displacements are similar to the results of previous simulations based on the elastic hyperbolic models performed by Szostak-Chrzanowski and Massiéra (2004) using rigid parameters and by Garneau et al. (1982) considering soft elastic behavior. Figure 5-8 compares the results of numerical modeling using different sets of parameters along with the measured values from the installed inclinometers at the center of the core of the dam. The maximum predicted settlement on the axis of the dam using the current

elasto-plastic model was about 24 cm which was slightly more than the measured 20 cm. The influence of the introduction of plasticity in the behavior of the LG4 dam is obvious in this figure which helps to better understand the behavior of the dam.

The overestimation of core settlements in the current study was a result of introducing the plastic behavior while maintaining the same set of elastic parameters for till core and filter zones and reducing the rigidity of the elements of the shell of the dam as shown in Figure 5-5. The dam zones which underwent plastic flow are shown in Figure 5-9. The concentration of plastic regions (i.e. regions containing elements which suffered plastic flow) was on the interfaces of adjacent zones, as well as small regions inside the filter/transition zones. Although the existence of these regions increased slightly the amount of the predicted settlements of the core, but the dilative behavior of yielded elements after the failure and the confinement provided by surrounding elements, prevent them to suffer very large displacements. The propagation of plastic regions was limited because of the relatively high rigidity of the material used in the construction of filter zones. If weaker material was used in these zones (e.g. lower compaction effort or inappropriate grain size distribution), localisation of plastic regions could have produced much larger displacements and eventually the local failure and fracture inside the body of the dam would have been expected.

The contours of Young's modulus at the end of construction of LG4 dam are shown in Figure 5-10. The value of the elastic modulus of each element depends on the material properties as well as the stress path of that particular element. The multi-stage modeling is important in order to follow the same stress path as in the field and to generate the actual stress state, secant modulus and the pattern of deformation for each element and the whole dam. The dashed line in this figure encompasses a relatively rigid area which with the support of the protecting shells and the solid bedrock foundation bore the weight of the softer upper portion of the dam resulting in very small settlements of the core, limited to less than 0.2 percent of the height of the dam.

Vertical stress contours of the dam at the end of construction are shown in Figure 5-11. The arching effect is easily observed in this figure. The placement of pressure cells in the

body of the dam is also shown. The measured stresses at the elevation of the foundation were 1500 kPa inside the core and 2350 kPa inside the filter zone. The calculated stresses at these points were 1800 kPa and 2250 kPa, respectively. The measured stresses at the height of 55 m were 1200 kPa inside the core and 1650 kPa inside the filter zone. The calculated stresses at these points were 1200kPa and 1500kPa, respectively. There were good agreements between calculated and measured values; and the model captured the arching of the stresses inside the core.

Figure 5-12 and Figure 5-13 show the profiles of maximum and minimum principal stress at different heights of the dam at the end of construction. The direction of the maximum principal stress was almost vertical inside the core with slight tilt towards the axis of the dam. The amount of the tilt increased in the filter zones; and near the both upstream and downstream faces of the dam, the direction of the maximum principal stress was parallel to the surface of the shell zone. The arching effect is distinguished by the abrupt change of the value of the maximum principal stress at the interfaces of the core and filter zones. The profile of minimum principal stress has also some irregularities at these interfaces but no significant transmission of stress (i.e. arching effect) was calculated for the minimum principal stress. The irregularities of the stress profile were also observed at the interfaces between the filter zones and the protecting shells in this figure, but with less intensity.

5.6 Analysis of the impoundment of the reservoir

The impoundment of the reservoir of the dam was modeled using the FLAC software and related deformations and stress changes inside the body of the dam were calculated using the proposed equations and algorithms of the previous chapter (i.e. modified stress relaxation technique). The impoundment of the LG4 dam started almost two years after the construction was complete and based on the piezometers data installed inside the body of the dam, the pore pressure of the construction stage had dissipated before the filling of the reservoir started (Paré et al., 1984). In other words, there was enough time after the end of the construction of the dam for the pore water to completely dissipate. The two year delay had some time effects on the behavior of the dam and the amounts of deformations which are not discussed here. Similar to the construction of the dam, the

impoundment was modeled using the multi stage modeling technique. In each stage, the rise of the water level of the reservoir was modeled by applying a new hydrostatic pressure and hydraulic boundary condition on the upstream face of the dam corresponding to the raised elevation of the water. Several hydraulic and mechanical loops were then carried out to bring the model into the equilibrium based on the new boundary conditions.

The phreatic line, flow patterns and pore pressures were calculated in hydraulic loops using Darcy's law which is the default of the FLAC software. The hydraulic conductivities of the materials of the different zones are shown in Table 5-5. The anisotropic values of hydraulic conductivity of the materials are due to the fact that the dam was constructed with horizontal layers resulting in greater horizontal permeability (Smith and Konrad, 2011). Moreover, the high contrast between the permeability of different zones resulted in the fact that almost all of the water head dropped in the core of the dam. Transient states of the flow in the upstream filter zone are shown in Figure 5-14. During the process of reaching the steady state flow in this zone, which took few days in time, the core made an impermeable boundary because of much lower permeability (i.e. almost 100 times smaller than filters). The calculated phreatic line is approximate and mesh-dependent. Because of the large elements used in the lower parts of the dam, ten meters of the downstream is saturated which is not realistic shell (height of the elements of the first layer of the dam over foundation is ten meters). However, this did not have large effects on the calculated values of deformation and stresses of the upstream side of the dam which is under focus in this study.

In each stage of the impoundment, based on the newly calculated phreatic line and patterns of pore water pressure, the internal unloading stress of the saturated elements and effects of the buoyancy forces were distributed over the finite difference mesh in mechanical loops. From a mechanical point of view, as shown in Table 5-6, the saturation resulted in a decrease of three parameters: elastic modulus number (K_E), bulk modulus number (K_B), and reference dilation angle (ψ_0), which was thoroughly discussed in the previous chapters. The relatively small amounts of reduction of these parameters represent the general condition of the material used in construction of rockfill dams in

Quebec, considering the high relative humidity of the air filling the voids and the standard compaction effort during the construction (Oldecop and Alonso, 2001; Verma et al., 1985). The parameters of the wetting state of the material were required for calculating the unloading of the saturated elements during the impoundment of the reservoir. After bringing the model into the equilibrium based on the new mechanical boundary conditions (i.e. change of the density of the saturated elements and patterns of pore water pressure), the internal unloading of the elements resolved an resulted in collapse settlements and shear stress on the face of saturation as shown in Figure 5-15.

The calculated vertical and horizontal displacement contours at the end of impoundment are shown in Figure 5-16 and Figure 5-17, respectively. Inclinometers installed inside the core and downstream filter recorded small values of less than 10 cm settlement during reservoir filling which is in agreement with the results of modeling and could be referred to the high resistance of the material used in the construction of the dam to wetting. However, three other effects of the rise in water level behind the dam could be distinguished in these figures: i) the hydrostatic pressure on the core caused horizontal displacements towards downstream; ii) The buoyant forces in the upstream side cause upward movements within the saturated zones; iii) Collapse of the upstream shell and transition zones cause downward movements within these zones. Since the dam behaved as a continuum, all of these patterns of displacement resulted in rotations of the body of the dam towards downstream or upstream. A limited region in the upstream shell demonstrated upward movements of about 6 cm, while the upstream filter zone had settled about 10 cm. The core and downstream side of the dam did not have large vertical displacements. These types of relative movements after the first filling of the reservoir may include the formation of cracks within the core of the dam, as reported in other dams worldwide (Giron, 1997; Hunter and Fell, 2003). However, this was not the case for LG4 dam due to the fact that the large and well-compacted transition zones which supported the core had relatively small collapse deformations.

All of the mentioned patterns of deformation were accompanied by changes in the stress state within the body of the dam and the source of plastic regions where large relative movements occurred. The calculated total vertical stress contours at the end of

impoundment are shown in Figure 5-18. The measured stresses at the elevation of the foundation were 2000 kPa inside the core and 2250 kPa inside the filter. The calculated stresses of these points were 2030 kPa and 2300 kPa, respectively. The measured stresses at the height of 55 m were 1310 kPa inside the core and 1600 kPa inside the filter. The calculated stresses at these points were 1350 kPa and 1450 kPa, respectively. There were good agreements between calculated and measured values at these locations. Comparing with stress contours before impoundment, as shown in Figure 5-11, the total stresses on the upstream side of the dam as well as the core have increased as a result of hydrostatic loading of the reservoir water and the increase of the density of the material from dry to saturated. After impoundment, the vertical total stress on the axis of the dam was increased by about 10 percent at the height of 55 m and about 20 percent over the foundation. A slight decrease of less than 5 percent of the vertical total stress was also observed within the downstream filter which was a result of redistribution of stress after the flow of water through the core and collapse of the saturated elements.

The calculated vertical effective stress contours at the end of impoundment and the measured values at specific locations are shown in Figure 5-19. The measured stresses at the elevation of the foundation were 1275 kPa inside the core and 2175 kPa inside the filter. These values were calculated using the data from the total pressure cells and piezometers installed inside the core and filter zones. The calculated stresses at these points were 1280 kPa and 2200 kPa, respectively. The measured stresses at the height of 55 m were 880 kPa inside the core and 1600 kPa inside the filter. The calculated stresses at these points were 1020 kPa and 1450 kPa, respectively. Comparing to the vertical stress contours before the impoundment as shown in Figure 5-11, the flow of water through the core increased the stress difference between the core and the downstream filter zone and hence the potential of hydraulic fracturing was increased. The effective stresses of saturated elements of the core were decreased more at the mid- height of the dam (e.g. more than 20 percent at the height of 55 m and about 10 percent over the foundation). The filter zone on the downstream side was not affected by the flow of the water and the effective stress remained almost unchanged resulting in an increase of arching effect between the core and the downstream filter. However this effect was less

important on the downstream side of the core because of the buoyancy forces acting on saturated filter zone.

Figure 5-20 and Figure 5-21 show the amount of the unloading stresses due to wetting in directions of the maximum and minimum principal stress, respectively, as calculated using the stress relaxation algorithms. The downstream filter and shell zones did not suffer any unloading and collapse due to the fact that those elements were above the phreatic line and did not get saturated during the first impoundment. Although the increase of the relative humidity or wetting by the rainfall could have also led to the collapse phenomena but this kind of behavior was neglected in the current study and the deformations of the dam were considered closely after the first impoundment. The amount of unloading stresses of the saturated elements were related to the stress state at the moment of saturation as well as the difference between dry and wet stress-strain relation of the material. A maximum unloading stress of about 250 kPa was calculated in the direction of maximum principal stress inside both downstream and upstream filter zones over the foundation, which was the same location of the maximum vertical stress of 2200 kPa as shown in Figure 5-11 (i.e. about 11 percent of the vertical stress was relaxed in the wetting process at this location). The maximum unloading stress in the direction of minimum principal stress was calculated inside the downstream filter zone, 50 m above the foundation, and was about 60 kPa. The calculated horizontal effective stress at this point was 250 kPa meaning that more than 20 percent of the horizontal stress was relaxed in the wetting process at this location. Contours of the horizontal effective stress after the impoundment are shown in Figure 5-22. As a result of saturation and increase of pore water pressure, the majority of the upstream elements had horizontal effective stress below 250 kPa. However, none of these elements reached the negative stress level which could have marked a risk of hydraulic fracture if so.

Comparing to the previous modeling of the impoundment of the LG4 dam made by Verma et al. (1985), the agreements between calculated and measured values improved. They have utilized the original hyperbolic model without the plasticity formulation. The dam elements which underwent the plastic flow, at least once during the calculation, are shown in Figure 5-23. The majority of the filter elements reached the plasticity criteria.

However, this does not imply that these elements reached the plasticity criteria all at once. The stress state of these elements reached the plastic envelope in a limited time span during the modeling process. The excessive deformations of these elements were restricted due to the bounding effect of the surrounding elements. Which brings us to one more point: the importance of having well-compacted filters and shell zones to prevent large settlements of the core during the impoundment. As if weaker material had been used for these zones, the chances of localization of plastic regions would have been higher and cracking of the core would have been expected due to large collapse settlements of these zones. On the other hand, the large amount of arching after impoundment was also considerable as shown in Figure 5-18. Although this effect also existed at the end of construction as shown in Figure 5-11, but the amount increased as a result of saturation of the core and upstream side of the dam. This effect was connected to the high contrast between the rigidities of the core and supporting filter/transition zones. This contrast should be kept to the minimum in order to minimize hydraulic fracturing.

5.7 Conclusion

This chapter describes the application of the HPD model (nonlinear hyperbolic model coupled with Mohr-Coulomb failure criteria) in dam engineering. The main advantages of this model for this purpose are capturing the following characteristics: (1) modulus stiffening and degradation due to different modes of loading; (2) Plastic deformations; (3) Shear induced volumetric changes. With the use of the nine parameters, the model was previously shown to provide satisfactory predictions of the behavior of the tested granular materials. In addition, this model is capable of reproducing the plastic deformations caused by wetting using the relaxation technique as originally proposed by Nobari and Duncan (1972).

The application of model was demonstrated in modeling the construction stage and impoundment of LG4 rockfill dam in Quebec, Canada. The results of the modeling showed good agreement with the instrumentation data. Different patterns of deformation occurred during construction and impoundment. During the construction, the maximum settlements were located at mid-height of the core. After the first filling of the reservoir, the maximum settlements were near the crest and on the upstream side of the dam due to

the collapse of the upstream elements after saturation. Maximum horizontal displacements occurred near the crest on the downstream side of the dam which was a result of the hydrostatic pressure of the reservoir acting on the core. Some regions on the upstream shell zones experienced upward movements as a result of buoyancy forces and small overburden pressure. The relative magnitudes of these deformations resulted in variety of stress states and formation of plastic regions within the body of the dam.

The plastic components of the constitutive model enhanced the predictions especially during the filling of the reservoir which involved more plastic deformations. By monitoring the change of different parameters of the model (e.g. elastic modulus or Poisson's ratio) during the modeling process, it was possible to locate the vulnerable elements of the dam which had stress state close to the failure envelope (e.g. elements close to the crest of the dam just before the first filling of the reservoir).

It was also shown that the relative rigidity of adjacent zones had great effect on propagation of regions with plastic behavior. Over-compacted filter zones would result in a high contrast of the compressibility with adjacent zones which may trigger hydraulic fracturing during the impoundment. On the other hand, weak and not sufficiently compacted filter and shell zones will not provide enough support for the core and excessive settlements during construction and impoundment will result in cracking of the core of the dam. In conclusion, the shell zones are better to be compacted to highest possible level but the compaction of transition zones should be kept to an optimum in order to prevent the abrupt change of the elastic modulus at the interface with the core and to avoid the hydraulic fracturing phenomenon.

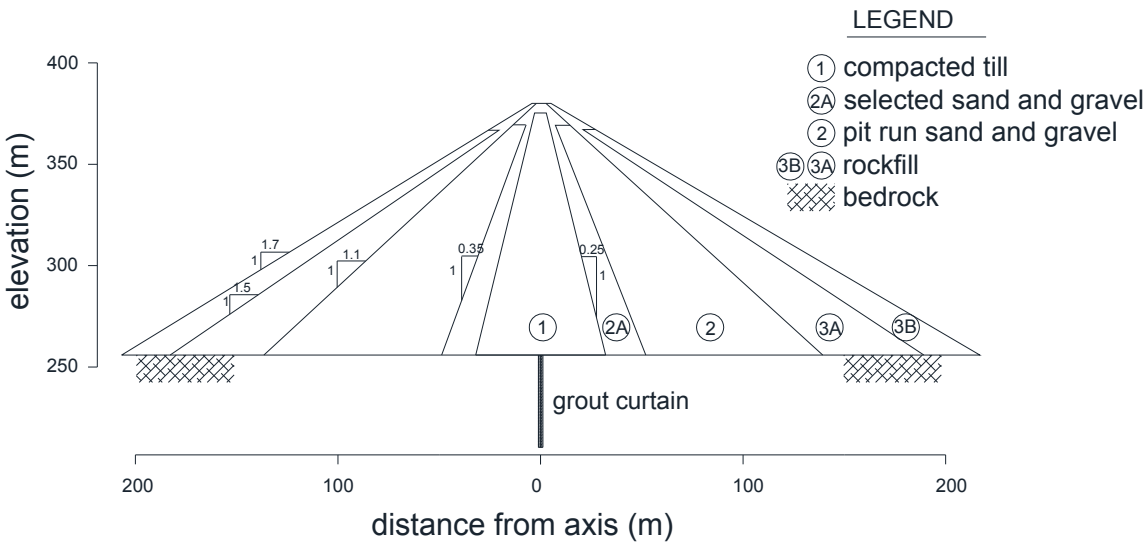

Figure 5-1- Cross section of LG4 dam at highest elevation of the crest

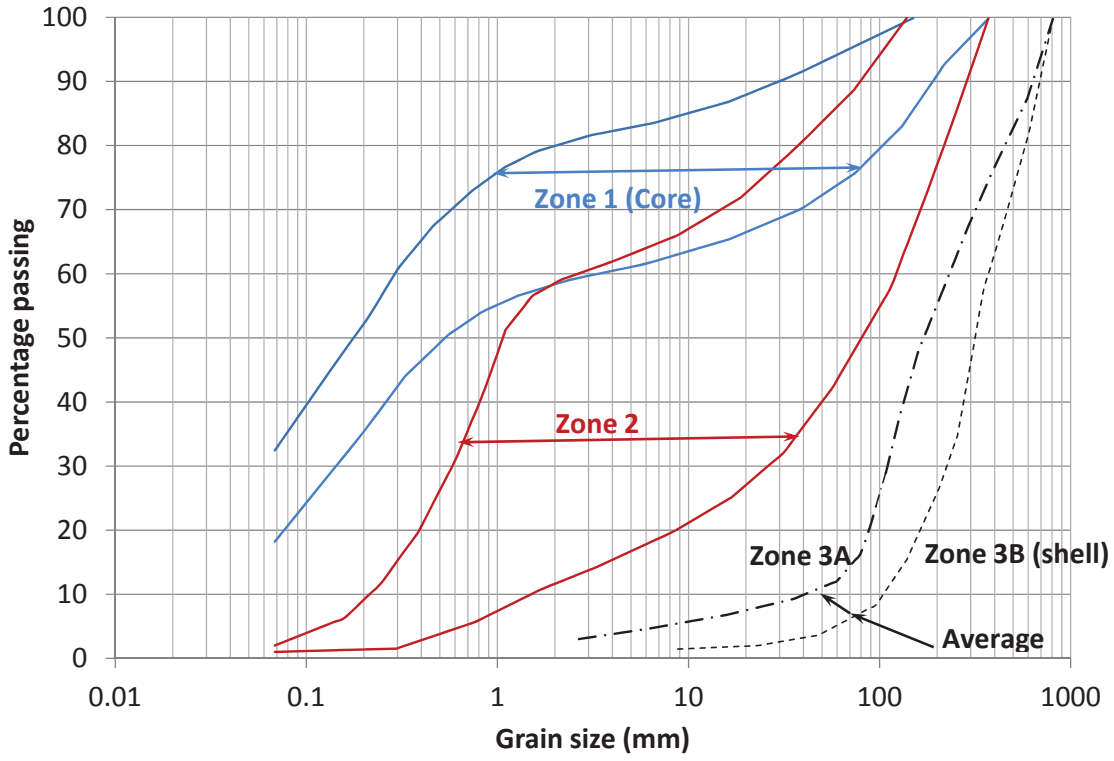

Figure 5-2- Grain size distribution of material used in construction of different zones of LG4 dam

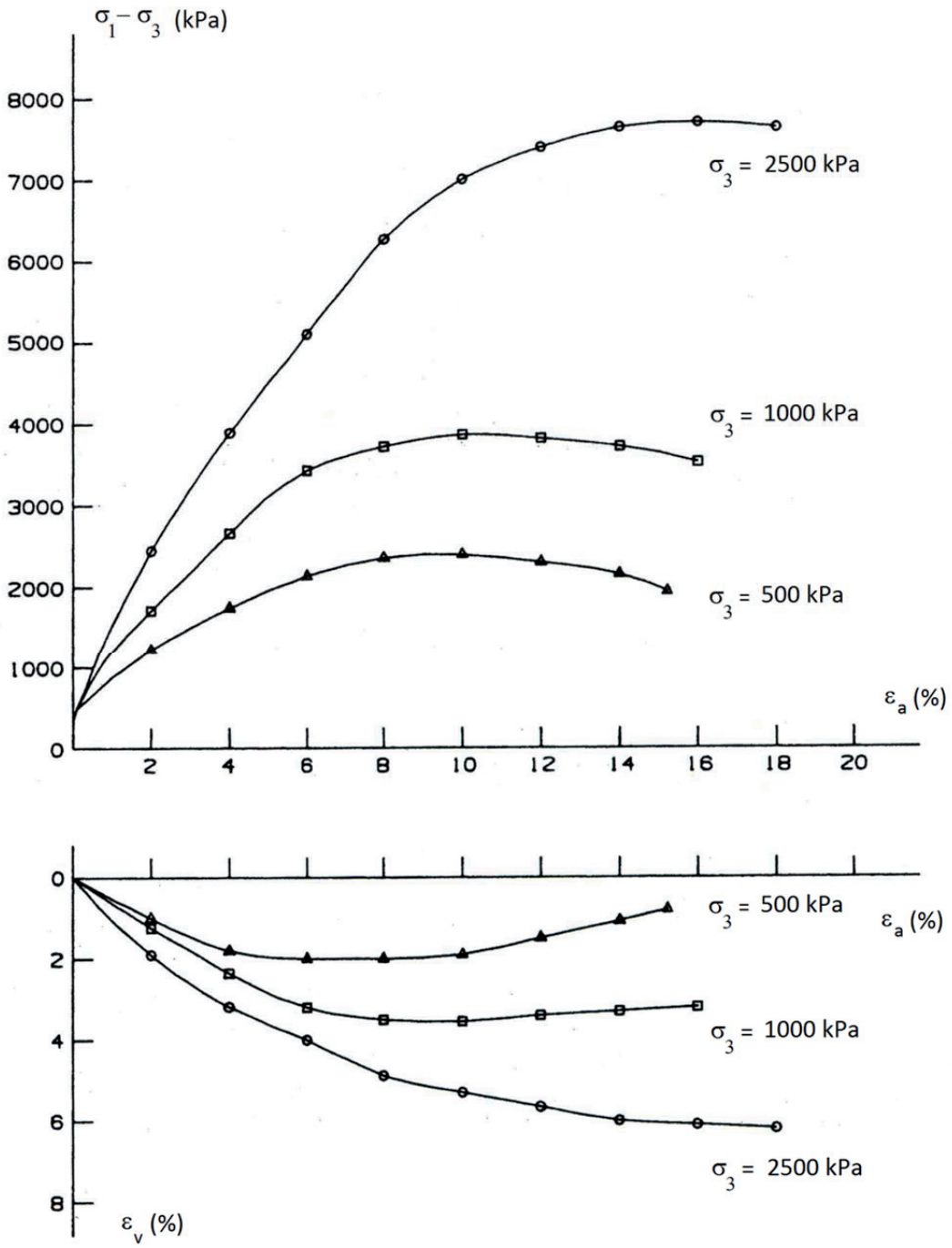

Figure 5-3- Results of triaxial test on a rockfill material similar to that of the shell of LG4 dam (zone 3); after Marsal (1967)

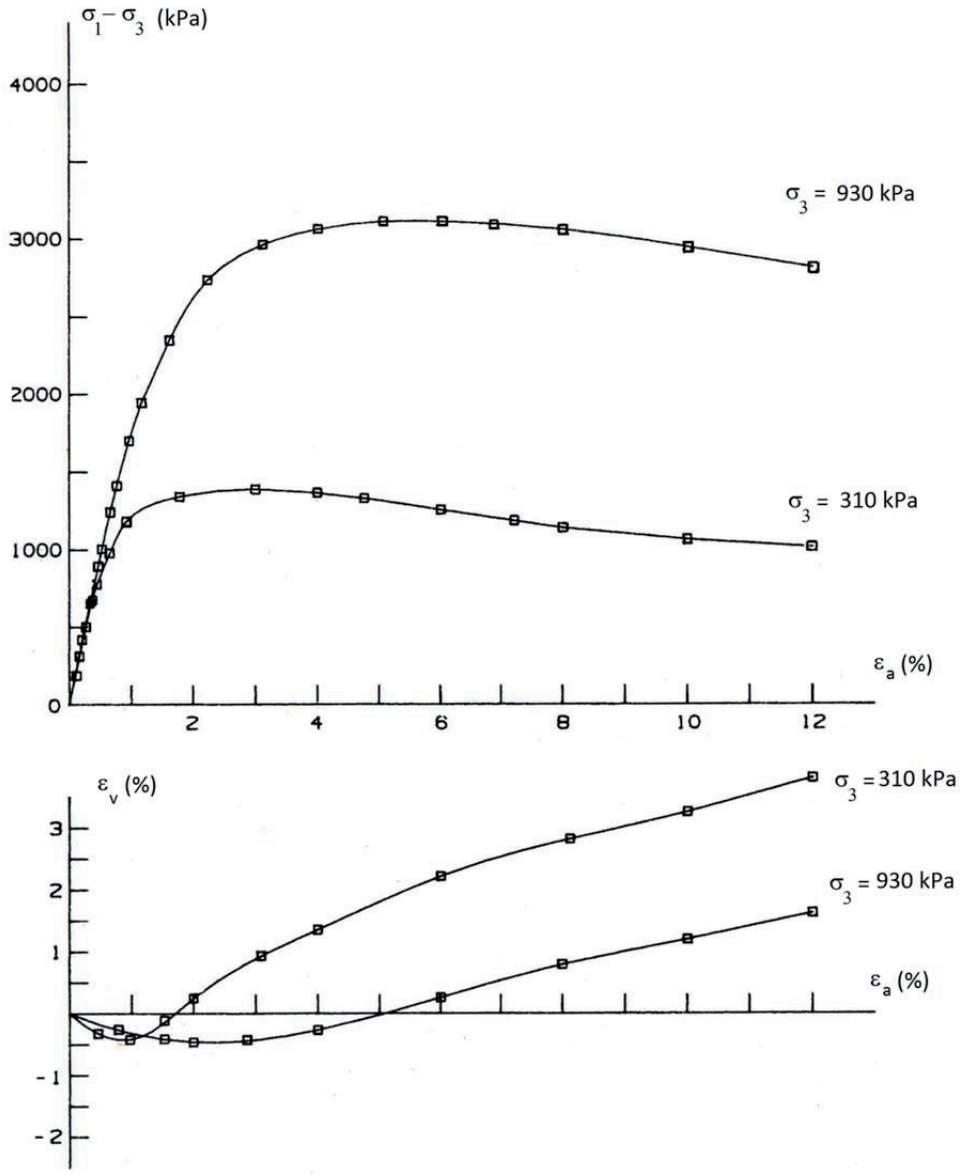

Figure 5-4- Results of triaxial test on the sand and gravel of the filter zone (zone 2); after Massiéra et al. (1989)

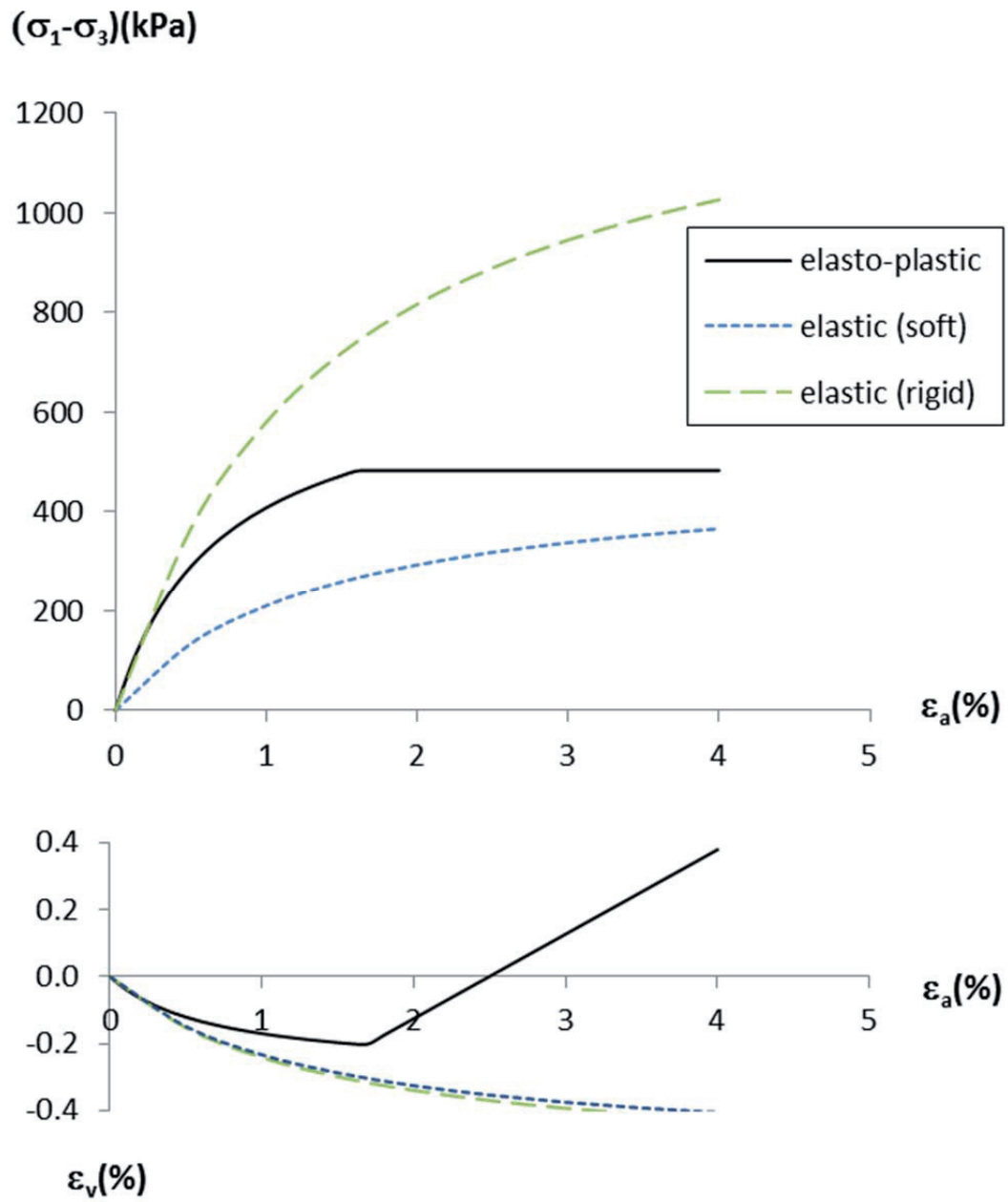

Figure 5-5- Comparison of different constitutive behaviors of the rockfill material of the shell of LG4 dam in virtual triaxial compression tests, generated by FLAC at reference confining pressure $\sigma_3 = P_a = 100\ kPa$.

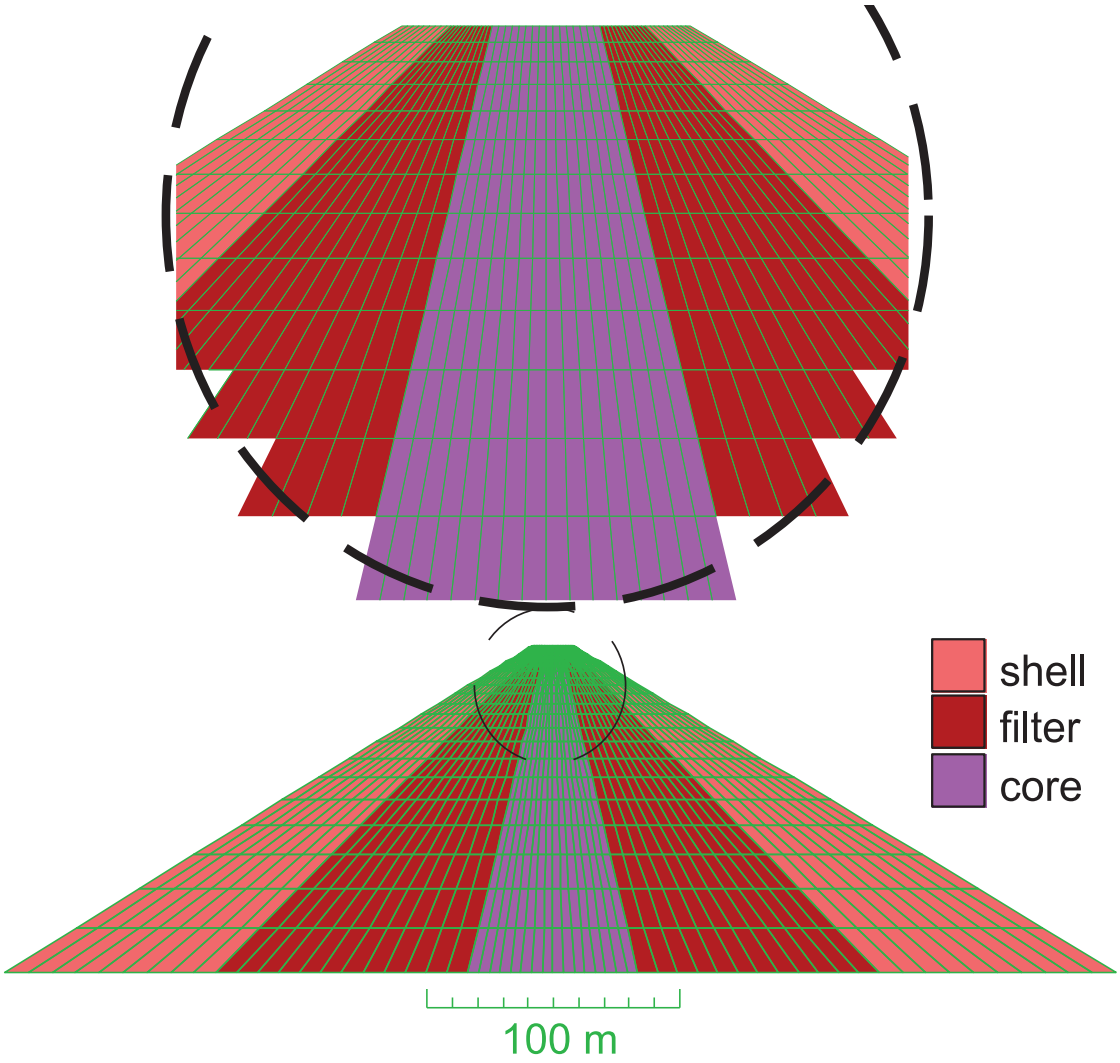

Figure 5-6- Finite difference mesh of LG4 dam

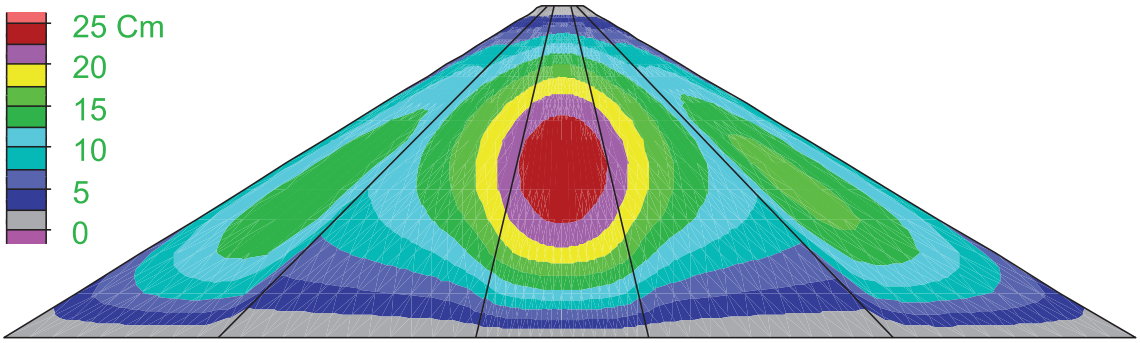

Figure 5-7- Settlement contours of LG4 dam at the end of construction

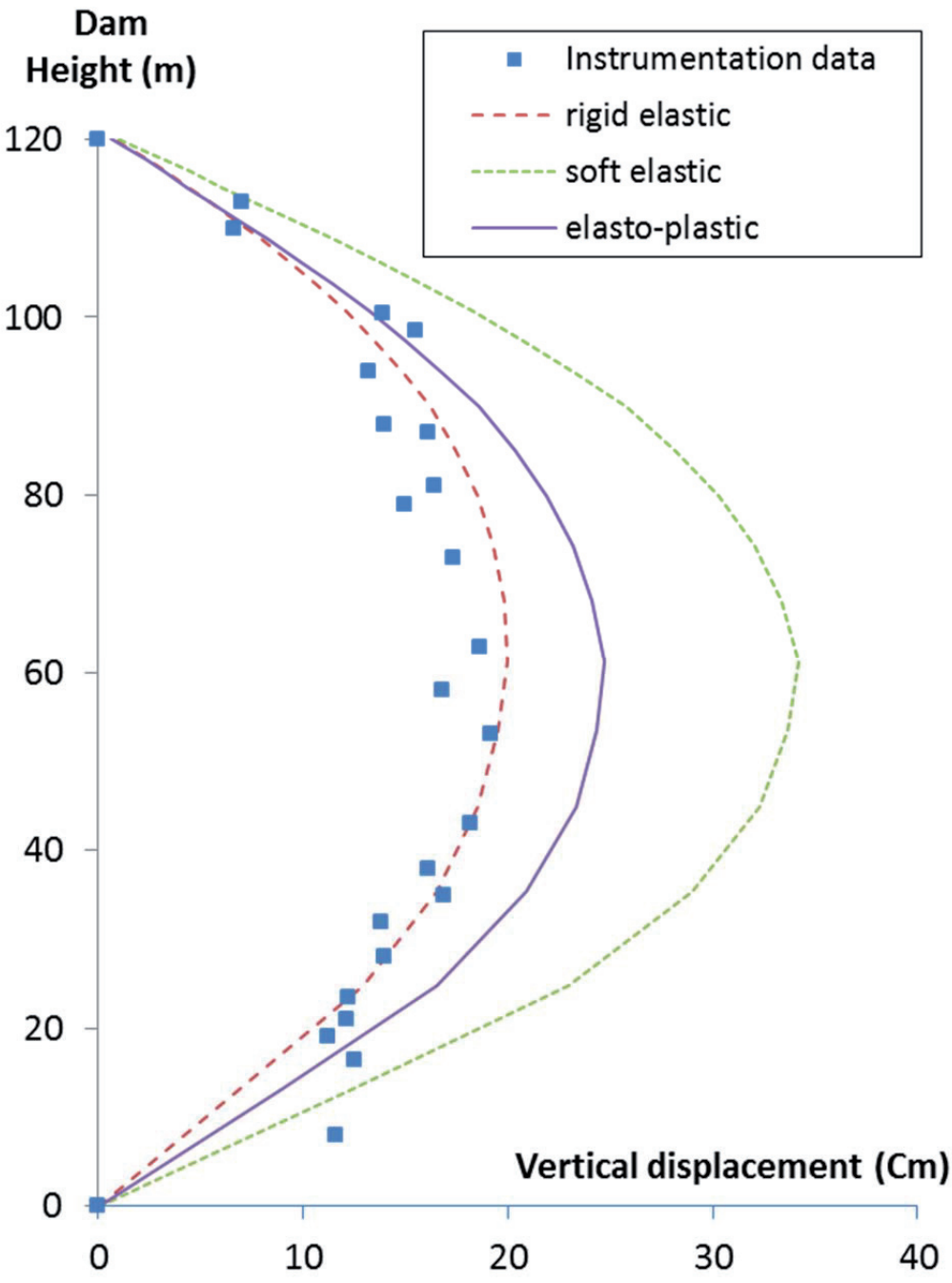

Figure 5-8- Measured settlements on the axis of the core of LG4 dam at the end of construction, with predictions of different constitutive models and parameters.

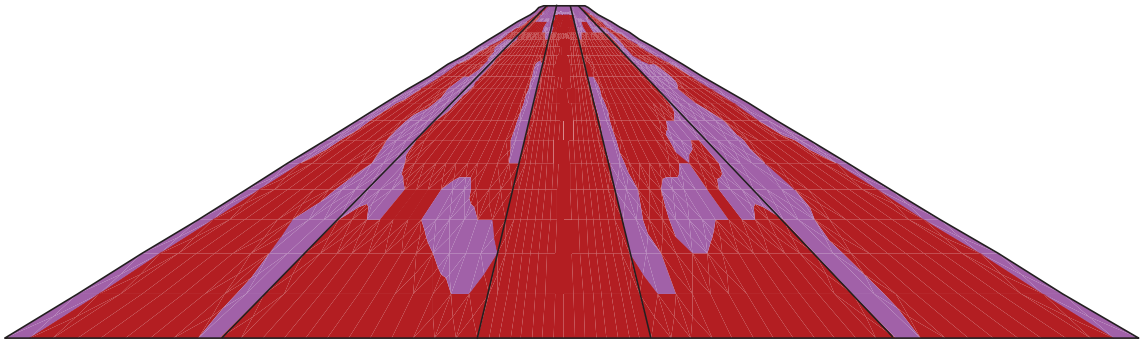

Figure 5-9- Elements reaching the failure envelope (in purple) during the simulation of construction stage.

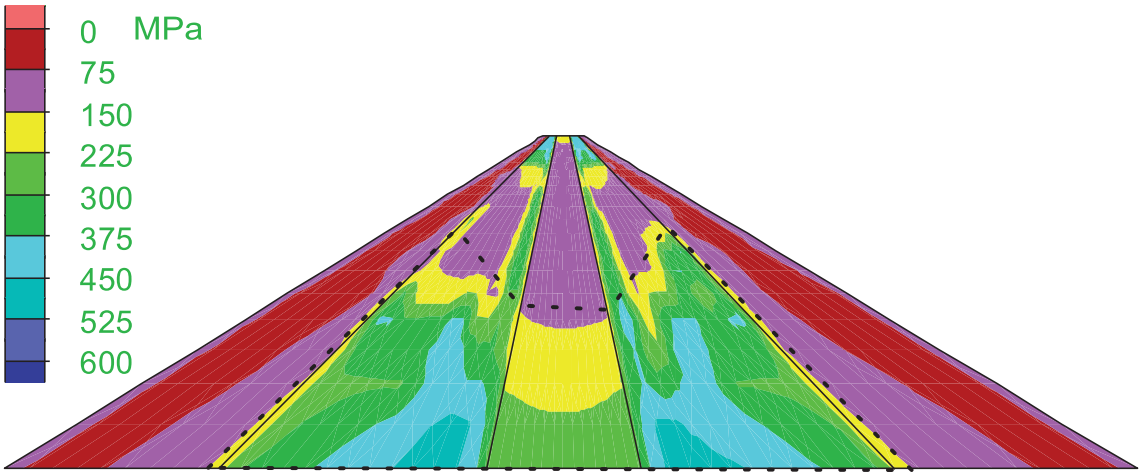

Figure 5-10- Contours of Elastic modulus at the end of construction of LG4 dam

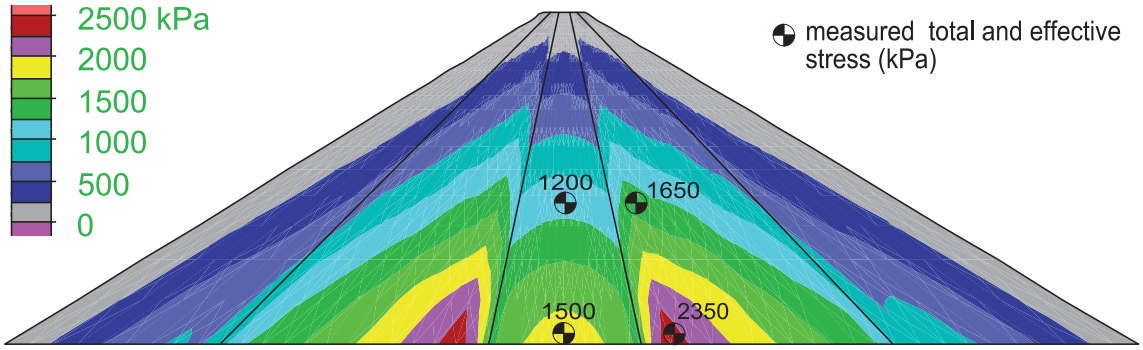

Figure 5-11- Calculated vertical stress contours of LG4 dam at the end of construction

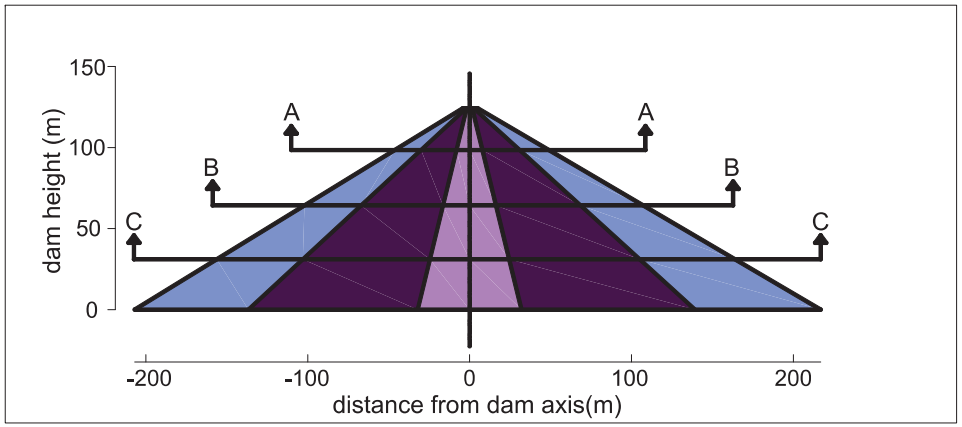

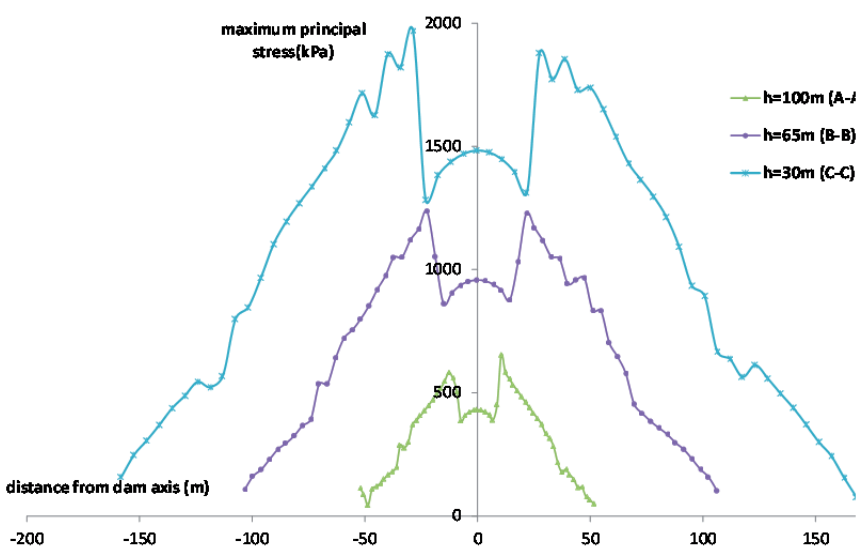

Figure 5-12- Profiles of maximum principal stress (kPa) at different heights at the end of construction.

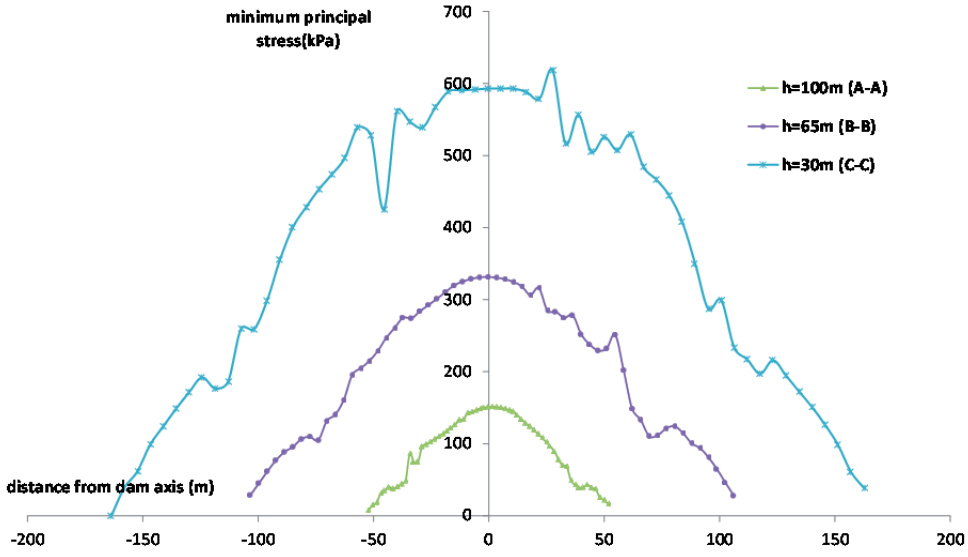

Figure 5-13- Profiles of minimum principal stress (kPa) at different heights at the end of construction.

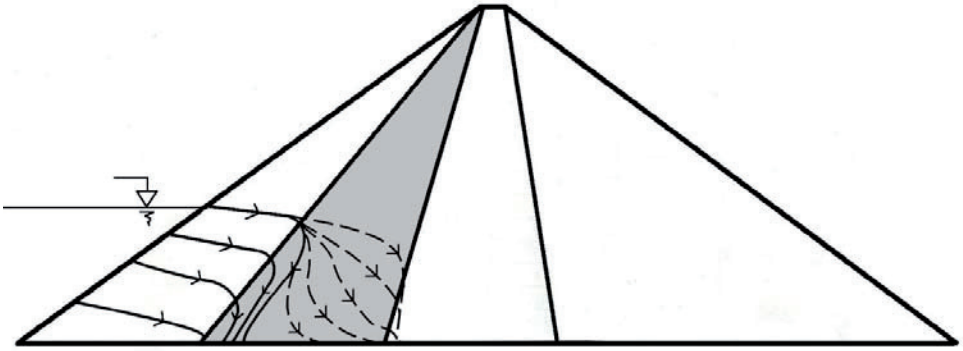

Figure 5-14 - Hydraulic transit states during the flow calculations in the filter zone.

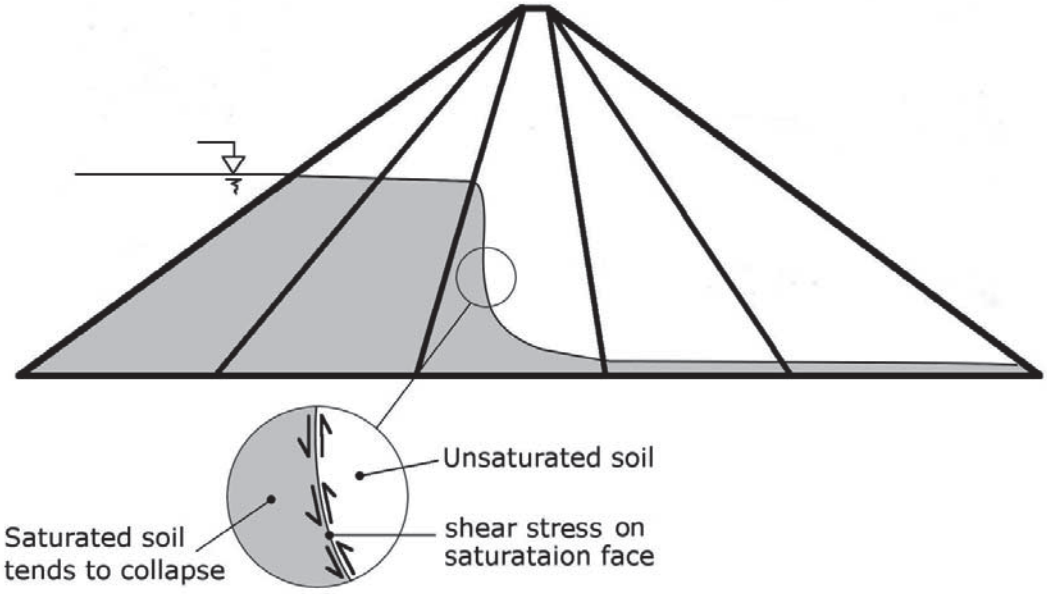

Figure 5-15- Collapse of the saturated elements result in shear stress on the face of saturation.

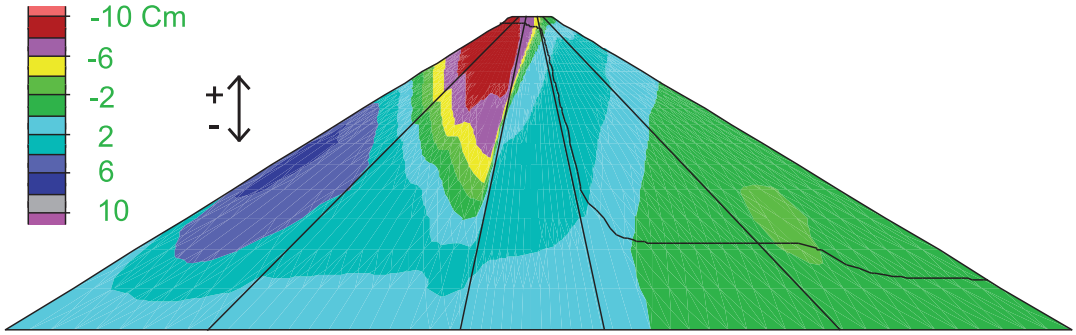

Figure 5-16- Calculated vertical displacement contours at the end of impoundment of LG4 dam

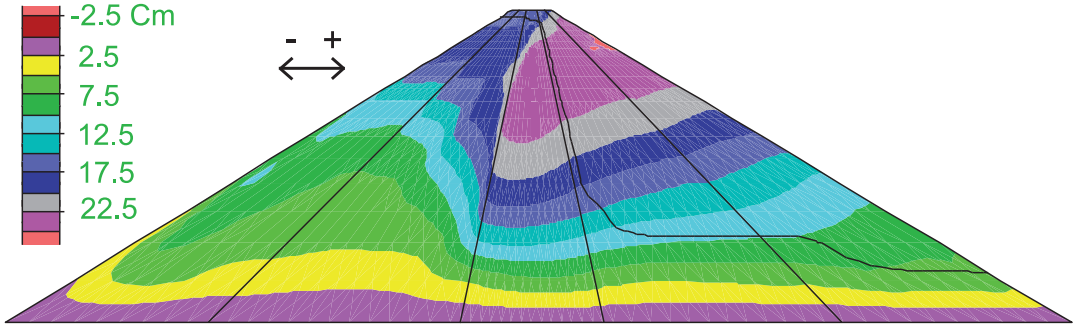

Figure 5-17- Calculated horizontal displacement contours at the end of impoundment of LG4 dam

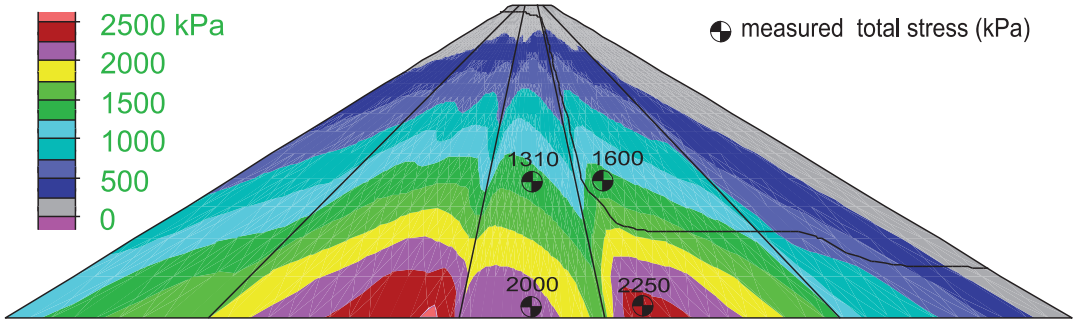

Figure 5-18- Calculated vertical total stress contours at the end of impoundment of LG4 dam and comparison with measured values.

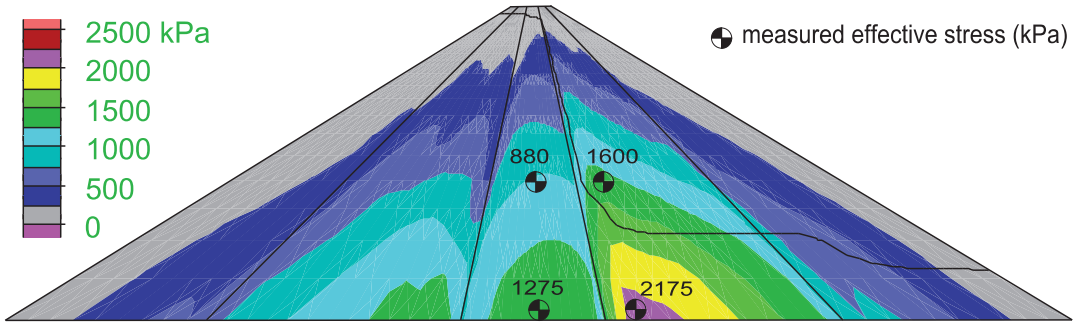

Figure 5-19- Calculated vertical effective stress contours at the end of impoundment of LG4 dam and comparison with measured values.

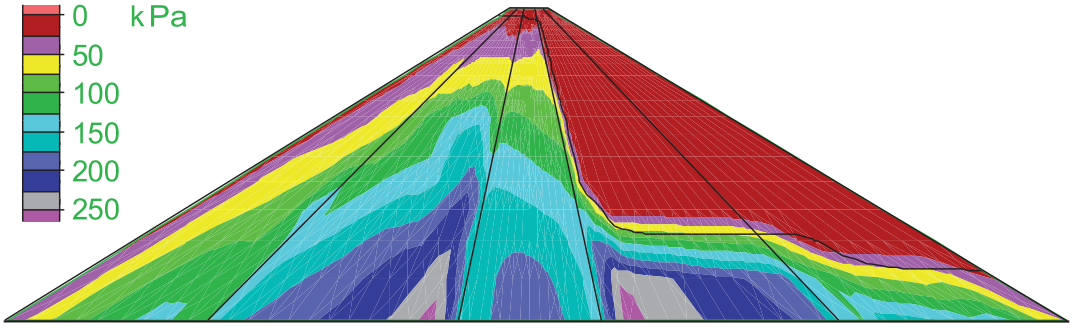

Figure 5-20- Contours of unloading stress due to wetting in the direction of the maximum principal stress

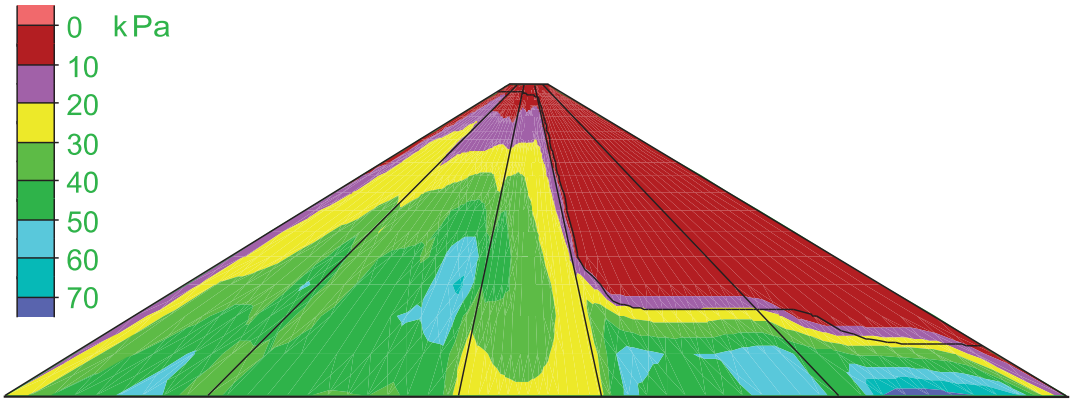

Figure 5-21- Contours of unloading stress due to wetting in the direction of the minimum principal stress

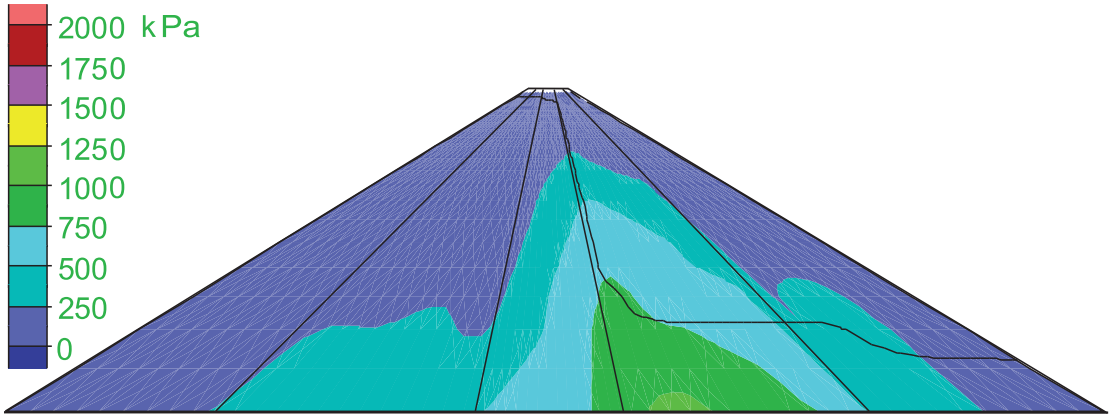

Figure 5-22 - Calculated horizontal effective stress contours at the end of impoundment of LG4 dam

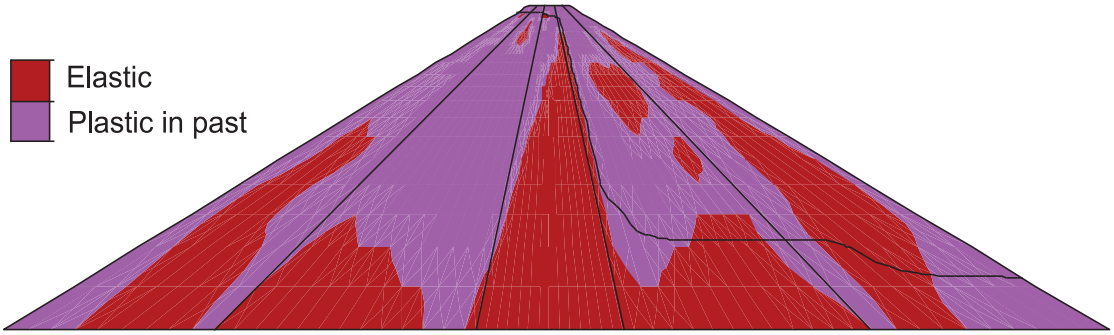

Figure 5-23- Elements reaching the failure envelope (in purple) during the simulation of the impoundment

Hyperbolic parameters (Elastic behaviour)		Plasticity and Dilation parameters	
K_E*	Elastic modulus number	ϕ_0	fiction angle at reference pressure P_a
n	Elastic modulus exponent	$\Delta\phi$	change of friction angle with confining stress
K_B*	Bulk modulus number	ψ_0*	dilation angle at reference pressure P_a
m	Bulk modulus exponent	$\Delta\psi$	change of friction angle with confining stress
R_f	coefficient to adjust the stress-strain curve (default value=0.7)		

* These three parameters are reduced with increasing water content

Table 5-1- Elastic and plastic parameters of HPD model

Zone	Lifts thickness	Compaction
1- Core (Till)	45 cm	4 passes of 45 ton pneumatic rollers (97% of Standard Proctor maximum dry density at water contents varying between -1% - +2% optimum)
2- Filters (Gravely Sands)	45 cm	3 passes of 5.5 ton vibratory rollers (minimum relative density of 70%)
3- Shell (Rockfill)	1 – 2 m	4 passes of 9 ton vibratory rollers

Table 5-2- Specifications for placement of materials of different zones of LG4 dam

	Till Core			Filter			Shell		
Reference*:	1	2	3	1	2	3	1	2	3
γ_{sat}(kg/m^3)	2340	2256	2144	2320	2276	2260	2000	1962	1962
ϕ	37	37	37	42	42	42	40	40	45
K_E	1000	1000	1670	1380	4000	4500	370	370	1000
K_B	-	800	1030	-	3200	2850	-	300	800
n	0,39	0,6	0,5	0,61	0,61	0,4	0,35	0,35	0,8
m	-	0,6	0,5	-	0,6	0,4	-	0,6	0,8
R_f	0,55	0,5	0,5	0,6	0,6	0,6	0,74	0,74	0,35

* Reference1: (Paré et al., 1984); Reference2: (Massiéra et al., 1989); Reference 3: (Szostak-Chrzanowski and Massiéra, 2004)

Table 5-3- Elastic parameters used in previous simulations of the construction stage of LG4 dam.

	γ_{sat}(kg/m^3)	φ_0	$\Delta\varphi$	ψ_0	$\Delta\psi$	K_E	n	K_B	m	R_f
Shell	1960	45	10	6	10	1000	0,8	800	0,8	0,7
Filter	2260	42	8	10	10	4500	0,4	2850	0,4	0,6
Core	2140	37	5	5	5	1670	0,5	1030	0,5	0,5

Table 5-4- HPD model parameters for different zones of LG4 dam used in current study (dry material).

Hydraulic Conductivity (m/s)	Core	Transitions and Filters	Shell
Horizontal	1.7×10^{-6}	1×10^{-4}	high
Vertical	1.7×10^{-7}	1.7×10^{-5}	high

Table 5-5- Hydraulic conductivities of different zones of the dam.

	ψ_0	K_E	K_B
Shell	6 (4)	1000 (800)	800 (640)
Filter	10 (8)	4500 (3600)	2850 (2280)
Core	5 (3)	1670 (1340)	1030 (825)

Table 5-6 – Effects of saturation on the parameters of the HPD model; the values in parentheses are for saturated material

6 Conclusion

In numerical modeling of rockfill dams selecting an appropriate stress-strain relationship for the material is primarily involved with balancing simplicity and accuracy. While it seems reasonable that more complex stress-strain relationships should be able to model the behavior of the rock particles more accurately, there is no benefit in using a very complex relationship to analyze the problem where the simpler representation of the stress-strain behavior would result in an acceptable accuracy. Moreover the applicability of the more complex constitutive models in simulating the rockfill material is often questionable because of: (i) the difficulty of the calibration of the model using the limited test results of such material in practice, and (ii) the initial assumptions and experimental relations taken in the formulation of some of these constitutive models are not necessarily extendible to compacted samples of large rock particles as exist in rockfill dams.

A non-exhaustive review was performed of the constitutive models which have been used in the past to model the behavior of rockfill dams during construction and impoundment. It was concluded that considering the high strength of the rock particles and resistance to the wetting of the material used in construction of rockfill dams in Quebec, the hyperbolic model if coupled with an appropriate failure criterion was the most balanced constitutive law for the purpose of numerical modeling of zoned rockfill dams. In the context of plasticity, the failure envelope and the potential functions should consider the dependency of both friction angle and dilation angle to key physical properties of the rock particles (e.g. stress state, density and degree of saturation).

Due to the elastic formulation of the traditional hyperbolic model, it cannot predict the behavior near the failure envelope or the dilative behavior of compacted assemblages of granular material. In order to overcome these shortages the classic constitutive equations were coupled with the Mohr-Coulomb plastic failure criteria, and with a non-associated flow rule to consider shear dilatancy. The implemented model, referred as HPD model, has nine parameters: four parameters to define the failure envelope and the potential function (φ_0, $\Delta\varphi$ and ψ_0, $\Delta\psi$) and five parameters to represent the initial nonlinear elastic behavior (K_E, K_B, m, n and R_f). The following characteristics of the rockfill element were modeled using this new implementation:

1. nonlinear stress-strain relation using the hyperbolic function.

2. modulus stiffening due to increasing confinment and modulus degradation due to increasing shear stresses based on the classical hyperbolic formulation.

3. steady state strength and plastic deformations on the failure envelope using the perfectly plastic formulation and Mohr-Coulomb failure criteria with a stress dependent friction angle and zero cohesion.

4. shear induced volumetric changes or dilative behavior of dense samples by the means of a non-associated flow rule which included the dependency of the dilation angle to stress state, rate of saturation and density.

The failure and potential functions had similar mathematical forms but were defined using different parameters (dilation angle and friction angles). The final strength of the rockfill sample was used to define the failure envolope (i.e. strength of the material in the final steady state or at large strains). The steady state friction angle at the reference pressure of 100 kPa was defined as the initial friction angle φ_0 which linearly decreased with increasing confinement at a rate of $\Delta\varphi$ in a logarithmic scale. The initial friction angle was shown to be independent of the density and degree of saturation of the material being modeled. Since no strain hardening rule was defined for the model, it could not capture the peak friction angle. This was chosen in order to keep the model as simple as possible. The potential function had the similar mathematical form as the failure function but with a different parameter (dilation angle instead of friction angle). The reference dilation angle ψ_0 was defined at the reference confining pressure of 100 kPa in the triaxial setup which decreased with increasing confinement using a similar logarithmic relation as used for the friction angle but with different rate of $\Delta\psi$. The dilation angle was shown to be dependent to both density and degree and saturation: it increased linearly with the dry density of the rockfill sample and decreased slightly (about 2 degrees) when changing from dry state to saturated. At each given initial dry density there existed a treshold confinig stress above which the dilative behavior of rock particles were prevented by excessive confining pressure.

In the initial elastic formulation, the axial and volumetric rigidities were defined by means of the Young's modulus and bulk modulus, respectively. Modulus numbers K_E

and K_B were used as dimensionless parameters to represent these two moduli at reference confining pressure of 100 kPa, respectively. Both of these two elastic moduli increased with confining stress in a logarithmic relation which was defined by means of the modulus exponents n and m, respectively. The higher were these exponents, the more dependent were the elastic modulus on the confining pressure. The modulus numbers but not the exponents were shown to be sensitive to density, degree of saturation and the time span of loading. This fact was utilized to model the softening of the material due to increasing of the degree of saturation or to calculate the time-dependent deformations using the stress relaxation technique. The adjustment parameter R_f was used to adjust the shape of the hyperbolic curve. After analyzing the database of more than twenty rockfill samples, it was concluded that 0.7 was often a good default value regardless of the physical properties of the sample. Smaller values of this parameter should be cautiously used as it would dramatically increase the elastic rigidity without changing the modulus numbers.

The HPD model was implemented into the commercial software, FLAC, to simulate the behavior of the assemblages of rock particles during the conducted drained triaxial monotonic compression tests. These tests were performed in two phases:

a) In the first phase, the drained monotonic compression tests were conducted in strain controlled condition on both dry and saturated specimens with different densities and at different confining pressures. A gradation curve parallel to the prototype rockfill was used for the preparation of the specimens in this phase. The results of these tests were used to calibrate the numerical model and to characterize the assemblage of rock particles during the tests.

b) In the second phase, two series of experiments were conducted and analysed with an emphesize on time effects and saturation. These experiments were monotonic triaxial compression tests in both strain-controlled and stress-controlled conditions. They were performed on compacted assemblages of granite rock particles prepared in the laboratory using different initial dry densities and a more uniform particle gradation curve compared to the prototype rockfill in order to increase the amount of time-dependent deformations and the collapse settlements due to wetting.

All the parameters of the HPD model can be easily calibrated using the results of the drained monotonic triaxial compression test conducted at least at two different confining pressures. The triaxial tests at this research were conducted at three different confining pressures of 100, 300 and 600 kPa. The first two pressures were used to calibrate the parameters of the model and the third test was predicted. Alternatively, a database of different rockfill samples was gathered from the literature which could be used to estimate the parameters from the general physical properties (e.g. density, gradation, particle shape and mineral constituencies). A procedure was proposed for calibrating the parameters of the model based on any of these two methods.

In the second phase strain controlled tests were conducted at constant strain rate, on both dry and saturated samples. The general trends conformed to the observed behavior during the first phase strain controlled tests which had denser specimens with wider grain size distributions. The time effects and collapse deformations due to wetting of the rock particles were studied using the results of the stress controlled tests. These tests were conducted at changing stress rate, on dry samples, and water was added at different stress levels which maintained constant during the saturation process in order to estimate the deformations caused by wetting. It was shown that rate and mode of loading had influence on the behavior of the samples which can be utilized to calculate the time-dependent deformations of rockfill masses. The longer the stress state was maintained over the assemblage of rock particles, the more deformation was recorded which indicated a softer behavior over time. The introduction of water into the dry specimens also increased the amount of deformations. The softening of the behavior after the introduction of water into the rockfill element or during a suspended stress state was related to the deterioration of the contact points between particles and propagation of micro fissures inside them which was more important at high shearing stress level (i.e. close to failure envelope).

The modulus numbers were considered as the key parameters in the modeling of the time and saturation-related behavior. The values of these two parameters reduced linearly with the duration of the suspended loading in a log-log scale. Saturation also reduces the values of these parameters by about ten percent. All the other parameters

remained unchanged for a given material regardless of the timespan of loading and degree of saturation. Having the new set of parameters, the resulting deformations can be calculated at any stress state using the Nobari-Duncan procedures (also known as stress relaxation technique), adapted to the new constitutive equations. The new algorithms were also implemented in order to minimize the computational effort during the numerical simulation. The equations in the new algorithm were separated into two independent systems to calculate the two stress components (σ_{1w}, σ_{3w}) separately; and each one with the desired precision. This enhancement also increased the stability of the numerical procedure. The minimum principal stress (σ_{3w}) was firstly calculated. Knowing the first unknown, the maximum principal stress (σ_{1w}) was readily calculated. This modified stress relaxation procedure was used to simulate the deterioration of contact points and reuslted deformations which were caused by keeping a constant anisotropic stress over time and also augmented by saturation of the specimens.

The elasto-plastic parameters used in the simulations of stress-controlled tests were exactly the same as those calculated from the strain-controlled tests except for the modulus numbers that changed with test method as well as durations. Smaller values of modulus numbers were calculated for the stress-controlled tests which took longer time comparing to strain-controlled tests. This was again explained as softer behaviors of the specimens over time. The gradual decrease of these parameters over time was formulated using the logarithmic relation which also complied to the classical creep theory (i.e. softening of the material decreases logarithmically over time to reach a steady state creep). These time effects must be considered when choosing the parameters of the model from results of laboratory tests for the short and long term analysis of the behavior.

In the last phase of the research, the application of the HPD model was demonstrated in modeling of the construction stage and impoundment of LG4 rockfill dam in Quebec, Canada. The results of the modeling showed good agreement with the instrumentation data. Different patterns of deformation occurred during construction and impoundment. During the construction, the maximum settlements were located at mid-height of the core. After the first filling of the reservoir, the maximum settlements were near the crest and on the upstream side of the dam due to the

collapse of the upstream elements after saturation. Maximum horizontal displacements occurred near the crest on the downstream side of the dam which was a result of the hydrostatic pressure of the reservoir water acting on the core. Some regions on the upstream shell zones experienced upward movements as a result of buoyancy forces and small overburden pressures. The relative magnitudes of these deformations resulted in variety of stress states and formation of plastic regions within the body of the dam.

Comparing to the previous efforts for modeling the behavior of this dam, the plastic components of the constitutive model enhanced the predictions especially during the filling of the reservoir which involved more plastic deformations. By monitoring the change of the values of different parameters of the model (e.g. elastic modulus or Poisson's ratio) during the modeling process, it was possible to locate the vulnerable elements of the dam which had stress state close to the failure envelope (e.g. elements close to the crest of the dam just before the first filling of the reservoir).

It was also shown that the relative rigidity of adjacent zones had great effect on propagation of regions with plastic behavior. Over-compacted filter zones would result in a high contrast of the compressibility with adjacent zones which may trigger hydraulic fracturing during the impoundment. On the other hand, weak and not sufficiently compacted filter and shell zones will not provide enough support for the core and excessive settlements during construction and impoundment will result in cracking of the core of the dam. Generally, it was concluded that the shell zones should be compacted to highest possible level but the compaction of transition zones should be kept to an optimum in order to prevent the abrupt change of the elastic modulus at the interface with the core and to avoid the hydraulic fracturing phenomenon.

In the future, the HPD model could be implemented in modeling of the behavior of other important rockfill dams in Quebec including Sainte-Marguerite-3 and Romaine-2. SM3 is a rockfill dam with till core and filter zones same as the LG4. The height of this dam is 175 m and it experienced longitude cracks on the crest after the impoundment in the year 2002. R2 is another rockfill dam with an asphaltic core and a height of 160 m which is under construction at the moment. Another opportunity for the continuation of this research is application of the HPD model in modeling of the

creep phenomena in rockfill dams. Although the procedures for modeling of the time-dependent deformations based on fracture mechanics were discussed in chapter 4, it was not applied in dam engineering in this thesis. More laboratory work and instrumentation data from previous dams are required in order to calibrate the parameters of the model for this purpose. New procedures are also needed to apply the stress relaxation technique in the modeling of creep in a rockfill dam and to calculate the deformations of the whole structure over time.

References

Adikari, G.S., and A.K. Parkins (1982) "Deformation behaviour of Talbingo dam," *Int. J. Numer. Anal. Meth. Geomech.*, Vol. 6, pp 353-382.

Alonso, E. E., A. Gens, and A. Josa (1990) "A Constitutive Model for Partially Saturated Soils," *Géotechnique*, Vol. 40, No. 3, pp 405-430.

Alonso, E.E., S. Olivella, and N.M. Pinyol (2005) "A review of Beliche dam," *Géotechnique*, Vol. 55, No. 4, pp 267–285.

Alonso, E.E., S. Olivella, A. Soriano, N.M. Pinyol, and F. Esteban (2011) "Modeling the response of Lechago earth and rockfill dam," *Géotechnique*, Vol. 61, No. 5, pp 387-407.

Arenson, L., and S. Springman (2005) "Triaxial constant stress and constant strain rate tests on ice-rich permafrost samples," *Canadian Geotechnical Journal*, Vol. 42, No. 2, pp 412-430.

Augustesen, A., M. Liingaard, and P.V. Lade (2004) "Evaluation of time-dependent behavior of soils," *International Journal of Geomechanics, ASCE*, Vol. 4, No. 3, pp 137–156.

Barton, N.R. , and B. Kjarnesli (1981) "Shear strength of rockfill," *J. Soil Mechanics and Foundations Division, American Society of Civil Engineers*, Vol. 107, pp 873-891.

Bauer, E. (1996) "Calibration of a comprehensive hypoplastic model for granular materials," *Soils and Foundations*, Vol. 36, No. 1, pp 13–26.

Bauer, E. (2009) "Hypoplastic modelling of moisture-sensitive weathered rockfill materials," *Acta Geotechnica*, Vol. 4, No. 4, pp 261-272.

Bauer, E. , and Y. Zhu (2004) "Constitutive modeling of the influence of pressure,density and moisture content on the mechanical behavior of rockfillmaterials.," *Proceedings of the 4th International Conference on Dam Engineering*. Nanjing: Rotterdam: Balkema, pp 139–146.

Bear, J. (1972) *Dynamics of fluids in porous media*, New York: Dover.

Blanton, T. L. (1981) "Effect of strain rates from 10-2 to 10 Sec-1 in triaxial compression tests on three rocks," *International Journal of Rock Mechanics and Mining Sciences*, Vol. 18, No. 1, pp 47-62.

Bolton, M.D. (1986) "The strength and dilatancy of sands," *Géotechnique*, Vol. 36, pp 65-78.

Boncompain, B., and M. Massiéra (1991) "Complexe La Grande - phase I - Déformation de noyaux de remblais zonés durant la construction : influence du zonage et de la nature des matériaux," *44th Canadian Geotechnical Conference*. Calgary, pp 98.91-98.98.

Bonelli, S., and P. Anthiniac (2000) "Modélisation hydroplastique du premier remplissage d'un barrage en enrochements," *53rd Canadian Geotechnical Conference*. Montréal, pp 255-262.

Broughton, N.O. (1970) "Elastic analysis for behavior of rockfill," *J. Soil Mechanics and Foundations Division, American Society of Civil Engineers*, Vol. Sept., pp 1715-1733.

Burland, J.B. (1965) "Some aspects of mechanical behavior of partly saturated soils," *International research and engineering conference on expansive clay soils*. Butterworth,Australia, pp 270-278.

Casagrande, A. (1965) "Hohe Staudamme." Vienna: Institute for Foundation Engineering and Soil Mechanics,Technische Hochschule, p 32.

Chu, Bin-Lin, Yeun-Wen Jou, and Meng-Chia Weng (2010) "A constitutive model for gravelly soils considering shear-induced volumetric deformation," *Canadian Geotechnical Journal*, Vol. 47, No. 6, pp 662-673.

Costa, L.M., and E. E Alonso (2009) "Predicting the behavior of an earth and rockfill dam under construction," *Journal of geotechnical and geoenvironmental engineering*, Vol. 135, No. 7, pp 851–862.

Cruz, P. T., B. Materón, and M. Freitas (2009) *Concrete face rockfill dams*, Leiden, The Netherlands: CRC Press/Balkema.

Cundall, P.A. (1987) *Distinct element models of rock and soil structures*: E.T. Brown, ed. London: George Allen and Unwin.

Duncan, J. M. (1992) "State-of-the-Art - Static Stability and Deformation Analysis," *Stability and Performance of Slopes and Embankments-Ii, Vols 1 and 2*, Vol. 31, pp 222-266.

Duncan, J. M. (1994) "The Role of Advanced Constitutive Relations in Practical Applications," *Thirteenth International Conference on Soil Mechanics and Foundation Engineering, Proceedings, Vol 5*, pp 31-48.

Duncan, J. M., P. Byrne, K.S. Wong, and P.M. Mabry (1980a) "Strength, stress-stain and bulk modulus parameters for finite element analyses of stresses and movements in soil masses." Berkeley: University of California.

Duncan, J. M., and C.Y. Chang (1970) "Nonlinear Analysis of Stress and Strain in Soils," *Journal of the Soil Mechanics and Foundations Division ASCE*, Vol. 96, No. 5, pp 1629-1653.

Duncan, J. M., H. B. Seed, K.S. Wong, and Y. Ozawa (1984) "FEADAM-84: A computer program for finite element analysis of dams." Berkeley: University of California.

Duncan, J. M., K.S. Wong, and Y. Ozawa (1980b) "FEADAM: A computer program for the finite element analysis of dams." Berkeley: University of California.

Eisenstein, Z., and S. T. C. Law (1977) "Analysis of Consolidation Behavior of Mica Dam," *Journal of the Geotechnical Engineering Division-ASCE*, Vol. 103, No. 8, pp 879-895.

Escuder, I. (2001) "Estudio del comportamiento tenso-deformacional de pedraplenes inundables mediante simulaciones numericas formuladas en diferencias finitas y calibradas con lecturas de instrumentacion." Valencia, Spain: Universidad Politecnica de Valencia.

Escuder, I., J. Andreu, and M. Rechea (2005) "An analysis of stress-strain behaviour and wetting effects on quarried rock shells," *Canadian Geotechnical Journal*, Vol. 42, pp 51-60.

Feizi-Khankandi, S., A.A. Mirghasemi, A. Ghalandarzadeh, and K. Hoeg (2008) "2D Nonlinear Analysis of Asphaltic Concrete - Core Embankment Dams ", *The 12th International Conference of International Association for Computer Methods and Advances in Geomechanics (IACMAG)* Goa, India

Fu, Z. , and E. Bauer (2009) "Hypoplastic constitutive modeling of the long term behaviour and wetting deformation of weathered granular materials," In: E. Bauer, S. Semprich, and G. Zenz, Eds., *Second International Conference on Long Term Behavior of Dams*. Graz., pp 437–478.

Garneau, R., J. J. Paré, N. S. Verma, and D. Cruickshank (1982) "Behaviour of the LG-4 main dam during construction," *35th Canadian Geotechnical Conference*. Montréal, pp 258-278.

Geddes, W. G. N., G. Rocke, J. Scrimgeo, M. F. Kennard, R. Glossop, H. W. Godden, R. K. Loraine, V. H. Collingr, W. B. Wilkinso, A. C. Allen, A. D. M. Penman,

T. Dymock, R. M. Telling, F. J. Kaul, A. Mcgown, R. C. S. Walters, A. L. Little, and N. G. Reid (1973) "Backwater Dam," *Proceedings of the Institution of Civil Engineers Part 1-Design and Construction*, Vol. 54, No. Feb, pp 133-155.

Giron, F.C. (1997) "Collapse settlement in the Canales dam," *19th International Congress on Large Dams*. Florence: ICOLD, pp 197-203.

Graham, J., and G. T. Houlsby (1983) "Anisotropic Elasticity of a Natural Clay," *Géotechnique*, Vol. 33, No. 2, pp 165-180.

Gudehus, G. (2004) "A visco-hypoplastic constitutive relation for soft soils," *Soils and Foundations*, Vol. 44, No. 4, pp 11-25.

Gudehus, G. (1996) "A comprehensive constitutive equation for granular materials " *Soils and Foundations*, Vol. 36, No. 1, pp 1-12.

Habib, P. , and M.P. Luong (1978) "Sols pulvérulents sous chargement cyclique," *Séminaire Matériaux et Structures Sous Chargement Cyclique*: école Polytechnique, pp 49-79.

Hall, E.B., and B.B. Gordon (1963) "Triaxial testing with large scale high pressure equipment," *STP 361-Laboratory shear testing of soils*: ASTM, pp 315-328.

Hendron, A. J. (1963) "The Behavior of Sand in One-Dimensional Compression." Urbana, Illinois: University of Illinois.

Houlsby, G.T. (1991) "How the dilatancy of soils affects their behaviour," *10th European Conference on Soil Mechanics and Foundation Engineering (ECSMFE)*. Florence: A.A. Balkema, Rotterdam, pp 1189-1202.

Huang, W., W. Wu, D.A. Sun, and S. Sloan (2006) "A simple hypoplastic model for normally consolidated clay," *Acta Geotechnica*: Springer, pp 15-27.

Hunter, G., and R. Fell (2003) "The deformation behaviour of embankment dams." Sydney: University of New South Wales.

ITASCA Consulting Group, Inc. (2008) "FLAC: Fast Lagrangian Analysis of Continua." Minneapolis.

Jansen, R.B. (1988) *Advanced Dam Engineering*, New York: Van Nostrand Reinolds Publishing.

Justo, J. L., and J. Saura (1983a) "3-Dimensional Analysis of Infiernillo Dam during Construction and Filling of the Reservoir," *International Journal for Numerical and Analytical Methods in Geomechanics*, Vol. 7, No. 2, pp 225-243.

Justo, J. L., J. Saura, and F. Segovia (1989) "A three-dimensional finite element method for the study of the behavior of embankment dams with thin earth core during construction and filling of the reservoir," pp 217-224.

Justo, J.L. (1988) "The failure of the impervious facing of Martin Gonzalo rockfill dam," *Sixteenth International Congress on Large Dams*. San Francisco, pp 252-262.

Justo, J.L. (1991) "Collapse : its importance, fundamentals and modelling," In: E. Maranha das Neves, Ed., *Advances in Rockfill Structures*. Netherlands: Kluwer Academic Publishers, pp 97-152.

Justo, J.L., and J. Saura (1983b) "Three-dimensional analysis of Infiernillo dam during construction and filling of the reservoir," *Int. Jour. Num. Anal. Meth. Gemech.*, Vol. I, No. 7, pp 225-243.

Kiekbusch, M., and B. Schuppener (1977) "Membrane Penetration and Its Effect on Pore Pressures," *Journal of the Geotechnical Engineering Division - ASCE*, Vol. 103, No. 11, pp 1267-1279.

King, I.P. (1965) "Finite element analysis of two-dimensional time-dependent stress problems," Univesity of California, Berkeley.

Konder, R.L. , and J.S. Zelasko (1963) "Hyperbolic stress-strain response: cohesive soils," *Journal of the Soil Mechanics and Foundations Division*, Vol. 89, No. 1, pp 115–143.

Kovacevic, N. , D. M. Potts, and P. R. Vaughan (2008) "Recent advances in the numerical modelling of embankment dams," *15th Conference of the British Dam Society: Ensuring Reservoir Safety into the Future*: Thomas Telford Ltd, pp 164-176.

Kovacevic, N., D. M. Potts, and P. R. Vaughan (1994) "Finite-Element Analysis of a Rockfill Dam," *Computer Methods and Advances in Geomechanics, Vol 3*, pp 2459-2464.

Lade, P. V. (1977) "Elastoplastic Stress-Strain Theory for Cohesionless Soil with Curved Yield Surfaces," *International Journal of Solids and Structures*, Vol. 13, No. 11, pp 1019-1035.

Lade, P. V., and S. B. Hernandez (1977) "Membrane Penetration Effects in Undrained Tests," *Journal of the Geotechnical Engineering Division-ASCE*, Vol. 103, No. 2, pp 109-125.

Lade, P. V., C. D. Liggio, and J. Nam (2009) "Strain Rate, Creep, and Stress Drop-Creep Experiments on Crushed Coral Sand," *Journal of geotechnical and geoenvironmental engineering - ASCE*, Vol. 135, No. 7, pp 941-953.

Lade, P. V., J. Nam, and C. D. Liggio (2010) "Effects of Particle Crushing in Stress Drop-Relaxation Experiments on Crushed Coral Sand," *Journal of geotechnical and geoenvironmental engineering*, Vol. 136, No. 3, pp 500-509.

Lade, P. V., and R. B. Nelson (1984) "Incrementalization Procedure for Elasto-Plastic Constitutive Model with Multiple, Intersecting Yield Surfaces," *International Journal for Numerical and Analytical Methods in Geomechanics*, Vol. 8, No. 4, pp 311-323.

Lade, P.V. , and H. Karimpour (2010) "Static fatigue produces time effects in granular materials," *ASCE Proc. Advances in Analysis, Modeling and Design, GeoFlorida*.

Lade, P.V., and J. M. Duncan (1975) "Elasto-plastic stress-strain theory for cohesionless soil with curved yield surfaces," *ASCE, GT Div.*, Vol. 101, pp 1037-1053.

Lemaître, J., and J.-L. Chaboche (1990) *Mechanics of solid materials*, Cambridge: Cambridge University Press.

Leps, T.M. (1970) "Review of shearing strength of rockfill," *J. Soil Mechanics and Foundations Division - ASCE*, Vol. 96, No. SM4, pp 1159-1170.

Leroueil, S., and D.W. Hight (2002) "Behaviour and properties of natural soils and soft rocks," *Workshop on Characterization and Engineering Properties of Natural Soils*. Swets and Zeitlinger, The Netherlands: Tan et al. eds., pp 29-254.

Lo Presti, D. C. F., O. Pallara, A. Cavallaro, and M. Maugeri (1999) "Non-linear stress-strain modelling of geomaterials under stable and unstable cyclic loading," *Earthquake Geotechnical Engineering, Vols 1-3*, pp 29-34.

Lowe, J. (1964) "Shear Strength of Coarse Embankment Dam Materials," *Proc. 8th International Congress on Large Dams*, pp 745-761.

Marachi, A.M., C.K. Chan, and H.R. Seed (1972) "Evaluation of Properties of Rockfill Materials,," *J. Soil Mechanics and Foundations Division - ASCE*, Vol. 98 No. SM1, pp 95-114.

Marachi, N.D., C.K. Chan, H.B. Seed, and J.M. Duncan (1969) "Strength and Deformation Characteristics of Rockfill Materials." Berkeley, USA: Civil Eng. Dept., Univ. of California.

Maranha das Neves, E., and A. Veiga Pinto (1989) "Modeling collapse on rockfill dams," *Computers and Geotechnics*, Vol. 6, No. 2, pp 131-153.

Marsal, R.J. (1967) "Large scale testing of rockfill material," *Journal of the Soil Mechanics and Foundations Division ASCE*, Vol. 93, No. 2, pp 27-43.

Masin, D. (2005) "A hypoplastic constitutive model for clays," *International Journal for Numerical and Analytical Methods in Geomechanics*, Vol. 29, No. 4, pp 311-336.

Masin, D. (2007) "A hypoplastic constitutive model for clays with meta-stable structure," *Canadian Geotechnical Journal*, Vol. 44, No. 3, pp 363-375.

Massiéra, M. , B. Boncompain, and J. Merheb-Harb (1999) "Interprétation des mesures inclinométriques durant la construction des remblais zonés des ouvrages de retenue du Complexe la Grande, phase I," *Canadian Geotechnical Journal*, Vol. 36, No. 3, pp 533-543

Massiéra, M., B. Boncompain, Y. Fakhri, and G. Lessard (1989) "Comportement contraintes-déformations du barrage LG-4," *42nd Canadian Geotechnical Conference*. Winnipeg, pp 196-207.

Matesic, L., and M. Vucetic (2003) "Strain-Rate Effect on Soil Secant Shear Modulus at Small cyclic strains," *Journal of geotechnical and geoenvironmental engineering*, Vol. 129, No. 6, pp 536–549.

Matsuoka, H., and T. Nakai (1974) "Stress-deformation and strength characteristics of soil under three different principal stresses," *Proc. JSCE, No. 232*, pp 59–70.

Mehta, P.K. , and P.J.M. Monteiro (1993) *Concrete: Structure, Properties, and Materials*, Englewood Cliffs, New Jersey: Prentice-Hall.

Mellah, R., G. Auvinet, and F. Masrouri (2000) "Stochastic finite element method applied to non-linear analysis of embankments," *Probabilistic Engineering Mechanics*, Vol. 15, No. 3, pp 251–259.

Merheb-Harb, J. (1993) "Influence de la géométrie, du zonage et de la nature de la moraine sur le comportement des barrages en remblai," *École de génie*. Moncton, N.B.: Université de Moncton.

Mitchell, J. K. (1976) *Fundamentals of soil behavior*, New York: Wiley.

Molenkamp, F., and H. J. Luger (1981) "Modeling and Minimization of Membrane Penetration Effects in Tests on Granular Soils," *Géotechnique*, Vol. 31, No. 4, pp 471-486.

Naylor, D. J. (1991) "Stress - Strain Laws and Parameter Values," *Advances in Rockfill Structures*, Vol. 200, pp 269-290.

Naylor, D. J., E. M. Dasneves, D. Mattar, and A. A. V. Pinto (1986) "Prediction of Construction Performance of Beliche Dam," *Géotechnique*, Vol. 36, No. 3, pp 359-376.

Naylor, D. J., and G. N. Pande (1981) *Finite elements in geotechnical engineering*, Swansea, U.K.: Pineridge Press.

Naylor, D. J., K. G. Stagg, and O. C. Zienkiewicz (1975) *Criteria and assumptions for numerical analysis of dams*, Swansea, U.K.

NGI (1987) "Analysis of displacements and stresses in Storvatn dam." Oslo, Norvege: Norwegian Geotechnical Institute.

Nobari, E.S., and J.M. Duncan (1972) "Effect of reservoir filling on stresses and movements in earth and rockfill dams." Berkley: University of California, p 165.

Oldecop, L. A. , and E. E. Alonso (2001) "A model for rockfill compressibility," *Géotechnique*, Vol. 51, No. 2, pp 127-139.

Oldecop, L. A., and E. E. Alonso (2007) "Theoretical investigation of the time-dependent behaviour of rockfill," *Géotechnique*, Vol. 57, No. 3, pp 289–301.

Omidvar, M. , Iskander M., and Bless S. (2012) "Stress-strain behavior of sand at high strain rates," *International Journal of Impact Engineering*.

Ozawa, Y., and J. M. Duncan (1973) " ISBILD: a computer program for analysis of static stresses and movement in embankment." Berkeley: University of California.

Paré, J. J., N. S. Verma, H. M. S. Keira, and A. D. McConnell (1984) "Stress-deformation predictions for the LG 4 main dam," *Canadian Geotechnical Journal*, Vol. 21, No. 2, pp 213–222.

Penman, A. D. M., J. B. Burland, and J. A. Charles (1971) "Observed and Predicted Deformations in a Large Embankment Dam during Construction," *Proceedings of the Institution of Civil Engineers*, Vol. 49, No. May, pp 1-21.

Potts, D. M., and L. Zdravković (1999) *Finite element analysis in geotechnical engineering - theory*, London Reston, VA: Telford ; Distributed by ASCE Press.

Potts, D.M., and L. Zdravkovic (2001) *Finite element analysis in geotechnical engineering: volume two - application*, London: Thomas Telford.

Press, W.H. , S.A. Teukolsky, W.T. Vetterling, and B.P. Flannery (2007) *Numerical Recipes: The Art of Scientific Computing*, New York: Cambridge University Press.

Rowe, P. W. (1971) "Theoretical meaning and observed values of deformation parameters for soil " In: R. H. G. Parry, Ed., *Roscoe Memorial Symposium*. Cambridge University, pp 143–194.

Rowe, P.W. (1962) "The stress-dilatancy relation for static equilibrium of an assembly of particles in contact," *Proc. R. Soc.* , pp 500-527.

Rűsch, H. (1960) "Researches toward a general flexural theory for structural concrete," *American concrete institute*, Vol. 57, No. 1, pp 1-28.

Saboya, F. J., and P. M. Byrne (1993) "Parameters for stress and deformation analysis of rockfill dams," *Can. Geotech. J.*, Vol. 30, No. 4, pp 690-701.

Schanz, T., and P.A. Vermeer (1996) "Angles of friction and dilatancy of sand," *Géotechnique*, Vol. 46, No. 1, pp 145–151.

Seed, H.B., J.M. Duncan, and I.M. Idriss (1975) "Criteria and methods for static and dynamic analysis of earth dams," In: Stagg & Zienkiewicz Naylor, Ed., *Int. Symp. Criteria and assumptionsfor numercal analysis of dams*, pp 564-588.

Silvani, C., T. ´ Desoyer, and S. Bonelli (2009) "Discrete modelling of time-dependent rockfill behaviour," *Int. J. Numer. Anal. Meth. Geomech.*, Vol. 33, pp 665–685.

Singh, M. K., J. S. Sharma, and I. R. Fleming (2009) "A design chart for estimation of horizontal displacement in municipal landfills," *Waste Management*, Vol. 29, No. 5, pp 1577-1587.

Skinner, A.E. (1975) "The effect of high pore water pressures on the mechanical behavior of sediments," Imperial college, University of London.

Smith, M., and J. M. Konrad (2011) "Assessing hydraulic conductivities of a compacted dam core using geostatistical analysis of construction control data," *Canadian Geotechnical Journal*, Vol. 48, No. 9, pp 1314-1327.

Szostak-Chrzanowski, A., and M. Massiéra (2004) "Modelling of deformations during construction of a large earth dam in the La Grande Complex, Canada." Olsztyn, Poland: Technical Sciences, UWM, pp 107-121.

Tatsuoka, F., H. Di Benedetto, T. Enomoto, S. Kawabe, and W. Kongkitkul (2008) "Various viscosity types of geomaterials in shear and their mathematical expression," *Soils and Foundations*, Vol. 48, No. 1, pp 41-60.

Tatsuoka, F., R.J. Jardine, D.C.F. LoPresti, H. DiBenedetto, and T. Kodaka (1997) "Theme Lecture: Characterizing the pre-failure deformation properties of geomaterials. In Proceedings of the," *14th International Conference on Soil Mechanics and Foundation Engineering*. Hamburg, Germany: A.A. Balkema, Rotterdam, the Netherlands, pp 2129–2164.

Taylor, D.W. (1948) *Fundamentals of soil mechanics*, New York: John Wiley.

Terzaghi, K. (1943) *Theoritical soil mechanics*, New York: John Wiley.

Touileb, B.N., S. Bonelli, P. Anthiniac, A. Carrere, O. Debordes, G. La Barbera, A. Bani, and G. Mazza (2000) "Settlement by Wetting of the Upstream Rockfills of Large Dams," *Proceedings of 53-rd Canadian Geotechnical Conference*, pp 263-270.

Verma, N. S., J. J Paré, B. Boncompain, R. Garneau, and A. Rattue (1985) "Behaviour of the LG-4 main dam," *11th conference of ICSMFE*. San Francisco: Balkema, Rotterdam, pp 2049–2054.

Weng, M.C., Jeng F.S., T.M. Hsieh, and T.H. Huang (2008) "A simple model for stress-induced anisotropic softening of weak sandstones," *International Journal of Rock Mechanics and Mining Sciences*, Vol. 45, pp 155-166.

Whitman, R. V. (1957a) "Testing soils with transient loads," *Soils for Engineering Purposes, ASTM Committee D-18*. Philadelphia: ASTM Special Technical Publication No. 232, pp 249–252.

Whitman, R. V. (1957b) "The behaviour of soils under transient loadings," *4th Int. Conf. on Soil Mechanics and Foundation Engineering*. London: Butterworths Scientific Publications, pp 207-210.

Wong, K.S., and J. M. Duncan (1974) "Hyperbolic stress-strain parameters for nonlinear finite element analysis of stresses and movements in soil masses." Berkeley: University of California.

Appendix 1 – FISH scripts

FISH is a programming language embedded within FLAC that enables the user to define new variables and functions. These functions may be used to extend FLAC's usefulness or add user-defined features. For example, new variables may be plotted or printed, special grid generators may be implemented, servo-control may be applied to a numerical test, unusual distributions of properties may be specified, and parameter studies may be automated.

FISH is a "compiler" (rather than an "interpreter"). Programs entered via a FLAC data file are translated into a list of instructions (in "pseudo-code") stored in FLAC's memory space; the original source program is not retained by FLAC. Whenever a FISH function is invoked, its compiled pseudo-code is executed. The use of compiled code (rather than interpreted source code) enables programs to run much faster. However, unlike a compiler, variable names and values are available for printing at any time.

New constitutive models may be written in the FISH language. Once compiled successfully, a new model behaves just like a built-in model as far as the user is concerned. A user-defined model can also use properties that are defined and given names by the model's author; these names act just like built-in properties. User-written models execute more slowly than built-in models. After optimization, a FISH model will typically run somewhere between one-quarter and one-third the speed of a built-in model. However, quite often, a user-written model needs only to be installed in a small part of the FLAC grid, since the particular behavior that it is designed to reproduce may only occur locally; the material elsewhere can be represented by a standard model. In any case, the increased runtimes of the special model may be compensated by decreased human time and effort, since less work may be done trying to force-fit an inappropriate model.

A user-written constitutive model is simply a FISH function containing some special statements and references to special variables that correspond to local entities within a single zone. The user-defined model (referred to as "UDM") is called by FLAC four times per zone (once per triangular subzone) for every solution step. It is the task of the UDM to supply a new set of stress components, given strain increments and the

old set of stress components. The fish scripts for the elastoplastic UDM and also the new procedures for the stress relaxation due to wetting are presented in the following two sections.

1- HPD model (UDM)

```
set echo off
def m_duncan
  constitutive_model 111
; Duncan parameters
  f_prop  d_k    d_kb    d_n    d_m    d_rf   d_pa
  f_prop  d_kw   d_kbw   d_nw   d_mw   d_rfw  d_betta d_s3t
  f_prop  d_coh  d_fric  d_nu   d_ms3
  f_prop  d_bulk d_shear d_kmax d_gmax
  f_prop  d_nphi d_csnp  d_cotp
  f_prop  d_poisson d_elas d_s1 d_s3 d_s d_t hyp_min elas_min
  f_prop  d_s2 d_q d_p
  f_prop  d_dphi d_phio m_ddil m_dilo
  float $elas $bulk $dif $dia $ms3 $ms1 $e1 $e2 $cap
  float $sphi $nphi $as11 $as22 $as33 $as12 $sl $aux $ei
  int   $m_err

; checking Duncan
  f_prop auxx           ;ultimate derivative stress
  f_prop hypp1 hypp2     ;hyperbolic functions 1:mathematical, 2:corrected(hyp_min)

; Mohr criteria
  f_prop  m_dil m_ten m_ind
  f_prop  m_csnp m_nphi m_npsi m_e1 m_e2 m_x1 m_sh2
  float   $spsi $s11i $s22i $s12i $s33i $sdif $s0 $rad $s1 $s2 $s3
  float   $si $sii $psdif $fs $alams $ft $alamt $cs2 $si2 $dc2 $dss
  float   $apex $pdiv $anphi $bisc $tco
  int     $icase

  f_prop  ini_d

; checking Mohr
;  f_prop  m_s1 m_s2 m_s3

  Case_of  mode
; ----------------------
; Initialisation section
; ----------------------
    Case 1
      hyp_min  = 0.05
      $cap     = d_pa /10.0
;      elas_min = d_k * d_pa * ($cap/d_pa)^d_n
      $m_err   = 0
      if d_fric > 89.0 then
```

```
      $m_err = 2
    end_if
    if d_coh  < 0.0 then
      $m_err = 3
    end_if
    if d_pa <= 0. then
      d_pa = 1.0
    end_if
    if d_nu >= 0.49 then
      d_nu = 0.49
    end_if
    if $m_err # 0 then
      nerr  = 126
      error = 1
   end_if

; --- frictional constants ---

;====== ==========Mohr initiation====================1
    $spsi    = sin (m_dil * degrad)
    m_nphi  = (1.0 + $sphi) / (1.0 - $sphi)
    m_npsi  = (1.0 + $spsi) / (1.0 - $spsi)
    m_csnp  = 2.0 * d_coh * sqrt(m_nphi)
    m_e1    = d_bulk+ 4.0 * d_shear/ 3.0
    m_e2    = d_bulk- 2.0 * d_shear/ 3.0
    m_x1    = m_e1 - m_e2*m_npsi + (m_e1*m_npsi - m_e2)*m_nphi
    m_sh2   = 2.0 * d_shear
    if abs(m_x1) < 1e-6 * (abs(m_e1) + abs(m_e2)) then
      $m_err = 5
      nerr  = 126
      error = 1
    end_if
; --- set tension to prism apex if larger than apex ---
    $apex = m_ten
    if d_fric # 0.0 then
      $apex = d_coh / tan(d_fric * degrad)
    end_if
    m_ten = min($apex,m_ten)
;==================Mohr initiation====================2

    $sphi  = sin (d_fric * degrad)
    $nphi  = (1.0 + $sphi) / (1.0 - $sphi)
    d_csnp = 2.0 * d_coh * sqrt($nphi)
    d_nphi = $nphi - 1.0
    if d_fric # 0.0 then
      d_cotp = d_coh / tan(d_fric * degrad)
    else
      d_cotp = 0.0
    end_if
   Case 2
```

```
; ---------------
; Running section
; ---------------
;===================Mohr stresses=======================1
     zvisc = 1.0
     if m_ind # 0.0 then
       m_ind = 2.0
     end_if
     $anphi = m_nphi
; --- get new trial stresses from old, assuming elastic increments ---
     $s11i  = zs11 + (zde22 + zde33) * m_e2 + zde11 * m_e1
     $s22i  = zs22 + (zde11 + zde33) * m_e2 + zde22 * m_e1
     $s33i  = zs33 + (zde11 + zde22) * m_e2 + zde33 * m_e1
     $s12i  = zs12 + zde12 * m_sh2
     $sdif  = $s11i - $s22i
     $s0    =  0.5 * ($s11i + $s22i)
     $rad   =  0.5 * sqrt ($sdif*$sdif + 4.0 * $s12i*$s12i)
; --- principal stresses ---
     $si    =  $s0 - $rad
     $sii   =  $s0 + $rad
     $psdif =  $si - $sii

; --- determine case ---
     section
       if $s33i > $sii then
; --- s33 is major p.s. ---
         $icase = 3
         $s1    = $si
         $s2    = $sii
         $s3    = $s33i
         exit section
       end_if
       if $s33i < $si then
; --- s33 is minor p.s. ---
         $icase = 2
         $s1    = $s33i
         $s2    = $si
         $s3    = $sii
         exit section
       end_if
; --- s33 is intermediate ---
       $icase = 1
       $s1    = $si
       $s2    = $s33i
       $s3    = $sii
     end_section

; verify mohr
;      m_s1=$s1
;      m_s2=$s2
```

```
;      m_s3=$s3

;=====================Mohr stresses=====================2

;=====================Mohr Criteria=====================1
     section
; --- shear yield criterion ---
       $fs    = $s1 - $s3 * $anphi + m_csnp
       $alams = 0.0
; --- tensile yield criterion ---
       $ft    = m_ten - $s3
       $alamt = 0.0
; --- tests for failure ---
       if $ft < 0.0 then
         $bisc = sqrt(1.0 + $anphi * $anphi) + $anphi
         $pdiv = -$ft + ($s1 - $anphi * m_ten + m_csnp) * $bisc
         if $pdiv < 0.0 then
; ---      shear failure ---
           $alams = $fs / m_x1
           $s1 = $s1 - $alams * (m_e1 - m_e2 * m_npsi)
           $s2 = $s2 - $alams * m_e2 * (1.0 - m_npsi)
           $s3 = $s3 - $alams * (m_e2 - m_e1 * m_npsi)
           m_ind = 1.0
         else
; ---      tension failure ---
           $alamt = $ft / m_e1
           $tco= $alamt * m_e2
           $s1 = $s1 + $tco
           $s2 = $s2 + $tco
           $s3 = m_ten
           m_ind = 3.0
           m_ten = 0.0
         end_if
       else
         if $fs < 0.0 then
; ---      shear failure ---
           $alams = $fs / m_x1
           $s1 = $s1 - $alams * (m_e1 - m_e2 * m_npsi)
           $s2 = $s2 - $alams * m_e2 * (1.0 - m_npsi)
           $s3 = $s3 - $alams * (m_e2 - m_e1 * m_npsi)
           m_ind = 1.0
         else
; ---      no failure ---
           zs11 = $s11i
           zs22 = $s22i
           zs33 = $s33i
           zs12 = $s12i
           exit section
         end_if
       end_if
```

```
; --- direction cosines ---
       if $psdif = 0.0 then
         $cs2   = 1.0
         $si2   = 0.0
       else
         $cs2   = $sdif       / $psdif
         $si2   = 2.0 * $s12i / $psdif
       end_if
; --- resolve back to global axes ---
       case_of  $icase
        case 1
          $dc2  = ($s1 - $s3) * $cs2
          $dss  =  $s1 + $s3
          zs11  = 0.5 * ($dss + $dc2)
          zs22  = 0.5 * ($dss - $dc2)
          zs12  = 0.5 * ($s1  - $s3) * $si2
          zs33  = $s2
        case 2
          $dc2  = ($s2 - $s3) * $cs2
          $dss  =  $s2 + $s3
          zs11  = 0.5 * ($dss + $dc2)
          zs22  = 0.5 * ($dss - $dc2)
          zs12  = 0.5 * ($s2  - $s3) * $si2
          zs33  = $s1
        case 3
          $dc2  = ($s1 - $s2) *$cs2
          $dss  =  $s1 + $s2
          zs11  = 0.5 * ($dss + $dc2)
          zs22  = 0.5 * ($dss - $dc2)
          zs12  = 0.5 * ($s1  - $s2) * $si2
          zs33  = $s3
       end_case
       zvisc = 0.0
     end_section
;====================Mohr Criteria====================2

; --- accumulate stresses for the zone ---
     $as11 = $as11 + zs11
     $as22 = $as22 + zs22
     $as33 = $as33 + zs33
     $as12 = $as12 + zs12
; --- update properties ---
     if zsub > 0.0 then
       $as11 = $as11 / zsub
       $as22 = $as22 / zsub
       $as33 = $as33 / zsub
       $as12 = $as12 / zsub
;      - minor compressive stress -
       $dif = $as11 - $as22
       $dia = sqrt ($dif*$dif + 4.0 * $as12 * $as12)
```

```
      $ms3 = min(-($as11 + $as22 + $dia) * 0.5,-$as33)
      d_s3 = $ms3
      $ms3 = max($ms3,$cap)
;     - major compressive stress -
      $ms1 = max(-($as11 + $as22 - $dia) * 0.5,-$as33)
      d_s1 = $ms1
      $ms1 = max($ms1,$cap)
      d_s2 = -($as11+$as22+$as33+d_s1+d_s3)
;-----------------------------------------------------------------
    if m_ind = 0.0 then       ;**check for plasticity
;     - new moduli -
      $aux = $ms3 * d_nphi + d_csnp
      $sl  =  max($ms1 - $ms3,0.0) / $aux
      $ei  = d_k * d_pa * ($ms3/d_pa)^d_n
      $elas= (1.0 - d_rf * $sl)^2 * $ei
;     minimum hyp
      $elas= max($elas,hyp_min*$ei)
;----------checking Duncan----------------
      auxx=$aux
      hypp1 = (1.0 - d_rf * $sl)^2
      hypp2 = $elas / $ei
;----------------------------------------
      $elas = min($elas,$ei)
      if d_kb = 0.0 then
;       - Poisson's ratio is constant -
        d_bulk    = $elas / (3.0 * (1.0 - 2.0 * d_nu))
        d_shear   = $elas / (2.0 * (1.0 + d_nu))
        d_poisson = (3.0 * d_bulk - 2.0 * d_shear) / (6.0 * d_bulk + 2.0 * d_shear)
        d_elas    = (9.0 * d_bulk * d_shear) / (3.0 * d_bulk + d_shear)
      else
;       - Poisson's ratio between 0 and 0.49 -
        $bulk   = d_kb * d_pa * ($ms3/d_pa)^d_m
        $bulk   = min($bulk, 17.0 * $elas)
        $bulk   = max($bulk, $elas / 3.0)
        d_bulk  = $bulk
        d_shear = 3.0 * $elas * $bulk / (9.0 * $bulk - $elas)
        d_poisson = (3.0 * d_bulk - 2.0 * d_shear) / (6.0 * d_bulk + 2.0 * d_shear)
        d_elas    = (9.0 * d_bulk * d_shear) / (3.0 * d_bulk + d_shear)
      end_if
    else                  ;**bypassing Duncan to Mohr model
      d_bulk    = d_kb * d_pa
      d_elas    = d_k  * d_pa
      d_shear   = 3.0  * d_elas * d_bulk / (9.0 * d_bulk – d_elas)
      d_poisson = (3.0 * d_bulk - 2.0 * d_shear) / (6.0 * d_bulk + 2.0 * d_shear)
    end_if
      $as11 = 0.0
      $as22 = 0.0
      $as33 = 0.0
      $as12 = 0.0
      d_s   = (d_s1 + d_s3) / 2.0
```

```
      d_t   = (d_s1 - d_s3) / 2.0
      d_q   = (d_s1 - d_s3)
      d_p   = (d_s1 + d_s2 + d_s3) / 3.0

;==============Mohr parameters update====================1
; ---stress dependent dialation and friction angle---
      d_fric  = d_phio - d_dphi * log($ms3/ d_pa)
      d_fric  = max (d_phio / 2.0 , d_fric)
      d_fric  = min (d_phio       , d_fric)
      m_dil   = m_dilo - m_ddil * log($ms3/ d_pa)
      m_dil   = max (0.0    , m_dil)
      m_dil   = min (m_dilo , m_dil)
; --- intermidiate parameters---
      $sphi   = sin (d_fric * degrad)
      $spsi   = sin (m_dil * degrad)
      m_nphi  = (1.0 + $sphi) / (1.0 - $sphi)
      m_npsi  = (1.0 + $spsi) / (1.0 - $spsi)
      m_csnp  = 2.0 * d_coh * sqrt(m_nphi)
      m_e1    = d_bulk+ 4.0 * d_shear/ 3.0
      m_e2    = d_bulk- 2.0 * d_shear/ 3.0
      m_x1    = m_e1 - m_e2*m_npsi + (m_e1*m_npsi - m_e2)*m_nphi
      m_sh2   = 2.0 * d_shear
      if abs(m_x1) < 1e-6 * (abs(m_e1) + abs(m_e2)) then
        $m_err = 5
        nerr  = 126
        error = 1
      end_if
; --- set tension to prism apex if larger than apex ---
      $apex = m_ten
      if d_fric # 0.0 then
        $apex = d_coh / tan(d_fric * degrad)
      end_if
      m_ten = min($apex,m_ten)
      $nphi  = (1.0 + $sphi) / (1.0 - $sphi)
      d_csnp = 2.0 * d_coh * sqrt($nphi)
      d_nphi = $nphi - 1.0
      if d_fric # 0.0 then
        d_cotp = d_coh / tan(d_fric * degrad)
      else
        d_cotp = 0.0
      end_if
;==================Mohr parameters update=================2

    end_if
  Case 3
; ----------------------
; Return maximum modulus
; ----------------------
    cm_max = d_kmax + 4.0 * d_gmax / 3.0
    sm_max = d_gmax
```

```
   Case 4
; ---------------------
; Add thermal stresses
; ---------------------
     ztsa = ztea * d_bulk
     ztsb = zteb * d_bulk
     ztsc = ztec * d_bulk
     ztsd = zted * d_bulk
  End_case
end
opt m_duncan
def ini_duncan
  loop i (1,izones)
  loop j (1,jzones)
;         j = build_j
;         i = build_i
;         j = 1
         if model(i,j) = 111 then
         if ini_d(i,j) # 7 then
;         - frictional constants -
          ini_d(i,j)=7
          d_fric(i,j)=d_phio(i,j) - d_dphi(i,j) * log(-sxx(i,j) / d_pa(i,j))
          d_fric(i,j)=min(d_phio(i,j)     ,d_fric(i,j))
          d_fric(i,j)=max(d_phio(i,j)/2.0 ,d_fric(i,j))
          m_dil(i,j)   = m_dilo(i,j) - m_ddil(i,j) * log(-sxx(i,j)/ d_pa(i,j))
          m_dil(i,j)   = max (0.0    , m_dil(i,j))
          m_dil(i,j)   = min (m_dilo(i,j) , m_dil(i,j))
;
          $sphi = sin (d_fric(i,j) * degrad)
          $nphi = (1.0 + $sphi) / (1.0 - $sphi)
          $csnp = 2.0 * d_coh(i,j) * sqrt($nphi)
          $nphi = $nphi - 1.0
          if d_fric(i,j) # 0.0 then
            $cotp = d_coh(i,j) / tan(d_fric(i,j) * degrad)
;         else
            $cotp = 0.0
          end_if
;         - minor compressive stress -
          $esxx= sxx(i,j) + pp(i,j)
          $esyy= syy(i,j) + pp(i,j)
          $eszz= szz(i,j) + pp(i,j)
          $dif = $esxx - $esyy
          $dia = sqrt ($dif*$dif + 4.0 * sxy(i,j) * sxy(i,j))
          $ms3 = min(-($esxx + $esyy + $dia) * 0.5,-$eszz)
          $ms3 = max($ms3,$cap)
          $ms1 = max(-($esxx + $esyy - $dia) * 0.5,-$eszz)
          $ms1 = max($ms1,$cap)
;
          $sl  = max($ms1 - $ms3,0.0) / ($ms3 * $nphi + $csnp)
;
```

```
          $ei = d_k(i,j)  * d_pa(i,j) * ($ms3/d_pa(i,j))^d_n(i,j)
          $elas = $ei * (1.0 - d_rf(i,j) * $sl)^2
;         - initial bulk and shear from initial Young modulus -
          if d_kb(i,j) = 0.0 then
;           - Poisson's ratio is constant -
            d_bulk(i,j)  = $elas / (3.0 * (1.0 - 2.0 * d_nu(i,j)))
            d_shear(i,j) = $elas / (2.0 * (1.0 + d_nu(i,j)))
          else
;           - Poisson's ratio between 0 and 0.49 -
            $bulk   = d_kb(i,j) * d_pa(i,j) * ($ms3/d_pa(i,j))^d_m(i,j)
            $bulk   = min($bulk, 17.0 * $elas)
            $bulk   = max($bulk, $elas / 3.0)
            d_bulk(i,j)  = $bulk
            d_shear(i,j) = 3.0 * $elas * $bulk / (9.0 * $bulk - $elas)
          end_if
;         - maximum bulk and shear for stability from max s3 -
          $elas = d_k(i,j)  * d_pa(i,j) * (d_ms3/d_pa(i,j))^d_n(i,j)
          if d_kb(i,j) = 0.0 then
;           - Poisson's ratio is constant -
            d_kmax(i,j)  = $elas / (3.0 * (1.0 - 2.0 * d_nu(i,j)))
            d_gmax(i,j)  = $elas / (2.0 * (1.0 + d_nu(i,j)))
          else
            $bulk = d_kb(i,j) * d_pa(i,j) * (d_ms3/d_pa(i,j))^d_m(i,j)
            $bulk = min($bulk, 17.0 * $elas)
            $bulk  = max($bulk, $elas / 3.0)
            d_kmax(i,j)  = $bulk
            d_gmax(i,j)  = 3.0 * $elas * $bulk / (9.0 * $bulk - $elas)
          end_if
        end_if
        end_if
      end_loop
      end_loop
end
```

2- Stress relaxation due to wetting

```
def collapse
if ex_1(zi,zj) # 7 then
;-----------------------------------------------
;       Equation Definitions
;-----------------------------------------------
;  --- initialization ---
   $coh    = d_coh(zi,zj)
   $sinphi = sin(d_fric(zi,zj) * degrad)
   $cosphi = cos(d_fric(zi,zj) * degrad)
   $Pa     = d_pa(zi,zj)
   $nw     = d_nw(zi,zj)
   $mw     = d_mw(zi,zj)
   $max_relax = $pa/20
```

```
;  --- initial stress state ---
   $s11   = -syy(zi,zj)
   $s22   = -sxx(zi,zj)
   $s33   = -szz(zi,zj)
   $s12   =  sxy(zi,zj)
   $diff  = $s11 - $s22
   $diaa  = sqrt ($diff * $diff + 4.0 * $s12  * $s12)
   $si_   = ($s22 + $s11 + $diaa) / 2
   $sii_  = ($s22 + $s11 - $diaa) / 2
   $psdif_ = $si_ - $sii_
;  --- determine case ---
   section
     if $s33 < $sii_ then
;  --- s33 is minor p.s. ---
       $icase_ = 3
       $s1_    = $si_
       $s2_    = $sii_
       $s3_    = $s33
       exit section
     end_if
     if $s33 > $si_ then
;  --- s33 is major p.s. ---
       $icase_ = 2
       $s1_    = $s33
       $s2_    = $si_
       $s3_    = $sii_
       exit section
     end_if
;  --- s33 is intermediate ---
     $icase_ = 1
     $s1_    = $si_
     $s2_    = $s33
     $s3_    = $sii_
   end_section
;  $S3d   = max(($s2_+$s3_)/2,$cap)
   $Scd   = max(($s2_+$s3_)/2,$cap)
   $S3d   = $s3_
;  $Sdd   = max($s1_,$cap) - $S3d     ; no need anymore, with mohr envolope
   $Sdd   = $s1_ - $S3d
   $S1d   = $Sdd + $S3d
;  ---  direction cosines ---
   if $psdif_ = 0.0 then
     $cs2_ = 1.0
     $si2_ = 0.0
   else
     $cs2_ = $diff / $psdif_
     $si2_ = 2.0 * $s12 / $psdif_
   end_if
;==================== ========================================
;  --- dry calculation ---
```

```
  $Sddf  = (2 * $coh * $cosphi + 2 * $s3d * $sinphi) / (1 - $sinphi)
  $Eid   = d_k(zi,zj) * $Pa * (($S3d/$pa) ^ d_n(zi,zj))
  $Esd   = (1 - d_rf(zi,zj) * $Sdd / $Sddf) * $Eid
;  if $Esd < 0.0 then               ; no need anymore, with mohr envolope
;     $Esd = 0.001 * $Eid
;  end_if
  $Bd    = d_kb(zi,zj) * $pa * (($S3d/$pa) ^ d_m(zi,zj))
  $Ead   = $Sdd/$Esd
  $Evd   = $Eid / 3 / $Bd  *  $Sddf * $Ead / ($Sddf + d_rf(zi,zj) * $Eid * $Ead)
;  $Evc   = d_betta(zi,zj) * ($S3d - d_s3t(zi,zj))
  $Scd   = max(0.0,$Scd - d_s3t(zi,zj))            ;isotropic collapse, based on confining
stress
  $Evc   = d_betta(zi,zj) * $Scd
  $Evc   = max(0.0,$Evc)
  $Eac   = $Evc / 3
  $Eal   = max (0.0,$Ead - $Eac)
  $Evl   = max (0.0,$Evd - $Evc)
;
  if $Eal = 0.0 then               ; so much isotropic collapse
    $answer = $max_relax
  else
    if $Evl = 0.0 then
      $answer = $max_relax
    else
      $answer = -7.7e-7
    end_if
  end_if
;============================================================
;  --- wet calculation ---
 if $answer = -7.7e-7 then
  $a     = (2 * $coh * $cosphi) / (1 - $sinphi)
  $b     = (2 * $sinphi) / (1 - $sinphi)
  $c     = d_rfw(zi,zj) * d_kw(zi,zj) * ($pa ^ (1 - $nw)) * $Eal
  $d     = 3 * d_kbw(zi,zj) * $Evl / d_kw(zi,zj) / ($pa ^($mw - $nw)) / $Eal
;---------------------------------------------
;          Numerical Recipes
;---------------------------------------------
;  --- Bracketing the answer ---> $xb1,$xb2
  $x1    = $max_relax         ; minimum limit
  $x2    = $S3d               ; maximum limit
  $dx    = ($x2 - $x1) / 50
  $answer= 0.0
  section
    $xb1= -13.0              ;flag for success of bracketting
    $xb2= -13.0
    $xc = $x1
    $fp = ($a * ($xc ^ ($nw - $mw)) + $b * ($xc ^ (1+$nw - $mw)))
    $fp = $fp / ($a + $b * $xc + $c * ($xc ^ $nw)) - $d
    loop iii(1,50)
      $xc = $xc + $dx
```

```
      $fc = ($a * ($xc ^ ($nw - $mw)) + $b * ($xc ^ (1+$nw - $mw)))
      $fc = $fc / ($a + $b * $xc + $c * ($xc ^ $nw)) - $d
      if ($fc * $fp) < 0 then
        $xb1 = $xc - $dx
        $xb2 = $xc
        exit section
      end_if
      $fp=$fc
    end_loop
  end_section
;  ---checking the bracket function success(flag) ----
  section
;    ---define $y1, $y2---
    $y1 = ($a * ($x1 ^ ($nw - $mw)) + $b * ($x1 ^ (1+$nw - $mw)))
    $y1 = $y1 / ($a + $b * $x1 + $c * ($x1 ^ $nw)) - $d
    $y2 = ($a * ($x2 ^ ($nw - $mw)) + $b * ($x2 ^ (1+$nw - $mw)))
    $y2 = $y2 / ($a + $b * $x2 + $c * ($x2 ^ $nw)) - $d
    if $xb1=-13.0 then
      if $y1 * $y2 < 0.0     ; there is answer but bracket could not get it
        $xb1 = $x1
        $xb2 = $x2
      else
        if $y1>0 then       ; there is no answer in bracket and $y1 , $y2 > 0
          $answer = $x1
          exit section
        end_if
        if $y2<0 then       ; there is no answer in bracket and $y1 , $y2 < 0
          $answer = $x2
          exit section
        end_if
      end_if
    end_if
  end_section
;  --- Solving with Bisection method ---
  section
  if $xb2#-13.0 then
    $f    = ($a * ($xb1 ^ ($nw - $mw)) + $b * ($xb1 ^ (1+$nw - $mw)))
    $f    = $f / ($a + $b * $xb1 + $c * ($xb1 ^ $nw)) - $d
    if $f<0.0 then
      $rtb = $xb1
      $dx  = $xb2 - $xb1
    else
      $rtb = $xb2
      $dx  = $xb1 - $xb2
    end_if

    loop iii(1,40)
      $xmid = $rtb + $dx / 2
      $dx   = $dx / 2
      $fmid = ($a * ($xmid ^ ($nw - $mw)) + $b * ($xmid ^ (1+$nw - $mw)))
```

```
        $fmid = $fmid / ($a + $b * $xmid + $c * ($xmid ^ $nw)) - $d
        if $fmid <= 0.0 then
          $rtb = $xmid
        end_if
        if abs($dx) < $pa/1000 then          ;precision of the $answer= $pa/1000
          $answer = $rtb
          exit section
        end_if
        if $fmid = 0.0 then
          $answer = $rtb
          exit section
        end_if
      end_loop
      if iii>39 then
        $answer = $rtb
      end_if
    end_if
    end_section
  end_if
;=============================================================
=
; --- wet stress calculation ---
;   $s3w   = $answer
;   $coef    = 0.5/($ead ^ 0.88)
;   $coef=exp(_coef * hypp1(zi,zj))
    $coef=(10.0*($s3d/$pa))^(hypp1(zi,zj))
    $answer2  = $s3d-($s3d-$answer)/$coef
    $s3w      = $answer2
    $s3w      = min($s3w , $s3d)
    $s3w      = max($s3w , $max_relax)
;
    if hypp1(zi,zj)>0.20 then
      $Eiw   = d_kw(zi,zj) * $Pa * (($S3d/$pa) ^ $nw)
      $Sdwf  = (2 * $coh * $cosphi + 2 * $s3d * $sinphi) / (1 - $sinphi)
      $n     = $Eal * $Eiw
      $m     = d_rfw(zi,zj) * $Eiw * $Eal / $Sdwf
      $sdw   = $n / (1 + $m)
    else
      $Eiw   = d_kw(zi,zj) * $Pa * ((($S3w+$S3d)/2)/$pa) ^ $nw)
      $Sdwf  = (2 * $coh * $cosphi + 2 * (($S3w+$S3d)/2) * $sinphi) / (1 - $sinphi)
      $n     = $Eal * $Eiw
      $m     = d_rfw(zi,zj) * $Eiw * $Eal / $Sdwf
      $sdw   = $n / (1 + $m)
    end_if
;
    $sdw   = min($sdw , $Sdd)
    $sdw   = max($sdw , 0.0)
    $s1w   = $sdw + $s3w
;   $delta1= abs($S1d - $s1w)   ;alternative determination of delta 1&2
;   $delta2= abs($S3d - $s3w)
```

```
  $delta2 = abs($S3d - $s3w)
  $delta1 = abs($sdd-$sdw+$delta2)

  $s1_   = max(0.0 , $s1_ - $delta1)
  $s2_   = max(0.0 , $s2_ - $delta2)
  $s3_   = max(0.0 , $s3_ - $delta2)
;=============================================================
;  ---  direction cosines ---
  if $psdif_ = 0.0 then
    $cs2_ = 1.0
    $si2_ = 0.0
  else
    $cs2_ = $diff / $psdif_
    $si2_ = 2.0 * $s12 / $psdif_
  end_if
; --- resolve to global axes ---
  case_of $icase_
    case 1
      $dc2      = ($s1_ - $s3_) * $cs2_
      $dss      =  $s1_ + $s3_
      syy(zi,zj) = -0.5 * ($dss + $dc2)
      sxx(zi,zj) = -0.5 * ($dss - $dc2)
      sxy(zi,zj) =  0.5 * ($s1_  - $s3_) * $si2_
      szz(zi,zj) = -$s2_
    case 2
      $dc2       = ($s2_ - $s3_) * $cs2_
      $dss       =  $s2_ + $s3_
      syy(zi,zj)  = -0.5 * ($dss + $dc2)
      sxx(zi,zj)  = -0.5 * ($dss - $dc2)
      sxy(zi,zj)  =  0.5 * ($s2_  - $s3_) * $si2_
      szz(zi,zj)  = -$s1_
    case 3
      $dc2       = ($s1_ - $s2_) *$cs2_
      $dss       =  $s1_ + $s2_
      syy(zi,zj)  = -0.5 * ($dss + $dc2)
      sxx(zi,zj)  = -0.5 * ($dss - $dc2)
      sxy(zi,zj)  =  0.5 * ($s1_  - $s2_) * $si2_
      szz(zi,zj)  = -$s3_
  end_case
; --- switching to wet properties ---
  d_k(zi,zj)  = d_kw(zi,zj)
  d_kb(zi,zj) = d_kbw(zi,zj)
  d_n(zi,zj)  = d_nw(zi,zj)
  d_m(zi,zj)  = d_mw(zi,zj)
  d_rf(zi,zj) = d_rfw(zi,zj)
;  - frictional constants -
  $sphi = sin(d_fric(zi,zj) * degrad)
  d_nphi(zi,zj) = (1.0 + $sphi) / (1.0 - $sphi)
  d_csnp(zi,zj) = 2.0 * d_coh(zi,zj) * sqrt(d_nphi(zi,zj))
  d_nphi(zi,zj) = d_nphi(zi,zj) - 1.0
```

```
  if d_fric(zi,zj) # 0.0 then
    d_cotp(zi,zj) = d_coh(zi,zj) / tan(d_fric(zi,zj) * degrad)
  else
    d_cotp(zi,zj) = 0.0
  end_if
;  - minor compressive stress -
  $esxx= sxx(zi,zj) + pp(zi,zj)
  $esyy= syy(zi,zj) + pp(zi,zj)
  $eszz= szz(zi,zj) + pp(zi,zj)
  $diff = $esxx - $esyy
  $diaa = sqrt ($diff*$diff + 4.0 * sxy(zi,zj) * sxy(zi,zj))
  $ms3 = min(-($esxx + $esyy + $diaa) * 0.5,-$eszz)
  $ms3 = max($ms3,$cap)
  $ms1 = max(-($esxx + $esyy - $diaa) * 0.5,-$eszz)
  $ms1 = max($ms1,$cap)
;    if m_ind = 0.0 then        ;BYPASSING the check for plasticity
;      - new moduli -
       $aux = $ms3 * d_nphi(zi,zj) + d_csnp(zi,zj)
       $sl  =  max($ms1 - $ms3,0.0) / $aux
       $ei  = d_k(zi,zj) * d_pa(zi,zj) * ($ms3/d_pa(zi,zj))^d_n(zi,zj)
       $elas= (1.0 - d_rf(zi,zj) * $sl)^2 * $ei
;      minimum hyp
       $elas= max($elas,hyp_min(zi,zj)*$ei)
;----------checking Duncan----------------
;       auxx(zi,zj)=$aux
;       hypp1(zi,zj) = (1.0 - d_rf(zi,zj) * $sl)^2
;       hypp2(zi,zj) = $elas / $ei
;----------------------------------------
       $elas = min($elas,$ei)
       if d_kb(zi,zj) = 0.0 then
;        - Poisson's ratio is constant -
         d_bulk(zi,zj)    = $elas / (3.0 * (1.0 - 2.0 * d_nu(zi,zj)))
         d_shear(zi,zj)   = $elas / (2.0 * (1.0 + d_nu(zi,zj)))
         d_elas(zi,zj)    = $elas
         d_poisson(zi,zj) = 0.5 - d_elas(zi,zj) / 6.0 / d_bulk(zi,zj)
       else
;        - Poisson's ratio between 0 and 0.49 -
         $bulk   = d_kb(zi,zj) * d_pa(zi,zj) * ($ms3/d_pa(zi,zj))^d_m(zi,zj)
         $bulk   = min($bulk, 17.0 * $elas)
         $bulk   = max($bulk, $elas / 3.0)
         d_bulk(zi,zj)    = $bulk
         d_shear(zi,zj)   = 3.0 * $elas * $bulk / (9.0 * $bulk - $elas)
         d_elas(zi,zj)    = $elas
         d_poisson(zi,zj) = 0.5 - d_elas(zi,zj) / 6.0 / d_bulk(zi,zj)
       end_if
;==================Mohr parameters update=====================1
       d_fric(zi,zj) = d_phio(zi,zj) - d_dphi(zi,zj) * log(-sxx(zi,zj)/$Pa)
       d_fric(zi,zj) = min(d_phio(zi,zj)     ,d_fric(zi,zj))
       d_fric(zi,zj) = max(d_phio(zi,zj)/2.0 ,d_fric(zi,zj))
       m_dilo(zi,zj) = m_dilo(zi,zj) - 1.5
```

```
      m_dil(zi,zj)  = m_dilo(zi,zj) - m_ddil(zi,zj) * log(-sxx(zi,zj)/$Pa)
      m_dil(zi,zj)  = max (0.0    , m_dil(zi,zj))
      m_dil(zi,zj)  = min (m_dilo(zi,zj) , m_dil(zi,zj))
;
      $sphi    = sin (d_fric(zi,zj) * degrad)
      $spsi    = sin (m_dil(zi,zj) * degrad)
      m_nphi(zi,zj)  = (1.0 + $sphi) / (1.0 - $sphi)
      m_npsi(zi,zj)  = (1.0 + $spsi) / (1.0 - $spsi)
      m_csnp(zi,zj)  = 2.0 * d_coh(zi,zj) * sqrt(m_nphi(zi,zj))
      m_e1(zi,zj)    = d_bulk(zi,zj)+ 4.0 * d_shear(zi,zj)/ 3.0
      m_e2(zi,zj)    = d_bulk(zi,zj)- 2.0 * d_shear(zi,zj)/ 3.0
      m_x1(zi,zj)    = m_e1(zi,zj) - m_e2(zi,zj)*m_npsi(zi,zj)
      m_x1(zi,zj)    = m_x1(zi,zj) + (m_e1(zi,zj)*m_npsi(zi,zj) -
m_e2(zi,zj))*m_nphi(zi,zj)
      m_sh2(zi,zj)   = 2.0 * d_shear(zi,zj)
      $fff           = 1e-6 * (abs(m_e1(zi,zj)) + abs(m_e2(zi,zj)))
      $ff            = abs(m_x1(zi,zj))
      if $ff < $fff then
        $m_err = 5
        nerr   = 126
        error  = 1
      end_if
; --- set tension to prism apex if larger than apex ---
      $apex = m_ten(zi,zj)
      if d_fric(zi,zj) # 0.0 then
        $apex = d_coh(zi,zj) / tan(d_fric(zi,zj) * degrad)
      end_if
      m_ten(zi,zj) = min($apex,m_ten(zi,zj))
      $nphi  = (1.0 + $sphi) / (1.0 - $sphi)
      d_csnp(zi,zj) = 2.0 * d_coh(zi,zj) * sqrt($nphi)
      d_nphi(zi,zj) = $nphi - 1.0
      if d_fric(zi,zj) # 0.0 then
        d_cotp(zi,zj) = d_coh(zi,zj) / tan(d_fric(zi,zj) * degrad)
      else
        d_cotp(zi,zj) = 0.0
      end_if
;====================Mohr parameters update=====================2

ex_1(zi,zj) = 7
ex_2(zi,zj) = $s3d
ex_3(zi,zj) = $s3w
ex_4(zi,zj) = $s1d
ex_5(zi,zj) = $s1w
ex_6(zi,zj) = $answer
ex_7(zi,zj) = $answer2
ex_8(zi,zj) = $coef
ex_9(zi,zj) = $delta1
ex_10(zi,zj)= $delta2
end_if
end
```

Appendix 2 – complete results of the modeling of LG4

1-construction stage

The numerical modeling for the construction stage has been performed in twenty steps. The output of the FLAC is presented in the following figures. These results are extracted from four stages of the construction with dam heights of 35 m, 75 m, 110 m and 125 m.

2-impoundement stage

Same as the construction stage, impoundment is also modeled using the multi-step modeling technique, and in 20 steps. The results are presented from four different reservoir levels: 30 m, 70 m, 100 m and 120 m.

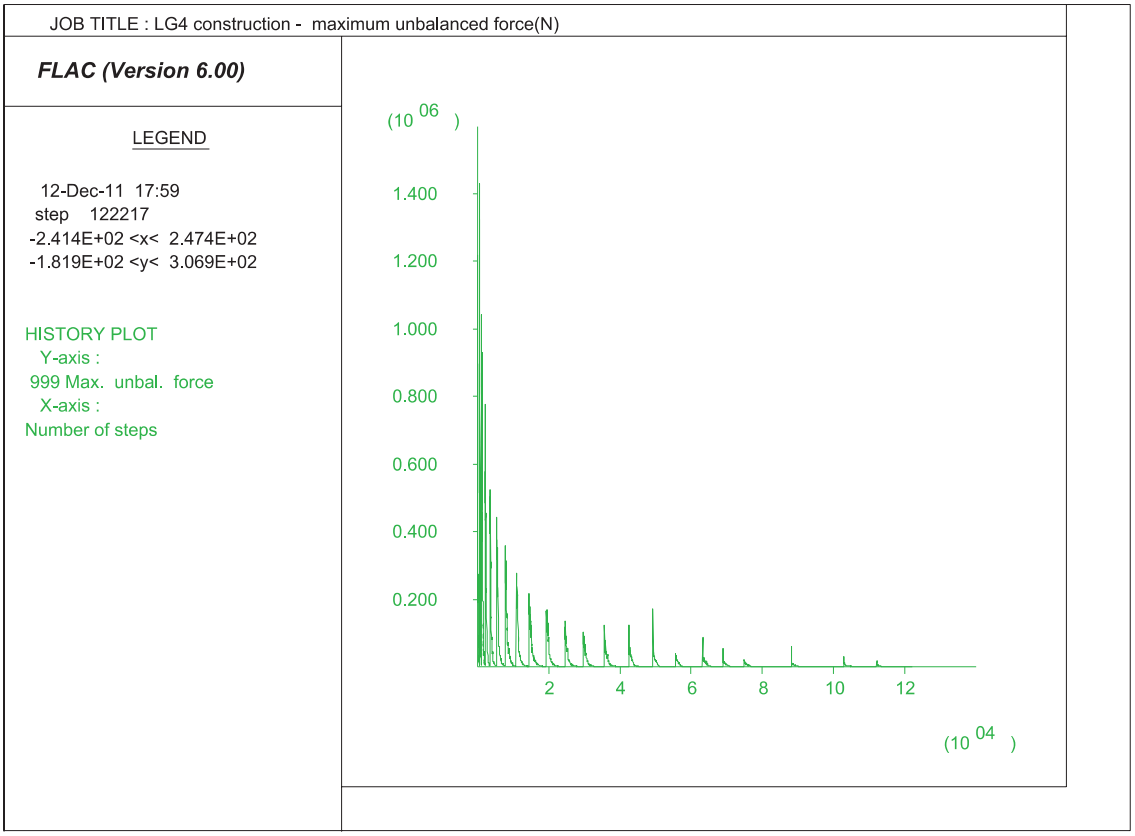

Figure 6-1. maximum unbalanced force (N) during simulation of the construction of LG4 dam. The model reaches the equilibrium after each placement of the materials.

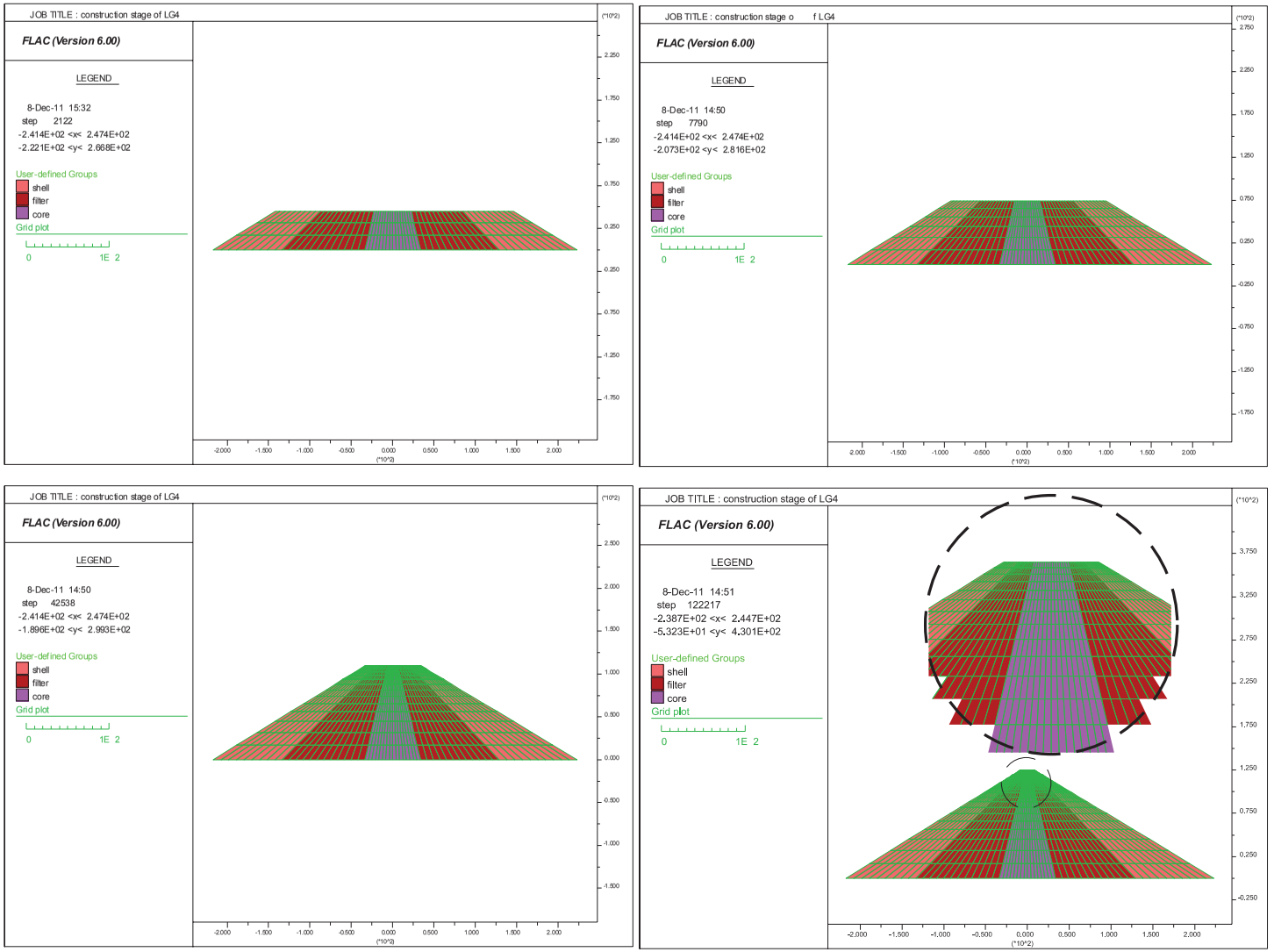

Figure 6-2 - Construction stage of LG4 dam

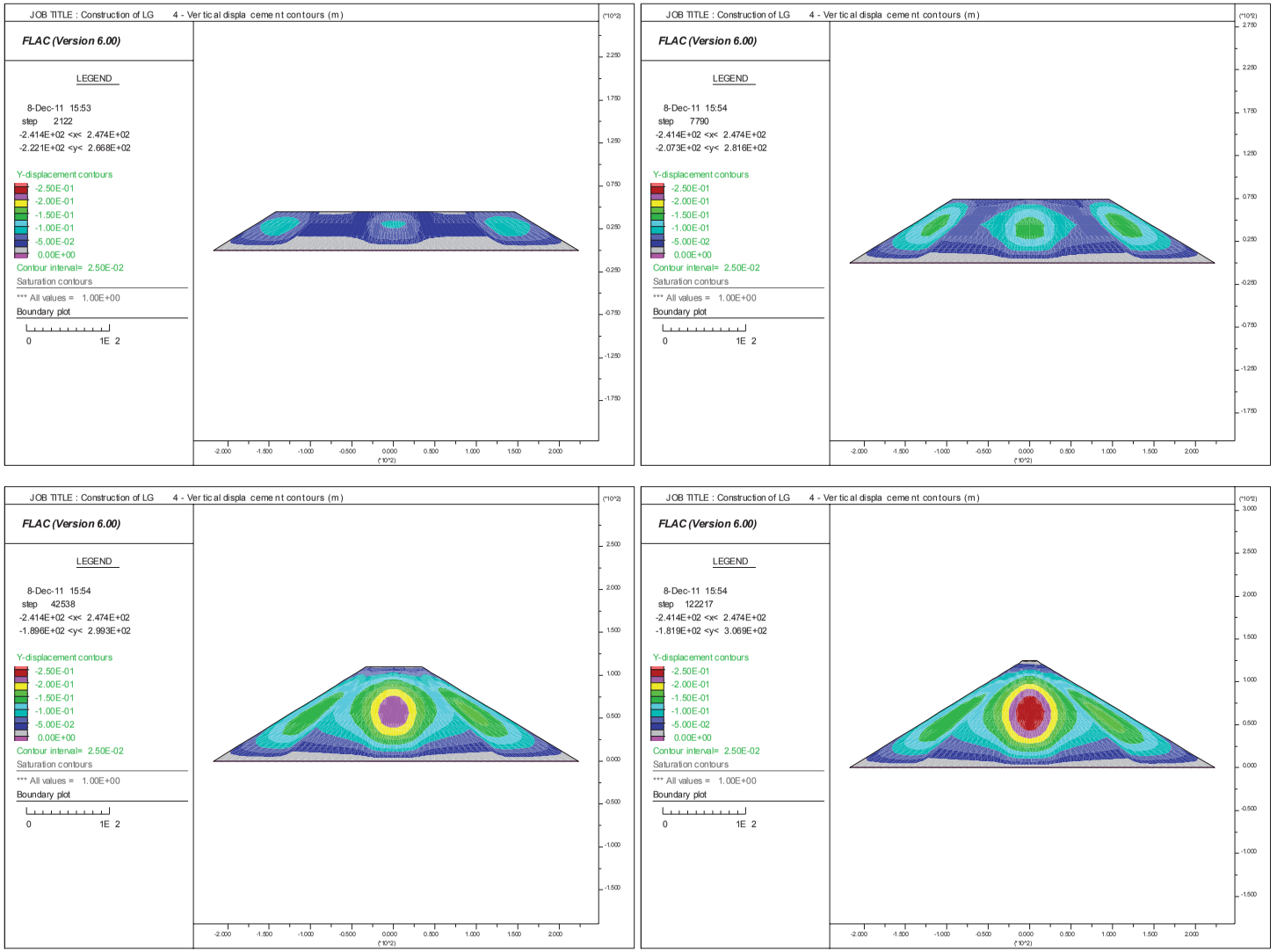

Figure 6-3 - vertical displacement contours (m) during construction

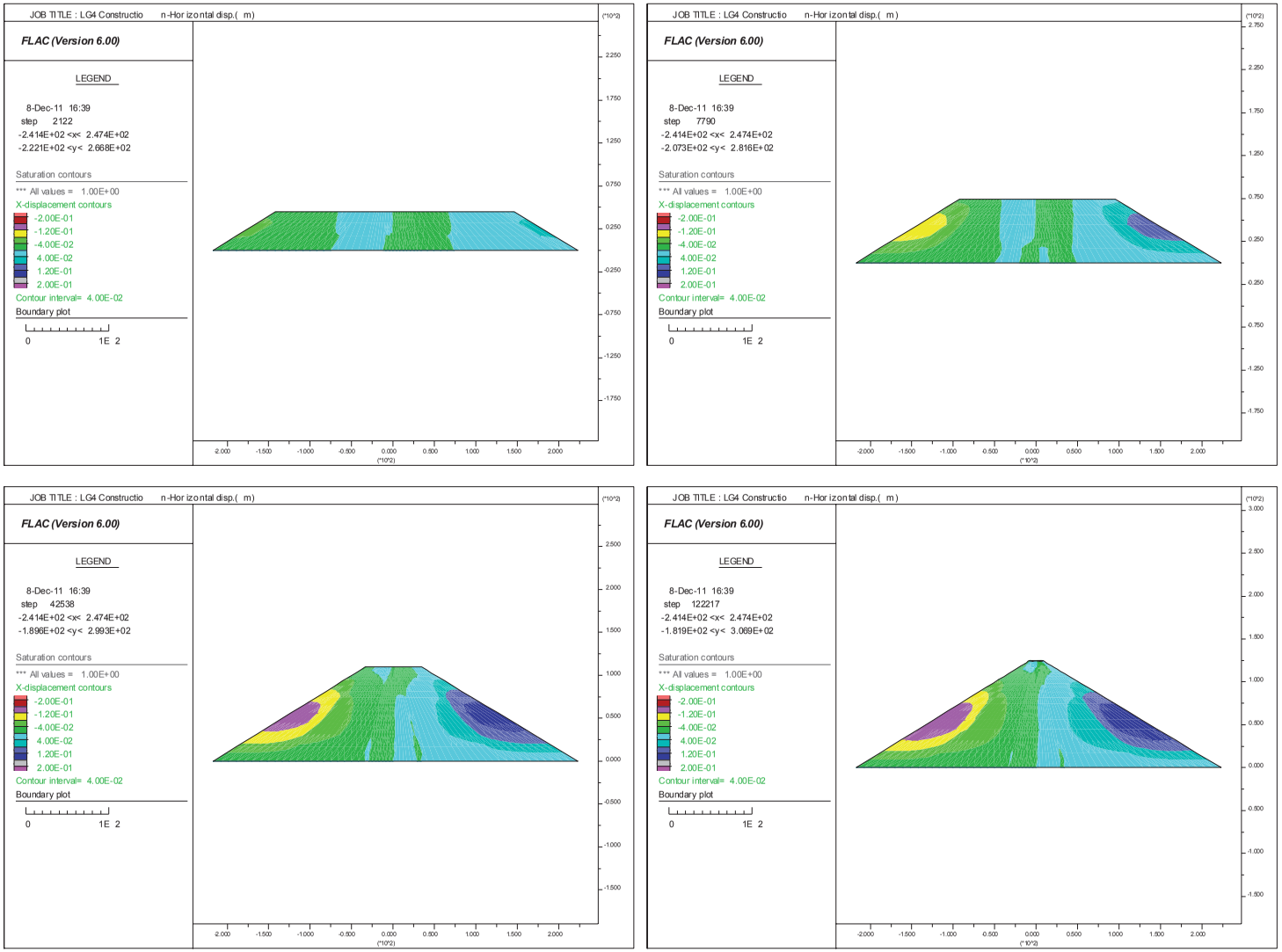

Figure 6-4 - horizontal displacement contours (m) during construction

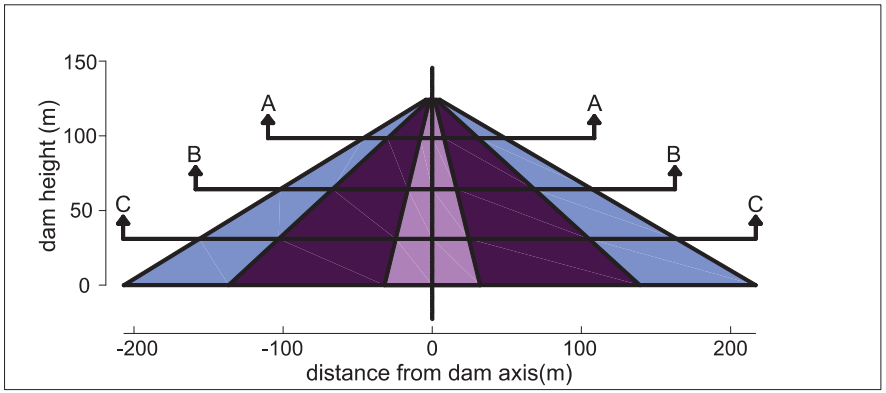

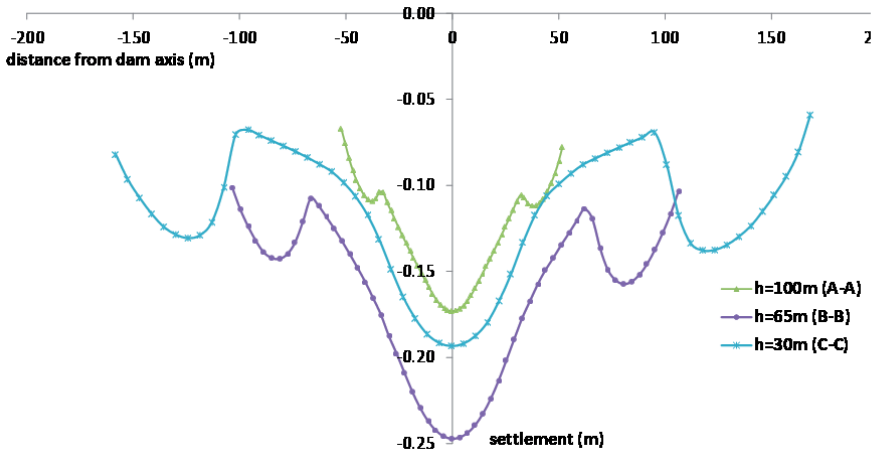

Figure 6-5 - vertical displacement profiles (m) at different heights at the end of construction

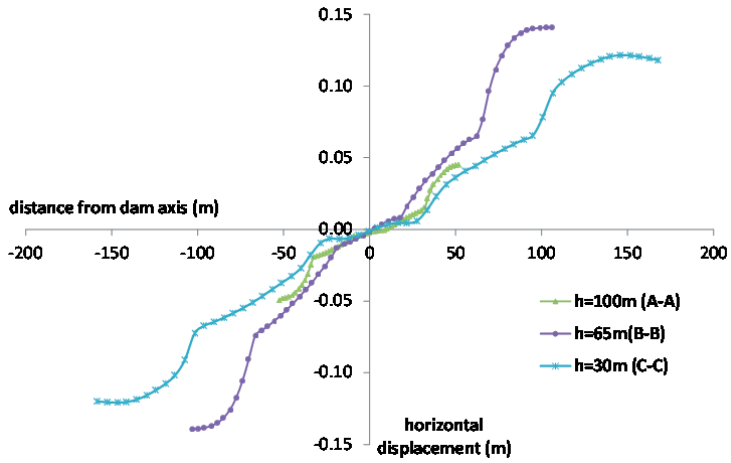

Figure 6-6 - horizontal displacement profiles (m) at different heights at the end of construction

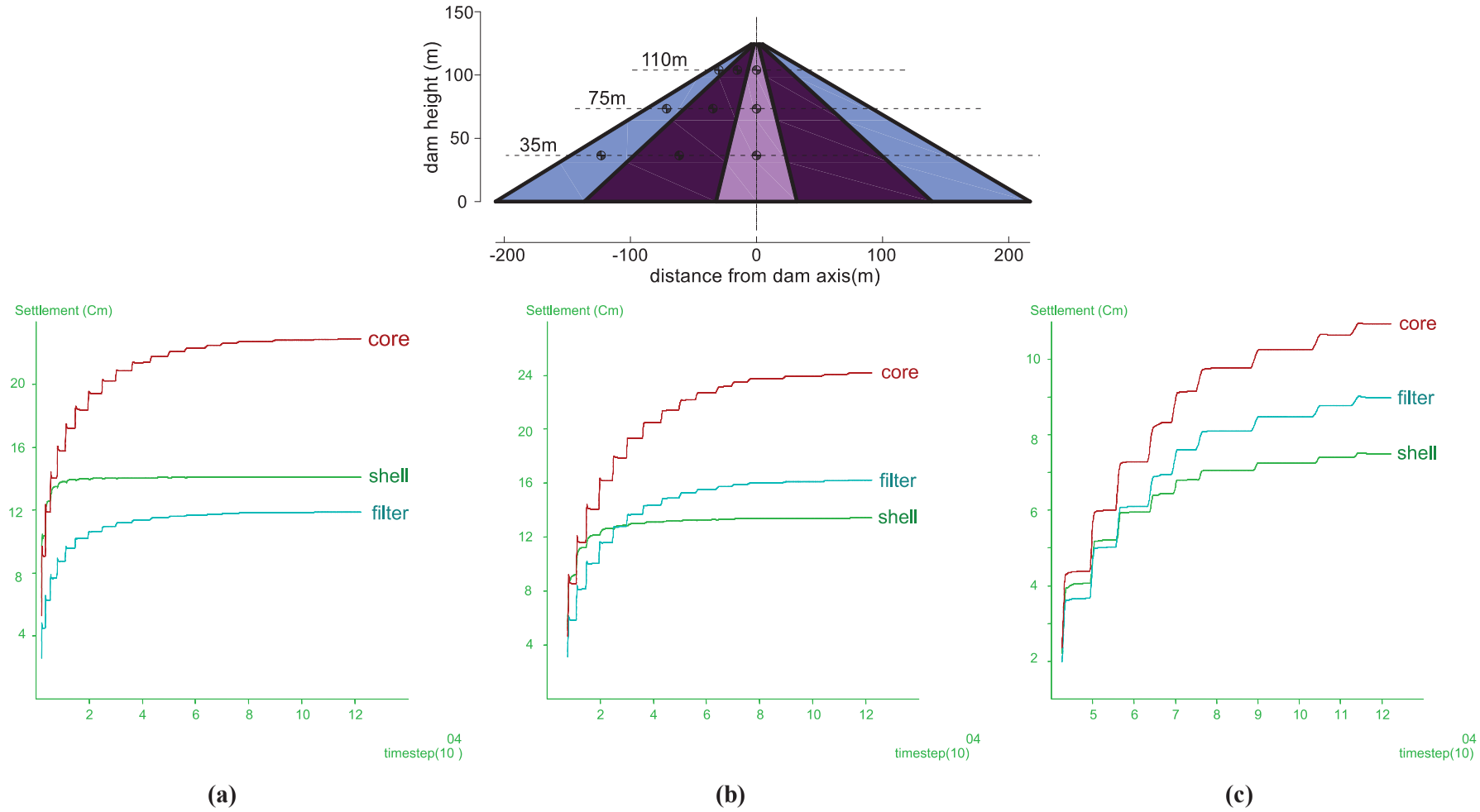

Figure 6-7 – settlement history at different zones, during construction of LG4 (a)35 m (b)75 m (c)110 m

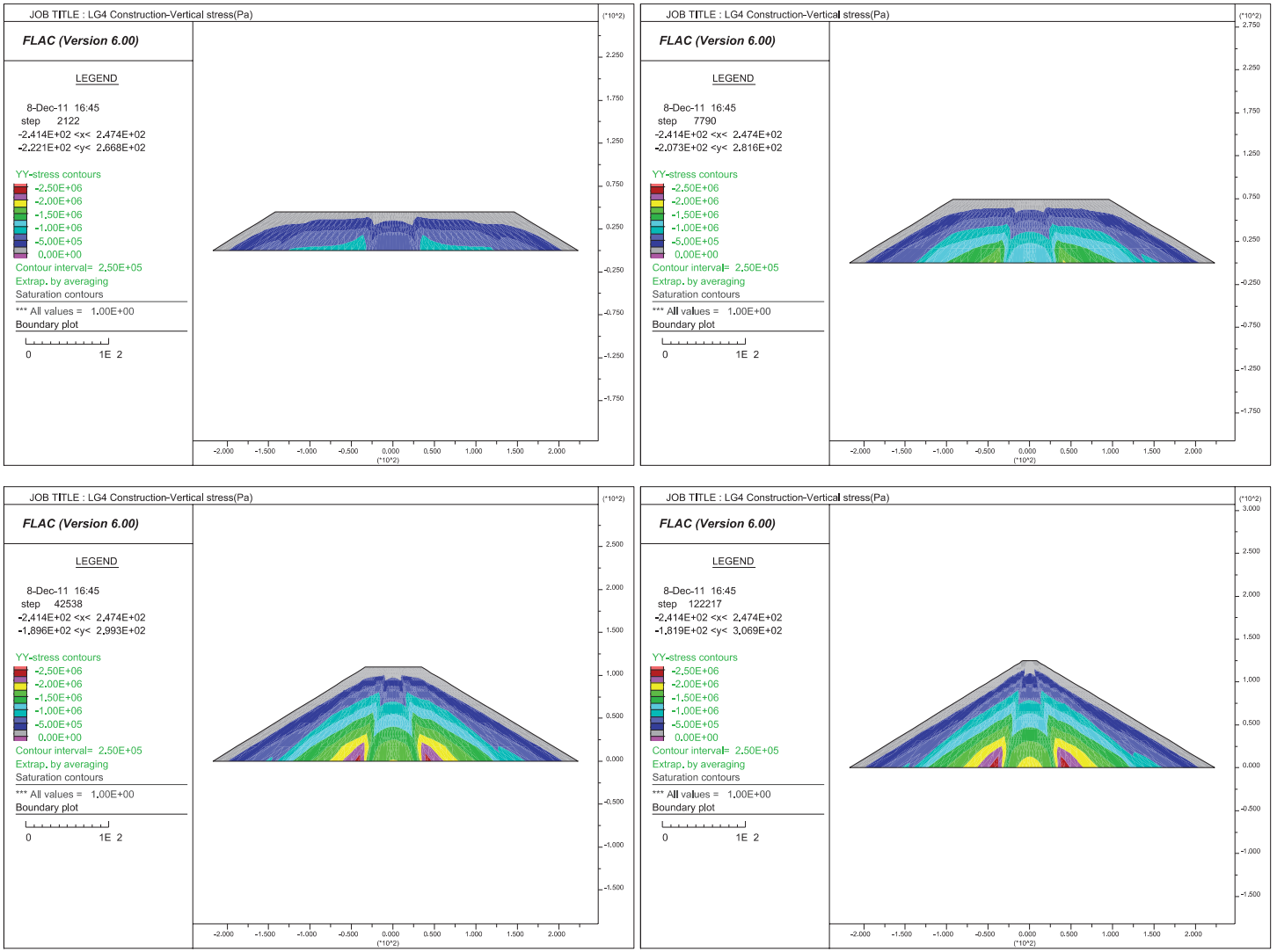

Figure 6-8 - total vertical stress contours (Pa) during construction

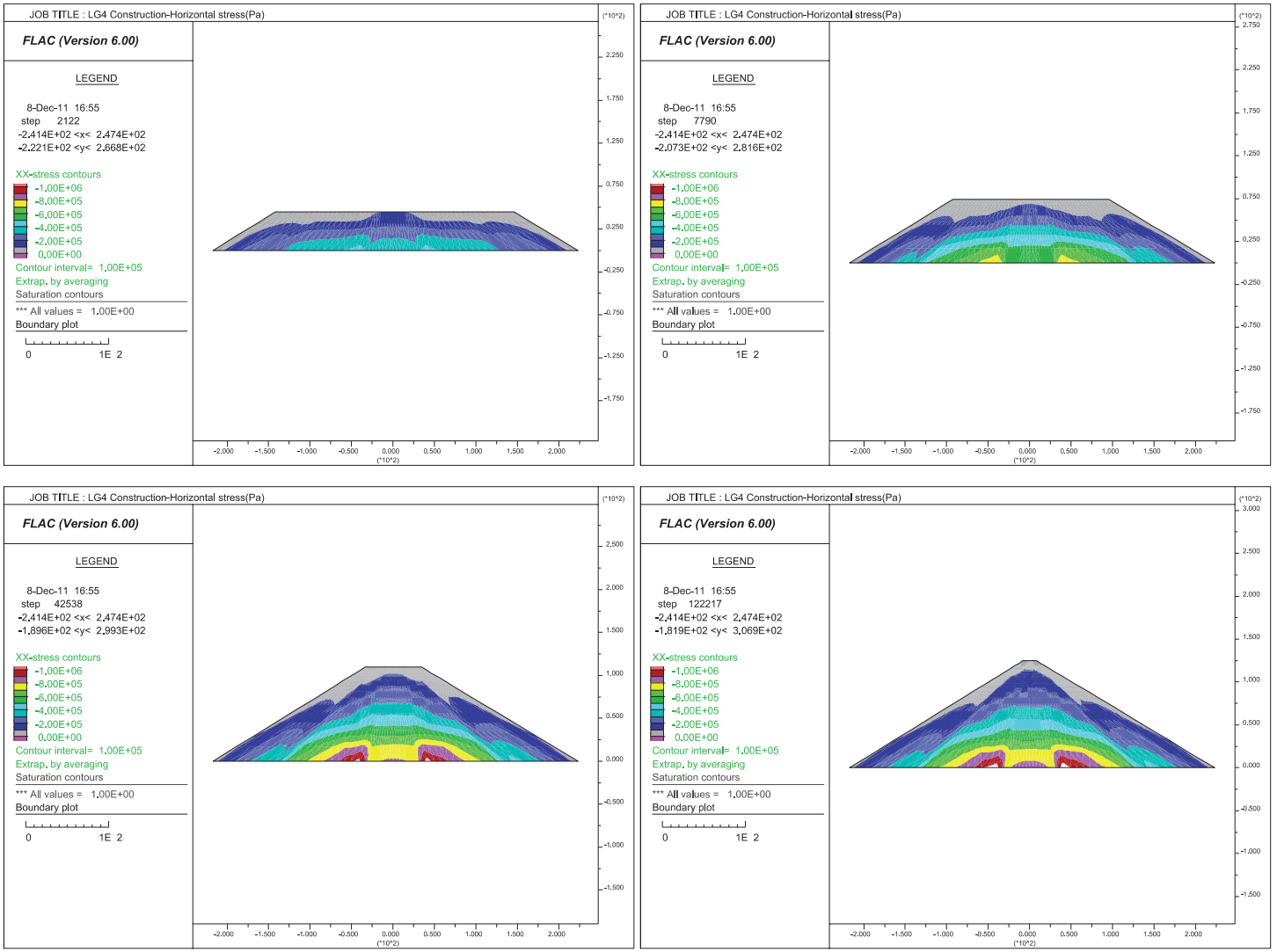

Figure 6-9 - total horizontal stress contours (Pa) during construction

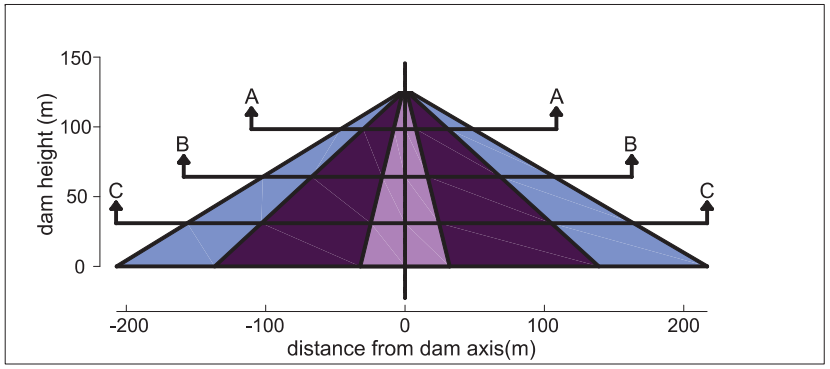

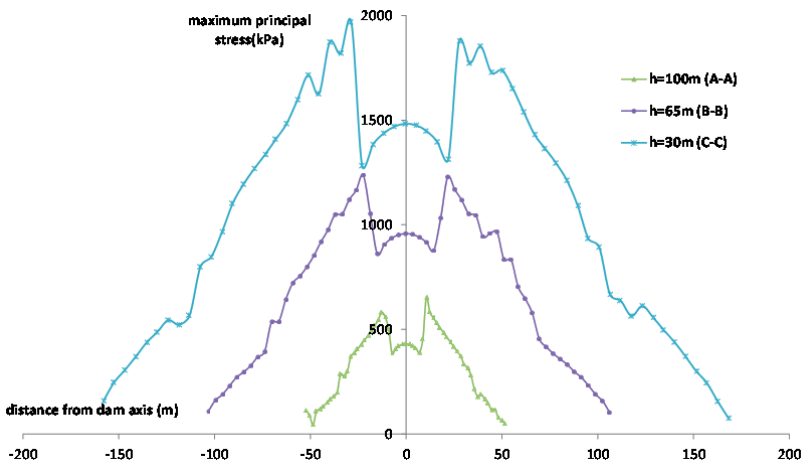

Figure 6-10- maximum principal stress (Pa) at different heights at the end of construction

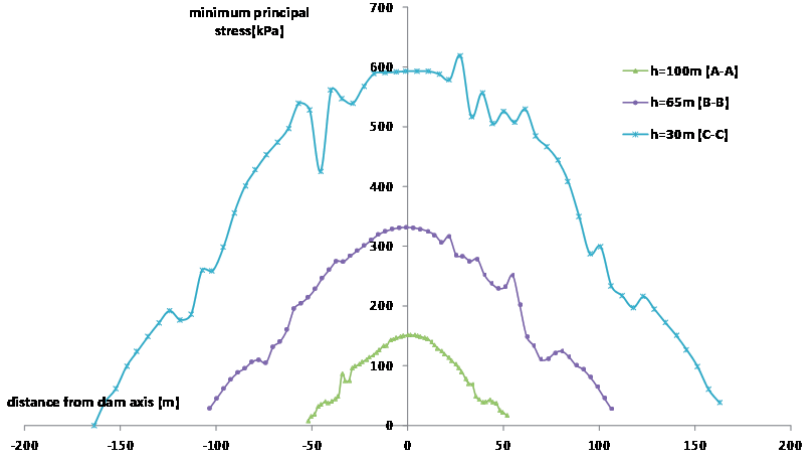

Figure 6-11- minimum principal stress (Pa) at different heights at the end of construction

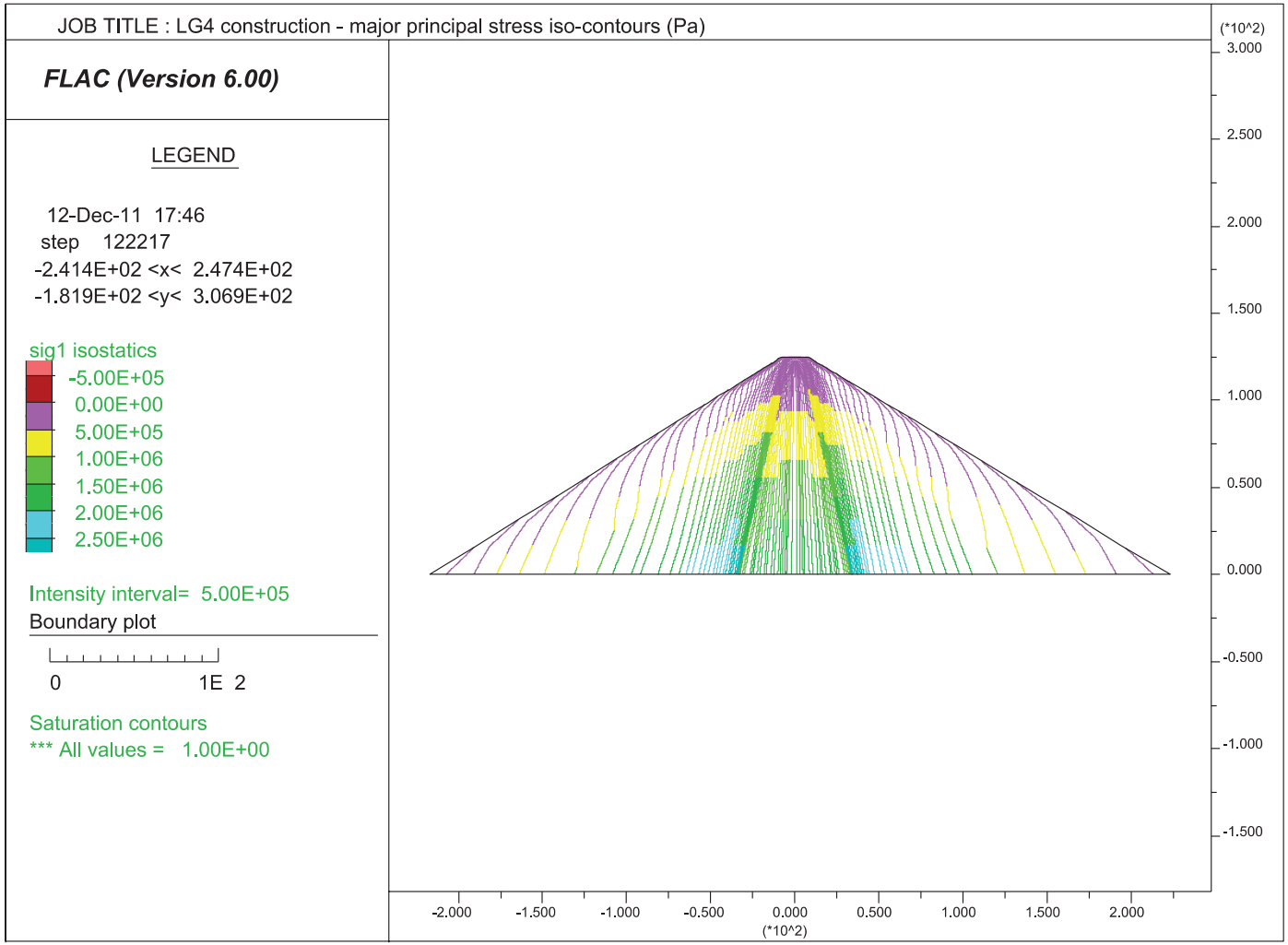

Figure 6-12 - maximum principal stress iso-contours (Pa) at the end of construction

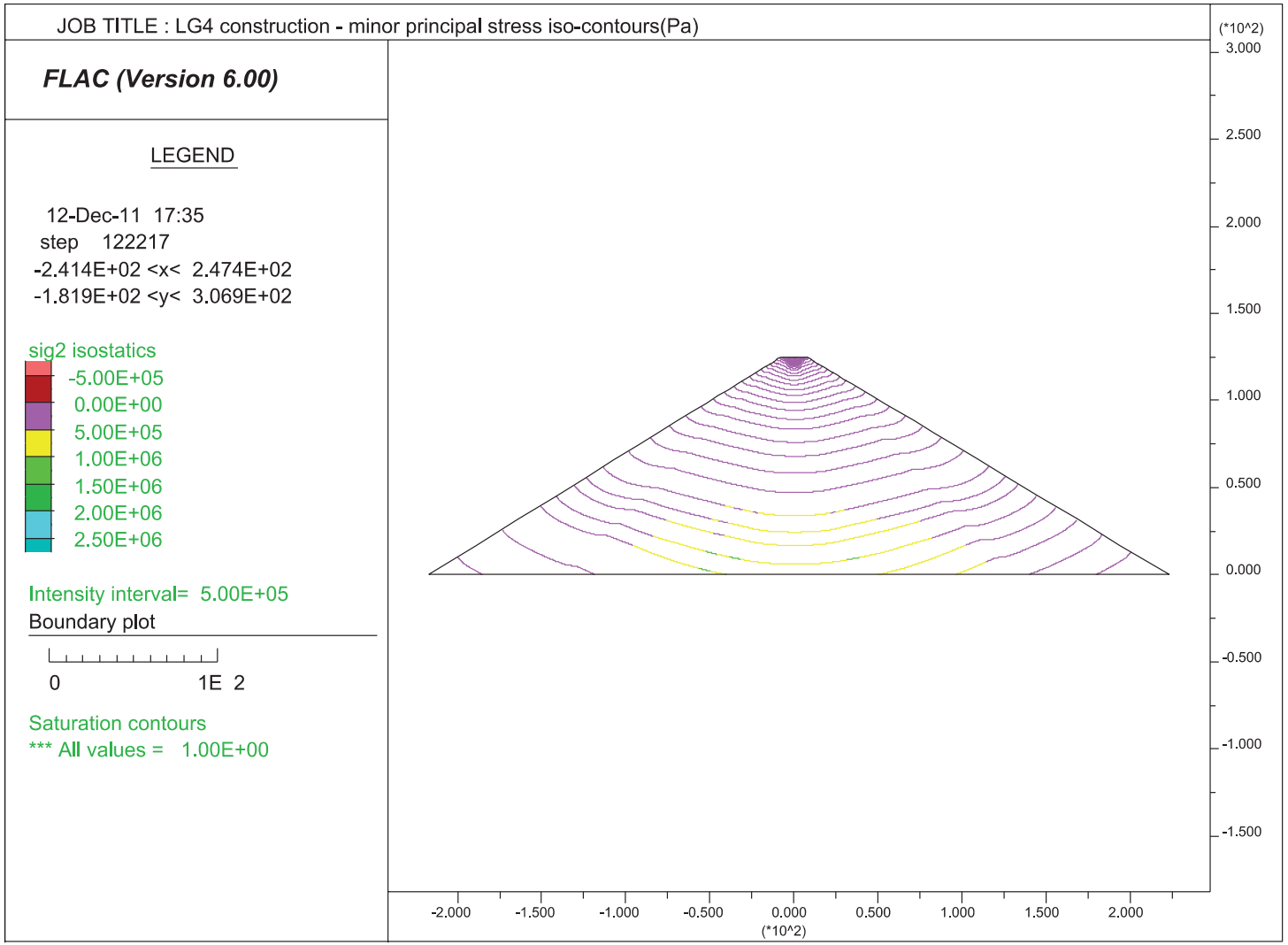

Figure 6-13 –minimum principal stress iso-contours (Pa) at the end of construction

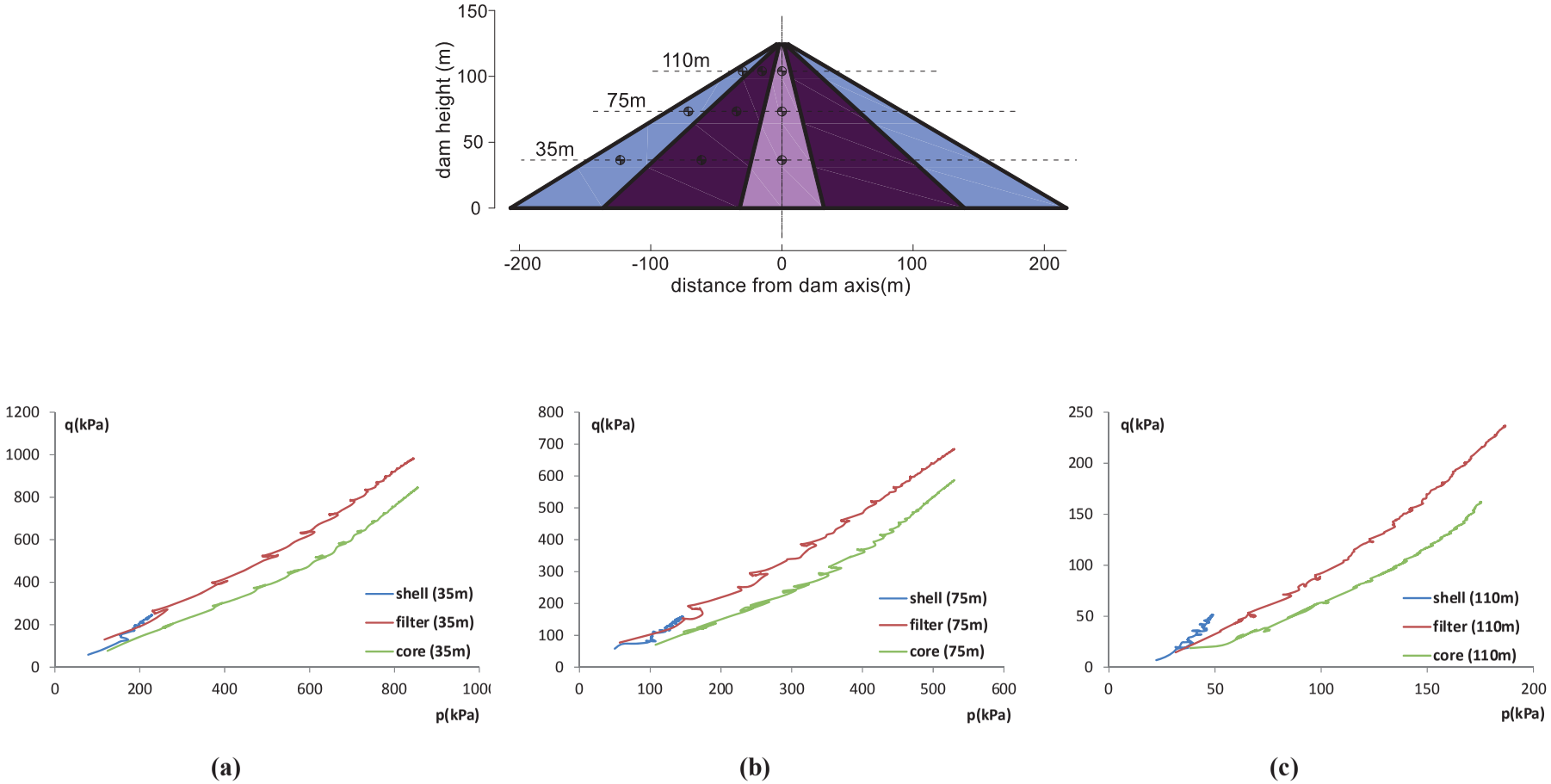

Figure 6-14 – stress path at different zones, during the construction (a)35 m (b)75 m (c)110 m

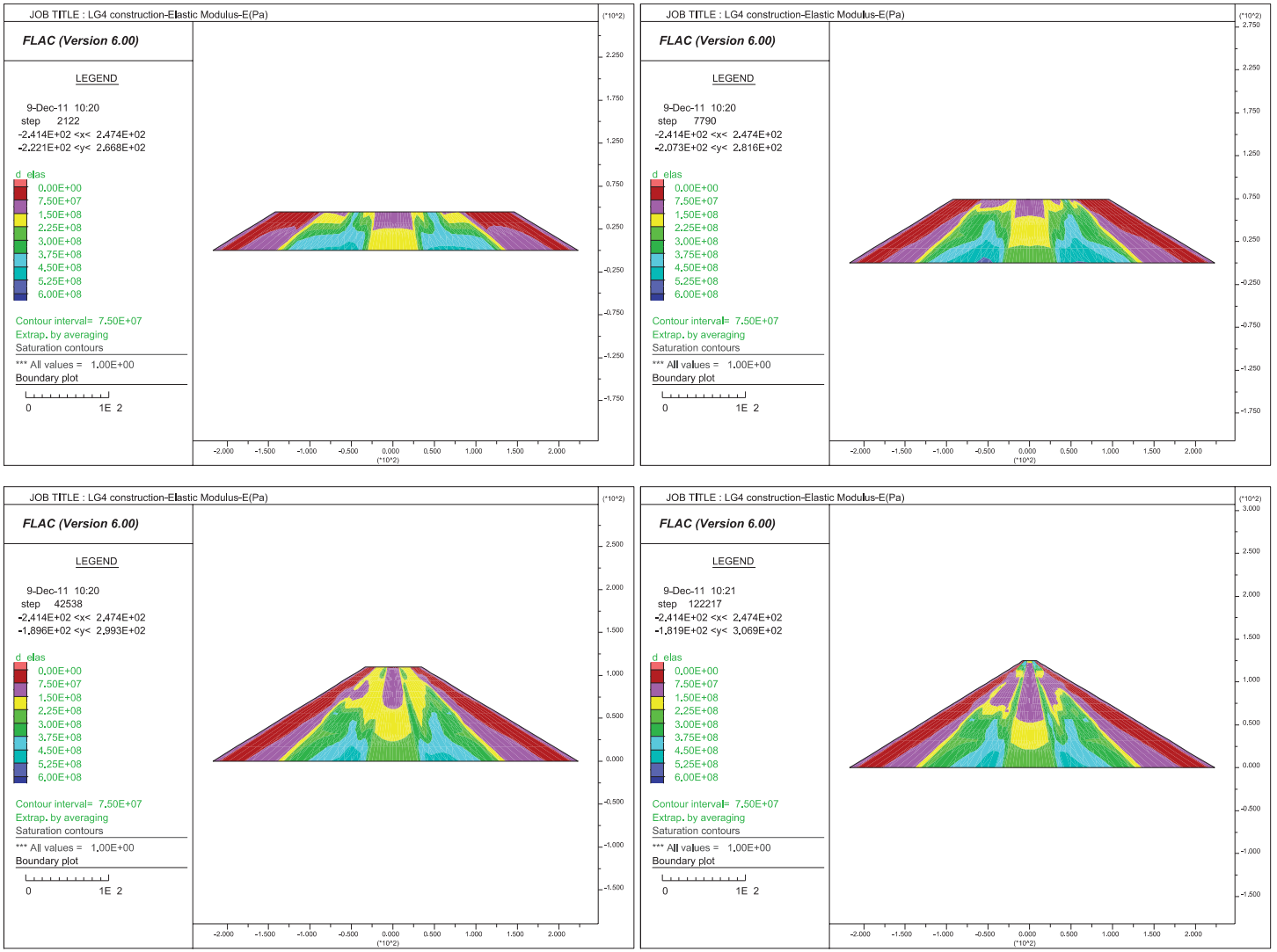

Figure 6-15 –elastic modulus (E) contours (Pa) during construction

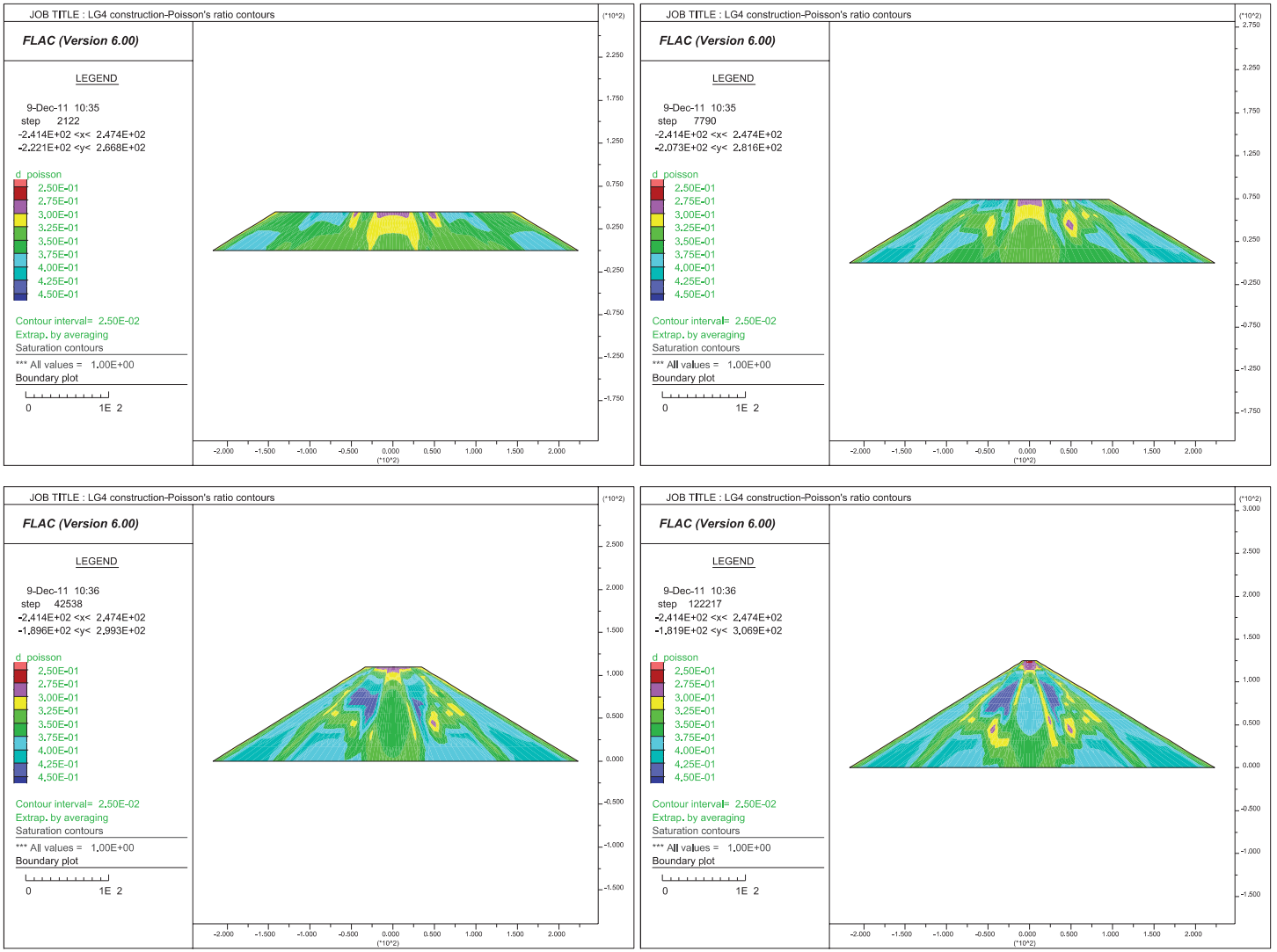

Figure 6-16- Poisson's ratio contours during construction

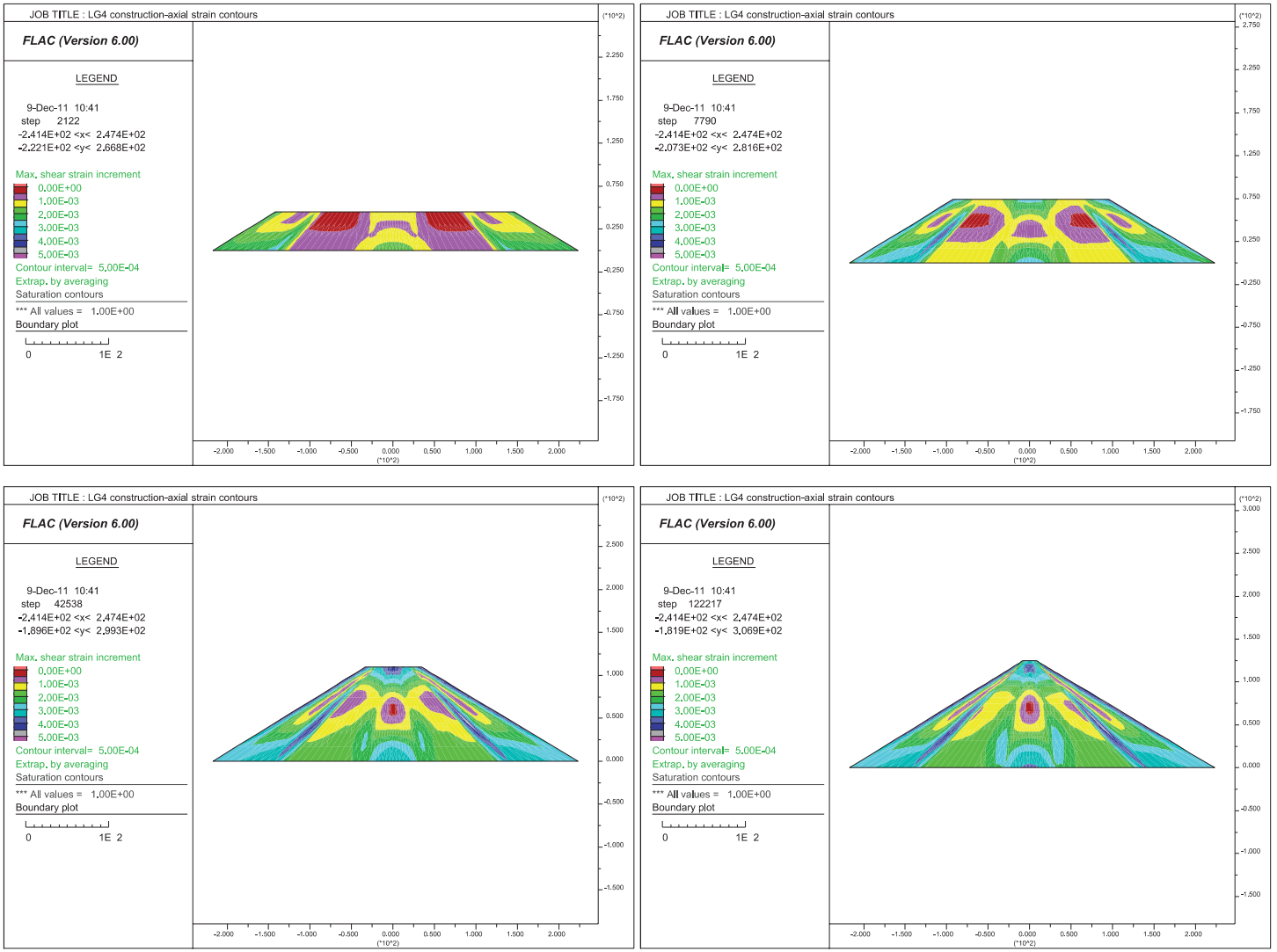

Figure 6-17- maximum shear strain ($\boldsymbol{\gamma}$) during LG4 construction

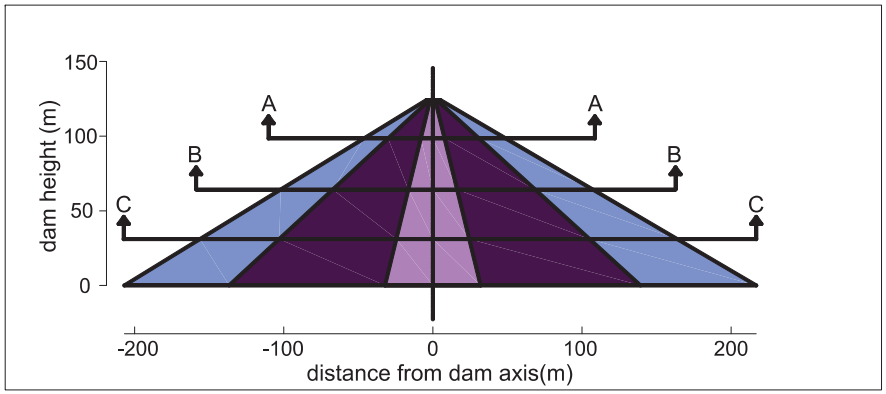

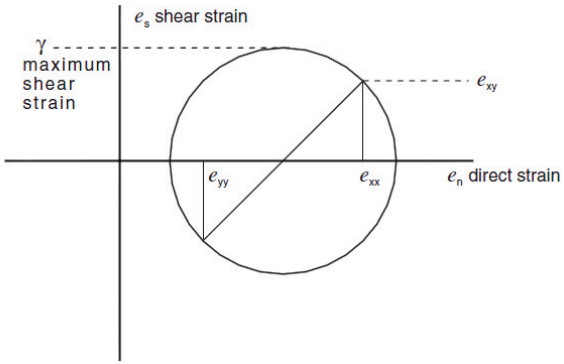

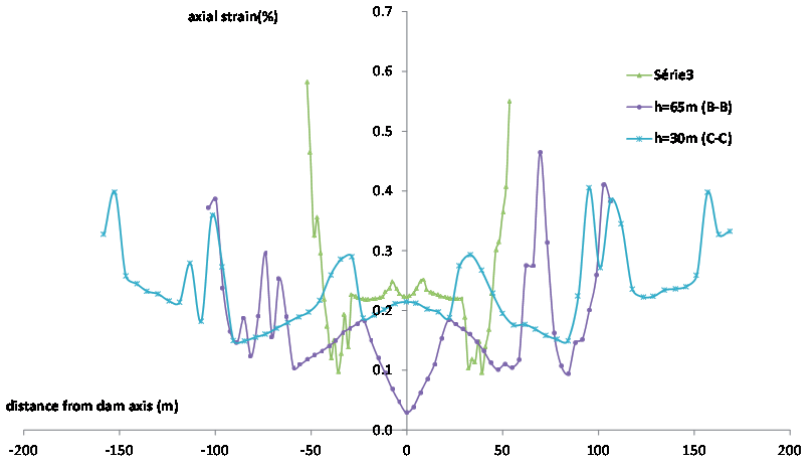

Figure 6-18- maximum shear strain (**ssi** ≡ **γ**) of elements at different heights at the end of construction

$$\mathrm{ssi} = \frac{1}{2}\sqrt{\left(\mathrm{e_{xx}} - \mathrm{e_{yy}}\right)^2 + 4\mathrm{e_{xy}}^2}$$

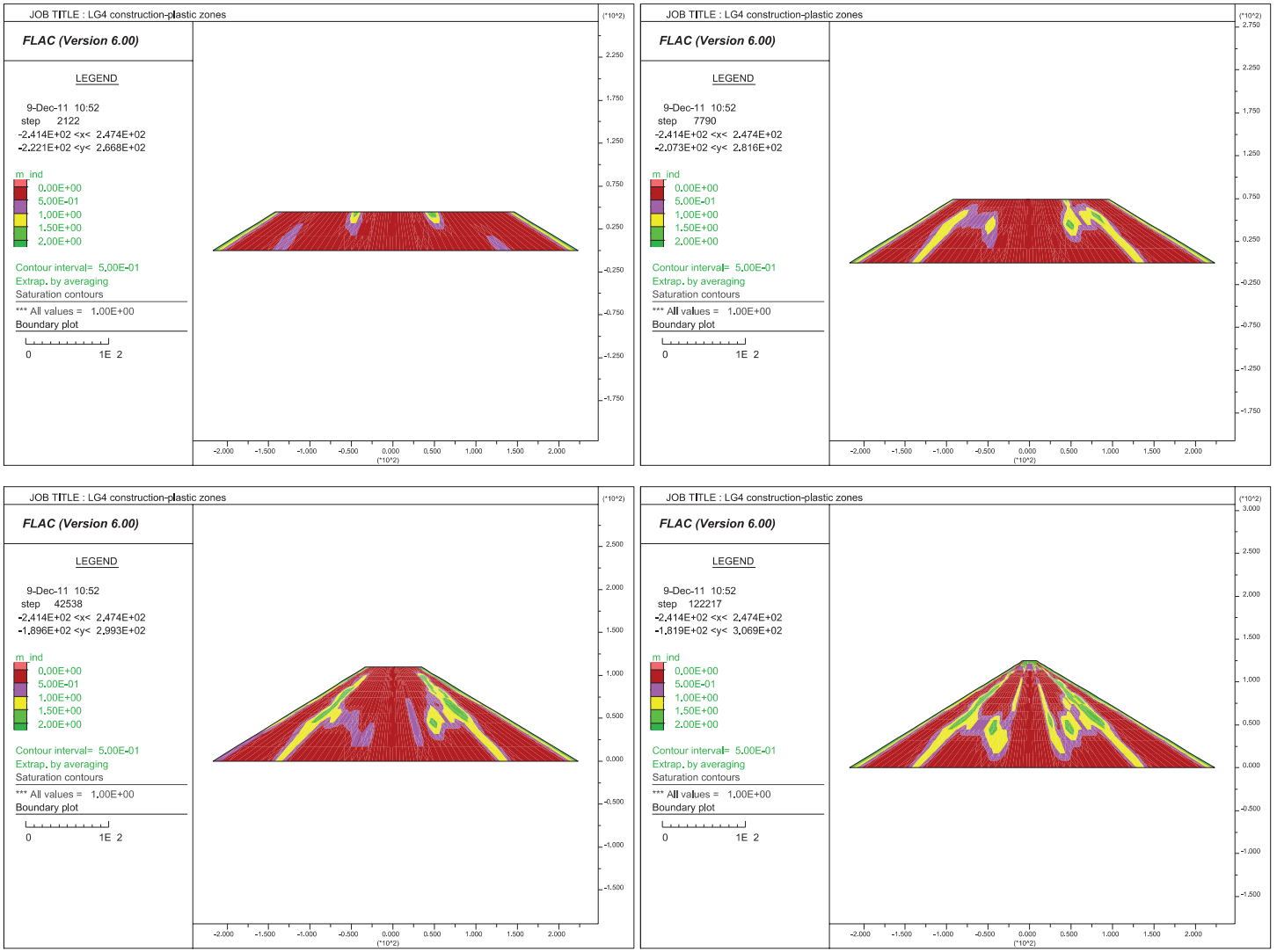

Figure 6-19 - zones reaching failure envelope during construction

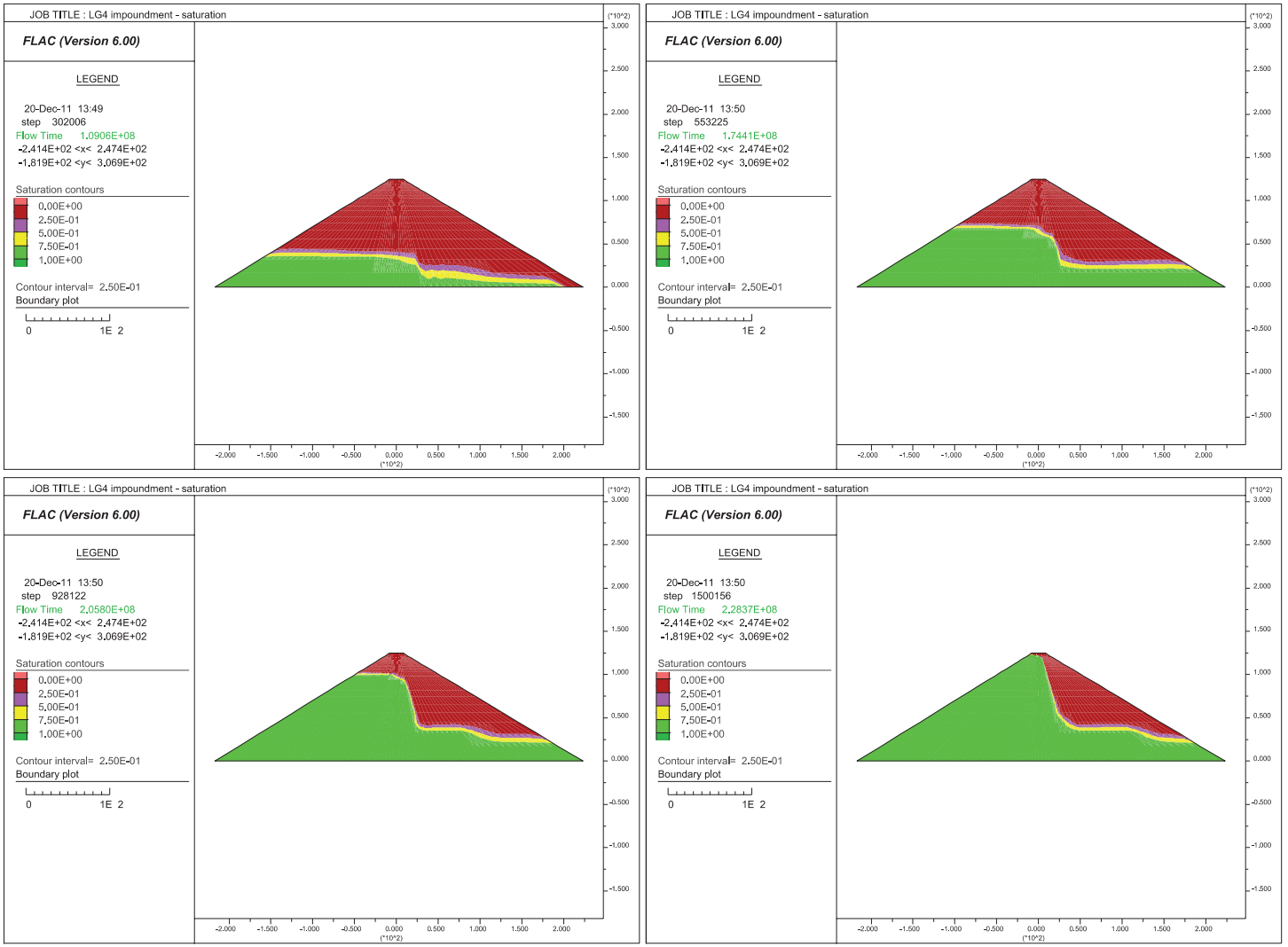

Figure 6-20 - saturated elements during impoundment (in green)

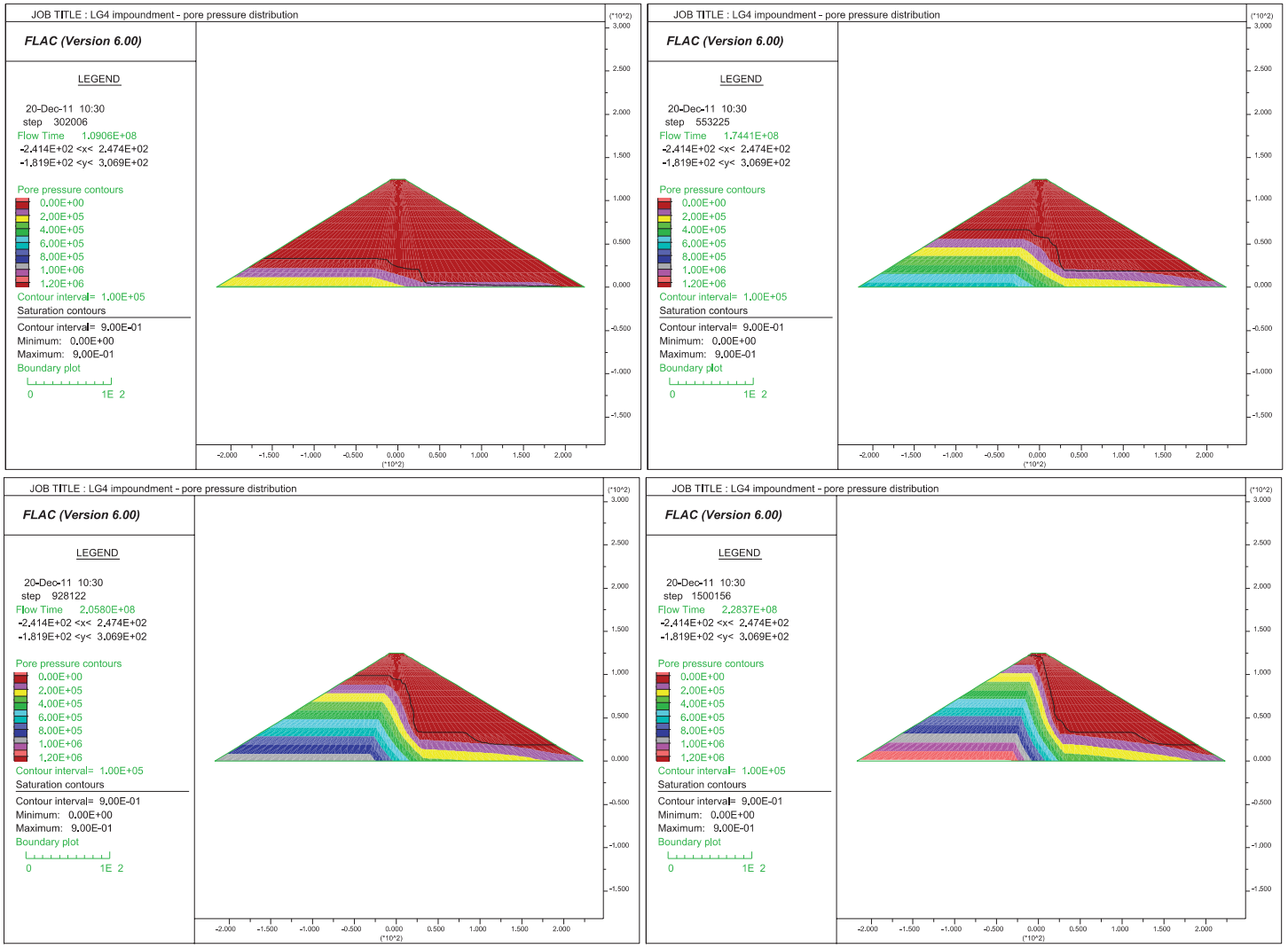

Figure 6-21 - pore pressure distribution during impoundment

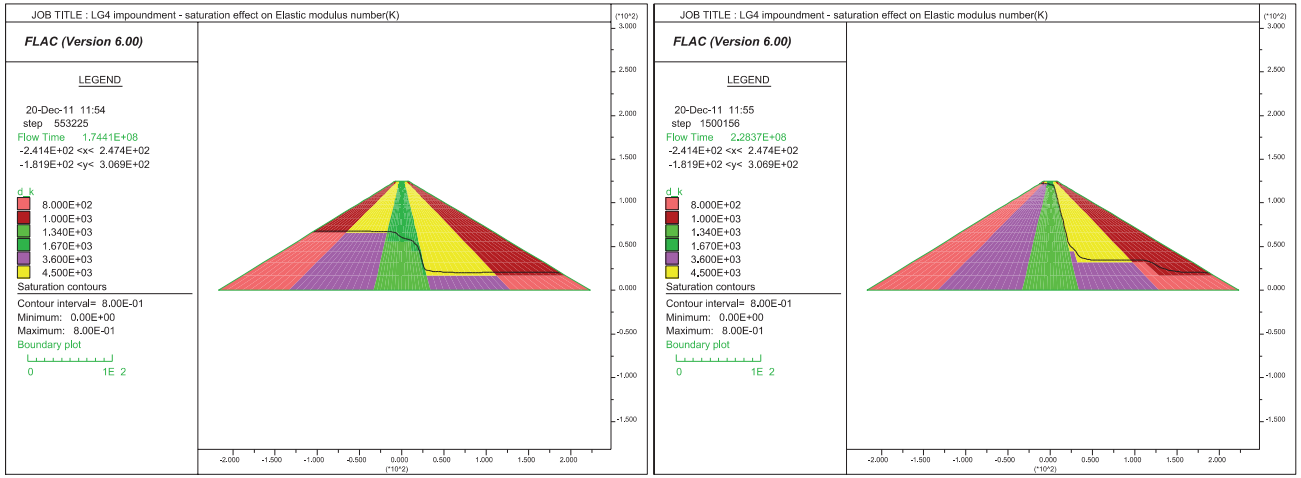

(a) elastic modulus number

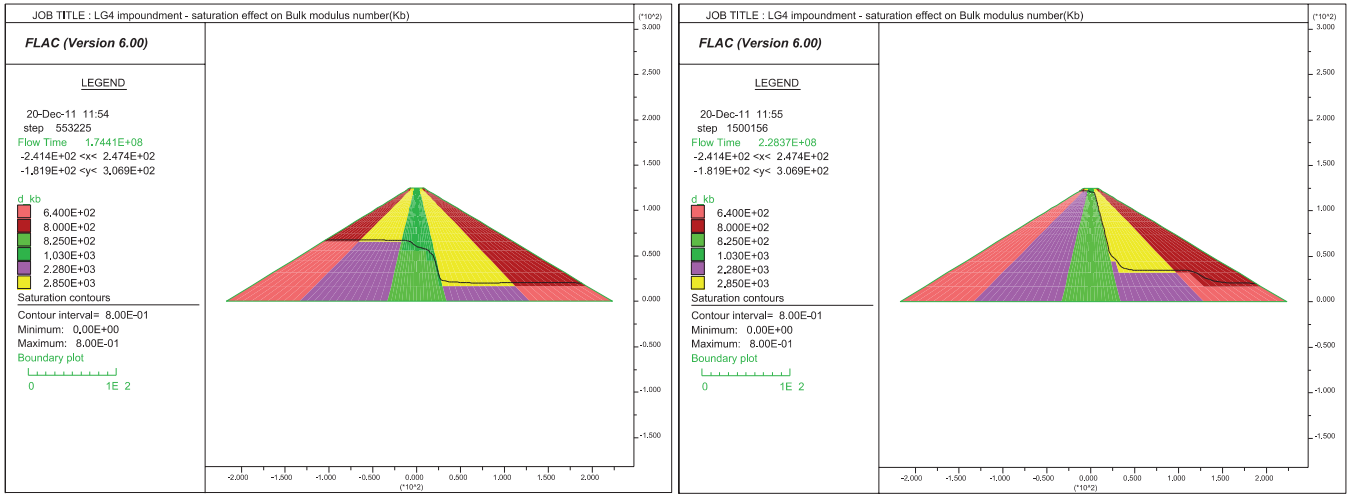

(b) bulk modulus number

Figure 6-22 – changing of the stiffness parameters due to saturation of elements during impoundment

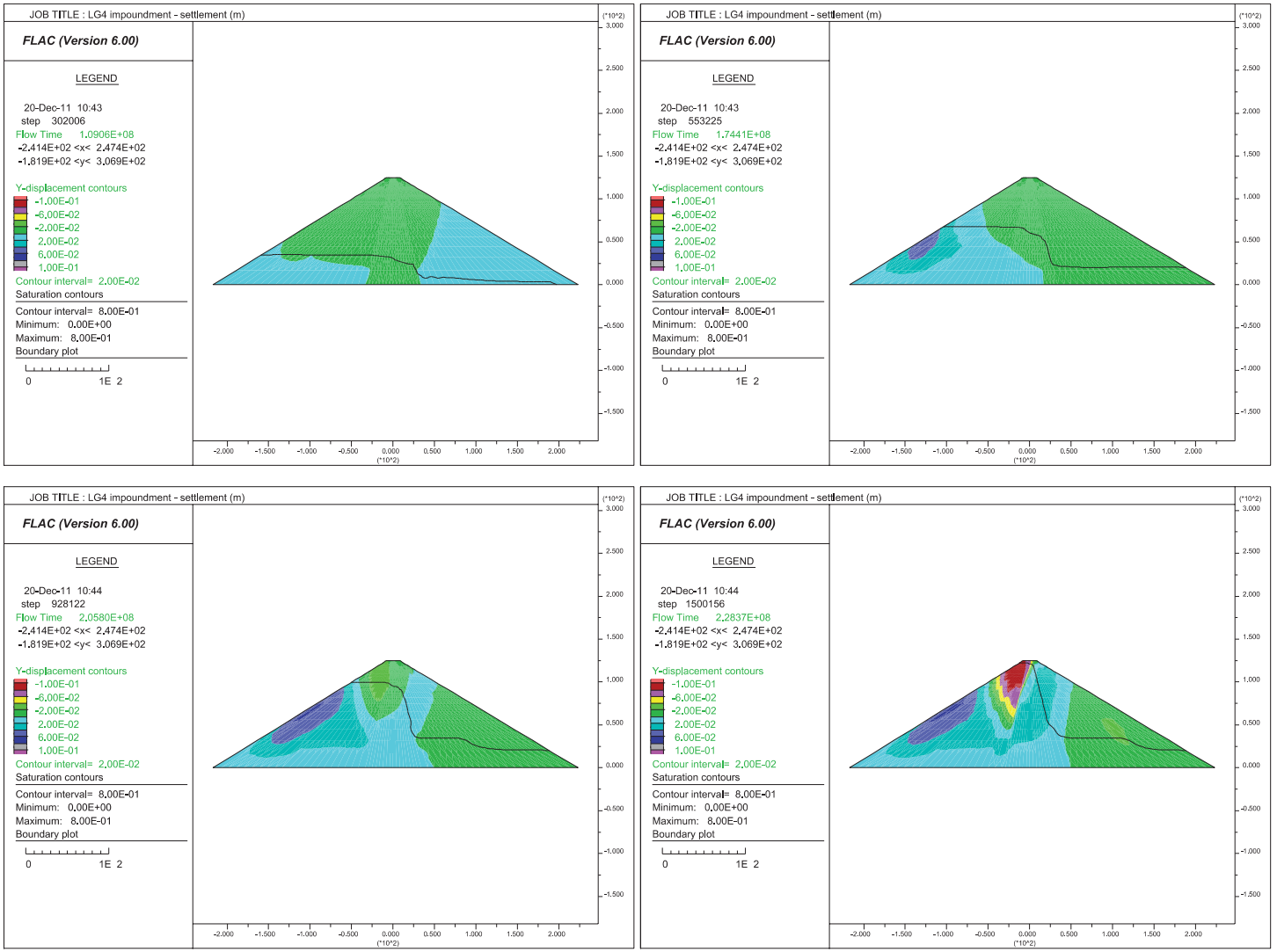

Figure 6-23 - vertical displacement contours (m) during impoundment

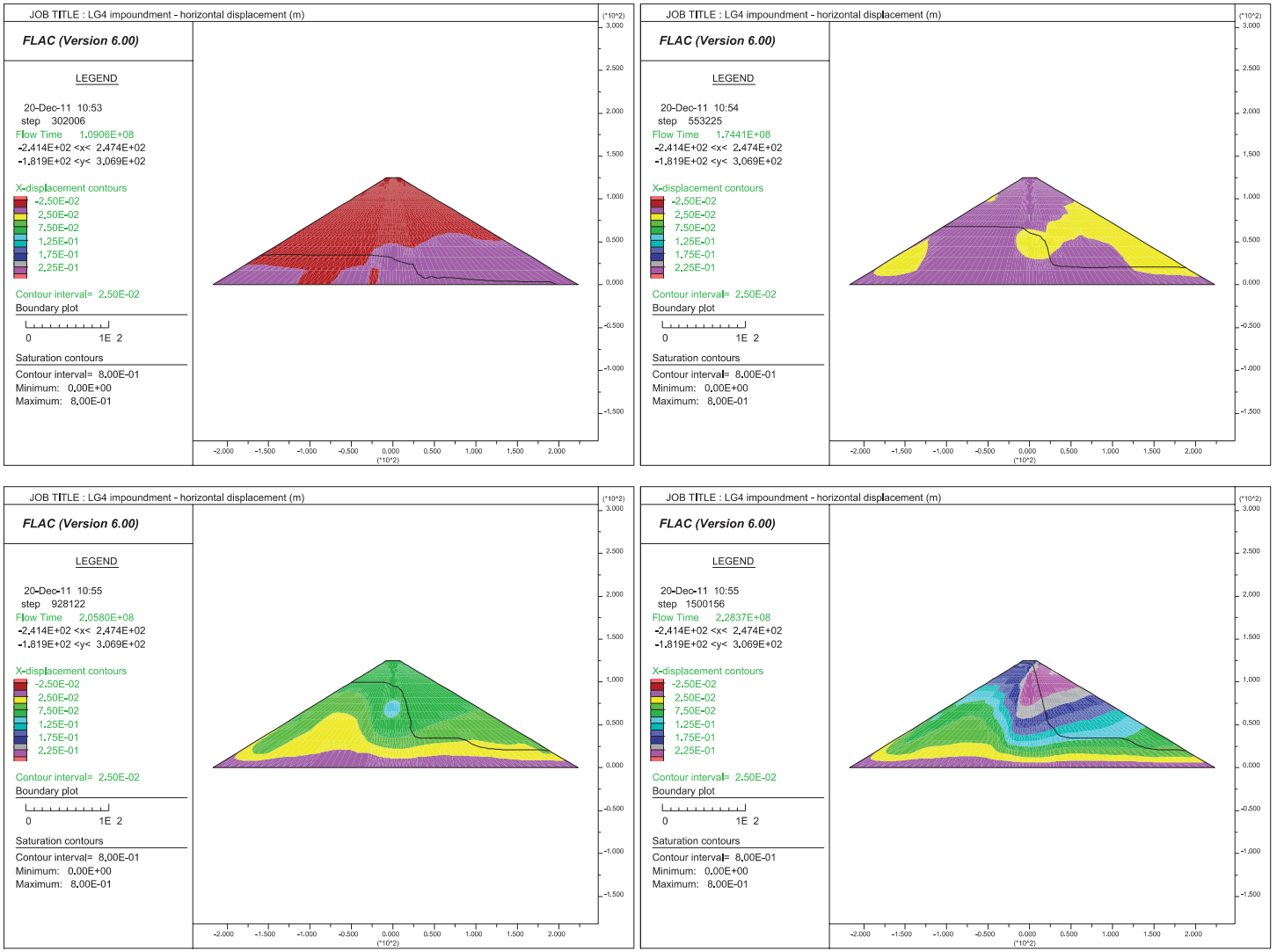

Figure 6-24 - horizontal displacement contours (m) during impoundment

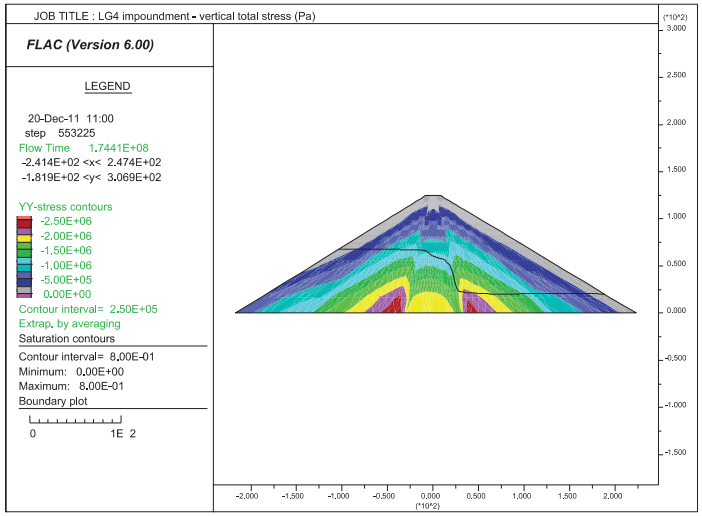

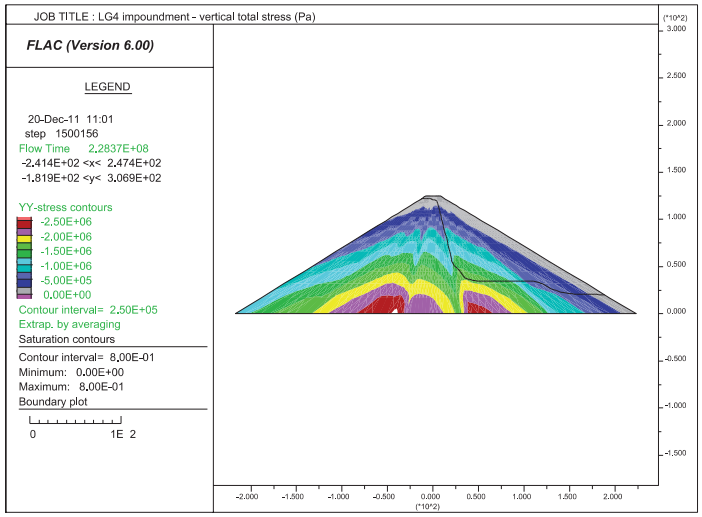

(a) Total stress

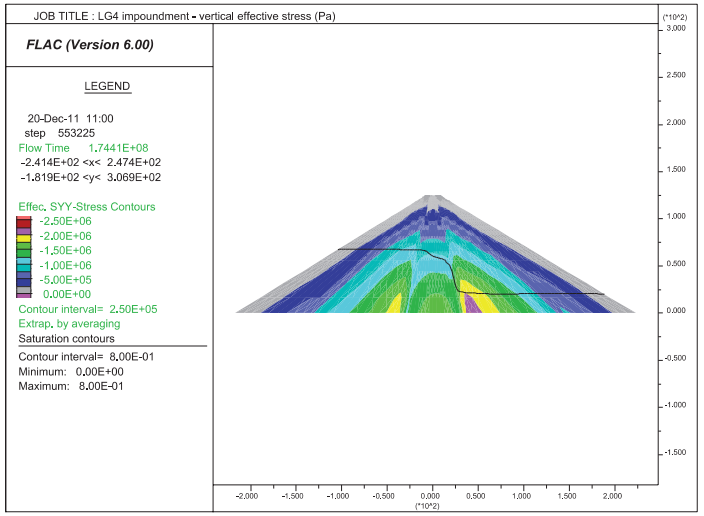

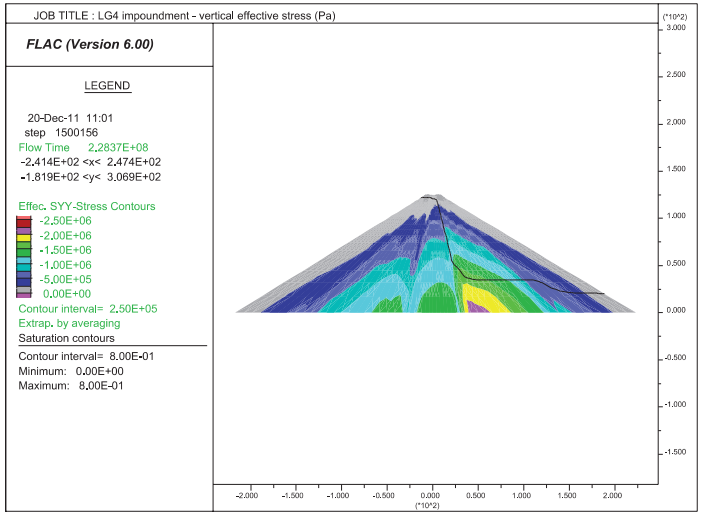

(b) Effective stress

Figure 6-25 - vertical stress contours (Pa) during impoundment

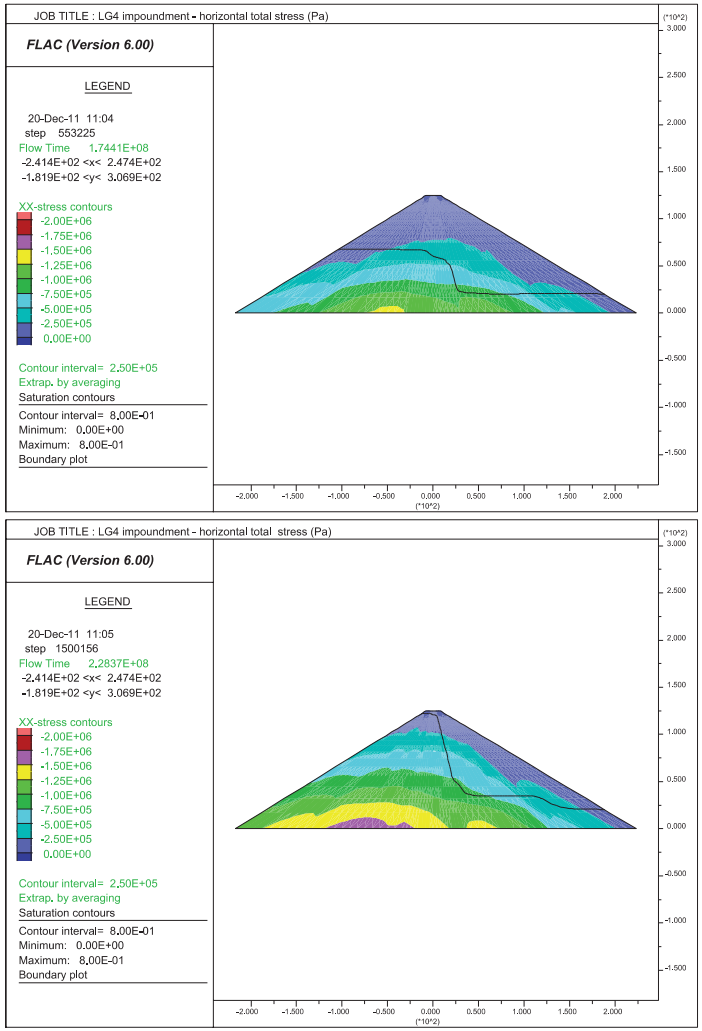

(a) Total stress

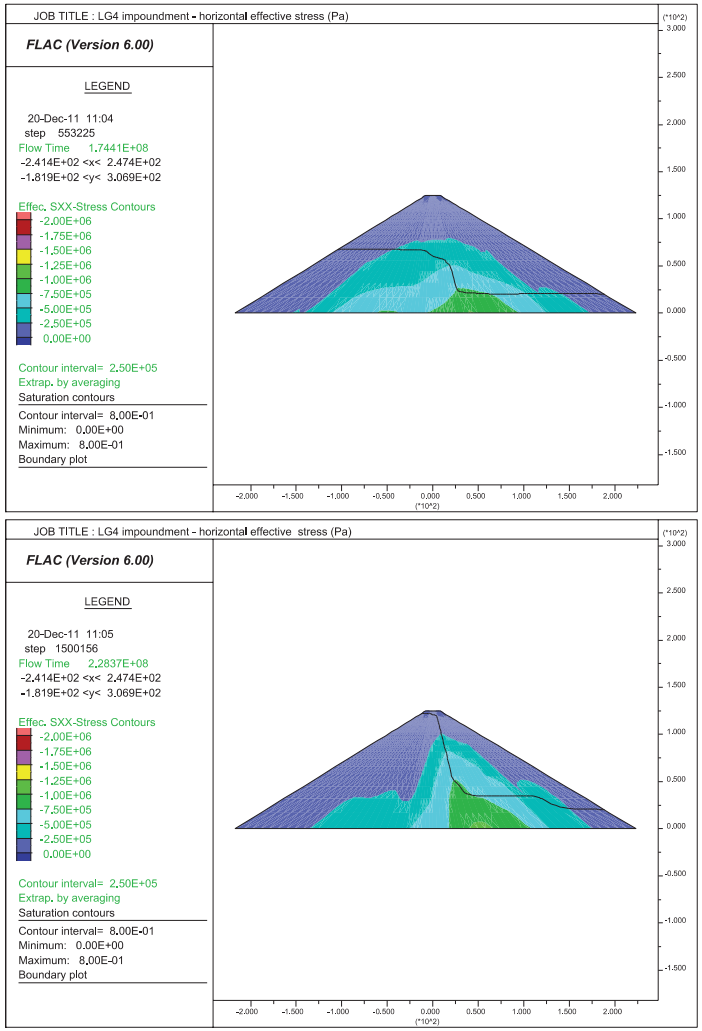

(b) Effective stress

Figure 6-26 - horizontal stress contours (Pa) during impoundment

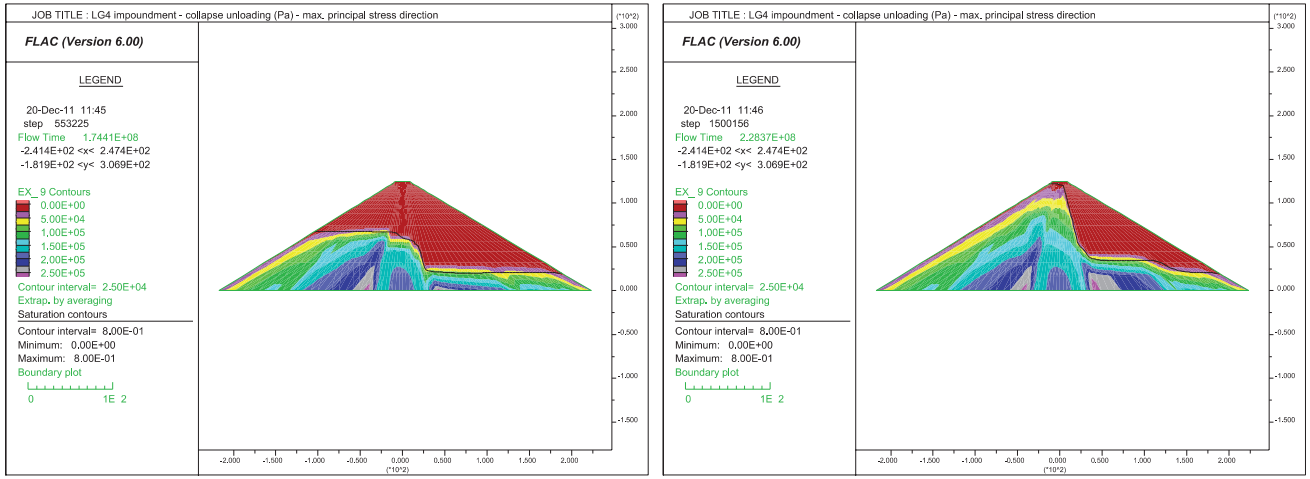

(a) maximum principal stress direction

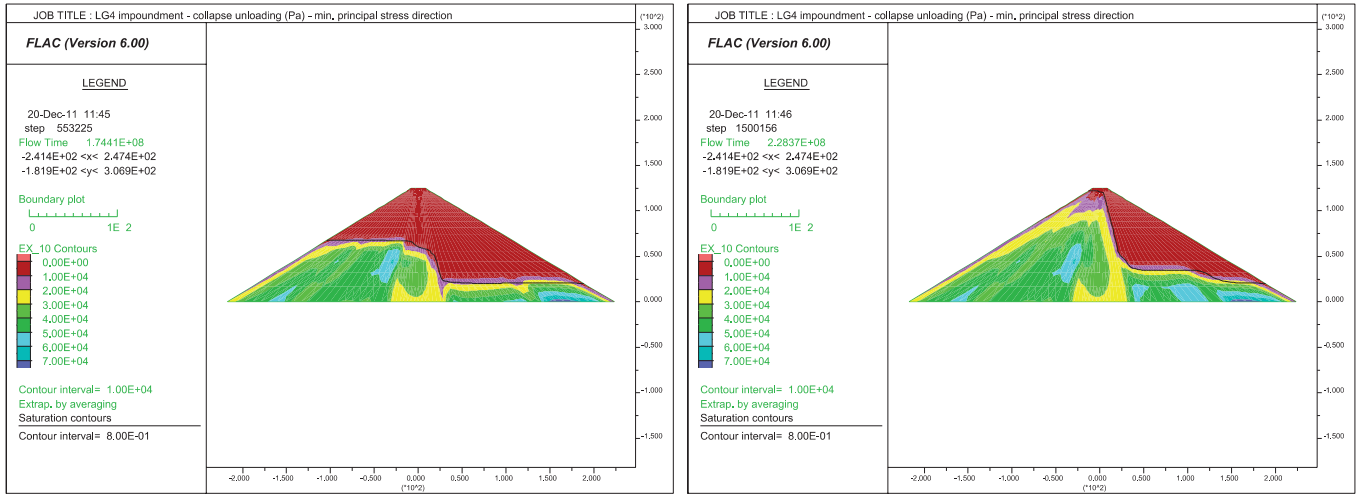

(b) minimum principal stress direction

Figure 6-27 – internal unloading stress of elements due to wetting collapse (Pa) during impoundment

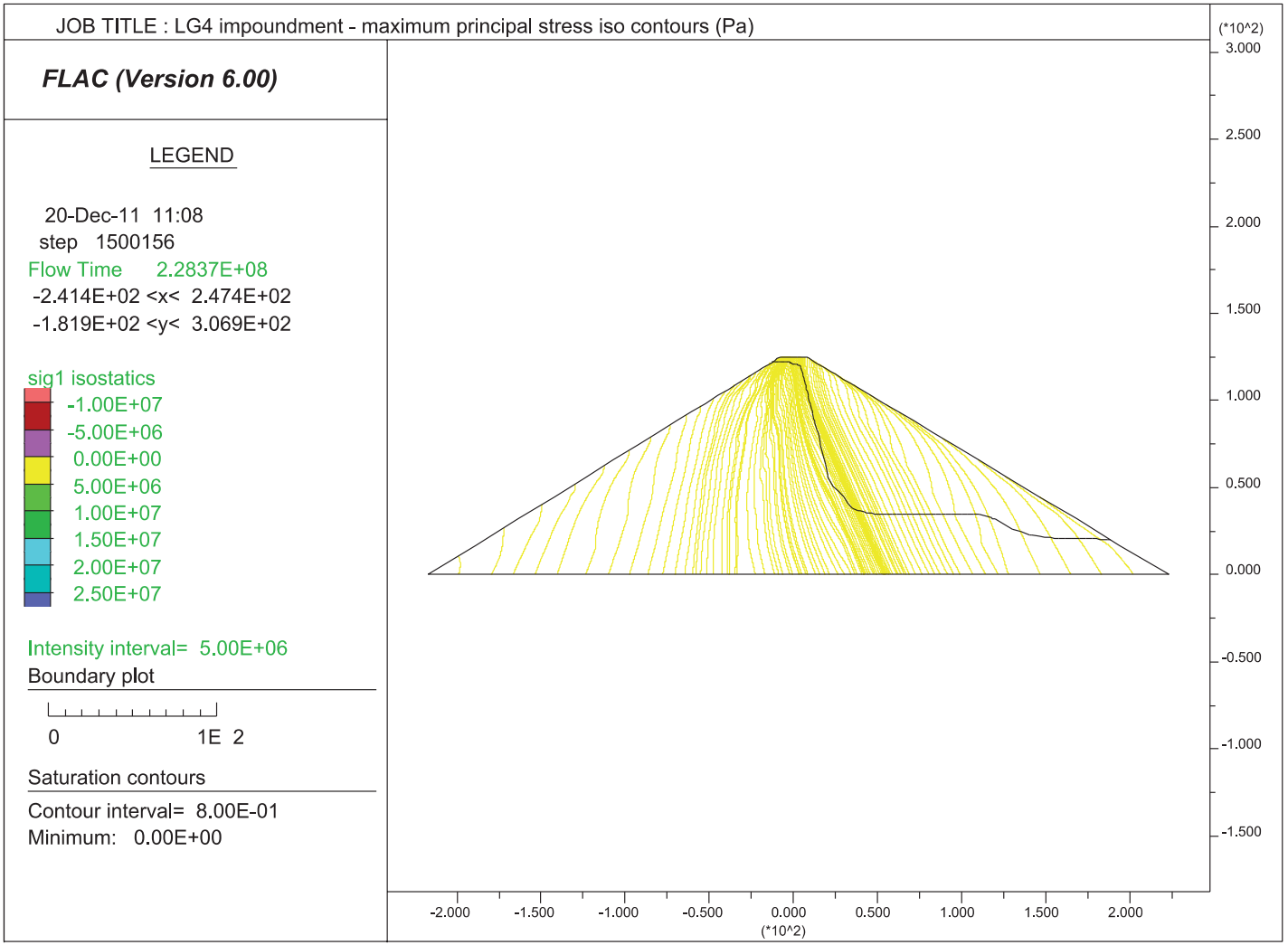

Figure 6-28 - maximum principal stress iso-contours (Pa) at the end of impoundment

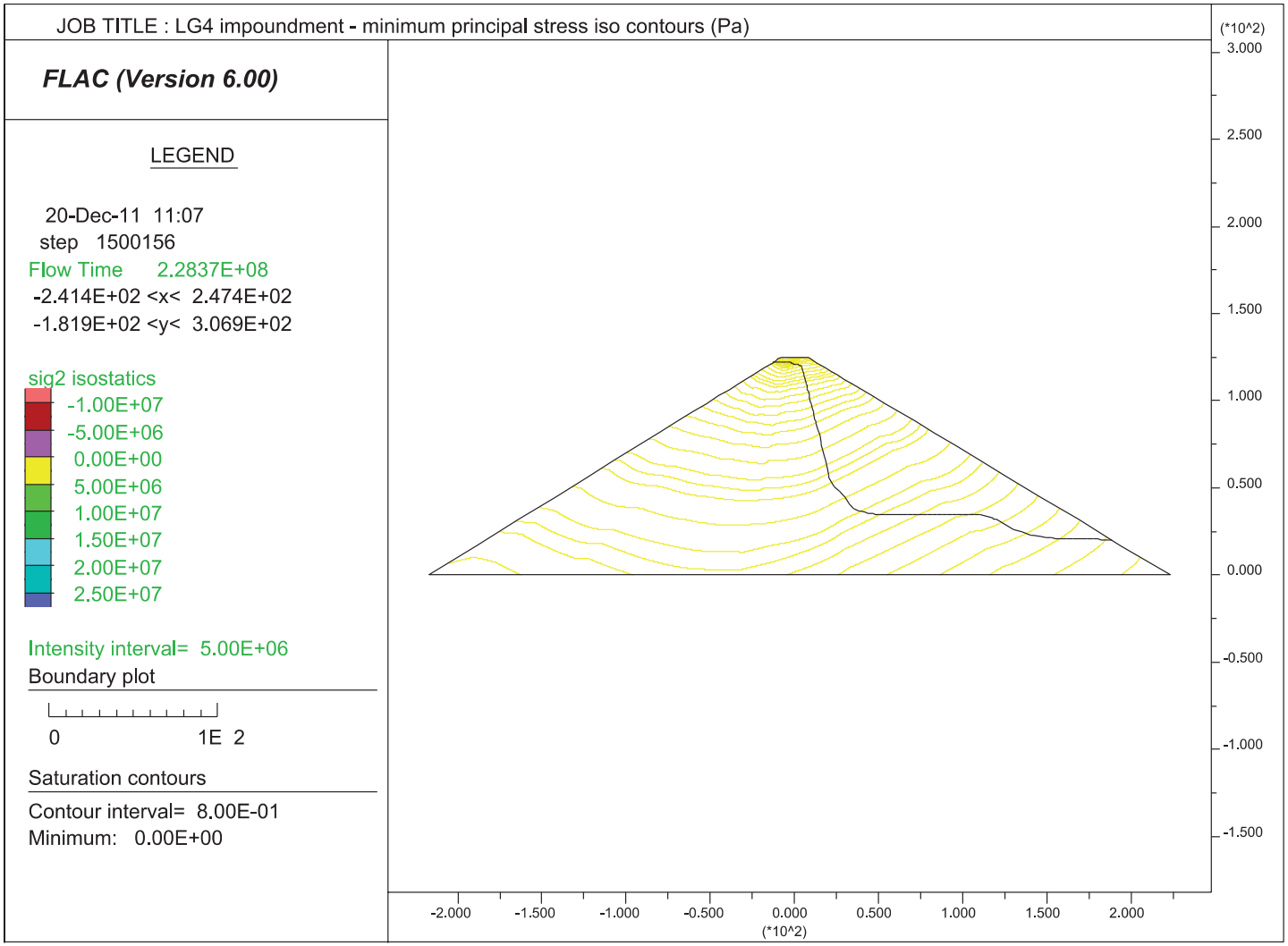

Figure 6-29 - minimum principal stress iso-contours (Pa) at the end of impoundment

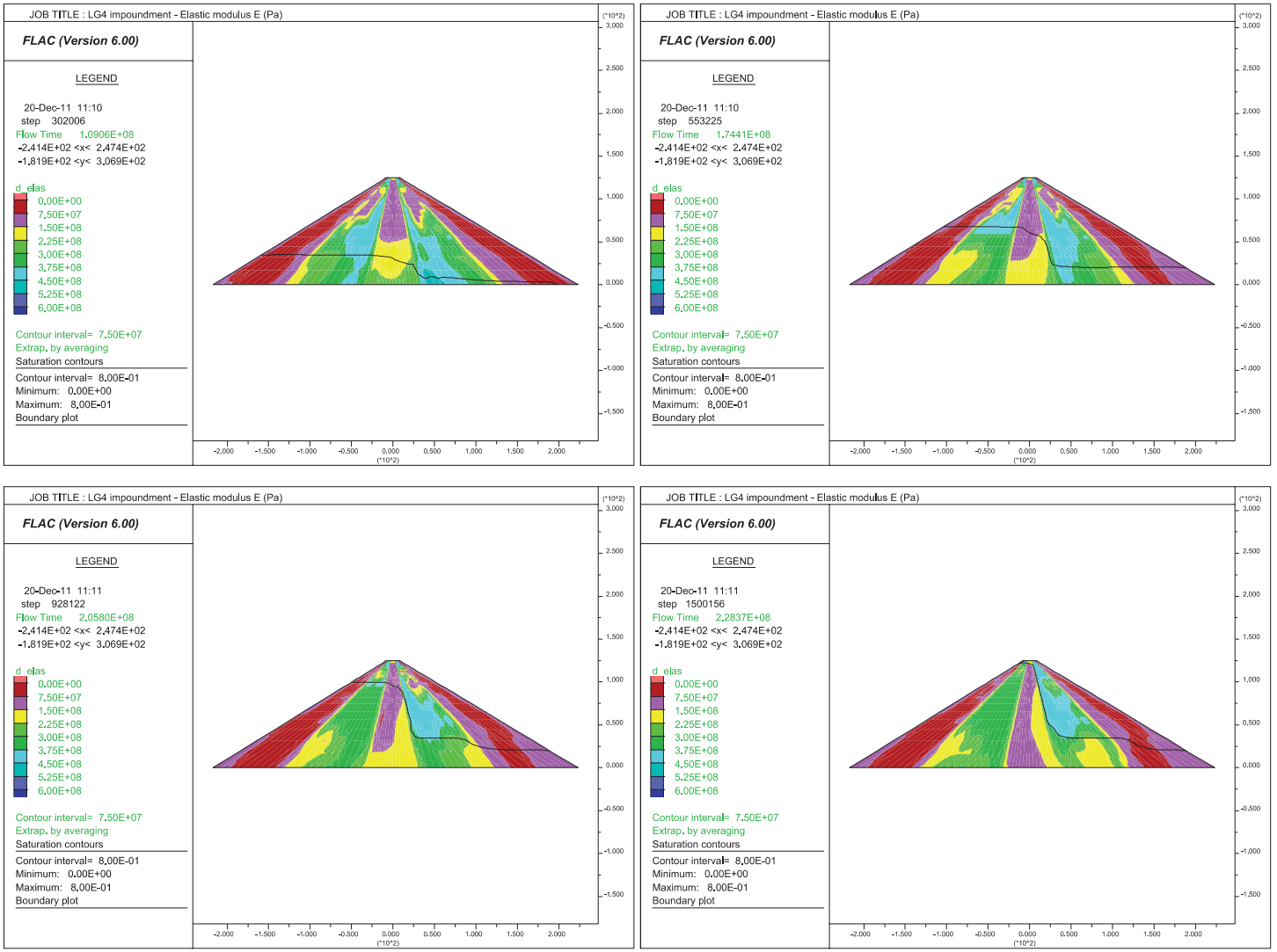

Figure 6-30 - elastic modulus (E) contours (Pa) during impoundment

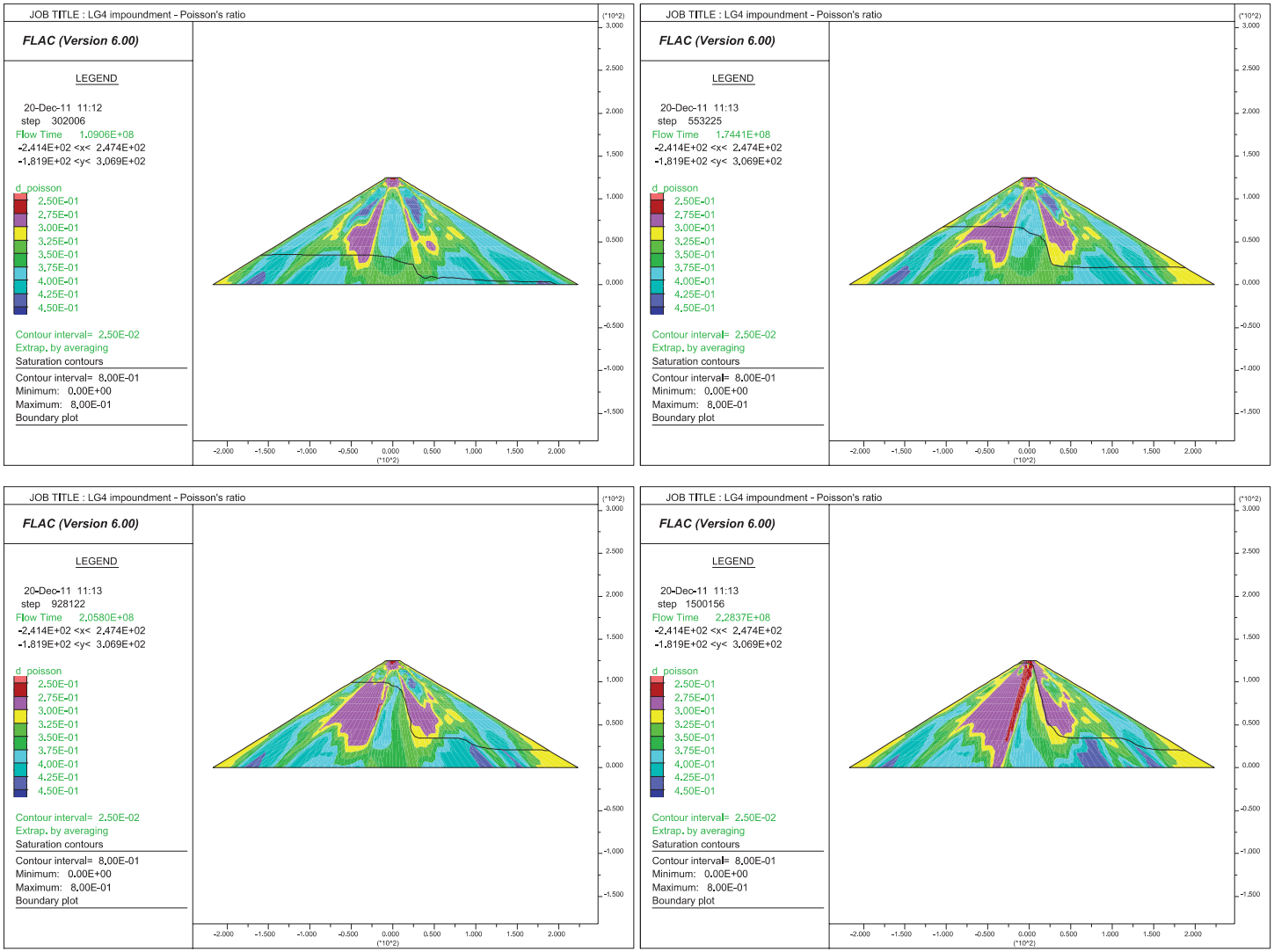

Figure 6-31 - Poisson's ratio contours during impoundment

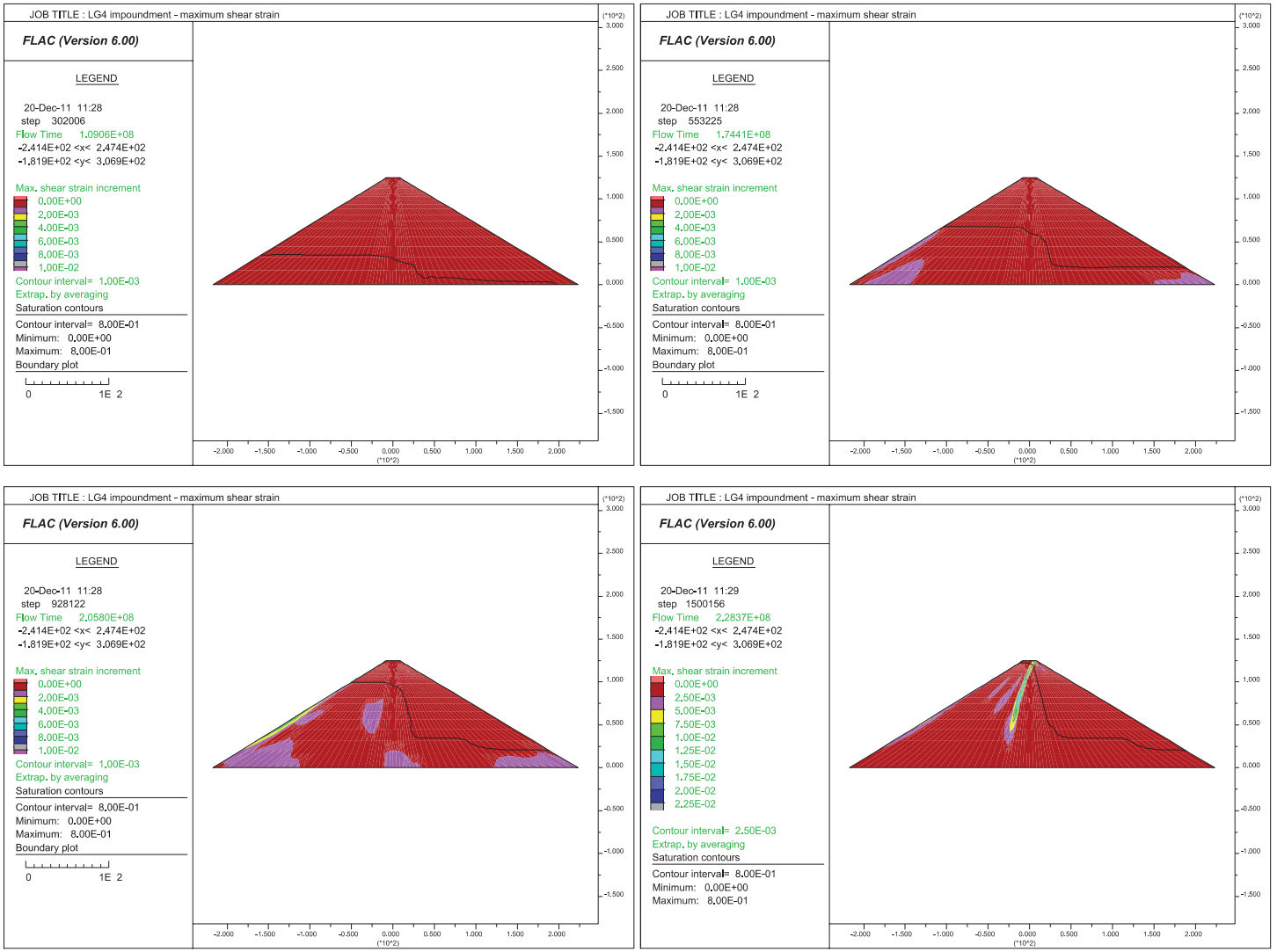

Figure 6-32 - maximum shear strain (γ) during impoundment

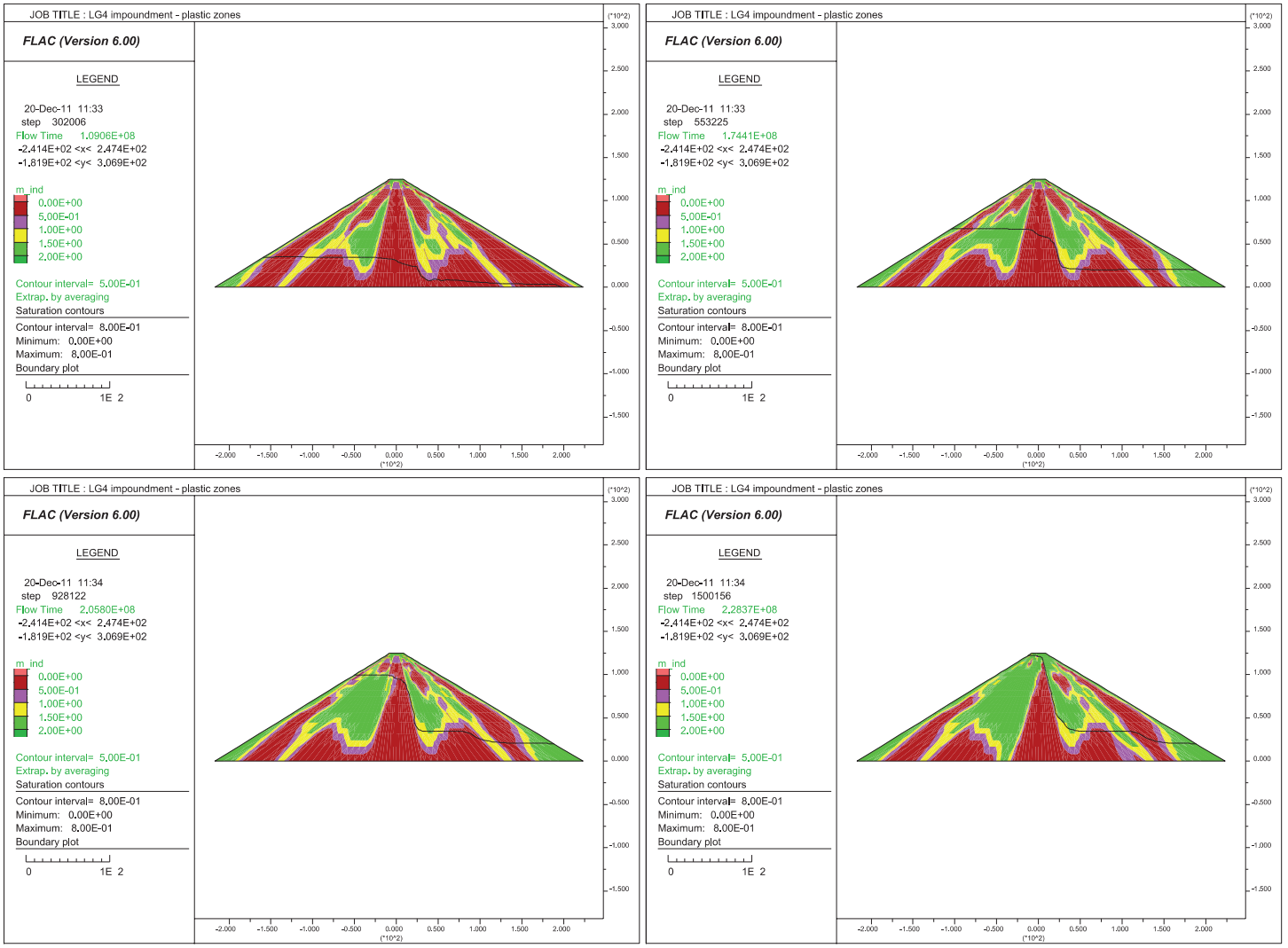

Figure 6-33 - zones reaching the failure envelope during impoundment (in green)